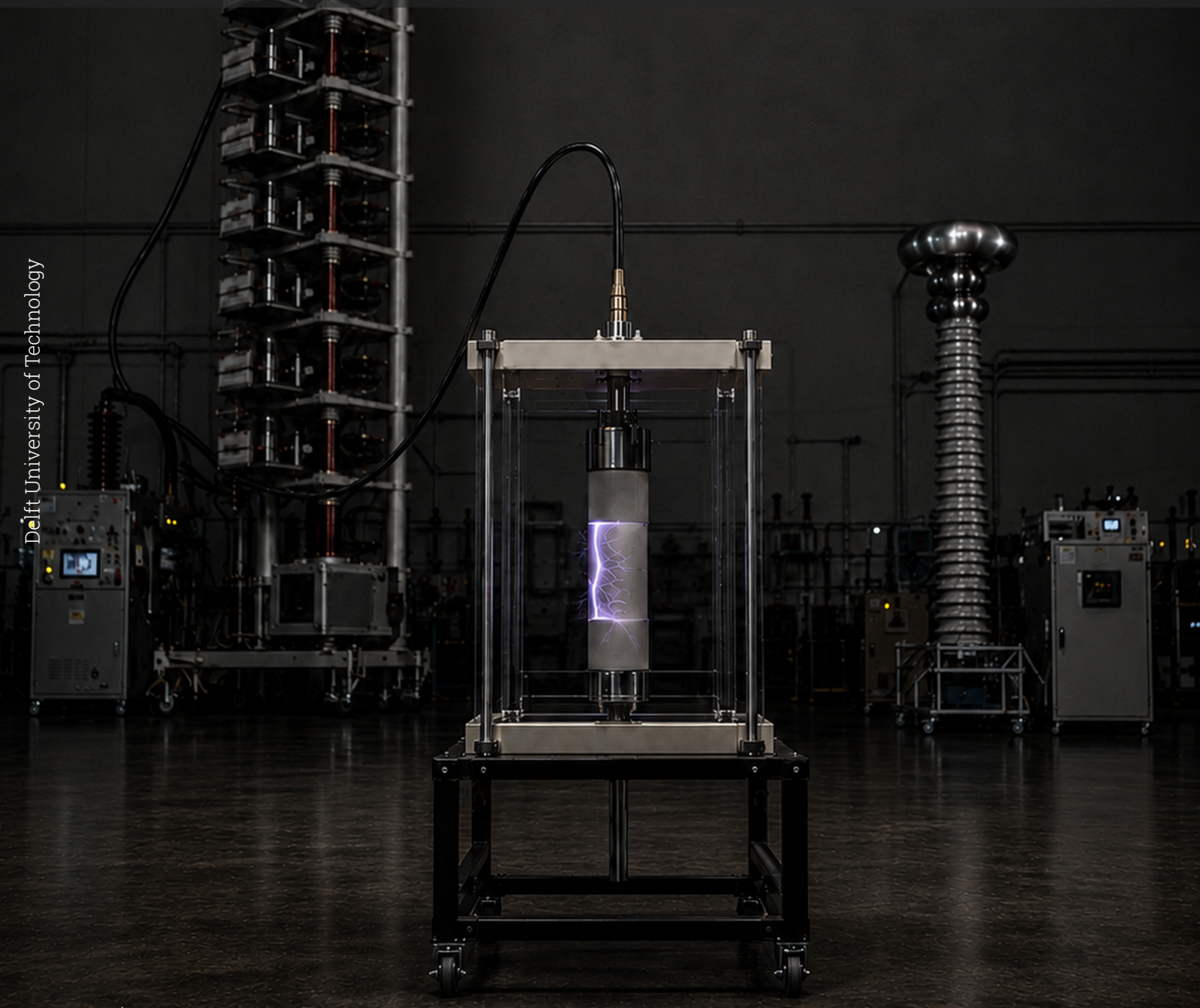
A Reduced Scale Test Bench for **Investigating** DC Spacer Flashover under Thermal Gradients

Bharat Naduvinamani



Delft University of Technology

TU Delft

HIGH VOLTAGE TECHNOLOGIES

A Reduced Scale Test Bench for Investigating DC Spacer Flashover under Thermal Gradients

Design, Simulation, and Experimental Method

Bharath Naduvinamani

Programme:	MSc Electrical Engineering – Electrical Power Engineering
Faculty:	Electrical Engineering, Mathematics and Computer Science
University:	Delft University of Technology
Student number:	6238505
Supervisor:	dr. ir. D. van der Born
Committee:	prof. ir. P.T.M. Vaessen Dr. W. (Wenli) Shi
Date:	19 August 2026

Delft University of Technology

Acknowledgements

The past two years at TU Delft have been an experience that I will remember for much more than the degree itself. Moving through the master's programme, and especially through this thesis, has changed the way I approach engineering problems. Many ideas that appeared simple at first became much less simple once they had to survive calculations, simulations, design constraints, and critical review. Somewhere between designs that had to be reconsidered, COMSOL models that refused to converge, and chapters that had to be rewritten more times than I would like to count, I learned that engineering is often as much about patience and judgement as it is about finding the right equation.

I would first like to thank my supervisor, Dr Dennis van der Born, for his guidance throughout this thesis. I am grateful for the discussions, questions, and technical feedback that helped me look at the work more critically and develop it further. More importantly, I appreciate the freedom I was given to explore the problem and make the project my own.

I would also like to thank Prof. Peter Vaessen. His lectures first introduced me to high-voltage engineering at TU Delft, and his feedback on this thesis repeatedly pushed me to ask a very useful question: can this be explained more clearly and more simply? The answer was usually yes. His comments have had a significant influence on the final form of this report and on the way I now think about communicating engineering work.

My thanks also go to everyone at the High Voltage Laboratory at TU Delft who contributed through technical discussions, practical advice, or simply by being willing to answer my questions. Working around people with experience in high-voltage engineering made it possible to see the difference between a design that works on paper and one that must eventually work in a laboratory.

Generative AI tools, including ChatGPT and Claude, were used during the preparation of this thesis for coding support, structuring and refining text, paraphrasing, and the creation or refinement of selected illustrative material. These tools supported the writing process; all technical decisions, interpretation, and final content remain my responsibility.

I am equally grateful to the friends I made during my time in Delft. The conversations, dinners, coffee breaks, celebrations, and occasional complaints about deadlines made the difficult parts of the master's considerably easier and the good parts much more memorable. Delft would not have been the same without them.

I would also like to thank my friends back home, who remained a constant part of my life despite the distance. Whether through long calls, messages or simply checking in from time to time, you gave me a sense of home even while I was far away. I am grateful that neither distance nor busy lives changed the friendships I carried with me to Delft.

Finally, I owe my deepest gratitude to my family. Their support has followed me much further than the distance between home and Delft. They have encouraged every decision that brought me here, remained patient through the difficult periods, and believed in me even when the next step was not always obvious. Whatever I have achieved during these years rests, in no small part, on the opportunities and confidence they gave me.

Looking back, I am grateful not only for what this thesis eventually became, but also for everything that did not work the first time. Those were often the parts from which I learned the most.

Bharat Naduvinamani
Delft, August 2026

Abstract

High-voltage direct current gas-insulated switchgear (HVDC GIS) uses a grounded enclosure and gas insulation to provide compact high-voltage equipment for DC transmission. Solid spacers support the high-voltage conductor and form the gas–solid insulation interface. Under DC conditions, the electric field distribution is governed mainly by the electrical conductivity of the insulation materials. The conductivity of epoxy is strongly temperature dependent. A temperature gradient across the spacer therefore changes the conductivity distribution and redistributes the electric field. The field also evolves during DC pre-stress as charge redistributes. This motivates investigation of how temperature gradient, gradient direction, voltage polarity, and DC pre-stress duration affect surface-flashover behaviour.

This thesis develops and numerically assesses a reduced-scale gas–epoxy test bench for future DC surface-flashover measurements. The design operates in atmospheric air near 1 bar with a maximum operating voltage of 50 kV DC. Either electrode can be heated to impose a temperature difference of 40–50 K without changing the field-defining electrode–spacer geometry. Two heating concepts were developed, together with a transparent chamber, diagnostic access, qualification requirements, and a test method. The electrode–spacer geometry was numerically verified against a reduced-scale coaxial GIS reference. The scientific contribution is an integrated methodology that combines the common test geometry, controlled thermal and electrical conditions, time-dependent electrothermal calculation, and a defined basis for future flashover measurements.

At 60 kV, the final electrode–spacer geometry reproduces the coaxial reference with differences of 0.8% in representative peak interface field and 2.2% in mean interface field. For the hot-oil numerical screening case with the HV electrode heated and the grounded electrode colder, the thermal gradient decreases the immediate hot-HV-edge field by about 13%, while the central minimum and grounded-side regional maximum increase by about 38% and 30%, respectively. The HV-to-GND regional-maximum ratio decreases from 1.77 to 1.34, showing a substantial redistribution of the DC interface field while the largest regional field remains on the HV side.

The time-dependent calculations further show that DC field formation is strongly position dependent. Between 1 and 12 h, the interval-based apparent relaxation times are about 3.2 h on the hot HV side and 15.8 h on the colder grounded side. The HV-side field is close to its stationary value after 12 h, whereas the grounded-side deviation remains about 3.9% after 24 h. Together with the non-monotonic central response, these results show that one common relaxation time cannot represent DC field formation along the complete spacer interface. Thermal condition and DC pre-stress duration must therefore be controlled in future flashover measurements. The developed test bench and test method provide the basis for the experimental investigation of RQ1–RQ3 after manufacture and physical qualification.

Contents

Acknowledgements i

Summary ii

Nomenclature xiii

1 Introduction 1
- 1.1 HVDC GIS and the spacer . . . 1
- 1.2 Surface flashover at the gas–solid interface . . . 1
- 1.3 The effect of a thermal gradient . . . 2
- 1.4 Knowledge gap and Objective . . . 3
- 1.5 Research questions and thesis approach . . . 3
- 1.6 Scope . . . 3
- 1.7 Thesis structure . . . 4

2 Theoretical Background 5
- 2.1 Gas discharge development in air . . . 5
- 2.2 electric field Formation under AC and DC Stress . . . 5
  - 2.2.1 Capacitive Field Distribution under AC and at DC Energisation . . . 6
  - 2.2.2 Charge Transport and Formation of the Resistive Field . . . 6
  - 2.2.3 Interfacial Polarisation and Relevant Time Scales . . . 8
  - 2.2.4 Charge-Controlled Evolution of the DC Electric Field . . . 9
- 2.3 Temperature Dependence of Conduction and Field Redistribution . . . 10
  - 2.3.1 Arrhenius Conductivity in Epoxy . . . 10
  - 2.3.2 Field Redistribution under a Thermal Gradient . . . 11
  - 2.3.3 Time Scales under a Thermal Gradient . . . 12
  - 2.3.4 Reduced Electric Field and Gas Density . . . 13
- 2.4 Surface Flashover and Critical Interface Regions . . . 13
- 2.5 Chapter conclusions . . . 15

3 DC Surface Flashover under Thermal Gradients 16
- 3.1 Framework for Evaluating the Literature . . . 16
- 3.2 DC Surface Flashover at Uniform Temperature . . . 16
- 3.3 Effects of Temperature on Gas–Solid Insulation . . . 18
- 3.4 DC Surface Flashover under a Temperature Gradient . . . 19
  - 3.4.1 Representation of the Thermal Condition . . . 19
  - 3.4.2 Evidence from Surface Charge and Electric Field . . . 21
  - 3.4.3 Evidence from Flashover Measurements . . . 21
  - 3.4.4 Gradient Direction and Voltage Polarity . . . 23
- 3.5 Predictive Scope and Validation of DC Spacer Models . . . 23
- 3.6 Transferability and the Remaining Experimental Gap . . . 25
  - 3.6.1 Transferability from SF_6 to Air . . . 25
  - 3.6.2 Comparison with the Closest Experimental Approaches . . . 25
  - 3.6.3 Coverage of the Required Experimental Conditions . . . 26
  - 3.6.4 Remaining Gap . . . 26
- 3.7 Chapter conclusions . . . 28

4 Design Methodology and Requirements 29
- 4.1 From the Research Questions to the Functional Requirements . . . 29
- 4.2 Functional Requirements . . . 30
  - 4.2.1 Electrical Stress and Voltage History . . . 30

4.2.2 Thermal Condition . . . 31
4.2.3 Environmental Condition . . . 31
4.2.4 Diagnostics and Traceability . . . 31
4.2.5 Assembly, Access, and Repeatability . . . 32
4.3 Governing Constraints . . . 33
4.3.1 Electrical Constraints . . . 33
4.3.2 Thermal and Material Constraints . . . 33
4.3.3 Environmental and Integration Constraints . . . 33
4.3.4 Safety Constraint . . . 34
4.4 Design-Decision and Qualification Framework . . . 34
4.5 Chapter conclusions . . . 36

5 Electrode and Spacer Geometry Design 37
5.1 Reference Coaxial Geometry . . . 37
5.2 Reference electric field Behaviour and Comparison Metrics . . . 38
5.3 Electrode-Profile Selection and First Geometry Screening . . . 39
5.4 Refinement of the Electrode-Spacer Geometry . . . 40
5.5 Verification against the Reference Geometry . . . 43
5.6 Chapter conclusions . . . 44

6 Thermal Management System 45
6.1 Thermal-System Design Requirements . . . 45
6.2 Heating-Concept Screening and Retained Architectures . . . 47
6.3 Hot-Oil Heating Architecture . . . 48
6.3.1 Heat-Transfer Path and Mechanical Integration . . . 49
6.3.2 HV Isolation and Remaining Checks . . . 50
6.4 Floating Cartridge-Heater Architecture . . . 50
6.4.1 Heater and Floating-Loop Design . . . 51
6.4.2 Mechanical and Electrical Integration . . . 51
6.4.3 Secondary-to-Ground Insulation Design and Screening . . . 52
6.5 Comparative Design Assessment . . . 54
6.6 Chapter conclusions . . . 55

7 Chamber, HV Connection and Housing 56
7.1 HV Connection and Electrode Support . . . 56
7.2 Chamber Enclosure and End Flanges . . . 57
7.3 Sealing and Chamber Retention . . . 59
7.4 Integrated Assembly . . . 60
7.5 Safety Provisions . . . 60
7.6 Chapter conclusions . . . 60

8 Coupled Electro-Thermal Simulation: Model Setup 62
8.1 Model Scope and One-Way Coupling . . . 62
8.2 Axisymmetric Geometry and Numerical Representation . . . 62
8.3 Material and Physical Models . . . 63
8.3.1 Thermal Model . . . 63
8.3.2 Air-Cavity Heat-Transfer Approximation . . . 63
8.3.3 Electrical Model and Temperature-Dependent Conductivity . . . 64
8.4 Boundary Conditions and Study Sequence . . . 65
8.4.1 Thermal Boundary and Initial Conditions . . . 65
8.4.2 Electrical Boundary Conditions and Study Sequence . . . 66
8.5 Numerical Verification . . . 66
8.6 Extracted Quantities and Comparison Basis . . . 66
8.7 Model Limitations . . . 68
8.8 Chapter conclusions . . . 68

9 Simulation Results 69
9.1 Thermal Response . . . 69
9.1.1 Whole-Domain Temperature Distribution . . . 69

9.1.2 Stationary Spacer Temperature Distribution . . . 70
9.1.3 Local Thermal Response . . . 70
9.2 Stationary DC Field Redistribution Under Thermal Conditions . . . 71
9.2.1 Whole-Domain electric field Distribution . . . 71
9.2.2 Coaxial Reference Response . . . 72
9.2.3 Test-Bench Interface-Field Redistribution . . . 73
9.3 Time-Dependent DC Field Formation . . . 74
9.3.1 Transient Interface-Field Development . . . 74
9.3.2 Whole-Interface Convergence . . . 75
9.3.3 Regional Relaxation . . . 76
9.4 Chapter conclusions . . . 76

10 Test-Bench Qualification and Experimental Method 78
10.1 Test Conditions . . . 78
10.2 Commissioning and Acceptance Tests . . . 79
10.3 Voltage Application . . . 79
10.4 Measurements . . . 81
10.5 Event Classification . . . 82
10.6 Reset Between Tests . . . 82
10.7 Test Matrix . . . 83
10.8 Data Analysis . . . 84
10.9 Chapter Conclusions . . . 85

11 Discussion 86
11.1 Design Evidence and Experimental Boundary . . . 86
11.2 DC Pre-Stress and Flashover Interpretation . . . 86
11.3 Interpretation of the DC Field Redistribution . . . 87
11.4 Competing Influences on the Earliest Visible Discharge Region . . . 88
11.5 Uncertainty, Transferability, and Evidence Boundaries . . . 89
11.6 Chapter conclusions . . . 90

12 Conclusion 91
12.1 Recommendations . . . 92

References 93

A Detailed Engineering Drawings 102
A.1 Final Assembly and Interface Integration . . . 103
A.2 Electrode–spacer assembly . . . 104
A.3 Electrode–adaptor–aluminium-rod assembly . . . 105
A.4 Hot-oil U-manifold assembly and component details . . . 107
A.5 PEEK end-flange assembly and sealing details . . . 111
A.6 PMMA chamber tube, tie rods, and chamber stack . . . 115
A.7 PMMA chamber tube, tie rods, and chamber stack . . . 118
A.8 PMMA chamber tube, tie rods, and chamber stack . . . 121
A.9 PMMA chamber tube, tie rods, and chamber stack . . . 124

B Material Specifications for Test-Bench Construction 126
B.1 Purpose and Scope . . . 126
B.2 Material Specifications . . . 126
B.3 Materials of the Alternative Heating Architectures . . . 128
B.3.1 Hot-Oil Architecture . . . 128
B.3.2 Floating Cartridge-Heater Architecture . . . 128
B.3.3 PMMA chamber tube . . . 128
B.4 Material Documentation Required Before Construction . . . 129
B.5 Boundary with the Engineering-Drawing Appendix . . . 129

C Thermal Sizing of the Hot-Oil Circulation Loop 130
C.1 Purpose and calculation method . . . 130
C.2 Design inputs . . . 130

C.3 Flow regime and pressure loss . . . 130
C.4 Heat demand and required oil temperature drop . . . 132
C.5 Pump and reservoir sizing . . . 133
C.6 Bend-radius check . . . 134
C.7 Preliminary hydraulic specification . . . 134
C.8 Proposed Control and Protection Logic . . . 134

D Preliminary Electrical Sizing of the Floating Cartridge-Heater Circuit 137
D.1 Purpose and Design Basis . . . 137
D.2 Preliminary Heater Rating . . . 137
D.3 Floating-Loop Conductor and Resistive Losses . . . 138
D.4 Heater-Power Control and Thermal-Control Logic . . . 139
D.5 Preliminary Cartridge-Heater Selection . . . 140
D.6 Common-Mode Insulation of the Floating Secondary . . . 142
D.6.1 Model Geometry . . . 142
D.6.2 Electric-Field Screening . . . 143
D.7 Preliminary Specification and Remaining Checks . . . 144

E Pressure Force and Tie-Rod Capacity Check 146
E.1 Purpose and design pressure . . . 146
E.2 Force acting on one end flange . . . 146
E.3 Design load shared by the tie rods . . . 147
E.4 Capacity of one M10 tie rod . . . 147
E.5 Conservative check including preload . . . 147
E.6 Result and limitations . . . 148

F Derivation and Assessment of the Effective Air-Cavity Conductivity 149
F.1 Modelling choice and scope . . . 149
F.2 Representative geometry and calculation inputs . . . 149
F.3 Rayleigh–Nusselt derivation . . . 151
F.3.1 Rayleigh number . . . 151
F.3.2 Nusselt correlation and selected multiplier . . . 151
F.4 Full-domain implementation and numerical assessment . . . 152
F.4.1 COMSOL implementation . . . 152
F.4.2 Resolved-convection assessment . . . 152
F.4.3 Temperature-profile consistency check . . . 153
F.5 Limitations and future refinement . . . 153
F.6 Reproducibility summary . . . 154

G COMSOL Model Definition and Reproducibility 155
G.1 Model architecture and studies . . . 155
G.2 Domains, material properties and boundary conditions . . . 156
G.3 Mesh, study sequence and solution transfer . . . 157
G.4 Post-processing definitions and model boundary . . . 158

H Qualification of the Reset Procedure and Run-to-Run Independence 159
H.1 Purpose and Operational Definition . . . 159
H.2 Sources of Carry-Over . . . 159
H.3 Reset Procedure and Long-Reset Reference . . . 160
H.3.1 Check for Initial Apparatus Conditioning . . . 160
H.3.2 Physical Reset . . . 160
H.3.3 Long-Reset Reference . . . 161
H.4 Measured Reset Indicators . . . 161
H.4.1 Thermal and Environmental State . . . 161
H.4.2 Grounded-System Current . . . 161
H.4.3 Current During the Prescribed Voltage Waveform . . . 162
H.4.4 Selected Surface-Potential Measurements . . . 162
H.5 Carry-Over Qualification Experiment . . . 162
H.5.1 Reference Condition and Test Matrix . . . 162

H.5.2 Execution and Recorded Responses 163
H.6 Statistical Assessment and Acceptance 164
H.6.1 Practical Equivalence 164
H.6.2 Ordered-Sequence Checks 164
H.6.3 Decision Rule 165
H.7 Campaign Monitoring and Required Records 166
H.8 Summary 166

List of Figures

1.1 Spacer location and reduced-scale test region . . . 2
1.2 Research questions and required test-bench functions . . . 4
1.3 Structure of the thesis from the theoretical basis to design, numerical assessment, and conclusion. . . . 4

2.1 Schematic radial electro-thermal profiles across the spacer under a thermal gradient. . . 12
2.2 Surface-flashover path and interface-field peaks . . . 14

3.1 Arrangement-specific time scales reported under uniform-temperature DC stress, comparing reconstructed surface charge, experimental flashover endpoints, and calculated field evolution, without treating them as one common relaxation curve [7], [27], [44], [45]. 17
3.2 Simplified comparison of the principal experimental arrangements used to study DC spacer behaviour under a thermal gradient (not to scale). Geometry, thermal direction, gas condition, voltage history, and measured endpoint changed together between studies. Based on Refs. [9], [10], [14], [15], [45], [50], [51], [52]. . . . 20
3.3 Selected quantitative evidence for temperature and thermal-gradient effects: gas-side breakdown (a), surface-potential response (b), statistical flashover voltage (c), and near-flashover maximum field (d), each from a different arrangement. Data reported by Hering et al. [40], Ma et al. [50], and Pan et al. [15]. . . . 22
3.4 Predictive scope and validation boundary of DC spacer models: the quantities a calibrated calculation can provide, and those that remain experimental endpoints. Synthesised from Winter and Kindersberger [5], Schueller et al. [7], Schueller et al. [11], Ma et al. [50], Zhao et al. [56], and Gremaud et al. [14]. . . . 24
3.5 How the closest previous studies and this thesis cover the conditions the intended test method needs. A blank or open mark means a condition was not covered; it does not mean the study was weak. . . . 27

4.1 Main functions of the proposed test bench. Voltage control, temperature control, air conditions, measurements, and assembly all support the same spacer test region. The lower band separates the work developed in this thesis from the physical tests still required before experiments can begin. . . . 30
4.2 Decision and qualification framework for design options. Selection is a design decision, not physical qualification. . . . 35

5.1 Reduced-scale coaxial reference geometry adopted from Li [60]. . . . 37
5.2 COMSOL implementation of the reduced-scale coaxial reference geometry. . . . 38
5.3 Field behaviour extracted from the coaxial reference case . . . 38
5.4 Early electrode–spacer profile screening cases. . . . 40
5.5 Intermediate electrode-spacer geometry and calculated electric field behavior for the 100 mm spacer case. . . . 41
5.6 Finalised electrode–spacer geometry and its electric field behaviour. . . . 42
5.7 Quantitative verification of the finalised electrode–spacer geometry against the reduced-scale coaxial GIS reference. . . . 43
5.8 Background electric field magnitude for the finalised electrode-spacer geometry and the coaxial reference case. . . . 43

6.1 Definition of the axial temperature difference for the HV-hot condition. . . . 46
6.2 Thermal-control architecture for the hot-oil and floating cartridge-heating concepts. . . 46
6.3 Hot-oil heating architecture for the HV-hot configuration. . . . 48
6.4 Internal assembly and flow path of the hot-oil module. . . . 49

6.5 PEEK U bend and mechanical tube-retention arrangement. 50
6.6 Power-transfer architecture of the HV-floating cartridge-heater circuit. 51
6.7 Internal integration of the floating cartridge-heater circuit: (a) heater and lead routing and (b) terminal arrangement. 52
6.8 Centred support and insulation arrangement of the floating conductor through the grounded transformer window. 53
6.9 electric field distribution for the centred floating conductor at the 60 kV numerical screening case. 54

7.1 HV-side cap–rod–adaptor–electrode assembly. 56
7.2 Mechanical details of the HV-side connection. 57
7.3 PMMA chamber tube and PEEK end-flange arrangement. Schematic, not to scale. 58
7.4 Split PEEK chamber-end feedthrough and sealing interfaces. Schematic, not to scale. . . 59
7.5 Integrated chamber, electrode-spacer and rod assembly in the HV-hot configuration. Schematic, not to scale. 61

8.1 Axisymmetric model and principal material domains 63
8.2 Comparison of air-cavity thermal representations 64
8.3 Numerical study sequence and applied voltage profile 65

9.1 Stationary temperature distribution of the test bench under the 100 °C upper thermal-design condition. 69
9.2 Stationary spacer-interface temperature profiles for the two heating concepts and the coaxial reference under the 100 °C upper thermal-design condition. 70
9.3 Temperature response at the midpoint P_T of the spacer-gas interface and corresponding first-order fits for the two heating concepts. 71
9.4 Whole-domain electric field distribution of the integrated test-bench geometry for the 60 kV numerical screening case. 71
9.5 Coaxial reference geometry showing the upper and lower spacer-gas interfaces used for the electric field profiles. 72
9.6 Stationary electric field magnitude along the upper and lower spacer–gas interfaces of the coaxial reference, with and without the imposed temperature gradient. 72
9.7 Stationary electric field magnitude along the test-bench spacer–gas interface for the temperature-independent reference and the two HV-hot thermal cases at the 60 kV numerical screening case. 73
9.8 Early development of the spacer–gas interface field for $\Delta T = 51.6$ K, compared with the stationary DC distribution. 74
9.9 Later development of the spacer–gas interface field for $\Delta T = 51.6$ K, compared with the stationary DC distribution. 75
9.10 Whole-interface deviation from the stationary DC field distribution for the two HV-hot thermal cases. 75

10.1 Commissioning and acceptance map for the test bench. 80
10.2 Voltage application sequence for one test; time intervals are not to scale. 81
10.3 Measurement arrangement and synchronised acquisition. 81
10.4 Classification and treatment of test outcomes. 82

A.1 Visual overview of the integrated test-cell assembly. The schematic is not to scale and is included only to illustrate the integration of the main components. 103

C.1 Proposed control and protection logic for the hot-oil heating system. The selected hot-side electrode is temperature-controlled, while the realised gradient is checked only after the thermal state has stabilised. 135

D.1 Proposed control and protection logic for the floating cartridge-heater circuit in the HV-hot configuration. The HV-electrode temperature is the controlled variable. The grounded-electrode temperature and the realised $|\Delta T|$ are acceptance checks after thermal stabilisation, not independent controller targets. Electrical power crosses the HV boundary only by magnetic coupling, while the temperature feedback crosses it through the fibre-optic measurement. 141
D.2 Geometry used for the 60 kV common-mode insulation screening of the floating secondary. 143
D.3 Electric-field magnitude around the floating cable for the 60 kV common-mode design case. Representative local field values are taken away from mesh-sensitive singular points. 144

E.1 Projected pressure area used in the tie-rod check. The same internal pressure acts over both regions. 147

F.1 Relationship between the simplified derivation geometry and the complete implementation domain. The Rayleigh–Nusselt screening calculation uses a representative 45 mm electrode–spacer air layer. The resulting multiplier is subsequently applied uniformly to the complete enclosed-air domain as a reduced-order approximation. 150
F.2 Spacer-temperature profiles obtained using conduction and radiation only, resolved natural convection in the simplified electrode–spacer geometry, and the final effective-conductivity model $k_{\mathrm{air,eff}}(T) = 4.5k_{\mathrm{air}}(T)$. The resolved-flow profile is used as a qualitative consistency check and not as validation of the complete chamber. 153

G.1 Final numerical representation of the test bench. The spacer–air interface used for electric-field extraction is the exposed epoxy boundary between the two electrode regions in panel (a). 156
G.2 Local view of the final physics-controlled mesh. The *Extremely fine* setting produces dense refinement around the spacer and electrode regions and progressively larger elements toward the outer chamber. 157

List of Tables

2.1 Dominant processes during AC stress and successive stages of DC stress. 7

3.1 Literature gaps and corresponding requirements for the intended method. 28

4.1 Consolidated functional requirement register. 32
4.2 Governing constraint register. 34

5.1 Dimensions of Li's demonstrator and reduced-scale coaxial reference model [60]. 37
5.2 electric field comparison metrics derived from the coaxial reference case at 60 kV DC. The coaxial-reference field profile is the pointwise mean of the upper and lower gas–spacer interface-field profiles. 39

6.1 Chapter 6 design response to the thermal requirements of Chapter 4. 47
6.2 Screening of candidate heating methods. 48
6.3 Comparison of the retained thermal-management architectures. 55

9.1 Stationary spacer–gas interface field metrics for the temperature-independent reference and the two HV-hot thermal cases. 74
9.2 Local deviation from the stationary DC field distribution at the three reference locations. Negative values indicate a transient field below the stationary value. 76

10.1 Test variables, controlled conditions, required records, and model-derived quantities. . 78
10.2 Test matrix and matched comparisons for RQ1–RQ3. 83

11.1 Interpretation limits for the principal future flashover observations. 89

B.1 Design-critical material specifications for the proposed test bench. 126
B.2 Minimum material documentation required for construction. 129

C.1 Inputs used for the preliminary hydraulic sizing. 130
C.2 Flow velocity and Reynolds number for the candidate flow range. 131
C.3 Calculated tube pressure loss and preliminary design pressure loss. 132
C.4 Preliminary hydraulic specification of the hot-oil loop. 134
C.5 Functional control requirements of the hot-oil system. 136

D.1 Functional control and measurement requirements for the floating cartridge-heater circuit. 140
D.2 Representative local electric-field levels from the 60 kV transformer-window screening model. 144
D.3 Preliminary design basis for the floating cartridge-heater circuit. 145

E.1 Summary of the tie-rod design check. 148

F.1 Inputs used to reproduce the Rayleigh–Nusselt screening calculation. 150
F.2 Calculated Nusselt-number branches and the selected reduced-order value. 152
F.3 Summary of the resolved-convection model assessment. 153
F.4 Reproducibility summary for the effective air-cavity conductivity treatment. 154

G.1 Final COMSOL model and study configuration. 155
G.2 Thermal and electrical properties used in the final model. 156

H.1 Possible sources of carry-over between successive runs. 160

H.2 Basic carry-over qualification matrix. 163
H.3 Acceptance criteria for the reset and independence qualification. 166
H.4 Minimum record for reset and carry-over qualification. 166

Nomenclature

This nomenclature lists the abbreviations, material designations, and symbols used repeatedly across the thesis or central to its main physical, numerical, and experimental arguments. Symbols used only in individual design calculations or appendices are defined locally where they first appear. Bold symbols denote vectors.

Abbreviations and material designations

Abbreviation	Meaning
AC	Alternating current
DC	Direct current
FKM	Fluoroelastomer (material designation)
FR	Functional requirement
GIS	Gas-insulated switchgear
GND	Ground or grounded side
HV	High voltage or high-voltage side
HVDC	High-voltage direct current
IEC	International Electrotechnical Commission
PFA	Perfluoroalkoxy alkane
PEEK	Polyether ether ketone
PMMA	Poly(methyl methacrylate)
PTFE	Polytetrafluoroethylene
RH	Relative humidity
RQ	Research question

Symbols

Symbol	Description	Unit
Electrical and interface-field quantities		
$\mathbf{D}$	Electric flux density	$\mathrm{C\,m^{-2}}$
$\mathbf{E}$, E	Electric field vector and its magnitude	$\mathrm{V\,m^{-1}}$
E/N	Reduced electric field	$\mathrm{V\,m^{2}}$
E_n, E_t	Normal and tangential electric field components at the spacer–gas interface	$\mathrm{V\,m^{-1}}$
I_g	Grounded-system or earth-return current	A
$\mathbf{J}$, J	Current-density vector and its magnitude	$\mathrm{A\,m^{-2}}$
ε	Absolute permittivity	$\mathrm{F\,m^{-1}}$
ε_r	Relative permittivity	–
ρ_s	Surface-charge density	$\mathrm{C\,m^{-2}}$
σ	Electrical conductivity	$\mathrm{S\,m^{-1}}$
$\sigma_{\mathrm{ep}}(T)$	Temperature-dependent bulk electrical conductivity of epoxy	$\mathrm{S\,m^{-1}}$
τ_d	Dielectric relaxation time, ε/σ	s or h
Thermal and reduced-order model quantities		
k	Thermal conductivity	$\mathrm{W\,m^{-1}\,K^{-1}}$
$k_{\mathrm{air,eff}}(T)$	Effective air thermal conductivity used in the reduced-order cavity model	$\mathrm{W\,m^{-1}\,K^{-1}}$
Nu_{eff}	Selected effective Nusselt-number multiplier for the enclosed-air approximation	–
Ra	Rayleigh number used to screen the importance of natural convection	–
T	Temperature	K or °C
T_{HV}, T_{GND}	High-voltage- and grounded-electrode temperatures	K or °C
ΔT	Electrode temperature difference, $T_{\mathrm{HV}} - T_{\mathrm{GND}}$	K
Pre-stress, flashover, and post-processing quantities		
t_{pre}	DC pre-stress duration measured from completion of the voltage ramp	s or h
U_{pre}	Selected DC pre-stress voltage	V
V_F	Recorded voltage of a confirmed complete surface flashover	V
V_{50}	Voltage corresponding to 50 % surface-flashover probability	V
$D_E(t)$	Normalised L_2 deviation of the transient interface-field profile from the stationary profile	%
$r_j(t)$	Relative residual of the transient field from the stationary field at reference location j	–
$\tau_{\mathrm{app},j}$	Interval-based apparent electrical relaxation time at reference location j	s or h
Γ	Spacer–gas interface extraction path	–
ξ	Normalised spacer-interface coordinate, s/L_{spacer}	–

1 Introduction

1.1. HVDC GIS and the spacer

Meeting the energy transition requires moving large amounts of power over long distances, across borders, and from offshore wind farms to onshore demand. ENTSO-E identifies 224 GW of additional cross-border transmission capacity as economically efficient for Europe by 2050, together with roughly 54,000 km of offshore transmission routes in European waters [1], [2].

High-voltage direct current (HVDC) is central to this expansion. It suits long cable links, offshore wind connections, interconnectors between asynchronous grids, and corridors where a wide right-of-way is unavailable. In these applications the equipment must provide the required withstand voltage within a limited volume. Gas-insulated switchgear (GIS) meets this by insulating with pressurised gas rather than air, which allows a much smaller enclosure [2].

This compactness is the main reason to choose GIS for HVDC. DC GIS uses up to 95% less space than equivalent air-insulated switchgear. It reduces the footprint of a transition station, where an overhead line meets underground cable; by up to 90%. The size of an offshore converter platform falls by up to 10% [3]. Smaller equipment lowers installation area, structural mass, and cost.

Inside the enclosure, the solid spacer supports the high-voltage conductor, defines the insulation geometry, and separates the gas compartments (Figure 1.1a). It must withstand the operating voltage without electrical discharge along its surface throughout the service life of the equipment. The region highlighted in red is the focus of this thesis. Figure 1.1b shows a simplified representation of this region to illustrate the interface between the gas and the solid spacer, the two electrodes, and the direction of the thermal gradient. The detailed electrode and spacer geometry developed for the test bench is presented in Chapter 5.

1.2. Surface flashover at the gas–solid interface

The interface between the gas and the spacer shown in Figure 1.1 is one of the critical insulation regions in a gas-insulated system. The electric field can be intensified near the spacer ends, where the conductor, the solid insulation, and the gas meet at points known as "triple junctions." Under a high enough voltage, a discharge can develop along the spacer surface and bridge the gap between the high-voltage and grounded electrodes. This surface discharge is called flashover, and it is the failure mode this thesis studies [4].

Flashover along a solid surface is harder to predict than breakdown in a plain gas gap. It depends on the spacer geometry, the material conductivity, the surface condition, the voltage polarity, and the voltage history, not on a single field value [4], [5].

AC and DC behave differently at this interface. Under AC, the field follows the permittivity of the materials. Under sustained DC, the long-time field is governed mainly by their conductivity. At the gas–solid interface, charge accumulates when the normal current through the solid differs from that

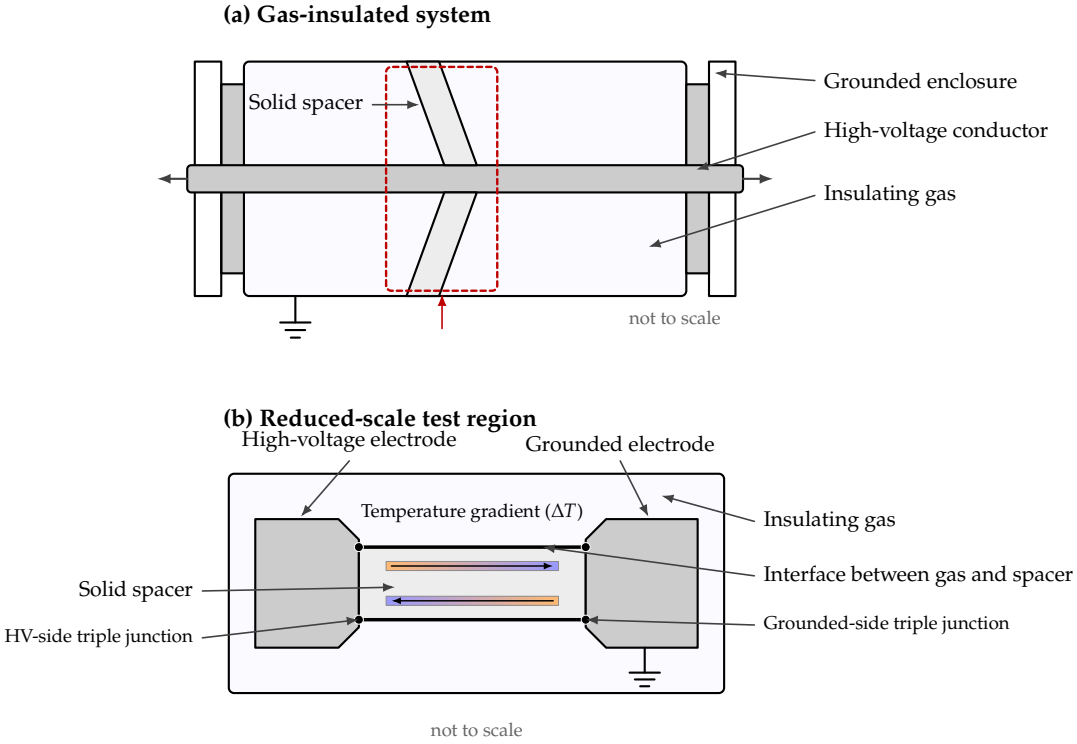


Figure 1.1: Location of a solid spacer in a gas-insulated system (a) and a simplified representation of the reduced-scale test region (b). Both directions of the temperature gradient are shown schematically.

through the gas, which causes the electric field to redistribute over time [5], [6], [7]. The field just after voltage is applied therefore differs from the field after hours of DC stress. Because DC GIS experience is still largely inherited from AC practice, this DC-specific redistribution is not yet fully captured by existing data [8].

1.3. The effect of a thermal gradient

In operation, the load current heats the conductor and produces a temperature difference across the spacer, from the hot conductor side to the cooler enclosure side. This matters because the bulk conductivity of epoxy rises strongly with temperature. Since the long-time DC field follows conductivity, a temperature gradient is a further operating condition that reshapes the field along the spacer surface [9], [10].

The warm end of the spacer conducts more than the cold end. Under DC voltage, this difference changes the conduction-current distribution in the epoxy and gradually redistributes the electric field. The chain studied in this thesis is

$$\Delta T \;\rightarrow\; \sigma(T) \;\rightarrow\; \text{time-dependent field redistribution} \;\rightarrow\; E_t(s,t),$$

where ΔT is the imposed temperature difference, $\sigma(T)$ is the temperature-dependent conductivity, and $E_t(s,t)$ is the tangential field along the interface—the component that drives surface flashover. This chain describes how the field evolves before flashover, not the flashover itself.

Bulk conduction is one contributor among several. Surface conduction, gas ions, and charge injection can also deposit charge on the interface, and can act together [4], [6], [11], [12]. Their balance depends on the geometry, the voltage waveform, and the surface condition.

Charge is also deposited by the measurement itself: the voltage rise before flashover adds surface charge [13]. The thermal settling time, the DC pre-stress duration, and the voltage rise are therefore part of the test. They must be fixed before flashover differences can be assigned to the intended variables.

1.4. Knowledge gap and Objective

Previous work covers parts of this problem: DC field redistribution in gas-insulated systems, surface-charge accumulation on epoxy spacers, the effect of spacer geometry, and the effect of temperature-dependent conductivity [4], [5], [10]. These are treated mostly in isolation. But the effect of a thermal gradient on the DC field cannot be separated from the geometry that shapes that field. A flashover result also cannot be read without knowing the DC pre-stress that preceded it. Studying the problem therefore needs one test bench that combines a GIS-relevant interface field, controlled thermal loading with either end heatable, defined DC pre-stress, repeatable specimen handling, and diagnostic access.

No such test bench was found in the reviewed literature for a thermally stressed DC spacer in air at atmospheric pressure. The gap has two sides. The physical side is what happens: how do a thermal gradient, conductivity-driven redistribution, polarity, and voltage history set the pre-flashover field? The practical side is how to impose and separate these conditions in one experiment so that future flashover results can be interpreted [9], [10], [14], [15], [16].

The need is reinforced by the maturing of DC GIS standardisation. IEC TS 62271-318:2024 sets DC-specific requirements for gas-insulated switchgear rated 100 kV and above [17]. Developing test methods still requires controlled experiments that link operating conditions, field evolution, and measured response.

The objective of this thesis is to design a reduced-scale gas–epoxy test bench and to calculate its temperature and DC electric field behaviour. The thesis also defines the test-bench qualification requirements and proposed test method needed for a future study of DC spacer surface flashover under a controlled thermal gradient, voltage polarity, and DC pre-stress duration.

1.5. Research questions and thesis approach

The study is motivated by three open questions:

RQ1. What effect does the temperature gradient across a GIS spacer have on the statistical distribution of surface-flashover voltage?

RQ2. What effect do voltage polarity and thermal-gradient direction have on the earliest visible surface-flashover region along the spacer–electrode interface?

RQ3. What effect does DC pre-stress duration have on the surface-flashover voltage distribution, and does this effect change when a thermal gradient is imposed?

These are not subquestions; each is a separate physical question. Together they set the electrical, thermal, environmental, diagnostic, and repeatability functions the test bench must provide (Figure 1.2). Combining those functions in one bench leads to the main thesis question:

> **Thesis question**
>
> What design of a reduced-scale gas–epoxy test bench enables controlled future investigation of RQ1–RQ3 under HVDC GIS-relevant conditions?

1.6. Scope

The work is a design and modelling study. The chamber is sized for a 6 bar mechanical design pressure: a conservative value covering the upper range of GIS operating pressures, which are reported as 3.3–5.3 bar [16]. The maximum operating voltage is 50 kV DC. A separate 60 kV case, 20% above this, is used only to check the electrical design with margin; it is not an operating or withstand rating. The thermal condition is an axial temperature difference of 40–50 K, with an unheated ambient-temperature reference condition. The 100 °C hot-source used in the thermal simulations is an upper design case, not the normal test temperature.

The reduced-scale arrangement (Figure 1.1b) reproduces the HVDC-GIS interface-field pattern and the conductivity-driven field redistribution caused by a thermal gradient. It does not reproduce the full-scale gas conditions which scale by volume [18].

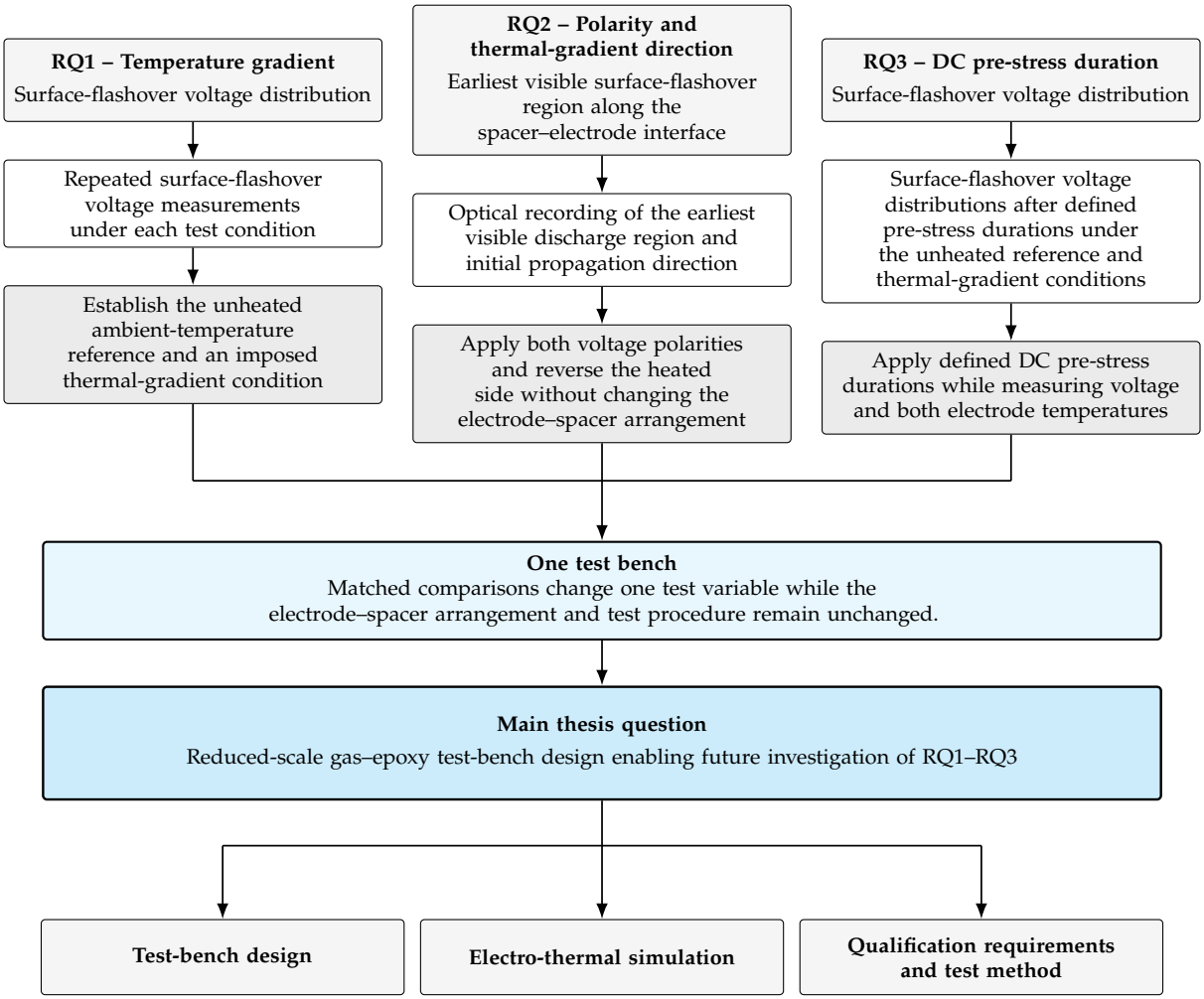


Figure 1.2: Relation between RQ1–RQ3, the required test-bench functions, and the three thesis outputs.

The electro-thermal model calculates the spacer temperature field and the time dependent DC electric field distribution. It does not model the discharge itself, so it does not predict the flashover voltage or its location. RQ1-RQ3 are intended for the future experimental investigation. They are not answered experimentally in this thesis because the test bench was not built and no flashover tests were carried out.

1.7. Thesis structure

The remainder of the thesis is organised as shown in Figure 1.3.

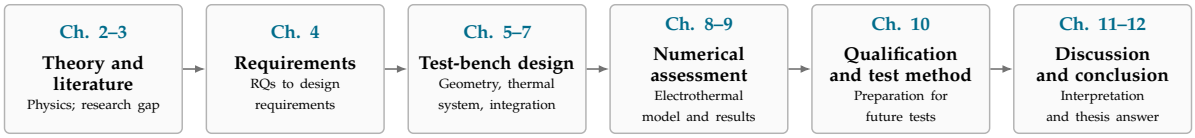


Figure 1.3: Structure of the thesis from the theoretical basis to design, numerical assessment, and conclusion.

2

Theoretical Background

This chapter presents the physics used in the design, simulation, and test method. It covers gas discharge development in air, the formation and time-dependent redistribution of the DC electric field, the temperature dependence of the solid's conductivity, and surface flashover at the gas–solid interface.

2.1. Gas discharge development in air

A gas discharge can begin when a free electron gains sufficient energy from the electric field to ionise neutral molecules. Repeated ionising collisions produce an electron avalanche. Its growth is described by the effective ionisation coefficient

$$\bar{\alpha} = \alpha - \eta, \tag{2.1}$$

where α is the first ionisation coefficient and η is the electron-attachment coefficient. An avalanche grows when $\bar{\alpha} > 0$. This avalanche multiplication is the primary Townsend ionisation process; a self-sustained Townsend discharge additionally requires secondary-electron production. The condition $\bar{\alpha} = 0$ therefore marks the transition from net attachment to net ionisation, but does not by itself define complete gas breakdown [18], [19].

As an avalanche grows, its space charge can distort the applied field and initiate a streamer. The enhanced field at the streamer head allows the discharge to propagate through regions where the background field is lower than that required for uniform avalanche growth. Breakdown occurs only if the discharge continues across the insulation gap and establishes a conducting path between the electrodes. The breakdown voltage consequently depends on the local field distribution, electrode geometry, voltage polarity and availability of initiating electrons [19], [20].

For approximately uniform, centimetre-scale gaps in atmospheric air, $3\,\mathrm{kV\,mm^{-1}}$ is a useful reference scale for gas breakdown. It is not a universal breakdown field or a direct limit for the tangential field along a solid surface. In a gas–solid insulation system, geometrical field enhancement near electrode edges and triple junctions can initiate a discharge at a lower average applied field. Whether this develops into surface flashover also depends on the interface charge, surface condition and discharge-propagation path, as discussed in Section 2.4 [4].

2.2. electric field Formation under AC and DC Stress

This section sets out how the electric field builds up in a gas–solid insulation system before a discharge can start. The same geometry can give different field distributions under AC and DC stress, depending on the balance between displacement current, conduction current and charge accumulation at the gas–solid interface.

2.2.1. Capacitive Field Distribution under AC and at DC Energisation

AC and DC fields obey the same electroquasistatic equations. What differs is the current contribution that dominates the field formation. For an electric potential V, the electric field and electric flux density are

$$\mathbf{E} = -\nabla V, \qquad \mathbf{D} = \varepsilon \mathbf{E}, \tag{2.2}$$

where ε is the permittivity. The total current density consists of a conduction-current contribution and a displacement-current contribution,

$$\mathbf{J}_{\text{tot}} = \sigma \mathbf{E} + \frac{\partial \mathbf{D}}{\partial t}, \tag{2.3}$$

where σ is the electrical conductivity [8], [18]. The electric field distribution is therefore not determined by the voltage waveform alone. It depends on the relative magnitude of the conduction and displacement-current contributions.

For a sinusoidal voltage with angular frequency ω, the ratio between the conduction-current and displacement-current magnitudes can be written approximately as

$$\frac{J_{\text{cond}}}{J_{\text{disp}}} = \frac{\sigma}{\omega \varepsilon}. \tag{2.4}$$

For a good insulator at power frequency, $\sigma \ll \omega\varepsilon$. The displacement current then dominates, and the field is governed mainly by geometry and permittivity. This is the capacitive field distribution. In this state, the normal component of electric flux density satisfies the dielectric-interface condition, while the tangential component of the electric field remains continuous across the interface [8], [18], [21].

Calling this field "permittivity-controlled" is therefore a useful approximation, not an absolute rule. If the conductivity is high enough, the frequency is low enough, or the surface is sufficiently conductive, conduction can still influence the field under AC stress. Conversely, displacement current remains important whenever a DC voltage is changing. The distinction between AC and DC field formation is therefore a matter of time scale and dominant current contribution, not a change in the governing equations.

A similar capacitive field appears immediately after DC energisation. At the first instant after a DC voltage is applied, charge has not yet moved far enough to establish a new distribution. If the insulation is initially uncharged, the field at $t = 0^+$ is therefore close to the capacitive solution,

$$\nabla \cdot (\varepsilon \mathbf{E}) = 0. \tag{2.5}$$

At this instant, geometry and permittivity govern the field in the same way as for the ideal capacitive AC case. This similarity is temporary. Once charge carriers begin to move, the field departs from its initial distribution and becomes dependent on how the complete gas–solid system carries current [5], [6], [7].

2.2.2. Charge Transport and Formation of the Resistive Field

When the applied DC voltage becomes constant, the displacement-current term decreases, but the conduction current does not generally vanish. Charge continues to move through the solid, along its surface and through the surrounding gas. Charge conservation requires

$$\frac{\partial \rho_{\text{v}}}{\partial t} + \nabla \cdot \mathbf{J}_{\text{c}} = 0, \tag{2.6}$$

where ρ_{v} is the free volume-charge density and $\mathbf{J}_{\text{c}}$ is the conduction-current density. Combining Equation (2.6) with Gauss's law gives

Table 2.1: Dominant processes during AC stress and successive stages of DC stress.

Field regime	Dominant current	Controlling quantities	Electrical memory
Power-frequency AC	Displacement current	Geometry, permittivity and frequency	Limited under ideal sinusoidal AC stress
Initial DC, $t = 0^+$	Displacement current during energisation	Geometry, permittivity and voltage-rise history	Any initial charge may influence the field
Transient DC	Conduction and charge-transport currents	Bulk and surface conductivity, gas-ion transport, charge injection, trapping and geometry	Surface and volume charge evolve with time
Stationary DC	Conduction current	Conductivity distribution and stationary charge state	Established charge remains part of the field solution

$$\nabla \cdot \left(\sigma \mathbf{E} + \frac{\partial (\varepsilon \mathbf{E})}{\partial t} \right) = 0. \tag{2.7}$$

Equation (2.7) describes the transition from the initial capacitive field to the long-time conduction-controlled field. It also explains the memory of the DC field: the field at a given time depends on the charge transported during the preceding voltage application [5], [22].

At the gas–solid interface, charge collects whenever the normal current arriving through the solid does not match the normal current leaving through the gas. With the unit normal $\mathbf{n}$ directed from the solid towards the gas, a general surface-charge balance can be written as

$$\frac{\partial \rho_s}{\partial t} = \mathbf{n} \cdot \left(\mathbf{J}_{\text{solid}} - \mathbf{J}_{\text{gas}} \right) - \nabla_s \cdot \mathbf{K}_s, \tag{2.8}$$

where ρ_s is the surface-charge density, $\mathbf{K}_s$ is the surface-current density and ∇_s denotes the surface divergence. Interface charge therefore changes for two reasons: the normal currents differ, or charge is redistributed laterally along the surface [6], [7], [23]. Three charge-transport routes must consequently be distinguished.

Through the solid. In the simplest terms, the bulk current through the solid is represented by Ohm's law,

$$\mathbf{J}_{\text{solid}} = \sigma_{\text{solid}} \mathbf{E}. \tag{2.9}$$

A real polymer is not this simple. Its measured current may also include electrode injection, trapping and detrapping inside the material, ionic migration and the formation of space charge. The effective conductivity can therefore depend on electric field, temperature, previous polarisation and the duration of the applied voltage. An Ohmic model is useful for predicting the macroscopic capacitive–resistive field shift, but it does not resolve the individual carrier populations responsible for the measured current [23], [24].

This distinction matters because volume charge and surface charge affect the field in different ways. Volume charge modifies the field inside the solid through Gauss's law, whereas surface charge introduces a discontinuity in the normal component of electric flux density at the interface,

$$\mathbf{n} \cdot \left(\mathbf{D}_{\text{gas}} - \mathbf{D}_{\text{solid}} \right) = \rho_s. \tag{2.10}$$

A conductivity-based field model can therefore reproduce the large-scale field redistribution without identifying the microscopic location of every trapped charge inside the polymer.

Through the gas. Air is not charge-free. Background radiation and natural ionisation continuously create positive and negative ions. These ions drift in opposite directions under the electric field, diffuse under concentration gradients and may recombine before reaching an electrode or the spacer surface. The gas current is therefore better described by charge-carrier transport than by one fixed gas conductivity [5], [6].

The number of gas ions reaching a given part of the spacer depends on the ion-generation rate, ion mobility, recombination, field-line topology and the gas volume feeding that surface region. An effective conductivity inferred from the local ratio J/E is therefore generally neither uniform nor constant [6], [23].

Natural ionisation is only the minimum gas-side charge source. Electrode roughness, microscopic protrusions, particles, field emission and discharges too weak to be detected by a conventional partial-discharge measurement can also supply charge. Schueller, Gremaud, Doiron and Franck showed that such microdischarge currents can exceed both the natural-ion current and the current through the solid, thereby becoming the dominant source of spacer charging [25]. Experimental studies on epoxy spacers have also reported charge patterns that could not be reproduced using only natural-ion transport and simplified conductivity models [24], [26].

The gas-side charging current is therefore not a material property of air alone. It is a response of the whole system, including the gas, electrode condition, geometry and discharge-free quality of the apparatus. This is one reason why identical spacer tests can develop different charging histories at the same applied voltage.

Along the surface. Charge may also travel laterally along the gas–solid interface. The resulting surface current is commonly represented as

$$\mathbf{K}_s = \kappa_s \mathbf{E}_t, \tag{2.11}$$

where κ_s is the surface conductance and $\mathbf{E}_t$ is the tangential electric field. Surface conduction spreads charge laterally, smoothing local charge peaks or transporting charge towards an electrode. It depends strongly on the surface state, including moisture, contamination, roughness, ageing and cleaning residues.

Changing the epoxy surface treatment alone can substantially change the accumulated charge [23], [27]. The surface must therefore be treated as part of the electrical system, not merely as a geometric boundary. Under the controlled dry conditions intended for the present test bench, surface conduction may be smaller than the bulk current, but it cannot be dismissed without measurement or a stated modelling assumption.

2.2.3. Interfacial Polarisation and Relevant Time Scales

When two materials with different ε/σ ratios are placed in series, the initial capacitive field does not generally satisfy conduction-current continuity at their boundary. Charge then builds up at the interface until the normal current becomes continuous. This accumulation is Maxwell–Wagner polarisation [8], [18]. It drives the field from its capacitive form towards its resistive form.

For one homogeneous material with constant permittivity and conductivity, the dielectric relaxation time is

$$\tau_d = \frac{\varepsilon}{\sigma}. \tag{2.12}$$

A low conductivity gives a long τ_d, which explains why field redistribution can be slow in highly resistive polymers. A real gas–solid spacer system cannot usually be represented by one such ratio. The gas, solid and surface carry current through different paths, and their transport properties may be nonlinear. The transient field can therefore contain several time scales at once: a faster stage from gas-ion drift or local polarisation currents, and slower stages from bulk conduction, surface transport or deep charge trapping [7], [8], [22], [23].

Equation (2.12) therefore provides a characteristic time scale, but does not prove that the complete field transition follows a single exponential. For an ideal first-order response, the completed fraction is $1 - \exp(-t/\tau)$; at $t = 4\tau$, this equals 0.9817, corresponding to the conventional 2 % settling criterion [28]. This approximation is valid only when the response can be represented by one dominant time constant. In a heterogeneous gas–solid insulation system, bulk, surface and gas-phase charge transport may introduce multiple characteristic time scales [5], [8], [23]. The required DC pre-stress duration must therefore be determined from the time-dependent electric field at the interface locations relevant to flashover.

Given enough time, the charge distribution stops changing appreciably, and the field reaches a stationary DC state. In that state,

$$\frac{\partial \rho_{\mathrm{v}}}{\partial t} = 0, \qquad \frac{\partial \rho_{\mathrm{s}}}{\partial t} = 0, \qquad \nabla \cdot (\sigma \mathbf{E}) = 0. \tag{2.13}$$

The resulting field is referred to as the stationary resistive field because, in an Ohmic description, its distribution is governed primarily by the conductivity distribution. Stationary does not mean uncharged. The accumulated surface and volume charges are part of the stationary solution required to maintain current continuity [6], [7].

The stationary resistive field can differ from the initial capacitive field in magnitude, direction and peak location. A geometry that appears well graded in a permittivity-based calculation may develop a more severe local field after conductive redistribution. Conversely, charge accumulation can reduce stress in one region while transferring it to another. A DC insulation geometry must therefore be assessed using both limiting fields and the time-dependent path between them.

2.2.4. Charge-Controlled Evolution of the DC Electric Field

The distinctive feature of DC stress is not simply zero frequency, but sustained polarity. A steady polarity allows charge supplied through the solid, surface, gas and electrodes to form a persistent distribution. Under ideal AC stress, the electric field reverses every half cycle and displacement current normally remains dominant. The insulation therefore does not build the same stationary, polarity-dependent conduction state that can form during prolonged DC energisation.

Charge accumulation is not exclusive to DC. Partial discharge, rectification, asymmetric voltage waveforms, contamination and low-frequency stress can also leave charge under nominally AC conditions. The important distinction is that sustained DC directly supports a long-lived charge distribution whose magnitude and sign depend on the complete voltage history.

This electrical memory becomes important whenever the voltage changes: at switch-off, under superimposed transients and during polarity reversal. Stored charge cannot disappear instantly, so its field is superimposed on the field of the new voltage. Depending on the sign and location of the charge, this superposition may either reduce or increase the local tangential and normal field components. Charge accumulated during long DC stress can therefore reduce the flashover voltage during polarity reversal [22], [27], [29].

How long this charge remains depends on the available decay paths. Kindersberger and Lederle distinguished three mechanisms [30], [31]:

- *bulk conduction*, which can reduce charge relatively uniformly under a simple Ohmic model;
- *surface conduction*, which spreads charge laterally before it reaches a grounded boundary;
- *gas-ion neutralisation*, which depends on local field lines and available ionisation volume, so it can remove charge faster from one region than another.

These mechanisms act together and may not produce a single exponential decay. A single time constant can therefore provide only an order-of-magnitude estimate for the charge-decay process.

The field from which a DC breakdown process begins is consequently defined by more than the instantaneous applied voltage. It also depends on the duration and polarity of the pre-stress, the temperature-dependent conductivity of the solid, the surface condition, gas-side charge sources and

any charge left by earlier voltage applications or discharges. A breakdown measurement performed before these quantities are controlled may compare specimens that are at the same applied voltage but in different internal electrical states.

For this thesis, this distinction has two direct consequences. First, the capacitive field immediately after energisation and the stationary resistive field must be treated as limiting states connected by a time-dependent transition. Second, the pre-stress duration is part of the test condition, not idle waiting time before the voltage rise to flashover. The electro-thermal model developed in Chapter 8 is built around this distinction and evaluates the initial, transient and stationary fields for the realised test-bench geometry.

The implemented field model represents the large-scale redistribution caused by the prescribed permittivity and conductivity distributions. It deliberately does not resolve every charge source identified in this section, such as individual gas-ion species, electrode injection, microscopic trapping or undetected microdischarge. Its output is therefore interpreted as the conductivity-driven pre-breakdown field. A clear departure from this behaviour in future experiments would indicate that additional charge-transport or discharge mechanisms are relevant.

After a DC voltage is applied, current through the solid, surface, and gas turns the initial capacitive field into a history-dependent conduction state. The surface and volume charges left behind set the field from which flashover begins—the subject of the next section.

2.3. Temperature Dependence of Conduction and Field Redistribution

Section 2.2 established that charge transport reshapes the field after a DC voltage is applied, and that the long-time field is set by the conductivity distribution. Temperature enters that mechanism directly, because the conductivity of epoxy depends strongly on it.

During loaded operation, a temperature difference develops across the spacer [32]. The central conductor carries the load current and is heated by its own ohmic loss, while the enclosure stays closer to ambient. Heat flows through the spacer, so a temperature gradient develops across it. In a horizontal GIS compartment, the conductor and enclosure are near 343 K (70 °C) and 313 K (40 °C), respectively [33].

2.3.1. Arrhenius Conductivity in Epoxy

Conduction in a solid dielectric is thermally activated. Raising the temperature raises both the mobility of the ions and the number of electrons lifted into conduction states, and both rise exponentially. For ionic and electronic conduction alike this is described by Arrhenius equation,

$$\sigma(T) = \sigma_\infty \, \mathrm{e}^{-E_\mathrm{a}/k_\mathrm{B}T}, \tag{2.14}$$

with E_a the material-specific activation energy and k_B the Boltzmann constant [18]. For calculation the relation is more convenient written against a reference point than an absolute prefactor,

$$\sigma_\mathrm{ep}(T) = \sigma_\mathrm{ref} \exp\left[-\frac{E_\mathrm{a}}{k_\mathrm{B}}\left(\frac{1}{T} - \frac{1}{T_\mathrm{ref}}\right)\right], \tag{2.15}$$

where σ_ref is the conductivity at the reference temperature T_ref. For a positive activation energy, conductivity rises as the temperature increases. The fitted parameters are material- and condition-specific, so Equation (2.15) holds only within the range for which the epoxy was characterised [18], [23].

The exponent is what matters. Between ambient and operating temperatures the conductivity of insulating materials can rise by four to five orders of magnitude [18]. In epoxy the effect is worth stating concretely: measured resistivities for one unfilled epoxy fall from $3 \times 10^{17}\,\Omega\,\mathrm{m}$ at 298 K to $3.2 \times 10^{15}\,\Omega\,\mathrm{m}$ at 348 K, so a 50 K rise raises the conductivity by a factor of about ninety [7]. A temperature difference of the order found across a spacer is therefore enough to change the conductivity by orders of magnitude from one side to the other.

2.3.2. Field Redistribution under a Thermal Gradient

Under a gradient the temperature varies with position, and through Equation (2.15) so does the conductivity: the hot region becomes more conductive than the cold one. Since the stationary field obeys $\nabla \cdot (\sigma \mathbf{E}) = 0$, the gradient does not perturb the resistive field—it defines it.

A one-dimensional current path gives the simplest interpretation. Under stationary conditions Equation (2.9) inverts to

$$E = \frac{J}{\sigma}. \tag{2.16}$$

If the same current density passes through two regions of different conductivity, the field is lower in the more conductive region and higher in the more resistive one. A larger part of the applied voltage therefore appears across the colder region. Figure 2.1 shows this inversion across the spacer.

A real spacer is not one-dimensional. Its current paths are shaped by the electrode geometry, the spacer profile and the surrounding gas, so there is no universal rule in which the field simply moves from the hot side to the cold side. The full conductivity distribution determines how much stress transfers and where the maximum field occurs [7], [34], [35].

Computed and measured results for disc-spacer geometries show what this can look like. Space charge forms in the bulk and collects in the regions of lower conductivity, away from the hot conductor, with an effect on the field much like the high-voltage electrode becoming larger. That bulk charge then drives charge onto the gas-solid surface, even where the geometry has been shaped so that the capacitive field has no normal component there, that is, shaped specifically to prevent surface charging. Shaping a spacer against the capacitive field alone is therefore not sufficient once a thermal gradient is present[7].

Temperature acts on the other two transport routes of Section 2.2.2 as well, and not equally, which is what makes its effect hard to predict. Bulk and surface conduction need not change together, so a gradient shifts the balance between them—and they do different things: a higher bulk conductivity accelerates charge accumulation, whereas a higher surface conductivity can change which path dominates altogether, and the resulting surface-charge distribution may even reverse polarity [34]. Surface charge is therefore the outcome of competing currents, not a direct measure of bulk conductivity. Heating also promotes the injection, trapping and migration named in Section 2.2.2: it releases trapped carriers, raises their mobility, and eases injection from an electrode. Measurements on alumina-filled epoxy under a gradient show the consequence—injection and migration increased near the heated electrode, the surface potential there moved towards the electrode potential, and a larger part of the applied voltage was carried near the opposite end of the specimen [36]. Microscopic charge motion can thus produce the same redistribution that conductivity theory predicts.

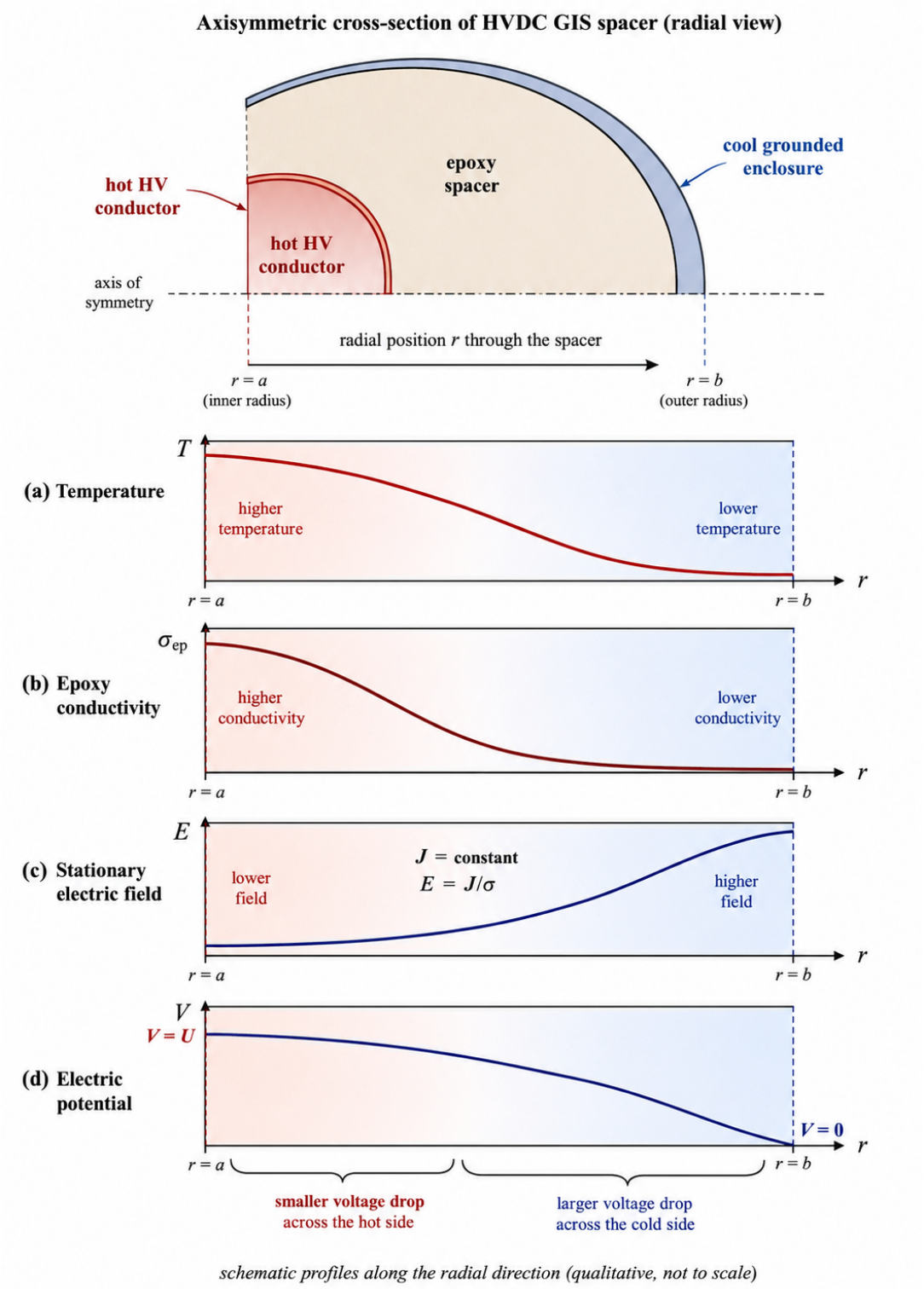


Figure 2.1: Schematic radial electro-thermal profiles across the spacer under a thermal gradient.

2.3.3. Time Scales under a Thermal Gradient

Temperature also changes how quickly the new state develops. The relaxation time of Section 2.2.3 depends on temperature through σ, and since the permittivity varies only weakly with temperature while the conductivity does not [18], [37], a gradient makes the relaxation time spatially dependent:

$$\tau_{\mathrm{d}}(\mathbf{x}) = \frac{\varepsilon(\mathbf{x})}{\sigma_{\mathrm{ep}}[T(\mathbf{x})]}. \tag{2.17}$$

The hot region relaxes faster than the cold one. Where Section 2.2.3 found several timescales because the materials conduct differently, a gradient adds a further spread within the solid itself: parts of the spacer may already sit close to their long-time field while others are still changing. The tangential field can therefore keep developing after the temperature distribution has settled [5], [23], [34].

The effect is large enough to be used deliberately: in HVDC GIS qualification testing, raising the ambient temperature from 20 °C to 40 °C shortened the time needed to reach 90 % of the steady DC field across the insulator surface [37].

Temperature therefore acts twice on the same field: it sets where the resistive field concentrates, and it sets how soon that field is reached. The field reached after a given time depends on the conductivity throughout the spacer, so the same duration of applied voltage can correspond to a nearly stationary state at a high temperature and an earlier transient state at a lower one.

2.3.4. Reduced Electric Field and Gas Density

The surrounding air changes with temperature too. At approximately constant pressure its molecular number density is

$$N = \frac{p}{k_{\mathrm{B}} T}, \tag{2.18}$$

with p the gas pressure, so air near the hot region is less dense. For the same local field, the reduced electric field becomes

$$\frac{E}{N} = \frac{E\, k_{\mathrm{B}} T}{p}. \tag{2.19}$$

Electron transport, ionisation and attachment in air all depend on E/N [38], [39], so heating changes the local conditions for discharge inception even when the field magnitude is unchanged; the breakdown voltage of a gas-insulated arrangement falls accordingly as the gas temperature rises [18], [40]. This gas-density effect is separate from the conductivity-driven redistribution in the solid, and the two act at once: the gradient changes the field applied to the gas, and it changes the gas density against which that field acts.

The solid-side sequence is therefore

$$\Delta T \longrightarrow T(\mathbf{x}) \longrightarrow \sigma_{\mathrm{ep}}[T(\mathbf{x})] \longrightarrow \mathbf{J}(\mathbf{x}, t) \longrightarrow \rho_{\mathrm{s}}(s, t) \longrightarrow E_{\mathrm{t}}(s, t), \tag{2.20}$$

where the temperature-dependent conductivity redistributes the current within the solid, and any imbalance between the currents arriving at and leaving the gas–solid interface produces a time-dependent surface charge $\rho_{\mathrm{s}}(s, t)$. This charge modifies the tangential field along the interface. The change in gas density acts alongside this solid-side mechanism. Conductivity climbs steeply with temperature, and under DC it is conductivity that sets the field. Temperature is therefore not a condition the insulation sits in; it is part of the stress the insulation carries. At the gas–solid interface that stress appears as the tangential field E_{t}—the quantity that drives surface flashover, and the subject of the next section [35], [41].

2.4. Surface Flashover and Critical Interface Regions

Introducing a solid spacer can lower the withstand of a gas gap. The dielectric strength of atmospheric air is of the order of $3\,\mathrm{kV\,mm^{-1}}$, whereas electrical-insulation-grade filled epoxy has a bulk breakdown strength of the order of $25\,\mathrm{kV\,mm^{-1}}$ [42]. This difference indicates that bulk puncture is unlikely to be the limiting failure mode at the field levels considered here. Instead, failure is expected to develop in

the gas along the solid boundary. The electrode-gas-solid interface distorts the local field and provides a path along which an initial gas discharge can extend; under DC, the interface charge established in the preceding sections adds a further field of its own. The solid surface can also supply seed electrons more readily than the undisturbed gas volume, which favors discharge inception near the interface. Surface flashover therefore develops in stages: a discharge first initiates in the gas, propagates along the interface and finally bridges the two electrodes. The tangential field $E_t(s,t)$ is tracked because it acts along this propagation path. The gas limit E_{lim} indicates where local inception becomes possible, but reaching it at one position does not imply complete flashover. The discharge must still propagate across the spacer surface [4], [18].

At both ends of the spacer, the electrode, gas and solid meet at a triple junction. The local stress in these regions depends on the electrode curvature, the material discontinuity, microscopic gaps at the contact and the surface condition. The high-voltage-side and grounded-side junctions are therefore candidate inception regions, although flashover does not necessarily begin at either one. The electric field at an ideal sharp corner is not a useful physical quantity because the calculated value becomes increasingly large near the corner. The relevant quantity is the macroscopic field in a finite region adjacent to the junction [4], [22], [43].

Figure 2.2 provides a conceptual illustration of the two triple-junction regions, a possible surface-discharge path and the associated tangential-field peaks. The larger peak is placed at one end only to illustrate that the two junctions can become electrically non-equivalent.

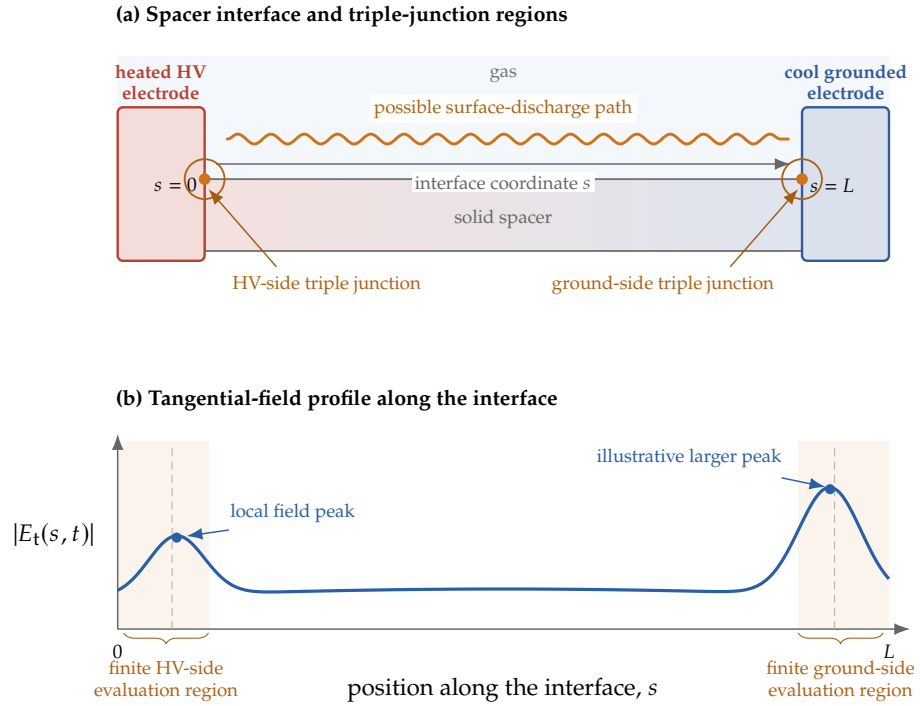


Figure 2.2: Possible surface-discharge path and tangential-field peaks near the two triple junctions.

The redistribution established in the preceding section can make the two junctions electrically non-equivalent. In a heated-electrode epoxy arrangement, measured surface potentials showed that the voltage drop concentrated near the grounded junction, where the calculated field increased several-fold. Heating can therefore move the dominant interface stress from one end of a specimen to the other rather than simply raising or lowering the field everywhere. The most highly stressed junction may consequently depend on the gradient direction, voltage polarity and pre-stress history. These dependencies make the full spatial distribution of $E_t(s,t)$ more informative than its value at a single predefined location [36].

The coupled problem can now be stated compactly. The solid–gas permittivity mismatch sets the initial

capacitive field. After a DC voltage is applied, the temperature-dependent conductivity of the solid governs the redistribution of current and interface charge, while the local gas state determines whether the resulting field can initiate a discharge. Together, these mechanisms set the magnitude and position of $E_t(s,t)$. Field calculations can identify the most highly stressed interface regions, but they cannot determine the flashover voltage alone because discharge propagation also depends on electrode contact, surface condition, material properties, temperature and electrical pre-stressing. Flashover voltage therefore remains an experimental endpoint rather than a value obtained directly from the electric field solution.

2.5. Chapter conclusions

- Under sustained DC stress, the electric field evolves in time from an initial capacitive distribution towards a stationary distribution governed mainly by conductivity.
- Immediately after energisation, the field is close to the capacitive, permittivity-controlled distribution. As charge is transported and redistributed, the field moves towards the stationary DC distribution, which can differ in magnitude, direction, and peak location.
- A DC insulation geometry must therefore be assessed using both limiting field distributions and the time-dependent transition between them. The DC pre-stress duration is consequently part of the test condition.
- The conductivity of epoxy increases strongly with temperature and can vary by orders of magnitude across the spacer. A thermal gradient therefore changes both the stationary field distribution and the rate at which it develops.
- A thermal gradient can make the two triple-junction regions electrically non-equivalent. The complete distribution of the tangential field $E_t(s,t)$ is therefore more informative than its value at one predefined location.
- electric field calculations can identify regions of elevated interface stress, but surface-flashover voltage remains an experimental quantity. Discharge propagation also depends on the electrode contact, surface condition, material properties, temperature, and preceding electrical stress.

3

DC Surface Flashover under Thermal Gradients

This chapter reviews what previous work has established about DC surface flashover at uniform temperature and under a thermal gradient. It distinguishes experimental measurements from calculated results and compares studies according to the conditions under which their results were obtained.

3.1. Framework for Evaluating the Literature

Chapter 2 showed that a field calculation can identify the most highly stressed interface regions, but flashover voltage remains an experimental endpoint. The literature is therefore assessed by distinguishing direct measurements, reconstructed quantities, calculated field states and flashover observations. A calculated increase in tangential field is not a measured decrease in flashover voltage, and a reconstructed surface-charge map does not by itself identify where a discharge began.

The evidence is also compared under its complete electrical and thermal history. Polarity, ramp rate, pre-stress duration, surface condition and temperature distribution can all change the interface state before a voltage-rise test begins. Results obtained under different histories or arrangements are therefore interpreted within their own test conditions rather than ranked as directly equivalent. Uniform-temperature studies provide the reference against which the additional influence of a thermal gradient is judged.

3.2. DC Surface Flashover at Uniform Temperature

Published studies report charge and field evolution over periods ranging from hours to months, but these durations are arrangement-specific. Figure 3.1 compares representative results without treating them as one common relaxation curve. Pre-stress duration alone does not define the field at the start of a later voltage ramp; geometry, material state, charge sources, transport routes and the endpoint used to observe the change must also be considered.

The active charging route depends on the complete arrangement. Nakanishi et al. measured strong, localised heterocharge on untreated epoxy spacers. A water-jet treatment containing fine sand roughened the surface by approximately 10 µm to 20 µm and removed an estimated 20 µm to 30 µm outer layer. The treated specimens accumulated less charge and the remaining charge was more uniform around the circumference. The authors attributed this to removal of locally inhomogeneous conductive regions, although the local conductivity distribution was not measured. Electrode roughness produced a different charge pattern, which they attributed to field emission from the conductor [27].

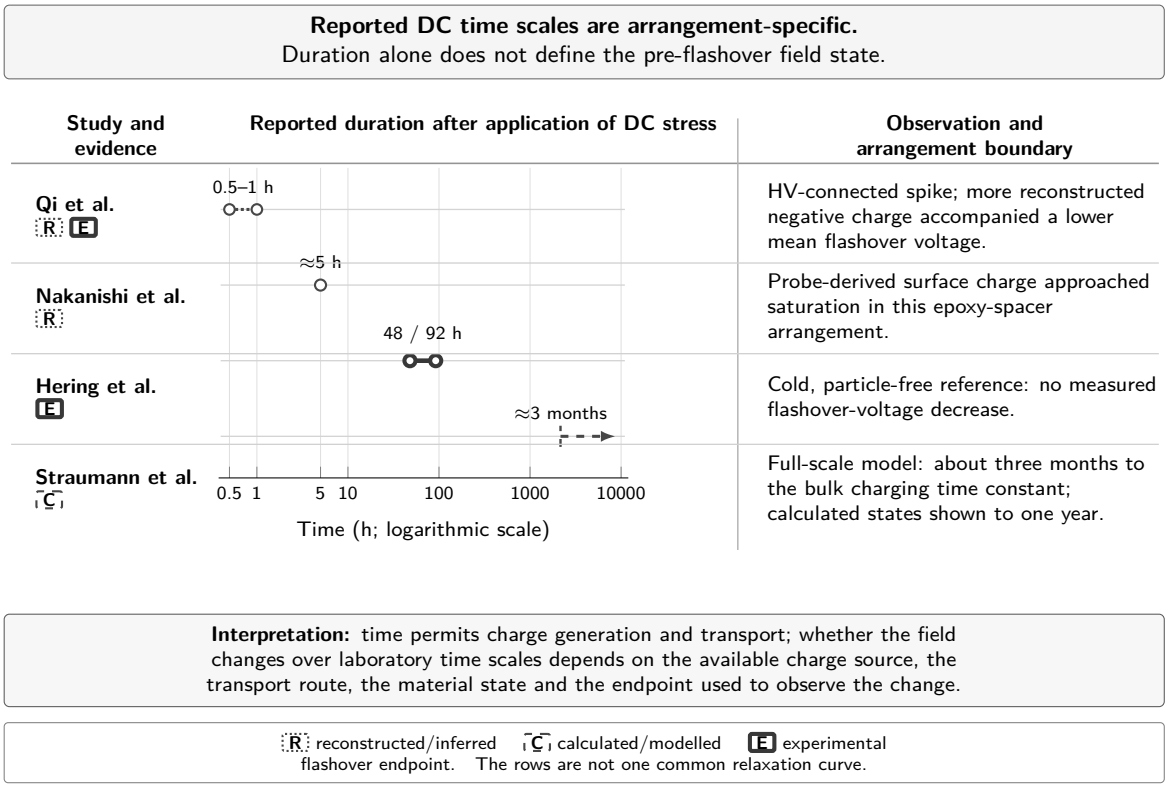


Figure 3.1: Arrangement-specific time scales reported under uniform-temperature DC stress, comparing reconstructed surface charge, experimental flashover endpoints, and calculated field evolution, without treating them as one common relaxation curve [7], [27], [44], [45].

The balance between gas-side and solid-side charging also depends on voltage and scale. In the model of Straumann et al., naturally produced gas ions dominated at low voltage, whereas current through the epoxy became more important at nominal voltage. Fujinami et al. likewise related measured charge patterns to the initial normal field while identifying several possible sources, including natural ionisation, particles, field emission and microdischarges [7], [29]. Scaling geometry and voltage together preserves the field strength but changes the gas volume connected to the spacer. A reduced-scale specimen may therefore reproduce the interface-field shape without reproducing the same balance between gas-side and solid-side charging [7].

Accumulated charge affects flashover through its superposition with the later voltage. Nakanishi et al. found that a large heteropolar charge distribution did not reduce flashover voltage during continued DC stress of the same polarity, but became more severe after abrupt polarity reversal. Fujinami et al. reported a related reduction of approximately 20 % to 40 % in opposite-polarity impulse flashover field in their arrangements [27], [29]. The same charge state can therefore have little effect under one voltage sequence and a marked effect under another.

Deliberately prepared charge distributions confirm that polarity and location matter. Li et al. reported lower mean flashover voltage after heteropolar corona precharging, whereas homopolar charge produced little change under their negative DC ramps [36]. Qi et al. used a modified basin-insulator model with a 45 mm metal spike connected to the HV conductor. Greater reconstructed negative charge near the spike was accompanied by a reduction in mean flashover voltage from 61.0 kV to 47.1 kV. Because the spike generated local discharge activity and guided the flashover region, the reported 22.8 % reduction is specific to that defect arrangement [44].

Time is therefore a test condition rather than an independent cause of reduced flashover voltage. It is the interval during which charge can be generated, transported and redistributed. A complete electrical history must record the duration and polarity of the DC stress, the subsequent voltage sequence, the surface condition and the way in which charge was produced.

Repeated discharge tests must also be treated statistically. Yildirim and Korasli showed that conditioning breakdown in compressed SF_6 was better represented by a probability distribution than by a single deterministic threshold. Their study concerned gas breakdown rather than spacer flashover, so it does not establish the correct distribution for the present problem; it demonstrates why a distribution should be fitted and checked rather than assumed [46].

The flashover studies reviewed here differ substantially in statistical support. Li et al. used 50 repetitions, Qi et al. used five repetitions per condition, and Hering et al. reported broad scatter despite controlled specimen preparation [36], [44], [45]. A single flashover value cannot distinguish a shift in characteristic voltage from a change in test-to-test variability. Where a Weibull representation is supported by the data, V_{50} describes the voltage at 50 % flashover probability and the shape parameter β describes the steepness of the distribution.

Uniform temperature is therefore a useful reference condition, but not a history-free one. Measurable changes occurred when charge was deliberately introduced, generated by a local discharge source, or made more severe by polarity reversal or an opposite-polarity impulse. Field evolution can also occur without a measurable change in flashover when charge generation and transport remain slow. Temperature adds a further influence by changing both the local gas state and the transport properties of the insulation.

3.3. Effects of Temperature on Gas–Solid Insulation

Temperature does not have one universal effect on gas–solid insulation. It can change the local gas strength and the rate at which charge develops or decays in the solid insulation. These effects may act at different locations and over different time scales, so a measured change in flashover voltage cannot be attributed to temperature without knowing the thermal distribution and the preceding electrical history.

The gas-side contribution can be isolated by removing the spacer. Hering et al. measured SF_6 breakdown between heated electrodes and reported a decrease from 486 kV at 20 °C to 459 kV at 94.8 °C, or 5.6 %. Their calculation indicated that breakdown still initiated near the HV electrode, where the field was sufficiently high, although the gas density was lower near the heated grounded electrode. Heating a

sealed enclosure also increased its average pressure and partly offset the local density reduction. The result therefore depends on where high field and low gas density overlap, and is specific to the tested SF_6 geometry and thermal condition [40].

Temperature also changes the rate of charge transport. Gremaud et al. measured surface-potential decay on corona-charged alumina-filled epoxy plates in SF_6 between 22 °C and 95 °C; the inferred effective mobility changed by approximately three orders of magnitude across this range. Wendel, Kindersberger and Hering similarly found that heterocharge developed faster at 60 °C than at 25 °C in pulsed-electroacoustic measurements of alumina-filled epoxy. These studies show faster charge development and decay in the tested materials, but they do not directly determine the field along a practical spacer or the resulting flashover voltage [47], [48].

A potential-decay curve does not identify the transport route by itself. In the Gremaud experiment, the potential peak decreased without spreading noticeably along the surface, which was consistent with removal through the bulk or neutralisation by gas ions rather than dominant lateral surface transport. Kindersberger and Lederle showed more directly that bulk conduction, surface conduction and gas-ion neutralisation can all contribute, and that the measured decay depends on the vessel geometry and connected gas volume [31], [47]. A faster decay at the hot side therefore does not imply that the complete interface becomes less stressed; charge may persist longer in a colder region.

Direct spacer-flashover evidence is available for one thermal direction. Li et al. heated the HV electrode while maintaining the grounded electrode near 20 °C. As the hot-side temperature increased to 120 °C, the reported corona-inception voltage and surface-flashover voltage both decreased, while positive streamers developed from the colder grounded side. The surface potential, flashover voltage and streamer images were measured; the detailed explanation based on thermally assisted injection and migration was the authors' interpretation. The material-scale, non-coaxial experiment used one voltage polarity and did not reverse the thermal direction [10].

The evidence therefore does not support a general rule that a higher temperature always lowers flashover voltage. Local heating can weaken the gas where reduced density overlaps with high field, while increased solid conductivity can redistribute the DC field towards a colder region. The full temperature distribution, its direction and the DC stress duration are therefore more informative than the maximum temperature alone.

3.4. DC Surface Flashover under a Temperature Gradient

The gradient literature must be compared through the imposed thermal profile, the preceding voltage history and the quantity measured at the end of the test. Published studies differ substantially in all three respects.

3.4.1. Representation of the Thermal Condition

Thermal gradients have been produced using internally heated electrodes, circulating oil and load-current heating. Equal endpoint temperature differences do not make these methods thermally equivalent. Hallas et al. showed that approximately 4600 A AC reproduced the conductor temperature rise and insulator gradient produced by 5000 A DC in commercial gas-insulated equipment; applying the same numerical current under AC would have produced greater thermal stress because of additional AC losses. A representative thermal test must therefore reproduce the conductor temperature rise and the gradient across the insulation, not merely the heating current [49].

The temperature distribution along the spacer must also be known. Ma et al. compared a calculated surface-temperature profile with measurements at three positions and obtained agreement within approximately 1.5 K for a 20.5 K gradient. The profile was non-linear because conduction, radiation and gas convection contributed differently along the spacer. Gremaud et al. also observed azimuthal temperature differences around a real-scale insulator due to natural convection. Similar values of ΔT can therefore correspond to different conductivity distributions along the gas–solid interface [14], [50].

Figure 3.2 places the principal arrangements on a common visual basis. It shows why their results cannot be combined as one controlled factorial experiment: thermal direction, geometry, gas, voltage history, and endpoint changed together.

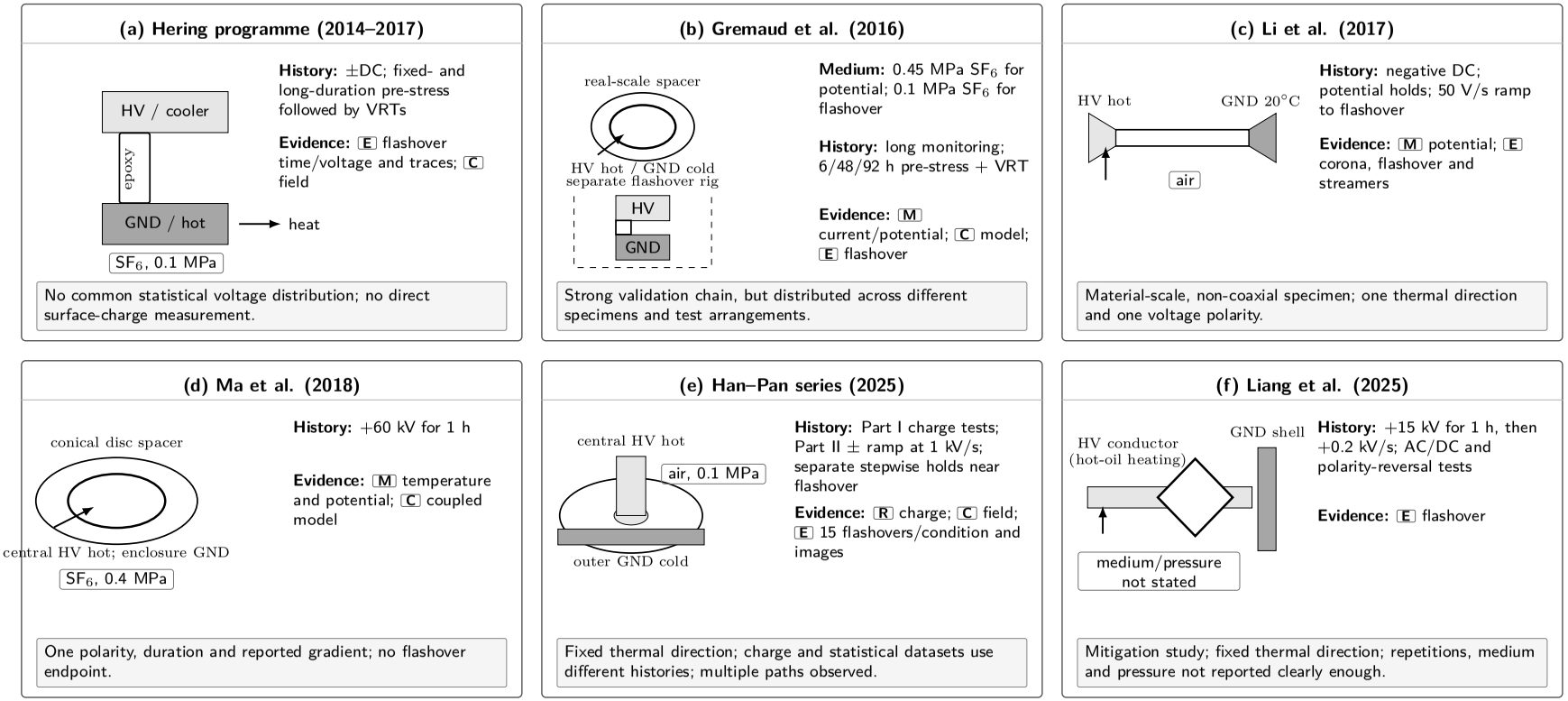


Figure 3.2: Simplified comparison of the principal experimental arrangements used to study DC spacer behaviour under a thermal gradient (not to scale). Geometry, thermal direction, gas condition, voltage history, and measured endpoint changed together between studies. Based on Refs. [9], [10], [14], [15], [45], [50], [51], [52].

3.4.2. Evidence from Surface Charge and Electric Field

A thermal gradient changes the spatial charge pattern, but the measured response is not universal. Zhang, Qi and Zhang studied a conical epoxy spacer in 0.1 MPa SF_6 with the central region near 70 °C and the outer region near 30 °C. Under positive DC voltage, the reconstructed charge distribution became more concentrated near the heated conductor and followed the temperature-dependent conductivity profile. The authors attributed the broad pattern mainly to bulk current and associated isolated charge speckles with possible microdischarges, although this source was not measured independently [53].

Ma et al. measured surface potential on a conical disc spacer rather than charge directly. Raising the central-conductor temperature increased both the mean surface potential and its radial variation, while the coupled electrothermal model reproduced the measured trend more accurately than an isothermal model. Han et al. later measured the temperature profile and reconstructed surface charge on a flat annular spacer in air. They observed stronger charge accumulation as the conductor-side gradient increased, whereas the bulk, surface and gas-current pathways used to explain the result were calculated rather than measured [50], [51].

Complex geometry can produce a different spatial response. Hu et al. measured surface potential over a three-post spacer in 0.1 MPa SF_6 and reconstructed the surface-charge density. Heating the central conductor mainly increased charge on the legs rather than on the central body. At 100 kV and a conductor temperature of 70 °C, the reported density reached approximately 100 $\mu C\,m^{-2}$; the heated charge state approached saturation after about six hours, compared with about twelve hours at ambient temperature [54].

Calculated studies broadly place the conductivity-driven high-field region towards the colder side. Zhou et al. reported increases of approximately 18 % in peak tangential field as the conductor temperature rose in an operating DC-GIL model. Liang et al. similarly calculated a shift of the high-field region towards the colder grounded shell in a uniform basin-type spacer. These values were model outputs, not measurements [52], [55].

Pan et al. showed why this smooth stationary redistribution may not represent the field immediately before flashover. Their stationary calculation became more uniform as the gradient increased and therefore did not explain the measured decrease in flashover voltage. A second calculation included the reconstructed surface-charge clusters obtained close to flashover. The resulting local maximum field increased for both voltage polarities and became consistent with the observed flashover trend. The comparison supports a distinction between broad conductivity-driven redistribution and local field enhancement associated with the near-failure charge state [15].

3.4.3. Evidence from Flashover Measurements

Thermal-gradient flashover studies use different endpoints: time to breakdown at fixed voltage, ramp flashover after DC pre-stress, a Weibull characteristic voltage and flashover under transient voltage sequences. These results are not directly equivalent.

Hering et al. heated the grounded electrode of a cylindrical epoxy specimen and applied fixed positive or negative DC voltages. Measured times to breakdown showed substantial scatter, and some tests continued for more than one week without flashover. After long DC stress, root points and surface traces appeared in the region towards which the calculated high field had moved. The tests connected thermal condition and stress duration to the eventual failure path, but the endpoint was time to breakdown rather than a statistical voltage distribution [9].

Gremaud et al. developed the strongest validation chain among the reviewed studies. Material currents, gas currents and real-scale surface potential were measured independently, while flashover was tested on a separate cylindrical arrangement after defined pre-stress periods. Heated tests after 48 h of pre-stress showed an average strength approximately 10 % below the warm voltage-rising reference. Some longer tests survived for 14 or 27 days, beyond the prediction based on solid conduction alone; adding a small gas-side injection current improved agreement. The complete chain was nevertheless distributed across different specimens and setups [14].

Pan et al. reported the most complete statistical dataset. Fifteen voltage-rise tests were performed for each gradient and polarity, with voltage increased from zero at 1 $kV\,s^{-1}$. Increasing ΔT from 0 K

to 63.4 K reduced the Weibull characteristic voltage at 63.2 % flashover probability by 14.3 % under negative voltage and 9.8 % under positive voltage [15].

The near-flashover charge distribution in the same study was obtained using a separate stepwise procedure. A voltage slightly below the minimum flashover value was held for 20 min and then increased in 2 kV steps with additional holds until flashover. This procedure captured cumulative charge development near failure, but it did not reproduce the continuous voltage-rise history used for the Weibull dataset. The reconstructed charge state may therefore not be identical to the state present during the statistical tests. High-speed recordings also showed surface, air and mixed propagation paths, so the fitted distribution included more than one observed path [15].

Liang et al. extended thermal-gradient testing to DC, AC/DC superposition and polarity reversal. The uniform reference spacer showed a downward flashover trend as the conductor-side gradient increased. The procedure used a one-hour DC pre-stress followed by a 0.2 kV s^{-1} voltage rise, but the study primarily evaluated a functionally graded mitigation concept and did not report repetitions clearly enough for a complete statistical comparison [52].

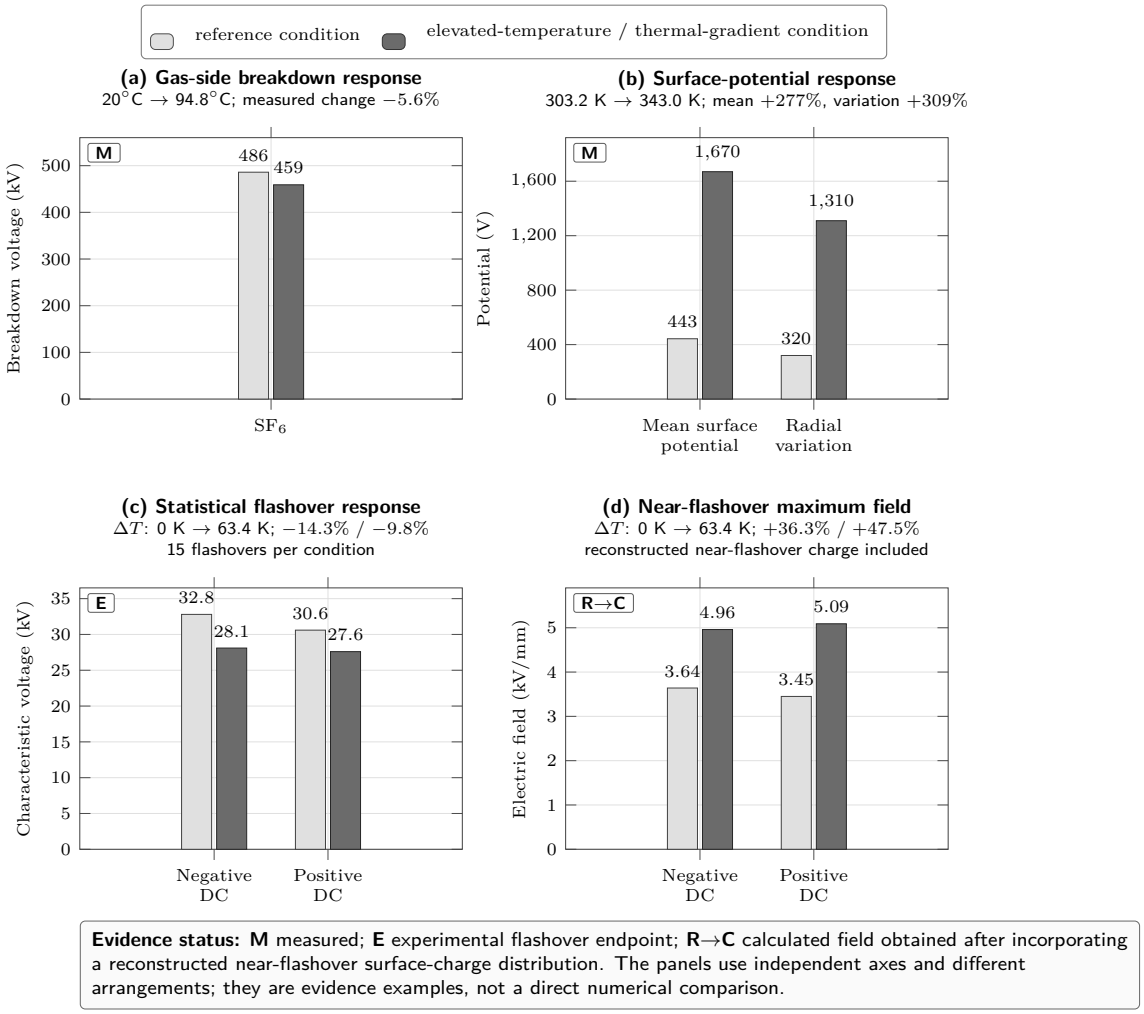


Figure 3.3: Selected quantitative evidence for temperature and thermal-gradient effects: gas-side breakdown (a), surface-potential response (b), statistical flashover voltage (c), and near-flashover maximum field (d), each from a different arrangement. Data reported by Hering et al. [40], Ma et al. [50], and Pan et al. [15].

Figure 3.3 keeps the evidence levels separate. It shows measured gas-side weakening, measured surface-potential redistribution, measured statistical flashover reduction and a calculated local field obtained after incorporating reconstructed charge. The combined evidence supports the effect of a thermal gradient, but not one universal quantitative relationship across the different arrangements.

3.4.4. Gradient Direction and Voltage Polarity

The literature covers both voltage polarities and both thermal directions, but not within one controlled comparison. Han–Pan and Liang retained conductor-side heating, while Hering heated the grounded electrode. Several studies tested both polarities, but the thermal direction remained fixed within each arrangement. Figure 3.2 makes the associated changes in geometry, gas and voltage history explicit [9], [14], [15], [51], [52].

No reviewed study independently reversed both thermal-gradient direction and voltage polarity on the same unmodified specimen while retaining the remaining conditions. The separate influence of polarity and thermal direction on the discharge location therefore remains unresolved. The studies establish changes in charge, field and flashover response, but many intermediate quantities are reconstructed or calculated rather than measured directly.

3.5. Predictive Scope and Validation of DC Spacer Models

Published DC spacer models range from conductivity-based electrothermal formulations to charge-transport models that additionally resolve surface conduction and gas-ion dynamics. These formulations calculate the evolution produced by prescribed mechanisms, but their outputs remain dependent on the material, gas and electrode parameters supplied to them [5], [7].

Increasing model detail therefore increases the number of arrangement-specific inputs that must be determined. Ion-pair generation, surface conductance, carrier mobility, recombination and electrode-related injection can all influence the result. A model may contain the relevant equations while still becoming unreliable when parameters are transferred from another material, geometry or environment.

Gas-side charging is a particular source of uncertainty. Schueller et al. obtained good agreement between measured and simulated surface potential where naturally generated ions explained the charging, but elsewhere the measured potential developed faster than predicted. Tests with deliberately added protrusions supported an electrode-related source, and additional charging occurred below the detected partial-discharge inception level. Natural-ionisation models can therefore reproduce background charging under restricted conditions, while electrode-related sources require separate representation and calibration [11].

This leads to a modelling trade-off. Surface and gas-ion transport can increase physical completeness, but only when the required inputs are known. Where temperature-dependent bulk conductivity is the only reliably characterised transport property, a bulk-conduction electrothermal model provides a transparent description of large-scale field redistribution without introducing unverified parameters. It does not represent every charging route, and that limitation must remain explicit [5], [7], [11].

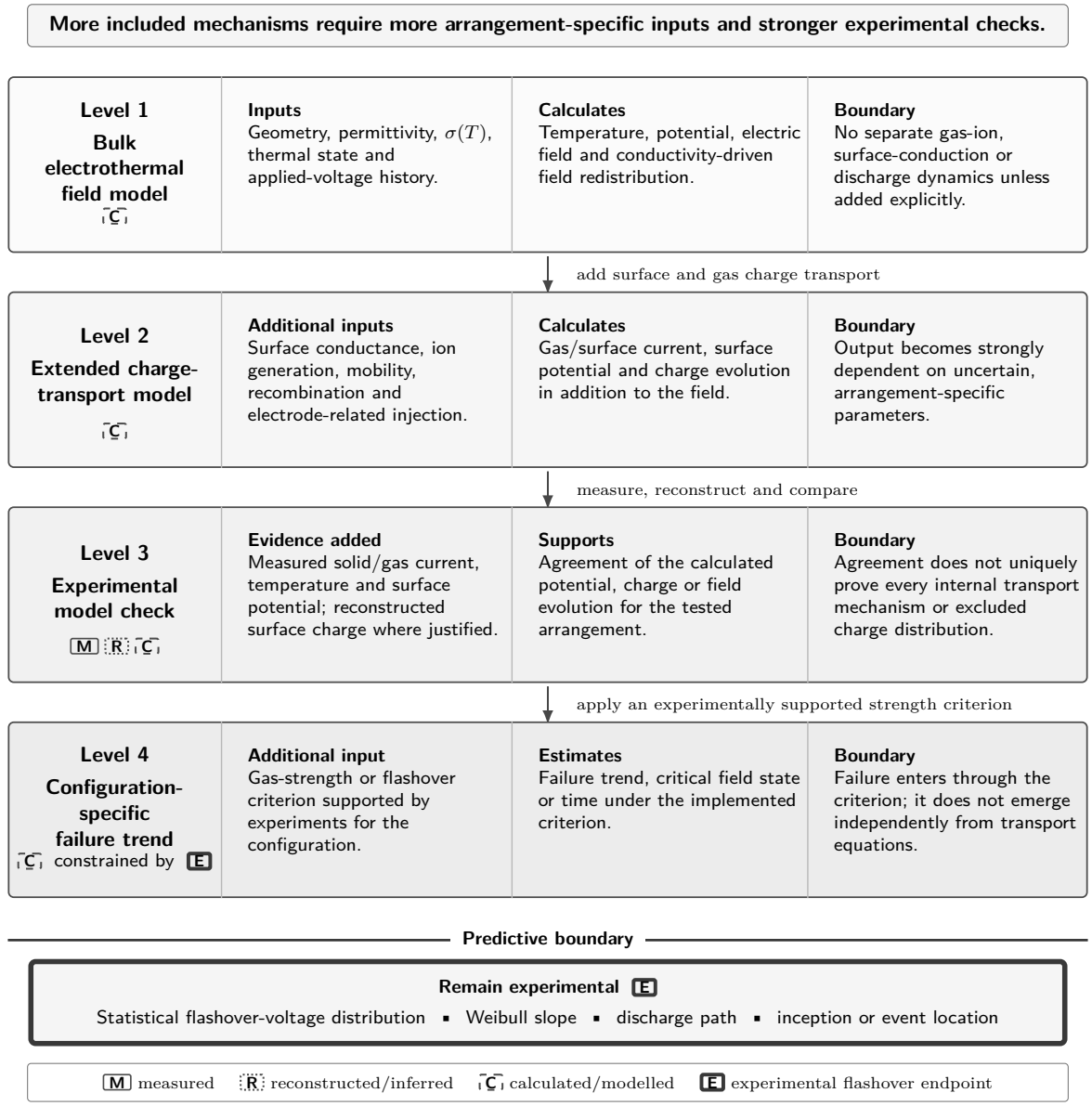


Figure 3.4: Predictive scope and validation boundary of DC spacer models: the quantities a calibrated calculation can provide, and those that remain experimental endpoints. Synthesised from Winter and Kindersberger [5], Schueller et al. [7], Schueller et al. [11], Ma et al. [50], Zhao et al. [56], and Gremaud et al. [14].

Validation against surface potential checks the calculated response for the tested arrangement. Winter and Kindersberger reproduced the direction and long duration of potential change on cylindrical epoxy insulators in dry air. Ma et al. reported a reduction in mean absolute percentage error from 32.0 % to 11.1 % when the thermal gradient was included. This supports the calculated potential response, not a flashover prediction [5], [50].

Comparison with reconstructed surface charge is a stronger but assumption-dependent check. Zhao et al. measured potential on both sides of a full-scale conical spacer and reconstructed interface charge using a three-dimensional potential-coefficient model. The inversion assumed that charge was located at the gas–solid interface and that no space charge was present inside the solid. Agreement therefore supports the model under those assumptions rather than proving the absence of other internal charge distributions. Circumferential non-uniformity also showed that local roughness or additional ion sources can create features that an axisymmetric model does not reproduce [56].

Gremaud et al. extended the validation chain furthest towards flashover. Independently measured solid and gas currents calibrated the model, which then reproduced real-scale surface-potential development under a thermal gradient. The calculated interface field was compared with an experimentally supported gas-strength criterion to estimate a time-dependent failure trend. Failure therefore entered through a configuration-specific criterion rather than emerging independently from the transport equations, and no statistical flashover distribution was produced [14].

The predictive boundary is therefore specific. Electrothermal and charge-transport models can calculate temperature, potential, charge and field development under the mechanisms and parameters included. After calibration, they may support a configuration-specific failure trend. Statistical flashover voltage, Weibull slope, discharge path and event location remain experimental endpoints, as summarised in Figure 3.4.

3.6. Transferability and the Remaining Experimental Gap

The reviewed evidence identifies two concurrent effects of a thermal gradient. Heating can reduce local gas density and weaken the gas near the hot region, while increased epoxy conductivity can shift the resistive voltage drop and interface field towards a colder region. Charge transport can further modify either state. Their relative influence depends on gas, pressure, material properties, interface-field topology and electrical history, and has not been isolated within one consistent experimental arrangement.

3.6.1. Transferability from SF_6 to Air

Studies in compressed SF_6 and air support the same general framework: the pre-flashover field depends on the conductivity distribution, accumulated charge and preceding voltage history. Bulk conduction, surface conduction and gas-side transport may all contribute. Their relative importance and time scales nevertheless depend on material, pressure, humidity, field strength, gas-ion sources and active gas volume. The mechanisms are transferable, but their numerical outcomes are arrangement-specific [31].

The Hering programme illustrates both the separation and interaction of the effects. The gas-temperature work isolated local density reduction, the 2014 spacer study examined conductivity-driven field redistribution under a thermal gradient, and the 2017 field-transition study showed that solid conductivity, charge-carrier transport and locally reduced gas strength act together. A conventional conductivity-based RC description did not reproduce the complete transition [9], [40], [45].

Compressed-SF_6 studies therefore establish that a gradient can change field distribution, charging and insulation strength, but they do not determine the statistical flashover response of an epoxy–air interface at atmospheric pressure. Air-based tests are required to determine how hot-side gas weakening interacts with conductivity-driven redistribution under the selected field topology and voltage history.

3.6.2. Comparison with the Closest Experimental Approaches

Gremaud et al. provide the strongest connection between material characterisation, thermal stress, surface-potential validation and flashover interpretation. Their programme used real-scale insulation in compressed SF_6, measured solid and gas currents and reproduced the temporal potential response with a coupled model. The current measurements, potential validation and flashover tests were nevertheless distributed across different specimens and arrangements rather than performed on one common test bench [14].

The Han–Pan series provides the closest statistical comparator. Its reduced-scale coaxial arrangement operated in air at approximately 0.1 MPa, tested both polarities and produced Weibull distributions from 15 flashovers per thermal condition. It also reconstructed surface charge and used it to interpret the near-flashover field. However, the thermal direction remained fixed, the charge and statistical datasets used different voltage histories, and the electrode arrangements were not completely identical [15], [51].

Liang et al. combined conductor-side heating with a one-hour DC pre-stress, a subsequent voltage rise, AC/DC superposition and polarity reversal. The scaled basin-type spacer retained a GIS-relevant interface-field condition, but the study primarily evaluated a functionally graded mitigation concept. The thermal direction remained fixed and the reported repetitions did not establish a complete statistical distribution [52].

Purnomoadi et al. demonstrated that an accessible reduced-scale specimen can reproduce a selected GIS interface-field distribution without copying the complete spacer shape. Their quasi-homogeneous arrangement was compared with the normalised field distribution of a 420 kV conical spacer. The study used compressed SF_6 under AC and impulse stress rather than DC thermal-gradient conditions, but it provides a direct precedent for assessing geometric relevance through the interface field [16].

These approaches are complementary. Gremaud is strongest in calibration and operational-scale validation; Han–Pan in air-based statistical flashover and charge diagnostics; Hering in separating and reconnecting the gas-density and conductivity effects; Liang in transient histories; and Purnomoadi in deliberate field matching. None combines these capabilities on one test bench while independently varying thermal direction, voltage polarity and pre-stress.

Geometric representativeness should therefore be assessed through the tangential and normal electric field distributions along the gas–solid interface, including peak location and triple-junction stress. Electrode shaping does not make a simplified specimen mechanically equivalent to a practical profiled spacer; it is used to reproduce the flashover-relevant interface-field topology while retaining an accessible and replaceable specimen.

3.6.3. Coverage of the Required Experimental Conditions

Figure 3.5 compares the closest preceding approaches against the conditions required for the intended method. Credit is given only when a condition was demonstrated directly on the relevant arrangement and with a compatible electrical history. The matrix evaluates integrated method capability, not the overall quality of each study.

The rightmost column distinguishes capabilities fixed by the design or test method from performance that still requires qualification. Atmospheric air, polarity reversal, thermal-direction reversal, the voltage sequence and the statistical procedure are architectural or procedural provisions. The realised temperature distribution, interface-field agreement and correspondence between the model and the physical test bench have not yet been demonstrated.

Direct surface-charge measurement is not required by the present method. The intended comparison uses measured thermal boundary conditions, a controlled voltage history, a calculated pre-flashover field and a planned statistical flashover response. Surface charge remains unmeasured, so any thesis statement about its distribution must be identified as model-based.

3.6.4. Remaining Gap

No reviewed study combines all eight conditions in Figure 3.5 on one test bench using a common specimen and electrode arrangement. The unresolved physical question follows from this capability gap: reduced gas density, conductivity-driven field redistribution and charge transport can favour different regions, but their relative influence has generally been studied using different geometries, histories or diagnostic arrangements.

A suitable test bench must therefore vary thermal direction, voltage polarity and pre-stress without changing the specimen geometry, electrode arrangement or statistical procedure. Measured T_{HV} and T_{GND} define the thermal boundary condition; an arrangement-specific model determines the corresponding interface-temperature and field distributions; and repeated flashovers distinguish systematic changes from test-to-test scatter. Table 3.1 converts the literature limitations into method requirements.

Together, these requirements define a test bench in which thermal direction, voltage polarity, electrical history and model inputs can be controlled without changing the test geometry.

The remaining need is a controlled test bench that combines these requirements while retaining one specimen geometry, field condition and statistical procedure. Such a bench is needed to compare future flashover observations consistently and to investigate how gas-density reduction, conductivity-driven redistribution and charge transport interact.

This thesis addresses the gap by designing the test bench, modelling its temperature and DC field, and defining the test procedure needed to study these conditions together

Required condition	Hering 2014 spacer	Gremaud 2016	Han–Pan 2025	Liang 2025	Purnomoadi 2020	This Thesis
Experimental control						
Thermal-gradient direction is reversible without changing the test geometry	○	○	○	○	○	A
Both DC polarities are tested under otherwise identical conditions	●	●	●	○	○	A
Tests are performed in controlled atmospheric air at $1\,\mathrm{bar}$	○	○	●	○	○	A
A common defined DC pre-stress and subsequent voltage-rise procedure is used for the primary comparison conditions	○	●	○	●	○	A
Repeated flashovers are sufficient for statistical comparison	○	○	●	○	○	A
Model linkage						
Measured boundary temperatures constrain the arrangement-specific thermal model	○	●	●	○	○	Q
The electrothermal model is checked using measurements from the same flashover bench and a compatible procedure	○	○	○	○	○	Q
Geometric relevance						
The test object provides a selected GIS-relevant interface-field topology	○	●	○	●	●	Q

Legend: ● demonstrated on the relevant arrangement; ○ not demonstrated or not reported sufficiently; A fixed by the present architecture/protocol; Q included in the present design but requiring experimental qualification.

Strict credit rule: evidence from another specimen, voltage history or diagnostic arrangement is not counted as complete coverage. A and Q apply only to the present work and do not denote experimental demonstration.

Figure 3.5: How the closest previous studies and this thesis cover the conditions the intended test method needs. A blank or open mark means a condition was not covered; it does not mean the study was weak.

Table 3.1: Literature gaps and corresponding requirements for the intended method.

Gap in prior work	Requirement for the intended method
Gas and pressure. The most complete validation studies use compressed SF_6, whose transport and flashover behaviour differ from atmospheric air.	Test in air at 1 bar and with controlled and recorded pressure, temperature and humidity.
Coupled thermal effects. Heating changes both gas density and the temperature-dependent conductivity of epoxy.	Measure the thermal boundary conditions, calculate the interface temperature and field, and determine the combined flashover response experimentally.
Polarity and gradient direction. These factors have not been varied independently within one fixed geometry.	Test both voltage polarities and both thermal-gradient directions using the same specimen, electrodes and voltage procedure.
Electrical history and statistics. Pre-stress, voltage-rise procedures and repetition counts differ between studies.	Apply one defined pre-stress and voltage ramp to every condition and use sufficient repetitions for statistical comparison.
Thermal-state definition. Endpoint temperatures or nominal ΔT do not define the complete interface-temperature distribution.	Measure T_{HV} and T_{GND} and use them as boundary conditions in an arrangement-specific thermal model.
Interface-field topology. Simplified accessible specimens may not reproduce the field distribution of a GIS spacer.	Shape the electrodes to reproduce the selected tangential and normal interface-field distributions.
Model-to-test correspondence. Model inputs and validation measurements are often obtained from different specimens or arrangements.	Use arrangement-specific inputs, compare the model with measurements from the same test bench, and state excluded physics explicitly.

3.7. Chapter conclusions

- A thermal gradient acts through two concurrent mechanisms: reduced gas density weakens the gas near the hot region, and increased epoxy conductivity shifts the DC field towards the colder region; charge transport can further modify either state.
- Across the reviewed studies, these effects have not been isolated within one consistent geometry, gas, and electrical history, so no single quantitative relationship transfers between arrangements.
- The mechanisms established in compressed SF_6 transfer to air, but the statistical flashover response of an epoxy-air interface at atmospheric pressure has not been determined and requires air-based testing.
- No reviewed study combines the required conditions; a GIS-relevant interface field, controlled air, independently reversible thermal direction and voltage polarity, defined pre-stress, and a repeatable statistical procedure on one test bench with a common specimen. This is a capability gap, not an absence of individual results.
- Electrothermal and charge-transport models can calculate temperature, potential, charge, and field, and after calibration can support a configuration-specific failure trend; statistical flashover voltage, Weibull slope, discharge path, and event location remain experimental endpoints.
- Geometric relevance is best assessed through the tangential and normal interface-field distributions, so electrode shaping can reproduce the flashover-relevant field topology without mechanically copying a profiled spacer.

4

Design Methodology and Requirements

This chapter turns the three research questions into the functions and constraints the test bench must satisfy, and the rule used to assess design options. The requirements defined here govern the designs developed in the following chapters.

4.1. From the Research Questions to the Functional Requirements

The thesis is motivated by three research questions:

RQ1. What effect does the temperature gradient across a GIS spacer have on the statistical distribution of surface-flashover voltage?

RQ2. What effect do voltage polarity and thermal-gradient direction have on the earliest visible surface-flashover region along the spacer–electrode interface?

RQ3. What effect does DC pre-stress duration have on the surface-flashover voltage distribution, and does this effect change when a thermal gradient is imposed?

RQ1 requires repeated surface-flashover voltage measurements under the same controlled condition, because a single event cannot represent a statistical distribution. The voltage history, temperatures, environmental condition, specimen preparation, and event classification must therefore be recorded for every test, following the statistical treatment in IEC 62539 [57] and the independence basis in Appendix H.

RQ2 requires both voltage polarities and both thermal-gradient directions to be studied without changing the field-defining geometry. The optical record identifies the earliest visible surface-flashover region and the initial propagation direction; it cannot identify the microscopic start of the discharge or preceding partial-discharge activity.

RQ3 requires DC pre-stress duration to be treated as a controlled experimental variable. The bench must apply and record defined hold times under both thermal-gradient and no-gradient conditions, with the pre-stress voltage, polarity, voltage ramp, voltage-rise procedure, specimen basis, and environmental condition held fixed while only the hold duration varies. The numerical model links the selected hold times to the predicted pre-flashover field in Chapters 8 and 9. Comparing the resulting surface-flashover voltage distributions then shows whether the response changes as the field redistributes over time, and whether that dependence changes under a thermal gradient.

These needs define the functional requirements developed in the rest of this chapter.

4.2. Functional Requirements

A functional requirement states what the bench must enable or record; it does not prescribe a component unless that component is fixed by a governing constraint. This lets different design options be compared against the same need.

The requirements are derived, not assumed. Each follows from a research question or from the capability gap identified in Chapter 3: RQ1 and RQ3 require repeated, controlled electrical and thermal conditions with complete records; RQ2 requires reversible polarity and gradient direction on a fixed geometry; and the gap requires that these conditions be combined on one bench with a common specimen. Each requirement is necessary, in that removing it prevents a research question from being answered or leaves a gap condition uncovered, and the set is treated as sufficient against the conditions Chapter 3 identified as missing from prior work. Completeness beyond this is not claimed: a requirement found missing during qualification would appear as an acceptance check with no matching entry, and could be added without disturbing the others.

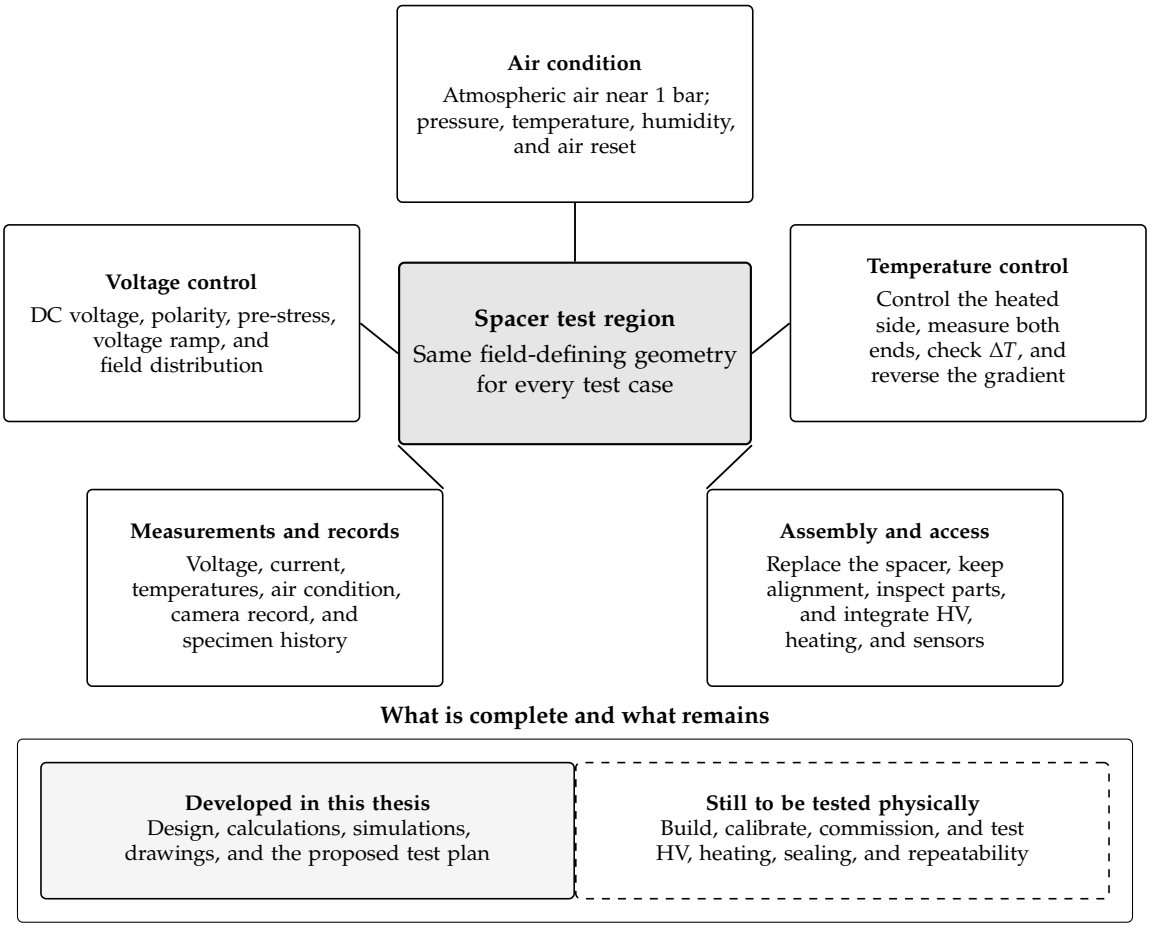


Figure 4.1: Main functions of the proposed test bench. Voltage control, temperature control, air conditions, measurements, and assembly all support the same spacer test region. The lower band separates the work developed in this thesis from the physical tests still required before experiments can begin.

The required functions form five groups — electrical control, thermal control, environmental control, diagnostics and traceability, and assembly and access — all acting on the same field-defining electrode–spacer arrangement. Each group is described below and specified, with its acceptance checks, in Table 4.1.

4.2.1. Electrical Stress and Voltage History

The operating voltage is not fixed in advance; it is derived from the field. With the electrode–spacer geometry fixed, the field in the air region is computed, and the maximum operating voltage is taken

as the highest DC voltage at which the peak air-region field stays below a defined margin against air breakdown. For the present geometry this criterion gives 50 kV (Chapter 9). At and below this voltage the bench must apply and record both polarities, the voltage ramp, the pre-stress level and duration, and the final voltage rise, without changing the field-defining geometry (FR-E1, FR-E4). For the RQ3 comparison, the actual hold start and end times are recorded so the realised pre-stress duration is traceable for every test.

The same geometry is assessed at 60 kV, above the derived operating voltage, to screen the design with reduced margin and to characterise non-target stressed regions (FR-E3). This is a numerical screening level, not a physical rating or withstand qualification; field comparisons use defined interface paths and finite end regions rather than raw solver maxima.

4.2.2. Thermal Condition

The thermal target is a realised axial temperature difference

$$|\Delta T| = 40\text{–}50\ \text{K}, \qquad \Delta T = T_{\text{HV}} - T_{\text{GND}}, \tag{4.1}$$

together with a matched no-gradient reference held to the same target within a stability band. The bench must establish and hold these two thermal states. The means used to hold them follow a stability criterion rather than being fixed here: the design applies the least control that meets the target, evaluating single-side regulation first and adding control of the second electrode only where the target cannot otherwise be held. Which case applies, for each gradient direction, is determined in Chapter 6.

The thermal-gradient direction must be reversible without changing the field-defining geometry (FR-T3), and the two directions are assessed separately because their thermal surroundings differ. The no-gradient reference (FR-T1) uses the same field-defining geometry, voltage sequence, measurement arrangement, specimen basis, and environmental controls as the gradient tests; its allowable residual temperature difference and stability period are established during qualification, not assumed from equal setpoints.

A prescribed 100 °C hot-source case is used as an upper numerical thermal-design condition. The value provides a high-temperature assessment case of the same order as upper thermal conditions used in the IEC 62271 framework, but it is not prescribed by the standard for the present test bench [17], [58]. It is not the normal experimental setpoint and does not define the allowable temperature of the complete bench. The physical operating envelope is set by the lowest applicable rating of the realised components and materials. The numerical condition and its results are documented in Chapters 8 and 9.

4.2.3. Environmental Condition

The experimental medium is atmospheric air near 1 bar; pressure, ambient temperature, and relative humidity are measured and recorded for every test, and the chamber retains a defined condition during a test with a controlled reset between tests (FR-V1, FR-V2). IEC 60060-1 informs the voltage-measurement and atmospheric-recording practice, and IEC TS 62271-318 provides the HVDC GIS insulation-testing context; the reduced air-at-1 bar bench does not claim conformity with the rated-voltage, gas, or pressure scope of that technical specification [17], [59].

4.2.4. Diagnostics and Traceability

The primary experimental endpoint is the voltage at complete surface flashover along or close to the gas–solid interface. The electrical and optical records must support event timing and distinguish the intended surface-flashover event from a gas-gap, feedthrough, chamber, heater, or external non-target discharge (FR-D1, FR-D2).

Every accepted test carries the data fields listed in FR-D1 and defined in Chapter 10, together with full specimen and electrode traceability: formulation, fabrication route, batch, preparation, storage, previous electrical history, and assembly and electrode condition (FR-D3). The generic epoxy properties and prescribed conductivity function used in the numerical model do not define an experimentally reproducible spacer material.

4.2.5. Assembly, Access, and Repeatability

The spacer must be replaceable without changing the field-defining geometry, with repeatable alignment and contact conditions, optical access to the interface, and access for inspection, sensing, heating-system integration, and maintenance (FR-R1, FR-R2). Alignment, contact, access, sealing, and repeated assembly remain physical qualification items, not satisfied by drawing intent alone.

The requirement identifiers use the prefix **FR** for functional requirement. The following letter identifies the family: **E** for electrical, **T** for thermal, **V** for environmental, **D** for diagnostics and traceability, and **R** for assembly and repeatability. The number identifies the individual requirement within that family.

Table 4.1: Consolidated functional requirement register.

ID	Functional requirement	Evidence developed in this thesis	Remaining physical qualification and acceptance check
FR-E1	Apply and record the specified DC voltage history up to the maximum operating voltage set by the air-region field-margin criterion, including selectable pre-stress durations.	The HV architecture and proposed procedure define polarity, voltage ramp, pre-stress voltage, hold duration, final voltage rise, and the required records; the field assessment sets this voltage at 50 kV for the present geometry (Chapter 9).	Calibrate the voltage and current measurements; verify the commanded sequence, actual hold duration, timing accuracy, and synchronised record; confirm operation up to the derived operating voltage without a non-target event during qualification.
FR-E2	Preserve the principal coaxial-reference interface-field topology.	Chapters 5 and 9 compare the interface profile and both end regions using defined extraction paths.	Reassess the realised geometry with the same paths and regions; report the deviations and apply the comparison rule fixed in the geometry chapter.
FR-E3	Screen non-target stressed regions and characterise the field at both spacer ends.	Numerical assessment at 60 kV examines the integrated geometry and finite end regions.	Perform integrated HV qualification; confirm that the intended spacer region remains the limiting test region and classify any non-target event.
FR-E4	Support both voltage polarities without changing the field-defining geometry.	The electrical and mechanical architecture provides the same test region for either polarity.	Verify both polarities with the same assembly, measurement chain, and environmental controls.
FR-T1	Establish and measure the required thermal states: a realised axial temperature difference of 40 K to 50 K an unheated ambient-temperature reference condition	Chapter 6 defines the gradient target and the two-temperature measurement basis. The same field-defining geometry, voltage system, measurement arrangement, specimen basis, and environmental controls are retained for gradient and no-gradient cases.	Calibrate both temperature measurements. Accept the gradient condition when $\lvert\Delta T\rvert$ = 40–50 K, and accept the unheated ambient-temperature reference only when both electrode temperatures have stabilised near the measured ambient temperature and the residual temperature difference remains within the tolerance established during qualification.
FR-T2	Establish and hold a stable target ΔT of 40 K to 50 K using the minimum control that meets the stability criterion.	Chapter 6 evaluates single-side regulation and determines where control of the second electrode is required.	Establish the stability band, settling time, and the control configuration needed for each gradient direction during qualification.
FR-T3	Reverse the thermal-gradient direction without changing the field-defining geometry.	Local heating provision is included at both electrode ends (Chapter 6).	Qualify the two directions separately; each must meet the 40 K to 50 K target (FR-T1) and the stability requirement (FR-T2).
FR-T4	Compare the modelled spacer-temperature profile with the coaxial reference arrangement.	Thermal simulations compare the designed arrangements with the reference case.	Use the measured electrode temperatures as model boundaries; confirm the required hot-to-cold direction and report the profile deviation using the Chapter 6 comparison method.
FR-V1	Operate in atmospheric air and record pressure, temperature, and relative humidity.	The experimental scope and required environmental records are defined.	Calibrate the sensors and accept tests only within the test-series ranges established during qualification.
FR-V2	Retain a defined chamber condition and restore it between tests.	Chapter 7 defines the chamber, sealing, access, and reset functions; Chapter 10 defines the proposed sequence.	Perform leak, retention, purge/reset, and settling checks; establish the allowed change during a test and the reset criteria between tests.

Continued on next page

Table 4.1: Consolidated functional requirement register (continued).

ID	Functional requirement	Evidence developed in this thesis	Remaining physical qualification and acceptance check
FR-V3	Use materials and seals compatible with the qualified electrical and thermal envelope.	Material families, component data, and unresolved specifications are documented in the design chapters and appendices.	Confirm grades, certificates, compatibility, and the lowest applicable rating; complete thermal, sealing, and HV checks on the assembled system.
FR-D1	Record the complete electrical, thermal, and environmental history.	Chapter 10 defines the required data fields, including commanded and actual pre-stress duration, hold start and end times, and the full voltage sequence.	Verify synchronised logging, hold start and end timestamps, actual hold duration, sensor status, and record completeness before accepting a test.
FR-D2	Record and classify the complete surface-flashover event.	Optical access, current recording, and the event definition are included in the design and procedure.	Demonstrate that the electrical and optical records can distinguish complete surface flashover from partial activity and non-target discharge.
FR-D3	Maintain specimen, electrode, preparation, assembly, and test-history traceability.	The required specimen and material records are defined in the procedure and Appendix B.	Require a complete, unique record for every accepted test; missing critical traceability information leads to exclusion or censoring.
FR-R1	Replace the spacer while preserving alignment and contact condition.	The mechanical design and drawings define the assembly basis and replaceable specimen.	Inspect or measure alignment and contact after repeated assembly; establish the allowable tolerance before the test series.
FR-R2	Provide optical, inspection, sensing, heating-system, and maintenance access.	Chapters 6 and 7 develop the integration and access provisions.	Demonstrate access and maintenance on the assembled bench without compromising alignment, sealing, insulation, or the optical view.

Every requirement is traceable to either evidence developed in this thesis or an assigned physical acceptance check. Where a numerical acceptance limit is not yet justified, the table states that the limit must be established during physical qualification rather than assigning an unsupported value.

4.3. Governing Constraints

The functional requirements describe what the bench must do. The constraints define boundaries that the design options are not allowed to violate.

4.3.1. Electrical Constraints

The maximum operating voltage is the 50 kV basis derived from the field-margin criterion (Chapter 9); the 60 kV case is reserved for numerical assessment (C-E1). Heating, sensing, and support systems must not create an unintended conductive path from the HV electrode to ground or a new dominant stressed region (C-E3). Field decisions use physically defined paths and finite regions, because idealised corners and contacts create solver maxima that are not valid physical acceptance values (C-E2).

4.3.2. Thermal and Material Constraints

The allowable temperature of the realised bench is the lowest applicable rating among the spacer, electrodes, seals, tubing, fittings, fluids, sensors, feedthroughs, cables, supports, and chamber materials; one component's rating is not the rating of the complete system (C-T1). Thermal expansion and repeated heating can affect alignment, contact pressure, sealing, and optical access, and must be checked physically before experimental use (C-T2).

4.3.3. Environmental and Integration Constraints

Atmospheric air near 1 bar is a deliberate scope constraint; the present work does not reproduce the gas density, pressure, or active gas volume of a full-scale GIS (C-V1). The field-defining geometry must remain unchanged when polarity, heated side, instrumentation, or specimen are changed, and services entering the chamber must not compromise the electric field, sealing, visibility, or maintainability (C-I1).

4.3.4. Safety Constraint

The final arrangement requires a defined grounding concept, interlocked access, controlled discharge before opening, protection against thermal and electrical faults, and a safe procedure for assembly and maintenance (C-S1). This chapter records these as design constraints; the detailed laboratory procedure and acceptance checks belong to Chapters 7 and 10.

Constraint identifiers use the prefix **C**. The following letter identifies the family: **E** for electrical, **T** for thermal and material, **V** for environmental scope, **I** for integration, and **S** for safety. The number identifies the individual constraint within that family. See Table 4.2 for the constraints list.

Table 4.2: Governing constraint register.

ID	Constraint	Design consequence	Evidence or qualification owner
C-E1	Keep the 50 kV operating basis separate from the 60 kV numerical assessment level.	No physical rating or withstand claim may be inferred from the 60 kV simulation.	Chapters 5, 8, 9, and 10.
C-E2	Use defined interface paths and finite end regions for field assessment.	Raw corner or global solver maxima are not used as physical design values.	Chapters 5, 8, and 9.
C-E3	Isolate HV-side heating and sensing from ground.	No unintended conductive return path or dominant local field enhancement is permitted.	Chapters 6 and 7; physical HV qualification.
C-T1	Respect the lowest applicable component and material temperature rating.	The complete system cannot inherit the highest rating of one selected component.	Chapters 6 and 7; Appendix B; physical qualification.
C-T2	Accommodate thermal expansion and repeated thermal cycling.	Alignment, contact, sealing, and visibility must remain acceptable after repeated conditioning.	Chapters 6 and 7; repeated-cycle qualification.
C-V1	Retain atmospheric air near 1 bar as the experimental scope.	Results are arrangement-specific and do not represent compressed-gas GIS operation directly.	Chapters 1, 3, 10, and 11.
C-I1	Preserve the field-defining geometry during integration and configuration changes.	Polarity reversal, gradient reversal, sensing, and specimen replacement must not redefine the test region.	Chapters 5–7; dimensional and integrated checks.
C-S1	Provide grounding, controlled access, discharge, fault protection, and safe opening.	The bench cannot enter experimental service until the laboratory safety procedure and interlocks are qualified.	Chapters 7 and 10; laboratory approval.

Throughout the following chapters, numerical assessment is reported separately from physical qualification: calculations and simulations provide design evidence, but they do not demonstrate the performance of a manufactured and commissioned test bench.

4.4. Design-Decision and Qualification Framework

Design options are evaluated against the same requirements and the same evidence standard. The decision rule is fixed before any option is retained, prioritised, or selected:

> A design option is rejected or changed if it fails a hard constraint. Options that pass the hard constraints are compared against the same functional requirements at the same level of detail. An option is selected only when the available evidence is sufficient for that design decision and every unresolved physical-performance question is recorded as a qualification requirement.

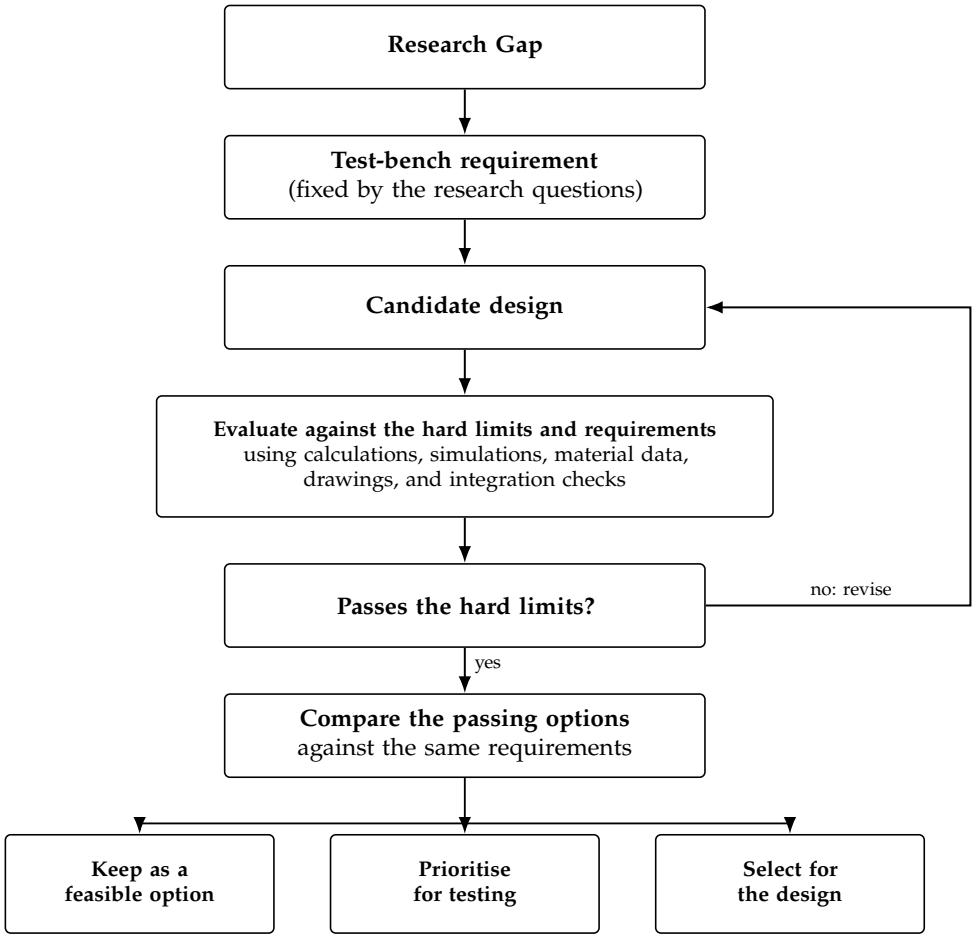


Figure 4.2: Decision and qualification framework for design options. Selection is a design decision, not physical qualification.

This framework is applied as an iterative loop rather than a single pass (Figure 4.2). A candidate design is evaluated against the hard limits and the functional requirements using the available evidence — calculations, simulations, material or manufacturer data, drawings, and integration checks. An option that fails a hard limit is revised and re-evaluated, while the requirements themselves remain fixed by the research questions. Options that pass are compared, and one is taken forward for the design while the others are retained as technically developed fallbacks.

The evidence types are not interchangeable, and none of them is physical qualification: a simulated temperature field does not prove that a heater can establish the prescribed boundary, and a numerical field assessment does not establish physical withstand. Selection at this stage is therefore a design decision; the physical performance, commissioning, and full-system tests that would qualify the realised bench remain outside the scope of this thesis.

Because neither option is physically qualified within this thesis, the comparison cannot rank demonstrated performance and is instead made on the criteria that govern feasibility. The comparison axes are the energy-delivery path and its HV integration, the provision for gradient reversal at either electrode, the numerical insulation screening at the design-verification level, and the principal unresolved feasibility gate remaining before thermal and electrical qualification. The option with the narrower feasibility gate is taken forward as the more direct candidate; the other is retained as a technically developed fallback rather than rejected.

This rule and these criteria are applied to the two retained thermal architectures in Chapter 6. Hot-oil circulation and floating cartridge heating both satisfy the thermal requirements and preserve the field-defining geometry; Chapter 6 compares their remaining feasibility gates and identifies the more direct candidate while retaining the other as a technically developed fallback.

4.5. Chapter conclusions

- The three research questions define five requirement families the test bench must satisfy electrical control, thermal control, environmental control, diagnostics and traceability, and assembly and access all acting on one field-defining electrode-spacer geometry.
- Each requirement is derived from a research question or the Chapter 3 capability gap, and is traceable to either evidence developed in this thesis or an assigned physical acceptance check, so no unsupported acceptance value is assigned.
- RQ3 requires DC pre-stress duration to be a controlled variable: selectable, recorded hold times applied identically under matched thermal-gradient and no-gradient conditions, with all other electrical, environmental, and specimen conditions held fixed.
- Functional requirements (FR) state what the bench must enable and record;governing constraints (C) bound the admissible design options.
- A fixed decision rule governs option selection: reject on any hard-constraint failure; otherwise compare options against the same requirements, and where neither is physically qualified, select the option with the narrower unresolved feasibility gate while retaining the other as a fallback.

5

Electrode and Spacer Geometry Design

This chapter develops the electrode–spacer geometry that defines the electric field distribution in the reduced-scale test bench. A reduced-scale coaxial GIS model from Li is used as the electrical reference, and candidate geometries are assessed using interface-field metrics derived from that case. The selected design uses a 50 mm spacer with shaped high-voltage and grounded electrodes. It is verified numerically against the reference under stationary DC conditions at 60 kV without an imposed thermal gradient.

5.1. Reference Coaxial Geometry

In a coaxial GIS, the high-voltage conductor is located inside a grounded enclosure and supported by solid spacers [60]. The test bench developed in this thesis does not reproduce the complete coaxial arrangement. Instead, its electrode–spacer geometry is designed to reproduce the main gas–spacer interface-field behaviour of a reduced-scale coaxial reference. The reference is the reduced-scale model reported by Haoluan Li [60]. Its main dimensions are shown in Figure 5.1 and summarised in Table 5.1.

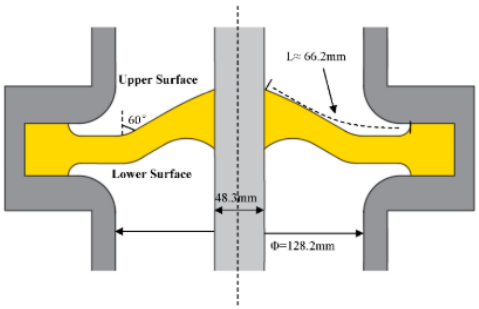


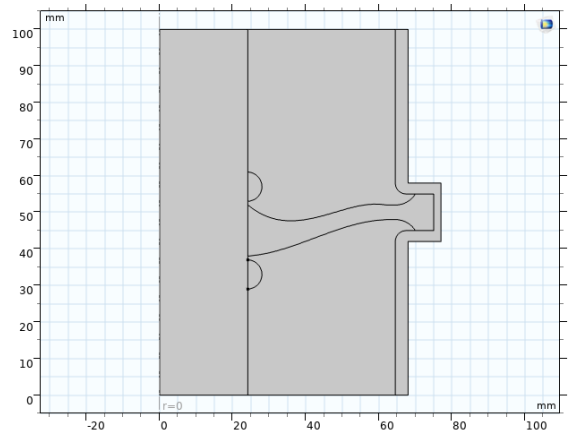
Figure 5.1: Reduced-scale coaxial reference geometry adopted from Li [60].

Table 5.1: Dimensions of Li's demonstrator and reduced-scale coaxial reference model [60].

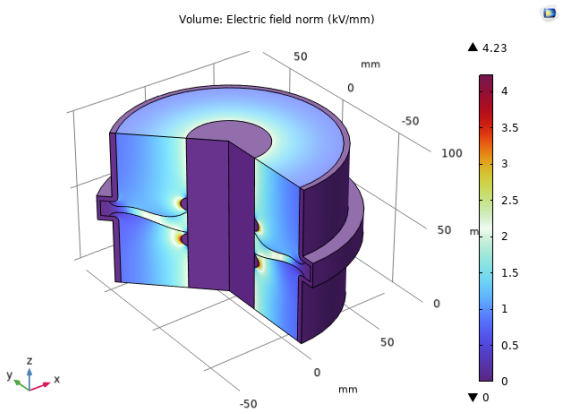
Parameter	Demonstrator	Reduced-scale model
Enclosure radius, R_e	270 mm	64.1 mm
Enclosure diameter, D_e	540 mm	128.2 mm
Conductor radius, R_c	95.5 mm	24.15 mm
Conductor diameter, D_c	191 mm	48.3 mm
Gas gap	174.5 mm	39.95 mm

The reference defines the electrical comparison basis rather than the mechanical layout of the test bench. The transferred quantities include the interface-field profile and the locations of the main high-field regions. The comparison also uses the finite end-region fields near the two spacer ends and the background gas-field variation away from the spacer interface. The coaxial enclosure, original operating conditions, and thermal hardware are not transferred. Figure 5.2 shows the COMSOL model used to calculate the reference electric field distribution.

The reference geometry was re-modelled in COMSOL as a 2D axisymmetric model using the adopted dimensions. Panel (a) shows the geometry used for the electric field calculation. Panel (b) shows the



(a) 2D axisymmetric reference geometry.



(b) Revolved reference model with electric field distribution.

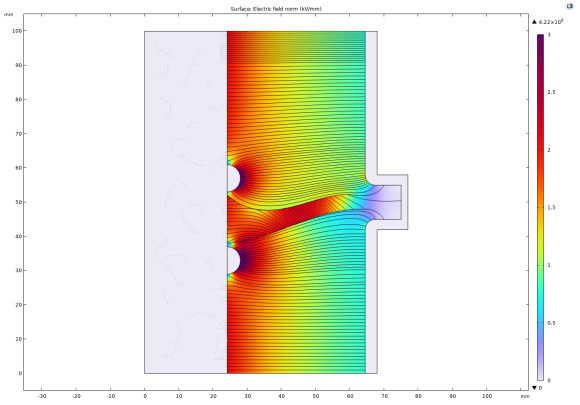
Figure 5.2: COMSOL implementation of the reduced-scale coaxial reference geometry.

revolved model and the corresponding coaxial field distribution. This model provides the electrical baseline from which the comparison quantities in Section 5.2 are derived.

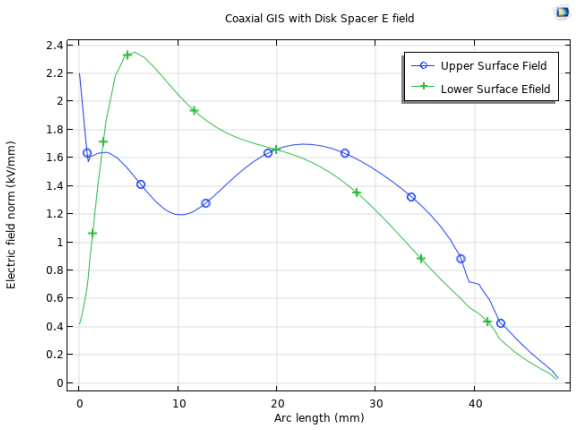
5.2. Reference electric field Behaviour and Comparison Metrics

The coaxial reference model provides the electric field quantities used to assess the electrode-spacer geometries. The comparison is based on the field magnitude along the gas–spacer interface and on finite end-region quantities derived from this profile.

Figure 5.3 shows the calculated electric field distribution and the extracted interface-field profiles. Panel (a) shows the field distribution around the spacer. Panel (b) shows the field magnitude along the upper and lower spacer surfaces from the high-voltage side towards the grounded side.



(a) electric field distribution in the coaxial reference case.



(b) electric field profile along the spacer surface.

Figure 5.3: Field behaviour extracted from the coaxial reference case

The reference field is HV-side dominated and decreases towards the grounded end. The upper and lower spacer surfaces form an envelope around the mean reference profile. Table 5.2 defines the quantities used for the geometry comparison.

Table 5.2: electric field comparison metrics derived from the coaxial reference case at 60 kV DC. The coaxial-reference field profile is the pointwise mean of the upper and lower gas–spacer interface-field profiles.

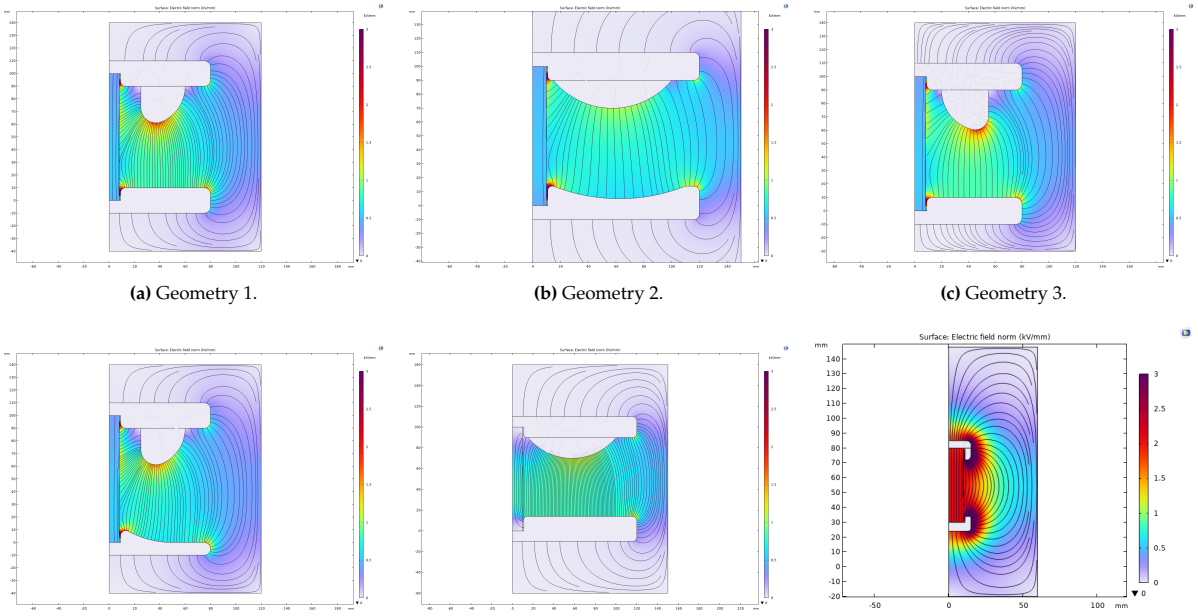
Metric	Expression	Coaxial reference value	Definition	Purpose
Representative profile peak	$\bar{E}_{\max} = \max_{0\le\xi\le1} \lvert\bar{E}(\xi)\rvert$	2.053 kV/mm	Highest field magnitude of the pointwise mean of the upper and lower coaxial interface-field profiles.	Compares the representative peak interface field between geometries.
HV-side end field	$E_{\mathrm{HV}} = \max_{0\le s\le 10\ \mathrm{mm}} \lvert E(s)\rvert$	2.053 kV/mm	Largest interface-field magnitude within the first 10 mm from the HV end.	Checks whether the dominant HV-side field feature of the reference case is retained.
Grounded-side end field	$E_{\mathrm{GND}} = \max_{L_{\mathrm{cp}}-10\ \mathrm{mm}\le s\le L_{\mathrm{cp}}} \lvert E(s)\rvert$	0.977 kV/mm	Largest interface-field magnitude within the last 10 mm adjacent to the grounded end.	Compares the grounded-side field feature between geometries.
HV/GND field ratio	$R_{\mathrm{HV/GND}} = \frac{E_{\mathrm{HV}}}{E_{\mathrm{GND}}}$	2.101	Ratio between the HV-side and grounded-side end fields.	Indicates the degree of HV-side field dominance.
Creepage length	$L_{\mathrm{cp}} = \int_{\Gamma_{\mathrm{gs}}} \mathrm{d}s$	48.9 mm	Length of the gas–spacer interface path used for field extraction.	Defines the comparison path for geometries with different interface lengths.
Mean interface field	$E_{\mathrm{mean}} = \frac{V}{L_{\mathrm{cp}}}$	1.227 kV/mm	Applied voltage divided by the gas–spacer interface creepage length.	Provides the mean field used in the utilisation factor.
Schwaiger utilisation factor	$\eta = \frac{E_{\mathrm{mean}}}{\bar{E}_{\max}}$	0.598	Ratio of the mean interface field to the representative profile peak.	Compares the overall field utilisation between geometries.
Profile character	Qualitative comparison of $\lvert E(\xi)\rvert$	GIS-type, HV-dominated	Overall interface-field trend, peak location, and dominant end region.	Checks whether the main field behaviour of the coaxial reference is retained.
Atmospheric-air reference field	$E_{\mathrm{air,ref}} \approx 3$ kV/mm	Reference only	Approximate breakdown-field scale for a smooth, approximately uniform centimetre-scale air gap at atmospheric pressure.	Used only as an electrical-stress screening reference; it is not a surface-flashover criterion or a universal local breakdown field.

A field of approximately 3 kV/mm is used only as a reference scale for breakdown in smooth, approximately uniform centimeter-scale atmospheric-air gaps. It is not treated as a universal local breakdown field or as a surface-flashover criterion [18], [20], [61].

5.3. Electrode-Profile Selection and First Geometry Screening

The first geometry screening applies the electrical requirements established in Chapter 4. The dominant field stress should occur at the gas-spacer interface rather than in a competing region of the gas gap. Candidate geometries are assessed using the interface-field behaviour and comparison quantities defined in Section 5.2. The electrode profile, electrode-spacer spacing, and spacer length are therefore treated as coupled design variables.

Previous studies show that spacer geometry, electrode contour, and the electrode–spacer contact region influence the local electric field distribution and surface-flashover behaviour [4], [22], [62], [63]. Smooth field-shaping electrodes are therefore used to limit unintended local field enhancement. Simplified electrode–spacer arrangements have also been used for controlled laboratory flashover studies at TU Delft [16]. The present screening examines whether each candidate profile places the dominant field stress at the intended gas–spacer interface. Figure 5.4 shows the profile families examined and the geometry retained for further refinement.



(a) Geometry 1. **(b)** Geometry 2. **(c)** Geometry 3.

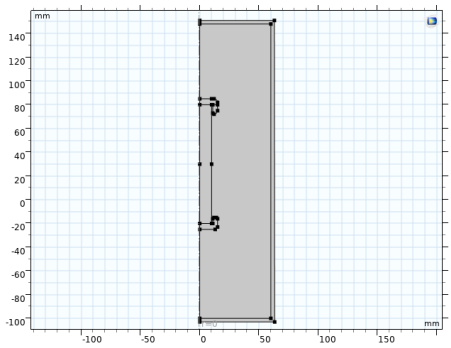
(d) Geometry 4. **(e)** Geometry 5. **(f)** Selected screening geometry.

Figure 5.4: Early electrode–spacer profile screening cases.

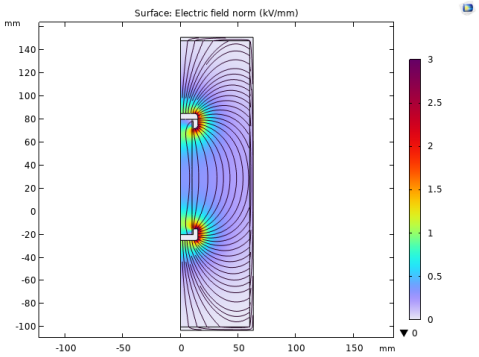
The screening was used to select a profile family rather than final dimensions. A smooth electrode contour alone did not place sufficient field stress at the spacer interface. The electrode also had to approach the spacer closely enough for the field to couple to the interface. Panel (f) was therefore retained for dimensional refinement. Its interface-field profile still differed from the coaxial reference, so the spacer length and the high-voltage and grounded electrode noses were subsequently adjusted.

5.4. Refinement of the Electrode-Spacer Geometry

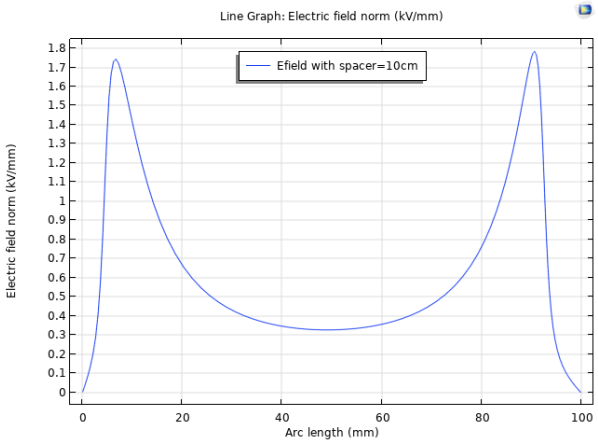
The profile-screening step in Section 5.3 produced an intermediate geometry whose interface-field profile still differed from the coaxial reference. The refinement therefore focused on two variables: spacer length and electrode-nose shape. Spacer length controls the creepage length L_{cp}, the mean interface field $E_{mean} = V/L_{cp}$ [60], and the utilisation factor η. The high-voltage and grounded electrode noses control the local end-region fields E_{HV} and E_{GND}. Figure 5.5 shows the geometry used as the starting point for this refinement.



(a) Intermediate electrode–spacer geometry.



(b) electric field distribution of the intermediate geometry.

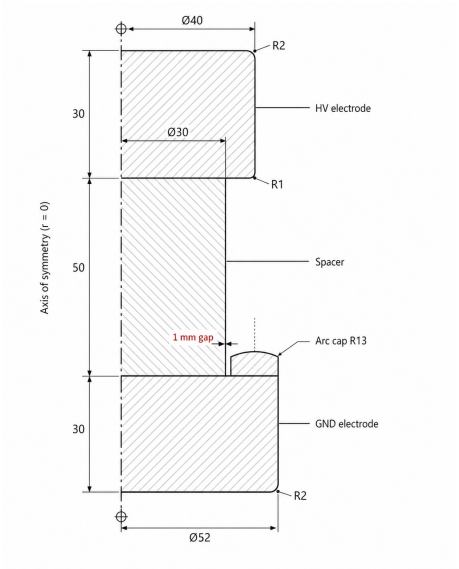


(c) Interface-field profile along the spacer surface.

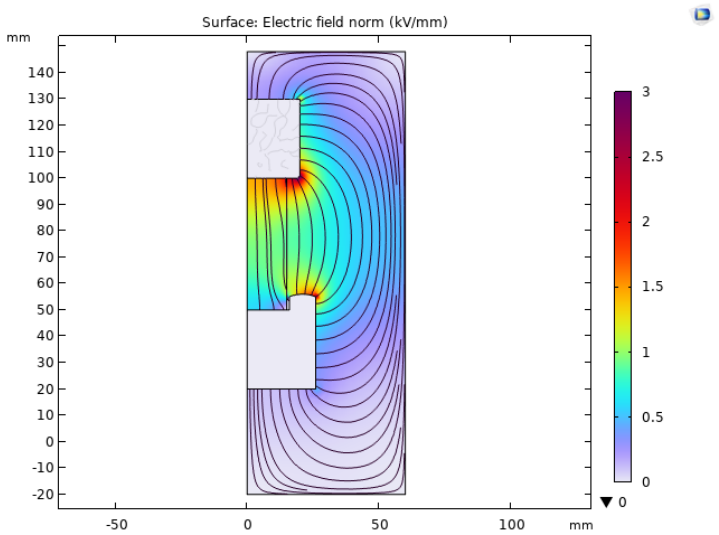
Figure 5.5: Intermediate electrode-spacer geometry and calculated electric field behavior for the 100 mm spacer case.

The intermediate geometry places the dominant field stress near the spacer ends, but its interface-field profile still differs from the coaxial reference. For the approximately 100 mm interface length, $E_{\text{mean}} \approx 0.50$ kV/mm at 50 kV. The extracted profile gives $E_{\max} \approx 1.78$ kV/mm and therefore $\eta \approx 0.28$. The spacer length was reduced to 50 mm to increase the mean interface field and improve the utilisation factor. Spacer length is therefore treated as an electrical field-shaping variable rather than only as a mechanical dimension.

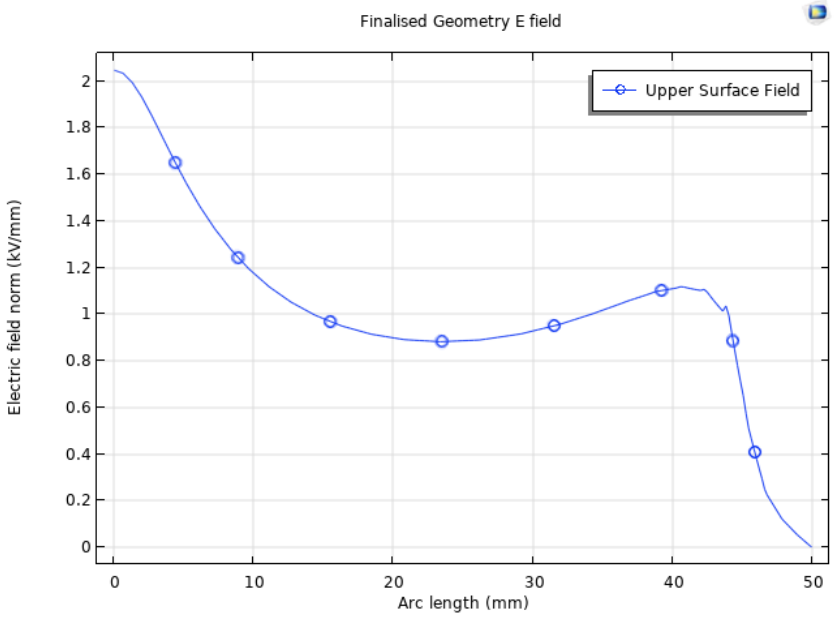
After reducing the spacer length, the electrode noses were adjusted to control the two end-region fields. Elevated fields near the spacer ends were retained because they are also present in the coaxial reference. The refinement therefore aimed to control their magnitude and location rather than eliminate them. The resulting electrode–spacer geometry is shown in Figure 5.6.



(a) Finalised electrode–spacer geometry.



(b) electric field distribution of the finalised geometry.



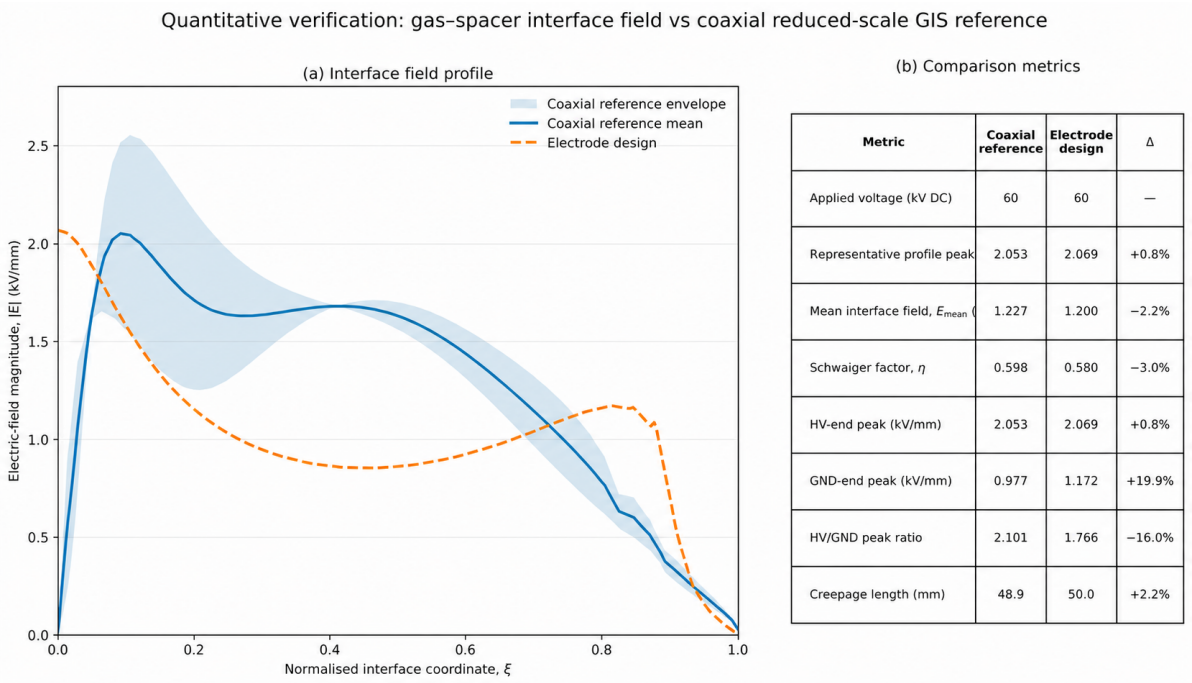
(c) Interface-field profile along the spacer surface.

Figure 5.6: Finalised electrode–spacer geometry and its electric field behaviour.

The selected geometry therefore combines a 50 mm spacer with shaped high-voltage and grounded electrode noses to control the interface-field distribution and the two end-region fields.

5.5. Verification against the Reference Geometry

The finalised electrode–spacer geometry is verified against the coaxial reference under stationary DC conditions at 60 kV without an imposed thermal gradient. The comparison uses the interface-field profile and the metrics defined in Section 5.2, as shown in Figure 5.7.



Metric	Coaxial reference	Electrode design	Δ
Applied voltage (kV DC)	60	60	—
Representative profile peak	2.053	2.069	+0.8%
Mean interface field, E_{mean} (	1.227	1.200	−2.2%
Schwaiger factor, η	0.598	0.580	−3.0%
HV-end peak (kV/mm)	2.053	2.069	+0.8%
GND-end peak (kV/mm)	0.977	1.172	+19.9%
HV/GND peak ratio	2.101	1.766	−16.0%
Creepage length (mm)	48.9	50.0	+2.2%

Figure 5.7: Quantitative verification of the finalised electrode–spacer geometry against the reduced-scale coaxial GIS reference.

Figure 5.8 provides a second comparison using the electric field magnitude away from the spacer interface. For each geometry, the field is evaluated along a straight line in the gas from the high-voltage side towards the grounded side.

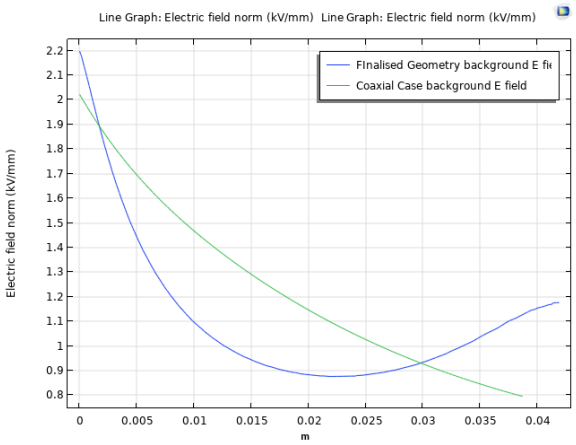


Figure 5.8: Background electric field magnitude for the finalised electrode-spacer geometry and the coaxial reference case.

The interface-field profiles retain the main HV-side-dominated behaviour of the coaxial reference. Exact point-by-point agreement is not expected because the creepage paths and surrounding geometries differ. Away from the spacer interface, the background field also follows the same general variation from the high-voltage side towards the grounded side.

The global field metrics show close agreement with the coaxial reference. The representative profile

peak differs by +0.8%, the mean interface field by −2.2%, and the Schwaiger utilisation factor by −3.0%. The finalised geometry therefore preserves the overall field level and utilisation of the reference case.

The largest difference occurs near the grounded end. The HV-side peak differs by only +0.8%, whereas the grounded-side peak increases from 0.977 kV/mm to 1.172 kV/mm, a difference of +19.9%. The corresponding HV/GND field ratio decreases from 2.101 to 1.766. Both geometries nevertheless remain HV-side dominated.

5.6. Chapter conclusions

- The finalised electrode and spacer geometry gives global interface-field metrics close to those of the coaxial reference. The representative profile peak differs by +0.8%, the mean interface field by −2.2%, and the Schwaiger utilisation factor by −3.0%.
- Both geometries remain HV-side dominated. The HV-side peak changes from 2.053 kV/mm to 2.069 kV/mm, while the grounded-side peak increases from 0.977 kV/mm to 1.172 kV/mm. The corresponding HV/GND field ratio decreases from 2.101 to 1.766.
- Spacer length acts as an electric field shaping variable. Reducing the interface length from approximately 100 mm to 50 mm increased the mean interface field and improved the field utilisation.
- The selected geometry combines a 50 mm spacer with shaped high-voltage and grounded electrodes while retaining the main interface-field behaviour of the coaxial reference.

6

Thermal Management System

This chapter develops the thermal system required to establish the prescribed temperature conditions on the fixed electrode–spacer geometry. The thermal requirements defined in Chapter 4, together with the need to preserve the field-defining geometry, form the design basis. Hot-oil circulation and floating cartridge heating are developed and compared to select a preferred candidate for physical qualification.

6.1. Thermal-System Design Requirements

The thermal system must establish the required temperature conditions without changing the field-defining electrode-spacer geometry. The axial temperature difference is defined as

$$\Delta T = T_{\mathrm{HV}} - T_{\mathrm{GND}}.$$

The gradient condition specified in Chapter 4 is

$$|\Delta T| = 40\text{–}50\ \mathrm{K}.$$

A positive ΔT denotes the HV-hot condition, while a negative ΔT denotes the ground-hot condition. Both electrode temperatures are measured independently so that the realised temperature difference is obtained from the measured values. Figure 6.1 illustrates this sign convention for the HV-hot condition.

The HV-electrode temperature is measured using a fibre-optic temperature sensor, while the grounded-electrode temperature is measured using a PT100 resistance temperature detector. Both sensors are mounted on the inner surface of the corresponding adaptor at the electrode–adaptor interface. Their leads are routed through the hollow aluminium rods, and the sensors are installed before the heating components.

An unheated ambient-temperature reference condition is also required. No heating is applied at either electrode, and both electrode temperatures are allowed to stabilise near the measured ambient temperature. The allowable residual temperature difference and stability period are established during physical qualification. The same field-defining geometry and fixed test conditions are retained for the unheated and heated conditions.

Heating and control. Heating provision is included at both electrode ends. For the unheated ambient-temperature reference condition, neither heater is energised. For a gradient condition, the selected hot-side electrode is regulated to a prescribed temperature, while both T_{HV} and T_{GND} are measured independently. The realised $|\Delta T|$ is then checked against the required 40–50 K range. Figure 6.2 shows the common control strategy used for both retained heating concepts.

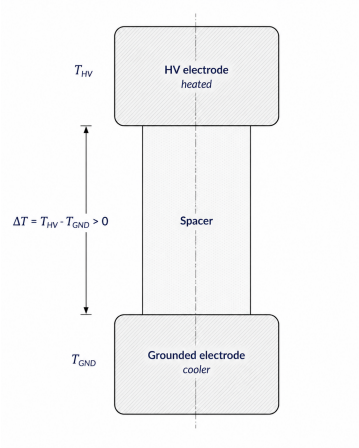


Figure 6.1: Definition of the axial temperature difference for the HV-hot condition.

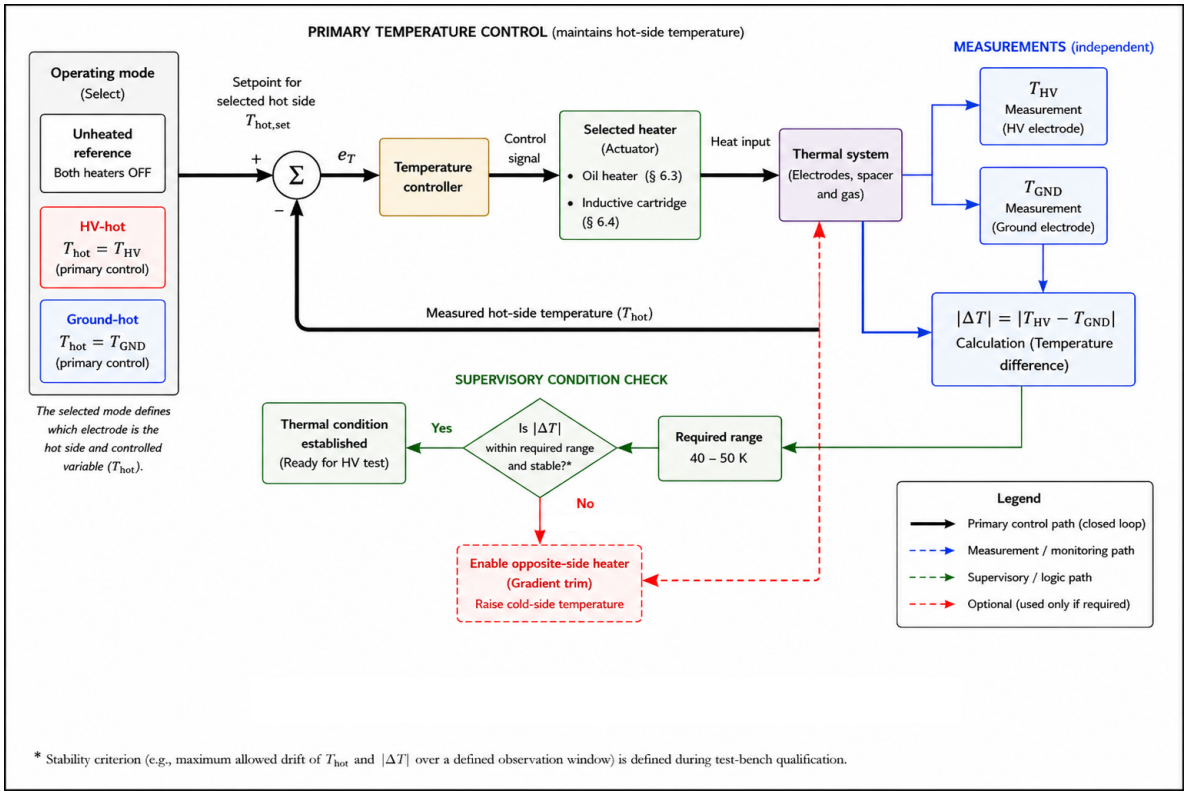


Figure 6.2: Thermal-control architecture for the hot-oil and floating cartridge-heating concepts.

The primary feedback loop acts on the selected hot-side temperature, T_{hot}, and remains active after the required thermal condition has been established. The controller acts on the temperature error $e_T = T_{\mathrm{hot,set}} - T_{\mathrm{hot}}$ and adjusts the selected heater accordingly. The opposite electrode is initially left unheated while its temperature is monitored.

Opposite-side heating is used only when the temperature of the unheated electrode results in a $|\Delta T|$ above the required range. Heating that electrode can then reduce $|\Delta T|$. It cannot correct a temperature difference that is already too small. The required stability band and final control settings are established during test-bench qualification.

The same control strategy is used for both gradient directions. For the HV-hot condition, $T_{\mathrm{hot}} = T_{\mathrm{HV}}$; for the ground-hot condition, $T_{\mathrm{hot}} = T_{\mathrm{GND}}$. Both electrode temperatures are retained because the same

$|\Delta T|$ can occur at different absolute temperatures. They also provide the boundary temperatures for the thermal model. The two gradient directions are qualified separately because their thermal surroundings are not identical.

Reference-profile comparison. The modelled spacer-temperature profile is compared with the coaxial reference arrangement using the normalised spacer coordinate

$$\xi = \frac{s}{L_{\text{spacer}}},$$

where s is the distance along the spacer surface and L_{spacer} is the corresponding surface length. The profiles are interpolated onto a common ξ coordinate so that geometries with different spacer lengths can be compared directly. The comparison considers the hot-to-cold direction, the overall temperature difference, and the maximum local temperature difference between the two profiles.

Upper numerical thermal condition. In addition to the 40–50 K experimental temperature-difference range, the thermal designs are assessed with the 100°C hot-source condition defined in Chapter 4. This is an upper numerical design condition rather than the normal experimental setpoint. The allowable temperature of the realised bench is governed by the lowest applicable component or material rating. The resulting spacer-temperature distributions are reported in Chapter 9.

Electrical integration. The thermal hardware is designed for the 50 kV DC operating basis. The integrated insulation geometry is numerically screened at 60 kV; this does not constitute a physical voltage rating. Heating and temperature measurement must not introduce an unintended conductive path to ground, change the field-defining geometry, or create a new dominant stressed region.

Table 6.1 summarises how the thermal design developed in this chapter responds to FR-T1–FR-T4 of Chapter 4. The requirement definitions remain those of Chapter 4.

Table 6.1: Chapter 6 design response to the thermal requirements of Chapter 4.

ID	Design response in Chapter 6	Remaining physical check
FR-T1	The design provides the unheated reference condition and both heated-gradient conditions. T_{HV} and T_{GND} are measured independently, and the realised ΔT is calculated from these temperatures.	Calibrate both temperature measurements. Demonstrate $\|\Delta T\|$ = 40–50 K for the gradient conditions and establish the residual-temperature-difference and stability limits for the unheated reference.
FR-T2	The selected hot-side electrode is regulated first while the opposite electrode is left unheated and its temperature is monitored. Heating at the second electrode is used only if required to bring the realised $\|\Delta T\|$ within the specified range.	Establish the setpoint tolerance, stability duration, opposite-electrode acceptance band, and thermal-protection limits during qualification.
FR-T3	Heating provision at both electrode ends allows the hot side to be changed without changing the field-defining electrode–spacer geometry.	Qualify the HV-hot and ground-hot conditions separately and demonstrate that both satisfy FR-T1 and FR-T2.
FR-T4	The spacer-temperature profiles are compared with the coaxial reference arrangement using the normalised-coordinate method defined in this section.	Use the measured electrode temperatures as model boundaries and report the temperature-profile deviation for the realised bench.

6.2. Heating-Concept Screening and Retained Architectures

Candidate heating methods were screened against four criteria derived from Section 6.1: the method must produce the required electrode-to-electrode temperature difference, allow either electrode to form the hot side, preserve the field-defining electrode–spacer geometry, and remain compatible with the HV insulation boundary. Table 6.2 applies these criteria to the candidate methods.

Hot-oil circulation. Circulating heated oil through a hollow conductor has experimental precedent in gas-insulated spacer studies. Zhang, Qi and Zhang used heating oil inside a hollow central conductor,

Table 6.2: Screening of candidate heating methods.

Heating method	Assessment for the present test bench	Decision
Service-current conductor heating	Reproduces the conductor-heating principle used in thermo-electric GIS testing [49], but requires a high-current path and return circuit that are not part of the fixed DC flashover arrangement.	**Not retained**
Uniform chamber heating	Raises the overall temperature but does not establish the required electrode-to-electrode temperature difference or allow the heated side to be swapped.	**Not retained**
Direct induction heating	Can heat the electrode without direct electrical contact, but requires an excitation coil and associated hardware close to the field-defining electrode.	**Not retained**
Hot-oil circulation	Transfers heat from an external source to the selected electrode through an insulated fluid path. The principle has experimental precedent in gas-insulated spacer arrangements.	**Retained: Concept 1**
Floating cartridge heating	Generates heat locally inside the electrode without changing its external profile. HV-side operation requires electrically isolated power transfer.	**Retained: Concept 2**

while Ma et al. used a hollow conductor connected to an external oil tank and pump [50], [53]. These studies support the heat-transfer principle used here. The tubing, U-bend, sealing, and electrical-isolation arrangement for the present test bench is developed in Section 6.3.

Floating cartridge heating. Local resistive heating of an HV electrode also has experimental precedent. Huang et al. heated the HV electrode using heating tape and separated the heater from the electrode by a 1 mm AlN ceramic layer [64]. The present design instead places a resistive cartridge inside the electrode so that the external electrode profile is unchanged.

The grounded-side cartridge can be supplied directly, whereas the HV-side cartridge requires electrical isolation from ground. Inductive coupling is therefore used to supply a floating heater circuit on the HV side. The inductive link transfers electrical power, while the cartridge generates heat resistively. This distinguishes the retained architecture from the direct induction-heating method rejected during the concept screening..

6.3. Hot-Oil Heating Architecture

The hot-oil architecture heats the oil in external equipment at ground potential and circulates it to the selected electrode through PFA supply and return tubes. The HV-hot configuration is considered because the tubes enter an electrode at HV potential and therefore require electrical isolation. The main elements of the arrangement are shown in Figure 6.3.

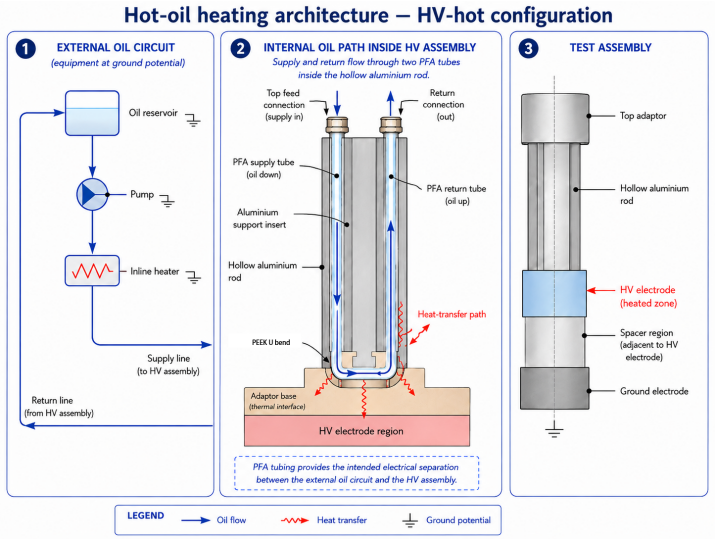


Figure 6.3: Hot-oil heating architecture for the HV-hot configuration.

6.3.1. Heat-Transfer Path and Mechanical Integration

The oil lines are housed inside the hollow aluminium rod so that the external electrode geometry remains unchanged. The rod has a 26 mm outer diameter and a 20 mm bore. The removable internal assembly and the supply and return flow paths are shown in Figure 6.4.

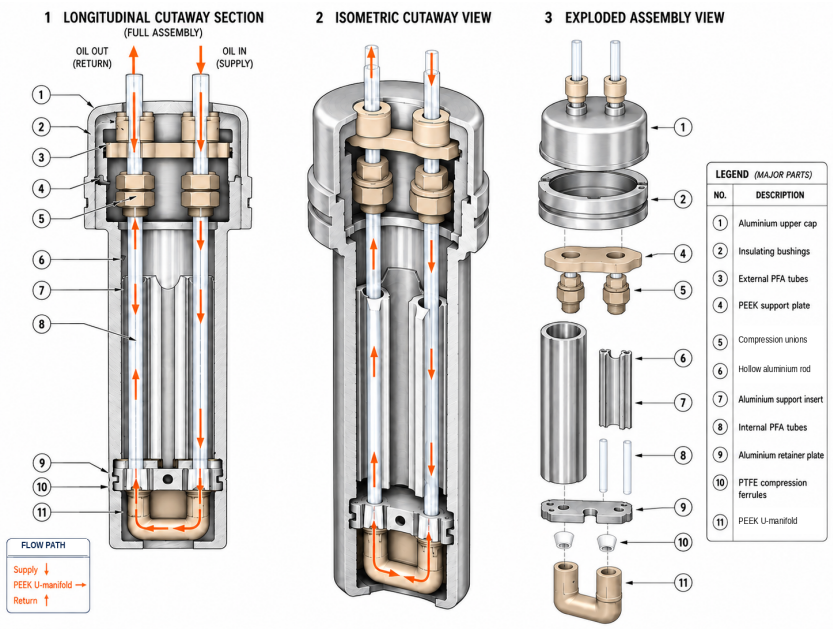


Figure 6.4: Internal assembly and flow path of the hot-oil module.

The supply and return lines use SMC TL0604 Super-PFA tubing with a 6 mm outer diameter and a 4 mm inner diameter. The tubing was selected for its fit within the 20 mm rod bore, its temperature range, and its compatibility with silicone fluid [65]. Its hydraulic suitability is assessed below.

The tubing cannot form the return bend directly inside the rod. The manufacturer gives a recommended bend radius of 35 mm, whereas the rod provides only about 10 mm radial space [65]. The flow is therefore reversed in the PEEK U-bend shown in Figure 6.5. PEEK is used for the U-bend because the return component must remain electrically insulating while supporting the tube and ferrule assembly. PTFE compression ferrules and a retainer plate locate and seal the two tubes. The retainer screw holes are positioned on the perpendicular axis and outside the internal U-channel so that they do not interrupt the oil passage.

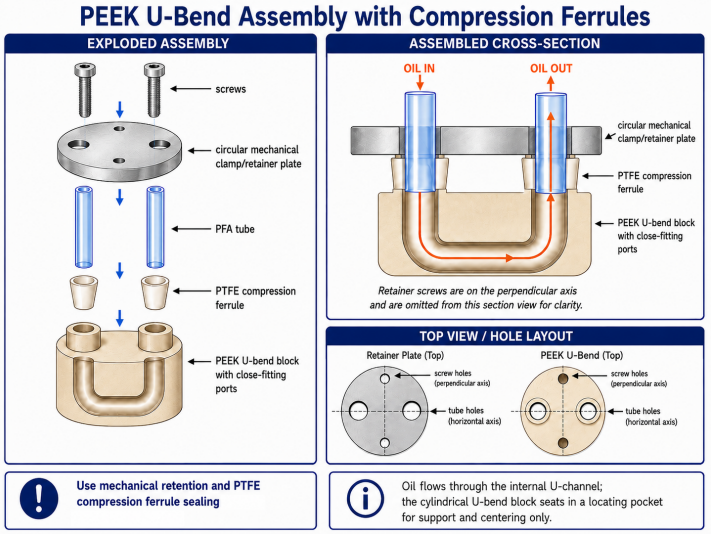


Figure 6.5: PEEK U bend and mechanical tube-retention arrangement.

Detailed dimensions of the internal oil-loop components are provided in Appendix C.

Hydraulic design. XIAMETER PMX-200 Silicone Fluid, 10 cSt, is used as the reference working fluid for the preliminary flow and pressure-loss calculations. The 10 cSt grade provides a low-viscosity basis for the small-bore oil circuit, while its density, thermal expansion and heat-capacity data are available from the manufacturer [66], [67].

A nominal flow of 200 mL/min is used for the preliminary design. At this flow, the estimated 50 W thermal demand can be transported with an oil-temperature drop of approximately 10 K. For the provisional 2 m supply-and-return path, the flow is strongly laminar and the calculated loop pressure loss is approximately 13 kPa. The resulting preliminary pump requirement is at least 0.30 L/min at 30 kPa.

The complete flow and pressure-loss calculation is given in Appendix C. The pressure-loss calculation must be repeated after the external tube routing is fixed. It establishes the fluid-transport requirement but not the thermal resistance between the oil and the electrode.

6.3.2. HV Isolation and Remaining Checks

HV isolation. The reservoir, pump and oil heater remain at ground potential. Heat is transferred to the selected electrode through the PFA supply and return tubes, so no grounded metallic fluid line or heater conductor enters the HV rod. The electrical insulation therefore depends on the complete fluid path, including the tubing, fittings, exposed surfaces and clearances at the tube-entry region. The tubing specification alone does not define the withstand of this assembly. The complete fluid path must therefore be tested as an assembly before operation at 50 kV DC.

Temperature control. The hot-oil concept uses the common control strategy defined in Section 6.1. The controller adjusts the external oil-heater power, while the pump maintains oil circulation. Oil temperature is monitored separately as a protection variable for the circulation loop.

Remaining checks. Before experimental use, the assembled oil circuit requires leak and circulation testing, measurement of the oil-to-electrode thermal response, calibration of the temperature measurements and an electrical withstand check of the complete fluid path. The flow and pressure-loss calculations define the required hydraulic operating point, but they do not establish the thermal or electrical performance of the assembled system.

6.4. Floating Cartridge-Heater Architecture

The second retained architecture generates heat locally inside the selected electrode using a resistive cartridge heater. At the grounded electrode, the heater can be supplied conventionally. For HV-side

heating, the heater circuit floats with the electrode potential and is supplied by inductive power transfer, as shown in Figure 6.6. Electrical power is transferred to the floating circuit, while heat is generated resistively in the cartridge heater.

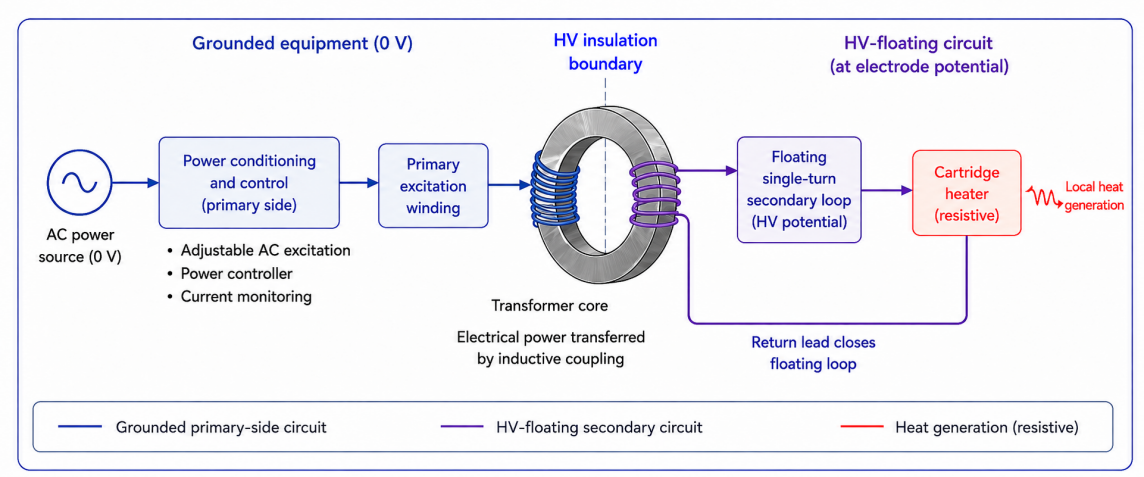


Figure 6.6: Power-transfer architecture of the HV-floating cartridge-heater circuit.

6.4.1. Heater and Floating-Loop Design

The cartridge heater is positioned in an internal pocket in the aluminium electrode so that the external gas-facing electrode profile remains unchanged. Preliminary sizing uses a 24 V, 75 W cartridge heater. Its rated current is approximately 3.1 A. The 75 W rating provides power margin above the approximately 50 W thermal demand used for preliminary sizing. The 50 W value is a design basis rather than a measured heat requirement; the power required to maintain the prescribed electrode temperature must be established on the realised assembly. Detailed calculations are given in Appendix D.

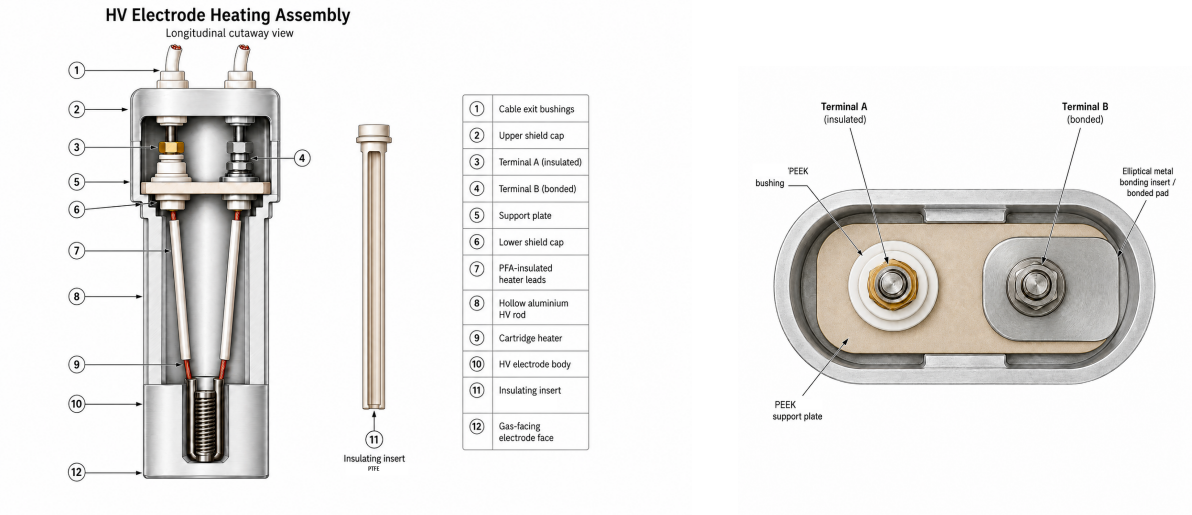
For the HV-side arrangement, the cartridge heater forms part of a closed electrical loop that floats with the electrode potential. A 4 mm^2 copper conductor is used as a provisional design-reference size for the floating-loop loss and insulation-geometry calculations. At the approximately 3.1 A rated heater current, the calculated loss of the provisional 2 m conductor route is approximately 0.11 W, which is negligible compared with the 75 W cartridge rating. Conductor current capacity is therefore not the governing design constraint.

For the preliminary insulation geometry, the dimensions of a Nexans HFIX 1×4 mm^2 XLPE-insulated conductor are used as a manufacturer-data reference. The stated average XLPE insulation thickness is approximately 0.8 mm and the insulated-core diameter is 3.8–4.7 mm [68]. This reference defines the geometry used in the insulation assessment; it does not constitute the final cable selection. The cable used in the realised bench must be selected from available laboratory or procured components and checked against the required conductor, insulation, routing and termination conditions.

Power-transfer requirement. The heater-side design requires approximately 20–24 V at 2.6–3.1 A over the preliminary 50–75 W operating range. These values define the required secondary output of the inductive power-transfer system; they are not measured characteristics of the existing transformer. The existing transformer is therefore characterised first under a representative resistive load. If it cannot provide the required voltage, current and continuous power, a suitable alternative transformer must be selected or designed.

6.4.2. Mechanical and Electrical Integration

The cartridge-heater leads are routed through the hollow aluminium rod to a terminal support above the rod. Figure 6.7 shows the internal heater arrangement and the corresponding terminal interface. Terminal A is insulated from the aluminium structure, while Terminal B is intentionally bonded to it.



(a) Internal heater assembly **(b)** Terminal arrangement

Figure 6.7: Internal integration of the floating cartridge-heater circuit: (a) heater and lead routing and (b) terminal arrangement.

Current path. Terminal A provides the insulated connection to one heater terminal. Current then passes through the cartridge-heater element to Terminal B, which provides the intentional bond to the return side of the floating circuit. The PTFE cable bushings and the PEEK support plate provide local insulation and mechanical support at the terminal interface. PFA-insulated heater leads are routed through the hollow aluminium rod to the cartridge heater. Where additional separation is required, a removable PTFE or PEEK guide can be fitted inside the rod to keep the leads away from the aluminium wall and reduce mechanical contact during assembly and operation. The cartridge sheath provides the mechanical and thermal interface to the electrode and is separate from the heater-terminal connection.

6.4.3. Secondary-to-Ground Insulation Design and Screening

Inductive coupling removes the galvanic connection between the grounded supply and the HV-side heater, but the floating secondary circuit must still be insulated from ground. During HV-side heating, the secondary loop remains near the electrode potential while the transformer core and primary-side equipment remain at ground potential. The conductor passing through the transformer window must therefore withstand the voltage between the floating secondary circuit and ground. A 60 kV numerical screening case is used to assess this arrangement, above the 50 kV intended operating limit. The 60 kV case does not define a physical withstand rating.

The floating conductor is routed through the centre of the open transformer window to maximise its minimum clearance to the grounded core. The window is approximately 330×360 mm and the complete insulated cable is approximately 28 mm in diameter. This gives a minimum clearance of approximately 151 mm horizontally and 166 mm vertically. Two insulating split clamps located outside the transformer core maintain the centred position without introducing support hardware into the open window. The arrangement is shown in Figure 6.8.

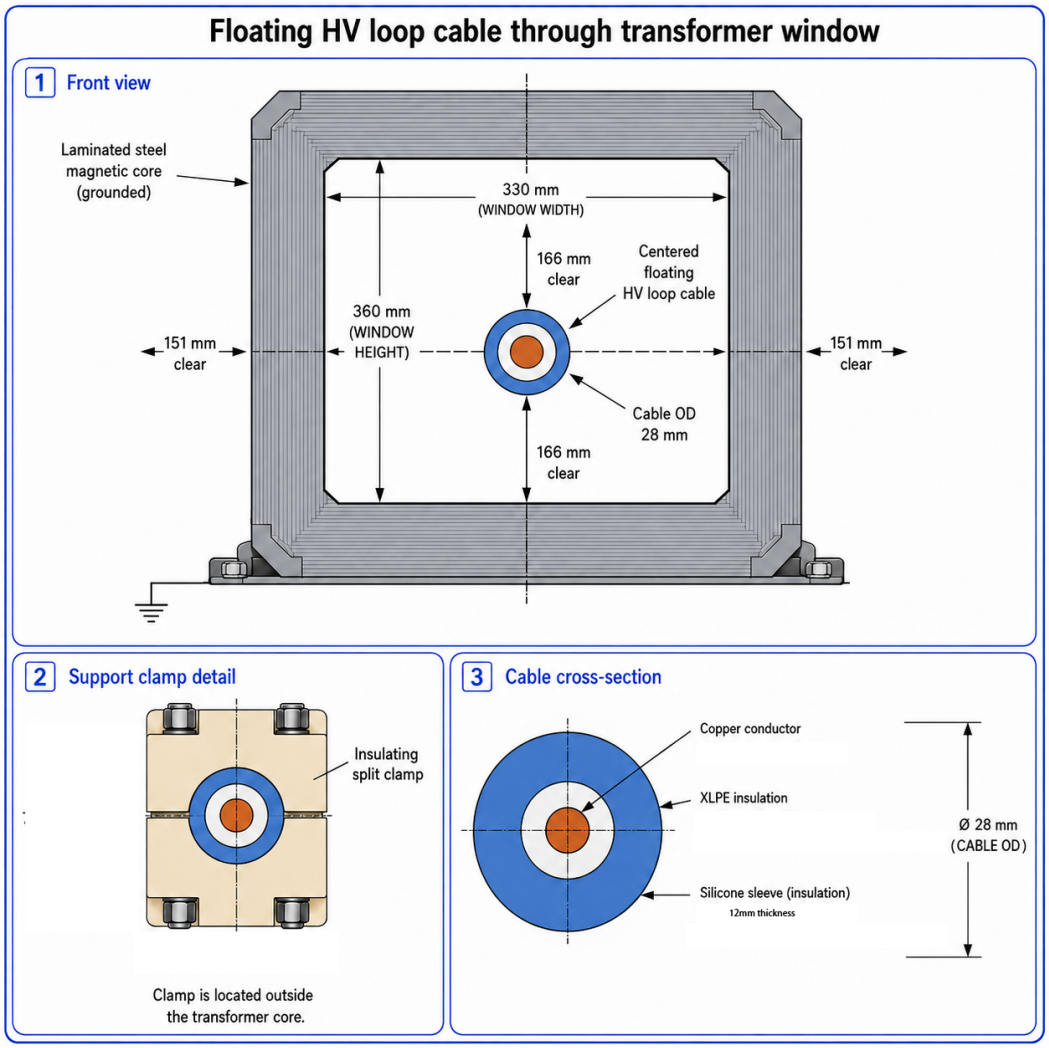


Figure 6.8: Centred support and insulation arrangement of the floating conductor through the grounded transformer window.

The secondary-to-ground insulation in the transformer window region consists of the XLPE-insulated floating conductor, an additional 12 mm radial silicone sleeve and the remaining air clearance to the grounded core. The design-reference HFIX cable has an insulated-core diameter of approximately 3.8–4.7 mm. Adding the silicone sleeve gives an overall insulated diameter of approximately 27.8–28.7 mm, which is consistent with the approximately 28 mm geometry used for the transformer-window design and numerical model.

As a first geometric check, the 60 kV screening voltage divided by the minimum 151 mm clearance gives an average field scale of approximately 0.40 kV/mm. This value is used only as a bulk-clearance check. It is not the local insulation stress because the field is non-uniform and the voltage is distributed across the solid insulation and surrounding air.

A two-dimensional electrostatic model was therefore used to evaluate the local electric field for the centred-conductor arrangement. The floating conductor is set to 60 kV and the transformer core is grounded. The model represents the conductor, cable insulation, silicone sleeve, surrounding air and grounded core. The external support clamps are outside the transformer window and are not part of this central cross-section. Figure 6.9 shows the resulting electric field.

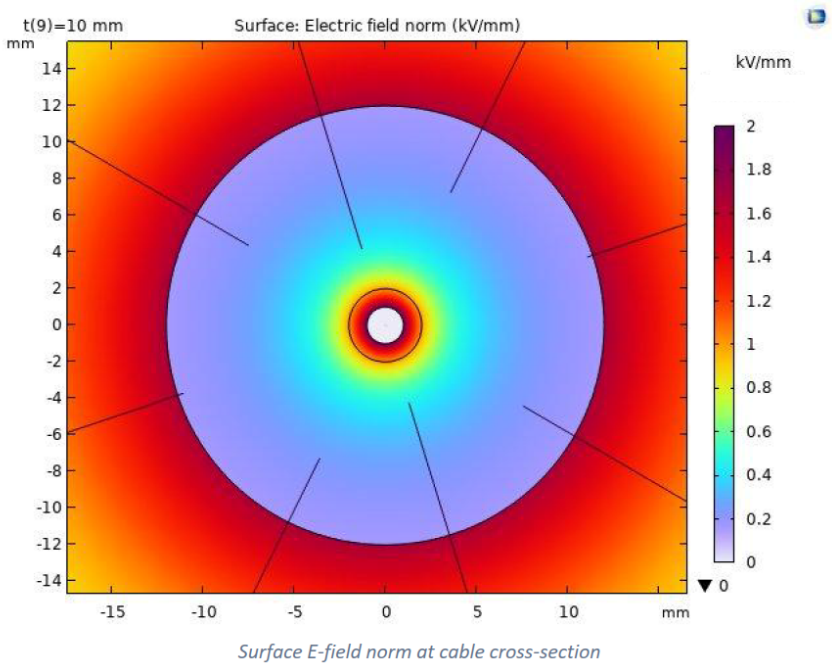


Figure 6.9: electric field distribution for the centred floating conductor at the 60 kV numerical screening case.

The model gives approximately 2.0 kV/mm at the conductor-cable-insulation interface, approximately 1.0 kV/mm in the cable insulation away from the inner interface, and approximately 1.2 kV/mm in the additional silicone insulation and at the outer silicone-air surface.

The calculated field is concentrated close to the floating conductor, while the centred arrangement retains the large clearance to the grounded transformer core. The numerical results characterise the electric field distribution of the proposed transformer-window insulation geometry for the 60 kV screening case. The screening addresses the cable crossing through the transformer window; the final terminations and completed floating-secondary assembly must be included in the electrical withstand check before operation at 50 kV DC.

Temperature control. The floating cartridge-heater concept uses the same temperature-control strategy. For HV-side heating, the controller demand acts on the grounded transformer primary.

6.5. Comparative Design Assessment

Both retained architectures are designed to provide the required thermal conditions while preserving the external field-defining geometry. The final comparison therefore considers ease of implementation, system complexity and the principal design risk associated with each concept. Table 6.3 summarises the comparison.

Table 6.3: Comparison of the retained thermal-management architectures.

Assessment criterion	Hot-oil architecture	Floating cartridge-heater architecture
Heat delivery	Heat generated externally and transferred to the electrode by circulating oil.	Heat generated locally inside the electrode by a resistive cartridge heater.
Implementation	Requires reservoir, pump, external heater, supply and return tubing, fittings and an internal U-bend.	Requires a cartridge heater, floating secondary loop and transformer for inductive power transfer.
System complexity	Includes hydraulic, sealing, thermal and electrical-isolation functions.	No circulating fluid system; the main additional requirement is isolation of the floating secondary circuit from grounded parts.
Principal design risk	Fluid-path integrity and sufficient oil-to-electrode heat transfer while maintaining electrical isolation.	Insulation of the floating secondary loop from ground, particularly its clearance from grounded surfaces.
Design evidence	Internal oil circuit and U-bend developed; preliminary hydraulic sizing completed.	Heater and floating-loop design completed; mechanical integration and transformer-window secondary-to-ground insulation screening performed.
Design position	Retained as the alternative heating concept.	Preferred candidate for physical qualification.

On this basis, the floating cartridge-heater architecture is selected as the preferred candidate for physical qualification, while the hot-oil architecture is retained as the alternative.

6.6. Chapter conclusions

- The thermal system supports an unheated reference condition and heating of either electrode while preserving the external electrode-spacer geometry. The required temperature difference is $|\Delta T| = 40$–50 K.
- Two heating architectures were developed. The hot-oil concept transfers heat through an electrically isolated fluid circuit, whereas the cartridge-heater concept generates heat directly inside the electrode.
- The floating cartridge-heater arrangement requires the secondary circuit to remain insulated from grounded parts. The transformer-window geometry and the 60 kV numerical screening support the proposed centred-cable insulation arrangement, which must still be verified on the completed assembly before 50 kV DC operation.
- The floating cartridge-heater architecture is selected as the preferred concept because of its simpler implementation and lower system complexity. The hot-oil architecture is retained as the alternative if the floating-loop insulation cannot be qualified.

7

Chamber, HV Connection and Housing

This chapter develops the chamber, HV connection and housing that integrate the fixed electrode-spacer geometry with the thermal interfaces of the test bench. The design builds on the requirements of Chapter 4 and the component designs of Chapters 5 and 6. The resulting assembly defines the electrode supports, enclosure, sealing, service routing and access provisions.

7.1. HV Connection and Electrode Support

The electrode-support assembly must maintain the electrode position while providing the electrical connection and the internal routing required by the thermal system. These functions are combined in the concentric cap–rod–adaptor–electrode arrangement shown in Figure 7.1.

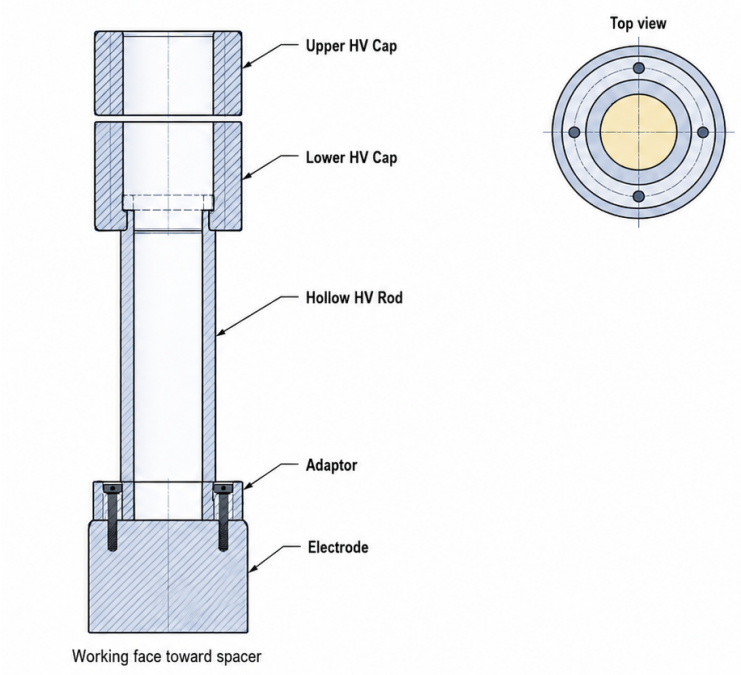


Figure 7.1: HV-side cap–rod–adaptor–electrode assembly.

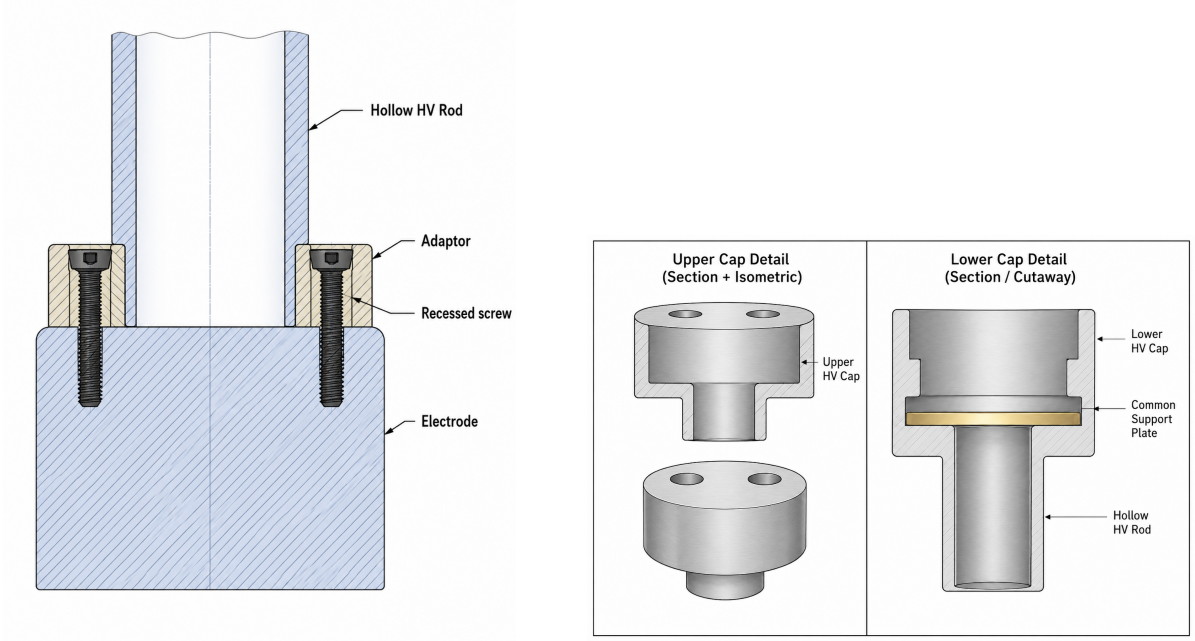
The upper cap provides the external electrical and service interface. The lower cap locates the hollow aluminium rod and supports the internal connections entering the rod bore.

The cap is divided into upper and lower parts to provide access to the service connections while maintaining the rod position. Locating spigot-and-socket features maintain concentric alignment between the cap and hollow rod. A common PEEK support plate inside the lower cap provides the mounting interface for either thermal architecture defined in Chapter 6.

Heating provision is included at both electrode ends. Corresponding hollow rods, adaptors and electrode interfaces allow either electrode to be heated without changing the spacer position or electrode contours.

The hollow rod provides the conductive connection to the electrode and its main axial support. Its bore routes the heating and sensing connections internally, keeping them away from the exposed gas region around the spacer.

The adaptor provides the detachable mechanical connection between the hollow rod and electrode. Mating faces locate the adaptor. Recessed screws engage blind threaded holes so that no screw head projects into the gas region near the electrode–spacer interface. The dimensions and fastening details are given in Appendix A and illustrated in Figure 7.2.



(a) Rod–adaptor–electrode connection.

(b) Upper and lower cap arrangement.

Figure 7.2: Mechanical details of the HV-side connection.

The detachable adaptor allows the electrode to be removed for spacer inspection or replacement without dismantling the cap and rod assembly. The same locating faces are used when the electrode is reassembled.

7.2. Chamber Enclosure and End Flanges

The chamber enclosure must provide optical access to the electrode-spacer region while locating the rod assemblies, accommodating the sealing interfaces and carrying the chamber-end load. The selected arrangement uses a transparent PMMA tube between two insulating PEEK end flanges.

The PMMA tube forms the lateral boundary of the enclosed air volume without defining the electrode profile. Its flat ends meet the PEEK flanges, and the HV and grounded rods pass through the centres of the flanges. The arrangement is shown in Figure 7.3.

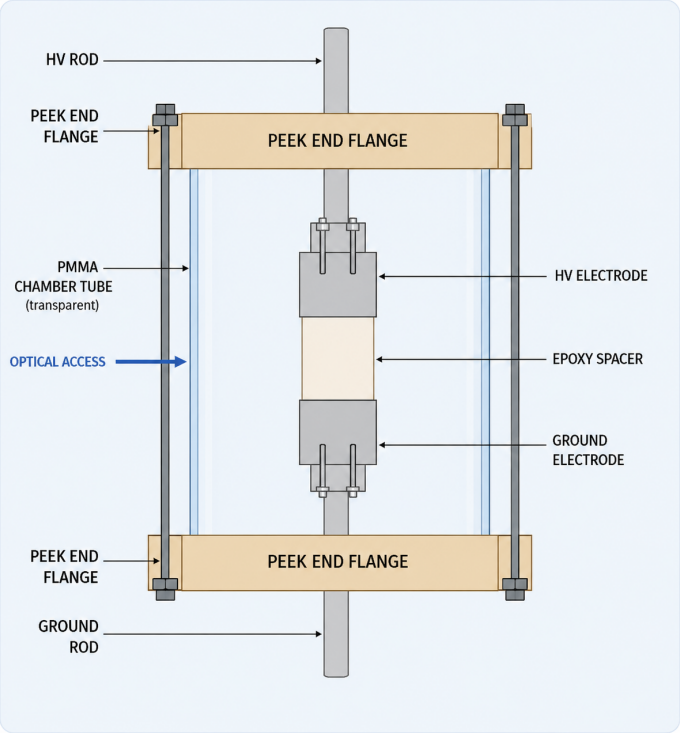


Figure 7.3: PMMA chamber tube and PEEK end-flange arrangement. Schematic, not to scale.

PMMA is selected for the chamber tube because its transparent wall provides optical access for assembly inspection, optical recording of surface-flashover events and post-test inspection. A clear cast PMMA tube is adopted as the design-reference chamber material. The commercial reference, nominal dimensions and supplier material data are given in Appendix B [69]. The supplied tube must be checked against the required dimensions, temperature, mechanical loading and cleaning procedure before use.

The planned tests use air near 1 bar(a). For mechanical sizing, the chamber adopts an internal-to-external differential pressure of $\Delta p_{\mathrm{design}} = 6$ bar $= 0.60$ MPa. This is a separate mechanical design condition and does not represent the experimental operating pressure or a certified chamber rating.

The pressure-load calculation uses the outside diameter of the PMMA face-seal groove as the conservative pressure boundary. The resulting axial load on one chamber end is approximately 17.8 kN. A thesis-specific screening factor of $\gamma_F = 2.0$ is applied to account conservatively for the simplifying assumptions of the preliminary load calculation. This gives a chamber-end design load of approximately 35.5 kN. The complete pressure-force and tie-rod calculation is given in Appendix E.

PEEK is selected for the chamber-end flanges because the flanges must provide electrical insulation, withstand the local operating temperature and maintain their dimensions under sustained mechanical load. Using an insulating flange also avoids introducing a large conductive surface near the rod entry and chamber ends. This reduces the risk of parasitic discharges outside the intended electrode-spacer region. The flanges locate the rods, contain the sealing interfaces and transfer the chamber-end load. PEEK provides the required temperature resistance together with good long-term creep resistance and dimensional stability, which helps maintain rod alignment, seal compression and flange preload [70]. The selected grade must be checked against the flange temperature, sustained stress and required service duration.

The end flanges also provide interfaces for controlled air exchange, venting and measurement of the chamber condition. The detailed fittings and dimensions are specified in the engineering drawings.

7.3. Sealing and Chamber Retention

Three interfaces require sealing: the PMMA tube-to-flange joint, the rod feedthrough, and the split plane between the two PEEK flange halves. These interfaces use a static FKM face seal, a spring-energised PTFE radial seal and a static FKM split-plane O-ring, respectively.

At each chamber end, the flat PMMA tube face seals axially against the PEEK flange. A static FKM O-ring is located in the flange face-seal groove. This arrangement follows the established axial O-ring sealing principle [71]. It avoids a radial interference fit on the PMMA tube and therefore reduces radial assembly stress.

The rod feedthrough requires radial sealing around the aluminium rod while allowing limited axial movement during assembly and thermal expansion. A spring-energised PTFE seal is therefore used between the finished rod surface and the PEEK gland. The internal spring provides the initial sealing contact. A positive chamber pressure can additionally load the seal lips [72].

The PTFE rod seal is installed in a split gland formed by the upper and lower PEEK flange halves. This allows the seal to be fitted around the rod without removing the rod–electrode assembly. Closing the two halves introduces a third leakage interface, which is sealed by a separate static FKM O-ring. The rod seal accommodates axial movement but does not define the electrode position; this remains fixed by the rod and adaptor assembly described in Section 7.1.

The selected arrangement separates the three sealing interfaces from the local gland closure and the principal chamber-retention path, as shown in Figure 7.4.

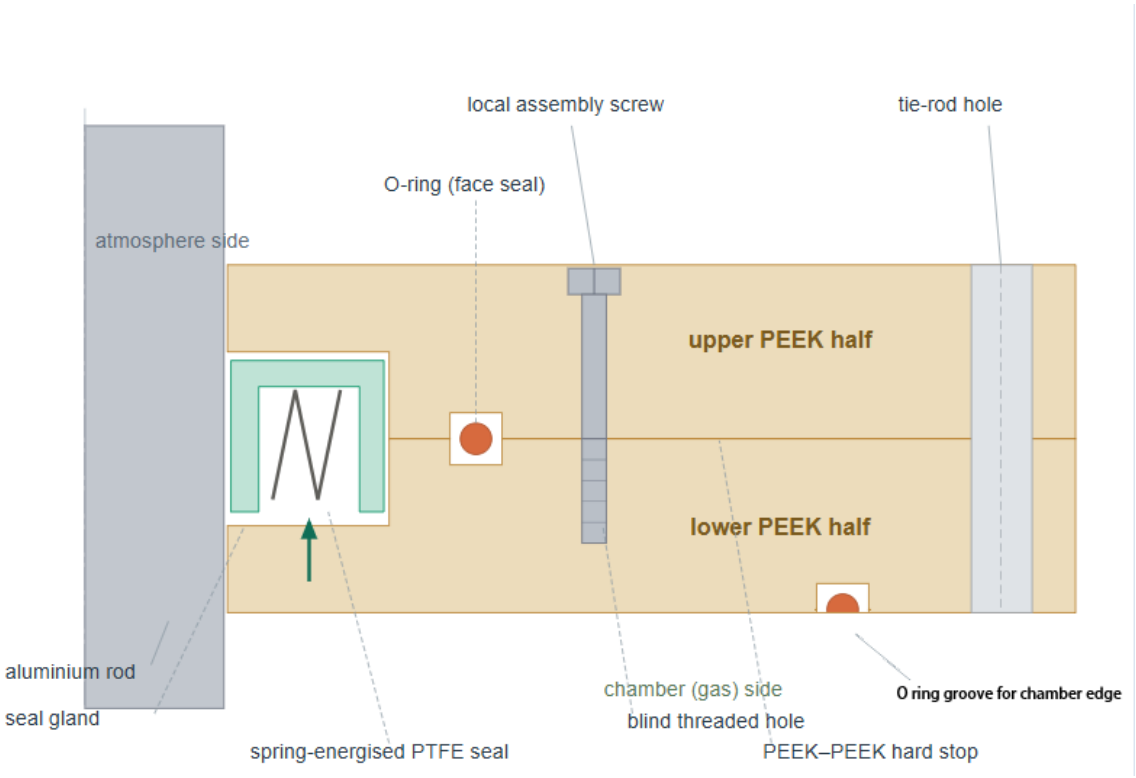


Figure 7.4: Split PEEK chamber-end feedthrough and sealing interfaces. Schematic, not to scale.

The two PEEK flange halves close against full PEEK-to-PEEK contact at the split plane. This contact forms the mechanical hard stop and defines the final gland width. Seal compression is therefore set by the machined gland geometry rather than by screw torque alone.

Eight recessed M6 screws close the split gland and maintain local contact between the two PEEK halves. The screws pass through clearance holes in the upper half and engage blind threaded holes in

the lower half. The blind threads avoid a direct through-hole between the chamber and the atmosphere. These screws are not credited with carrying the principal pressure-induced chamber-end load.

Eight M10×1.5 A4-80 tie rods provide the principal chamber retention and clamp the PMMA tube-end face seals. Under the factored chamber-end load defined in Section 7.2, the pressure-induced load is approximately 4.44 kN per tie rod. Before pressurisation, each tie rod is assumed to have an initial preload of 5.0 kN from tightening. For the screening check, the full pressure load is conservatively added to this preload, giving a total tensile load of 9.44 kN per tie rod. This is approximately 27% of the minimum proof-load capacity. The detailed calculation is given in Appendix E.

This calculation checks the tie rods against direct tensile loading. The complete flange joint must also be checked for PEEK deformation and creep, local bearing, joint opening and preload retention.

The aluminium rod forms part of the electrical connection to the electrode and therefore remains uninsulated. A defined sealing band on the rod provides the mating surface for the PTFE seal. Its surface finish must meet the seal requirements and be free from damage before assembly.

Final seal dimensions, material grades and mating-surface requirements must be fixed from the selected seal data before manufacture. Leak-tightness and pressure retention must then be demonstrated by commissioning and acceptance tests.

7.4. Integrated Assembly

The complete arrangement combines the two rod-electrode assemblies with the PMMA chamber tube, PEEK end flanges, sealing system and chamber-retention tie rods. The spacer remains centred between the two field-facing electrodes, while the hollow rods provide the electrical, mechanical and thermal connection through the chamber ends. Figure 7.5 shows the resulting integrated arrangement.

Changing the voltage polarity requires no mechanical change to the active electrode-spacer region. Changing the heated electrode changes the thermal connection and external supply arrangement, but the spacer position and electrode geometry remain unchanged. The HV-hot and ground-hot conditions therefore use the same field-defining geometry.

The detachable rod–adaptor–electrode connections allow the spacer to be removed for inspection or replacement without dismantling the complete chamber-end assembly. Locating faces in the mechanical design provide the reference for restoring the electrode position after reassembly.

7.5. Safety Provisions

The test-bench design provides for isolation of the HV source, grounding of the test object and independent disconnection of the heating and measurement circuits. The chamber also provides controlled venting and protection against contact with heated components. Access must be prevented while high voltage is applied or stored charge may remain. The associated interlocks, discharge arrangement and emergency shutdown functions must be verified before HV testing.

7.6. Chapter conclusions

- The integrated design allows the voltage polarity and the heated electrode to be changed without changing the electrode-spacer geometry. The spacer can also be removed and replaced without dismantling the complete chamber assembly.
- The chamber is mechanically designed for an internal-to-external differential pressure of 6 bar.
- A separate sealing arrangement is provided for each main leakage interface of the chamber.
- The selected eight M10×1.5 A4-80 tie rods have sufficient tensile capacity for the preliminary chamber load.
- The complete chamber assembly has not yet been physically verified. Leak-tightness, pressure retention, flange behaviour, HV performance and safety functions must be checked before experimental use.

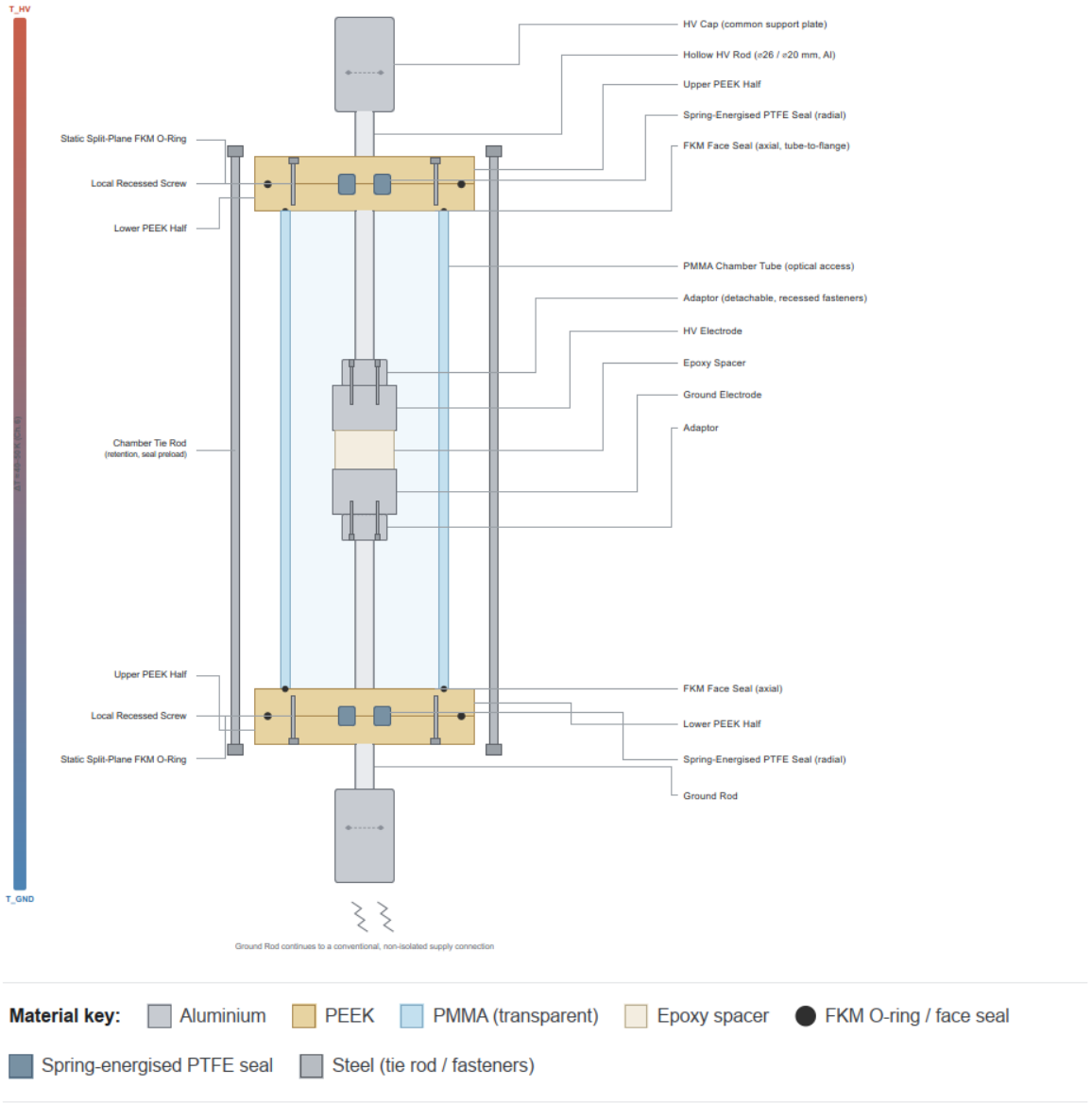


Figure 7.5: Integrated chamber, electrode-spacer and rod assembly in the HV-hot configuration. Schematic, not to scale.

8

Coupled Electro-Thermal Simulation: Model Setup

This chapter defines the electro-thermal model used to calculate the temperature distribution and time-dependent DC electric field in the electrode-spacer arrangement. The fixed electrode-spacer geometry and thermal boundary conditions established by the test-bench design form the modelling basis. The model definition specifies the geometry, physical models, boundary and initial conditions, numerical settings, extracted quantities and limitations used in the simulations.

8.1. Model Scope and One-Way Coupling

The thermal calculation is performed first. Stationary and time-dependent thermal studies calculate the temperature distribution. The stationary temperature distribution is then used to evaluate the temperature-dependent epoxy conductivity for the electrical calculation. During the electrical calculation, the temperature distribution remains fixed and electrical losses are not coupled back to the thermal model.

Li et al. used a comparable one-way treatment in a three-dimensional DC-GIL model when leakage-current heating was small compared with conductor heating [34]. The same one-way thermal-to-electrical coupling is adopted here as a modelling assumption. The applicability of this assumption to the present geometry has not been independently verified.

The electrical model calculates the macroscopic DC electric field redistribution caused by the prescribed conductivity distribution. The model excludes explicit gas-ion transport, surface-charge transport, charge injection and discharge propagation.

8.2. Axisymmetric Geometry and Numerical Representation

The numerical models were implemented in COMSOL Multiphysics 6.2 using a two-dimensional axisymmetric r–z representation. The electrode-spacer arrangement is rotationally symmetric about its central axis, so the meridional cross-section represents the nominal three-dimensional geometry. Circumferential variations are therefore not represented. Figure 8.1 shows the hot-oil model and its principal material domains.

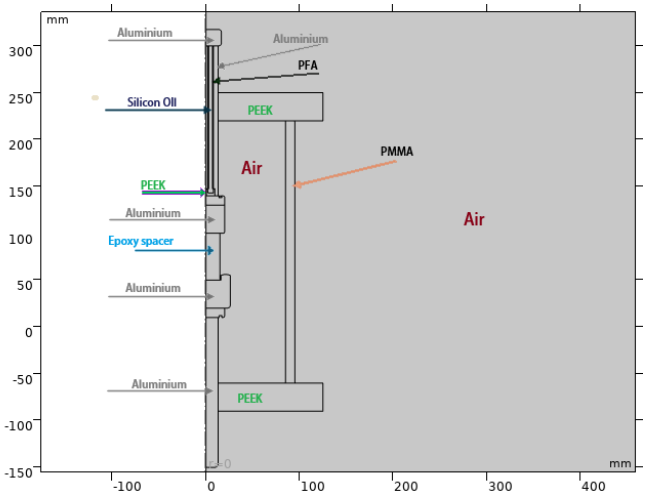


Figure 8.1: Axisymmetric model and principal material domains

The model includes the aluminium electrode structure, epoxy spacer, enclosed air and PMMA chamber. PEEK and PFA regions are included where they affect the thermal or electrical solution. External service hardware outside the modelled chamber region is omitted. Separate thermal models represent the hot-oil and floating cartridge-heater architectures. A separate coaxial model provides the thermal reference. The coaxial geometry is also used for a stationary electric field comparison, with the upper and lower spacer-gas interfaces extracted separately.

The detailed electrical calculations use stationary temperature distributions obtained with the hot-oil geometry. Two HV-hot thermal inputs are considered, with prescribed hot-side temperatures of 353 K and 393 K. The higher-temperature condition is used only as a numerical sensitivity case. No separate electrical calculation was performed with the cartridge-heater temperature distribution. This numerical simplification does not determine the preferred heating architecture.

8.3. Material and Physical Models

The thermal model includes conduction in the material domains, the reduced air-cavity heat-transfer treatment and radiative exchange between surfaces. Complete material properties, software expressions and implementation details are given in Appendix G.

8.3.1. Thermal Model

The thermal calculation uses conservation of energy with Fourier heat conduction [34]:

$$\rho c_p \frac{\partial T}{\partial t} + \nabla \cdot \mathbf{q} = 0, \qquad \mathbf{q} = -k \nabla T, \tag{8.1}$$

In Equation (8.1), T is temperature, k is thermal conductivity, ρ is density, c_p is specific heat capacity and $\mathbf{q}$ is the conductive heat-flux vector. Their units are K, $\mathrm{W\,m^{-1}\,K^{-1}}$, $\mathrm{kg\,m^{-3}}$, $\mathrm{J\,kg^{-1}\,K^{-1}}$ and $\mathrm{W\,m^{-2}}$, respectively. In the stationary thermal study, $\partial T/\partial t = 0$.

For the solid domains, k is the assigned material thermal conductivity. For the enclosed-air domain, k is replaced by the effective thermal conductivity defined in Section 8.3.2. Radiative heat transfer is solved separately and is therefore not included in $\mathbf{q}$ or in the air-conductivity multiplier.

8.3.2. Air-Cavity Heat-Transfer Approximation

Natural convection increases heat transfer through the enclosed air above that obtained from molecular conduction alone. The convection enhancement was estimated using the enclosed-air correlation of ElSherbiny, Raithby and Hollands [73]. For the simplified electrode-spacer air region, the screening calculation gives a Rayleigh number of approximately 3.8×10^5 and Nusselt-number values between approximately 4.4 and 4.9. The complete derivation is given in Appendix F.

A Nusselt-number multiplier of 4.5 was selected for the reduced thermal model. The multiplier is applied uniformly to the complete enclosed-air domain as

$$k_{\mathrm{air,eff}}(T) = 4.5\, k_{\mathrm{air}}(T), \tag{8.2}$$

where $k_{\mathrm{air}}(T)$ is the temperature-dependent molecular thermal conductivity of air. Equation (8.2) represents only the convection-enhanced contribution to heat transfer. Radiative heat transfer is solved separately.

Figure 8.2 compares the selected treatment with conduction and radiation alone and with resolved natural convection in the simplified electrode-spacer region. The effective-conductivity model moves the calculated spacer-temperature profile towards the resolved-convection result compared with conduction and radiation alone. The comparison supports use of the effective-conductivity treatment in the thermal calculations.

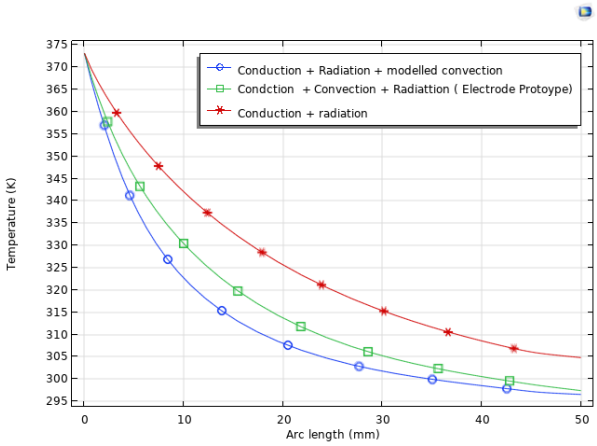


Figure 8.2: Spacer-temperature profiles for the three air-cavity heat-transfer representations.

The effective-conductivity model does not calculate the local gas-flow field. The multiplier 4.5 is therefore a global heat-transfer approximation and not a local Nusselt number throughout the chamber.

8.3.3. Electrical Model and Temperature-Dependent Conductivity

The electrical calculation uses the COMSOL Electric Currents interface for the time-dependent and stationary DC solutions. The formulation combines conduction and displacement current:

$$\mathbf{E} = -\nabla V, \qquad \mathbf{D} = \varepsilon_0 \varepsilon_r \mathbf{E}, \qquad \mathbf{J} = \sigma \mathbf{E} + \frac{\partial \mathbf{D}}{\partial t}, \qquad \nabla \cdot \mathbf{J} = 0. \tag{8.3}$$

In Equation (8.3), V is electric potential, $\mathbf{E}$ is electric field, $\mathbf{D}$ is electric flux density and $\mathbf{J}$ is total current density. Their units are V, V m^{-1}, C m^{-2} and A m^{-2}, respectively. The variable t denotes time in s. The vacuum permittivity ε_0 has units of F m^{-1}, ε_r is dimensionless and σ is electrical conductivity in S m^{-1}.

The conductivity σ in Equation (8.3) is assigned separately to each material domain. The epoxy domain uses $\sigma_{\mathrm{ep}}(T)$, while the air domain uses

$$\sigma_{\mathrm{air}} = 1.0 \times 10^{-14}\,\mathrm{S\,m^{-1}}.$$

Ground-level atmospheric air has an electrical conductivity of the order of 10^{-14} S m^{-1} under natural ionisation conditions [74]. The value used here is a prescribed model input and was not measured in the test chamber. The remaining electrical material properties are listed in Appendix G.

The epoxy conductivity follows the reference-form Arrhenius relation introduced in Section 2.3.1. Arrhenius-type conductivity relations are used to describe the temperature dependence of epoxy-based insulation, including epoxy materials investigated for HVDC GIS/GIL spacers [18], [75]:

$$\sigma_{\mathrm{ep}}(T) = \sigma_{\mathrm{ref}} \exp\left[\frac{E_a}{k_B}\left(\frac{1}{T_{\mathrm{ref}}} - \frac{1}{T}\right)\right], \tag{8.4}$$

In Equation (8.4), $\sigma_{\mathrm{ref}} = 1.0 \times 10^{-16}\,\mathrm{S\,m^{-1}}$ is the reference conductivity at $T_{\mathrm{ref}} = 293\,\mathrm{K}$. The activation energy is $E_a = 0.5\,\mathrm{eV}$, and $k_B = 8.617 \times 10^{-5}\,\mathrm{eV\,K^{-1}}$ is the Boltzmann constant. The selected activation energy follows a modified filled-epoxy precedent for HVDC GIS/GIL applications [75]. The relative permittivities are $\varepsilon_{r,\mathrm{ep}} = 4.4$ for epoxy and $\varepsilon_{r,\mathrm{air}} = 1.0$ for air. The epoxy conductivity depends on temperature but has no explicit electric field dependence in the present model. A separate stationary reference calculation was performed with the epoxy conductivity held constant at

$$\sigma_{\mathrm{ep}} = 1.0 \times 10^{-16}\,\mathrm{S\,m^{-1}}.$$

The constant value is equal to the reference conductivity in Equation (8.4). The geometry, relative permittivities, air conductivity and electrical boundary conditions remain unchanged. This reference removes the temperature dependence of the epoxy conductivity and provides the comparison basis for the stationary electric field redistribution.

8.4. Boundary Conditions and Study Sequence

The thermal and electrical studies use separate boundary and initial conditions. The stationary temperature distribution from the thermal model is transferred to the electrical model and remains fixed during the electrical calculation. Figure 8.3 summarises the solution transfer, time-dependent electrical study and applied voltage profile.

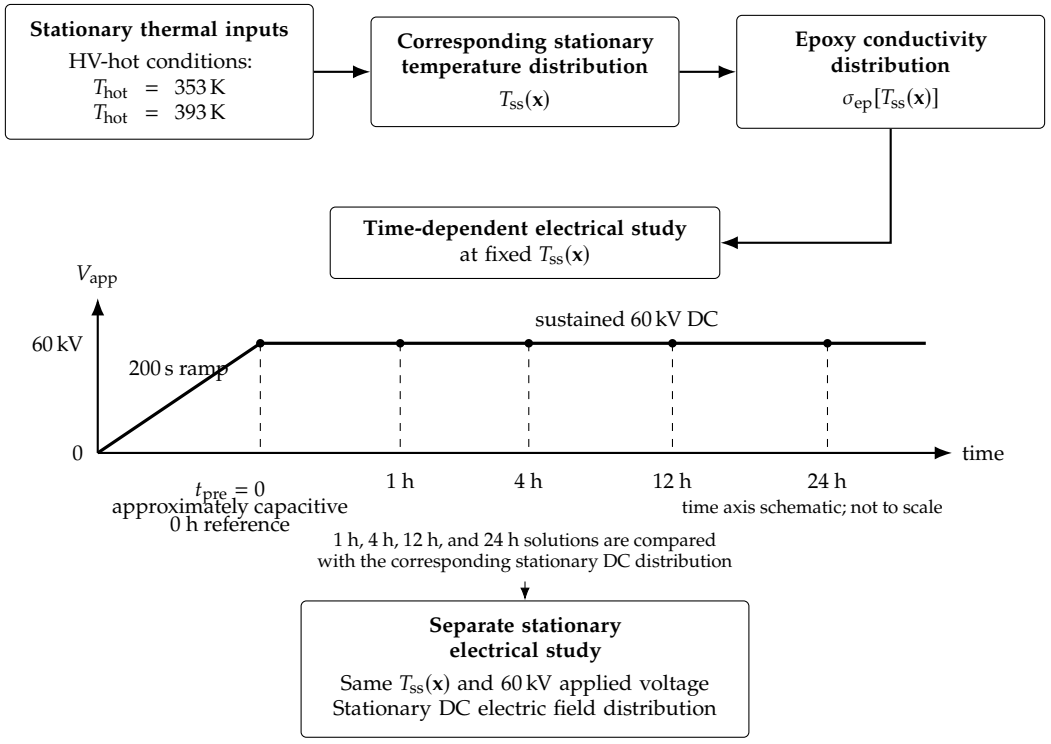


Figure 8.3: Simulation study sequence and applied voltage profile.

8.4.1. Thermal Boundary and Initial Conditions

The thermal studies use different hot-side conditions according to their purpose. For comparison of the heating concepts and the coaxial reference, the hot-oil model uses the 100 °C upper thermal-design condition. The remaining domains are initialised at 293 K in the time-dependent thermal study. The ambient temperature used for surface-to-ambient radiation is also 293 K.

The detailed electrical studies use two additional stationary HV-hot thermal solutions obtained with the hot-oil geometry. The prescribed hot-side temperatures are 353 K and 393 K. The 393 K condition is included only as a numerical sensitivity case. No temperature difference is imposed directly across the spacer.

Each thermal solution provides the temperature distribution along the spacer-gas interface and throughout the modelled domains. The corresponding stationary temperature distribution $T_{ss}(\mathbf{x})$ is transferred to the electrical model and remains fixed during that electrical calculation.

8.4.2. Electrical Boundary Conditions and Study Sequence

The electrical calculations use the 60 kV numerical screening case. The high-voltage electrode is assigned the applied potential, while the grounded electrode and grounded metallic structure are set to $V = 0$. The maximum operating voltage of the test bench is 50 kV DC.

For each HV-hot thermal case, the corresponding stationary temperature distribution $T_{ss}(\mathbf{x})$ is imported from the thermal study. The temperature distribution remains fixed during the electrical calculation and determines the spatial epoxy-conductivity distribution $\sigma_{ep}[T_{ss}(\mathbf{x})]$.

In the time-dependent electrical study, the voltage is ramped from 0 to 60 kV over 200 s and then held constant. Completion of the ramp defines

$$t_{pre} = 0.$$

The end-of-ramp electric field distribution is used as the approximately capacitive 0 h reference. Some conduction occurs during the finite voltage ramp, so this distribution is not identical to the ideal initial capacitive field distribution.

Time-dependent electric field distributions are extracted after 1 h, 4 h, 12 h, and 24 h of subsequent DC pre-stress. A separate stationary Electric Currents study uses the same thermal distribution and 60 kV applied voltage. Each transient solution is compared with the stationary DC electric field distribution corresponding to the same thermal condition.

All calculations use COMSOL's physics-controlled *Extremely fine* mesh. The stationary and time-dependent studies use the default COMSOL solver settings. The detailed mesh, solver and study configurations are given in Appendix G.

8.5. Numerical Verification

The implemented geometry and material domains were checked against the final electrode-spacer arrangement. The reduced air-cavity treatment was compared with conduction and radiation alone and with simplified resolved convection, as described in Section 8.3.2.

The electric field quantities near the electrode-spacer junctions were evaluated over finite interface regions. Values calculated exactly at ideal geometric corners were excluded because the local maxima are mesh-sensitive.

8.6. Extracted Quantities and Comparison Basis

The thermal outputs include the electrode temperatures and the temperature distribution along the spacer-gas interface. For the electrical comparison, the realised spacer temperature difference is defined between the HV-side and grounded-side ends of the spacer-gas interface as

$$\Delta T = T_{s,HV} - T_{s,GND},$$

where $T_{s,HV}$ and $T_{s,GND}$ are the calculated spacer temperatures at the two interface ends. A positive ΔT therefore corresponds to the HV-side end of the spacer being hotter.

The local thermal response is evaluated at P_T, the midpoint of the spacer-gas interface. A first-order response is fitted as

$$T(P_T, t) = T_\infty - (T_\infty - T_0)\exp\left(-\frac{t}{\tau_{\text{th}}}\right), \tag{8.5}$$

where T_0 is the initial temperature at P_T, T_∞ is the fitted final temperature and τ_{th} is the fitted local thermal time constant. The fitted value characterises the response at P_T and is not used as a criterion for complete thermal equilibrium of the model.

The electrical comparison is based on the electric field magnitude along the selected spacer-gas interface,

$$E_{\text{norm}}(s, t) = \|\mathbf{E}(s, t)\|,$$

where s is the arc length along the interface and Γ denotes the complete extracted interface path. E_{norm} has units of $\mathrm{V\,m^{-1}}$. The corresponding stationary DC field profile is denoted by $E_{\text{norm,ss}}(s)$.

The whole-interface deviation from the corresponding stationary DC distribution is defined as

$$D_E(t) = \frac{\left[\int_\Gamma (E_{\text{norm}}(s, t) - E_{\text{norm,ss}}(s))^2 \, \mathrm{d}s\right]^{1/2}}{\left[\int_\Gamma E_{\text{norm,ss}}^2(s)\mathrm{d}s\right]^{1/2}}. \tag{8.6}$$

Equation (8.6) is dimensionless. The arc-length integral weights the comparison by physical distance along the interface rather than by the number of sampled points. A value of $D_E = 0$ corresponds to exact agreement with the stationary profile. Results are reported as $100D_E$ in percent.

Local deviations are evaluated at fixed reference locations using

$$\delta_j(t) = \frac{E_{\text{norm}}(s_j, t) - E_{\text{norm,ss}}(s_j)}{E_{\text{norm,ss}}(s_j)} \times 100\%, \qquad j \in \{\text{HV}, \text{C}, \text{GND}\}. \tag{8.7}$$

For each thermal case, the three reference locations correspond to the stationary HV-side regional maximum, central minimum and grounded-side regional maximum. The positions s_j are then held fixed for all transient comparisons of that thermal case. Keeping the positions fixed separates temporal field changes from movement of the local extrema. The sign of δ_j indicates whether the transient value lies above or below the stationary value.

The absolute fractional local residual is defined as

$$r_j(t) = \frac{\left|E_{\text{norm}}(s_j, t) - E_{\text{norm,ss}}(s_j)\right|}{E_{\text{norm,ss}}(s_j)} = \frac{|\delta_j(t)|}{100}. \tag{8.8}$$

An interval-based apparent relaxation time is calculated from the reduction of this residual between two sampled times:

$$\tau_{\text{app},j} = \frac{t_2 - t_1}{\ln\left[r_j(t_1)/r_j(t_2)\right]}. \tag{8.9}$$

The reported regional comparison uses $t_1 = 1\,\text{h}$ and $t_2 = 12\,\text{h}$. The apparent relaxation time is evaluated only where the absolute residual decreases over the selected interval. The quantity $\tau_{\text{app},j}$ describes the sampled approach of the local field towards its stationary value and is not interpreted as a material or Maxwell–Wagner relaxation time.

The 1 h, 4 h, 12 h, and 24 h transient solutions are compared independently with their corresponding stationary DC distributions using D_E and δ_j. Both metrics use the electric field magnitude and do not separately evaluate the tangential component E_t.

8.7. Model Limitations

A formal mesh-convergence study and solver-tolerance sensitivity study were not performed. The reported results therefore refer to the adopted *Extremely fine* mesh and default solver configuration.

8.8. Chapter conclusions

- The electro-thermal calculation uses one-way thermal-to-electrical coupling. The stationary temperature distribution determines the spatial epoxy-conductivity distribution and remains fixed during the electrical calculation.
- Heat transfer through the enclosed air is represented by $k_{\mathrm{air,eff}}(T) = 4.5\, k_{\mathrm{air}}(T)$, with radiative heat transfer treated separately. Compared with conduction and radiation alone, the selected treatment moves the calculated spacer-temperature profile towards the simplified resolved-convection result.
- The time-dependent electrical study uses the 60 kV numerical screening case with a 200 s voltage ramp. The end-of-ramp field provides an approximately capacitive 0 h reference, while a separate stationary Electric Currents study provides the stationary DC electric field distribution.
- Electrical redistribution is evaluated from the electric field magnitude along the spacer-gas interface. The whole-interface metric D_E and the fixed-location deviations δ_j quantify convergence towards the stationary DC distribution. The interval-based τ_{app} provides an additional regional descriptor and is not interpreted as a material relaxation time.

9

Simulation Results

This chapter presents the thermal and electric field results obtained with the electro-thermal model defined in Chapter 8. The thermal results evaluate the temperature distribution of the test bench and compare the two heating concepts with the coaxial reference. The electrical results quantify stationary and time-dependent field redistribution along the spacer–gas interface for the 60 kV numerical screening case.

9.1. Thermal Response

9.1.1. Whole-Domain Temperature Distribution

Under the 100 °C upper thermal-design condition, the highest calculated temperatures remain concentrated around the heated electrode, rod, and adjacent PEEK components. The maximum temperature in the PMMA chamber is approximately 298 K (25 °C), while the maximum temperature in the PEEK components is approximately 370 K (97 °C). Both values remain within the material-temperature limits adopted for the test-bench design. Figure 9.1 shows the corresponding stationary temperature distribution.

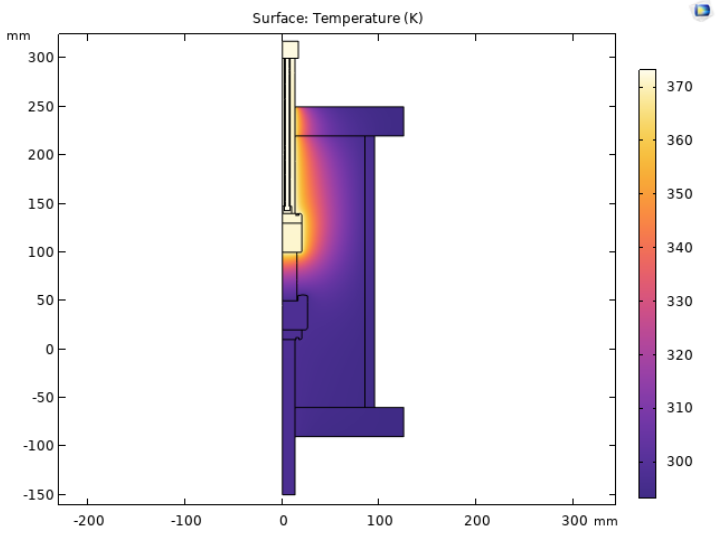


Figure 9.1: Stationary temperature distribution of the test bench under the 100 °C upper thermal-design condition.

The calculated temperature distribution is consistent with the adopted material placement. The transparent PMMA chamber remains in the cooler outer region, whereas the PEEK components are exposed to the higher temperatures near the heated chamber end. The thermal calculation does not assess long-term creep, which also depends on sustained mechanical stress and time.

9.1.2. Stationary Spacer Temperature Distribution

The spacer temperature profile determines the temperature distribution used in the electro-thermal comparison. Under the 100 °C upper thermal-design condition, the calculated end-to-end spacer temperature differences are approximately 74 K for hot-oil heating and 76 K for cartridge heating. The coaxial reference gives approximately 75 K. Figure 9.2 compares the three profiles on the normalised interface coordinate defined in Chapter 6.

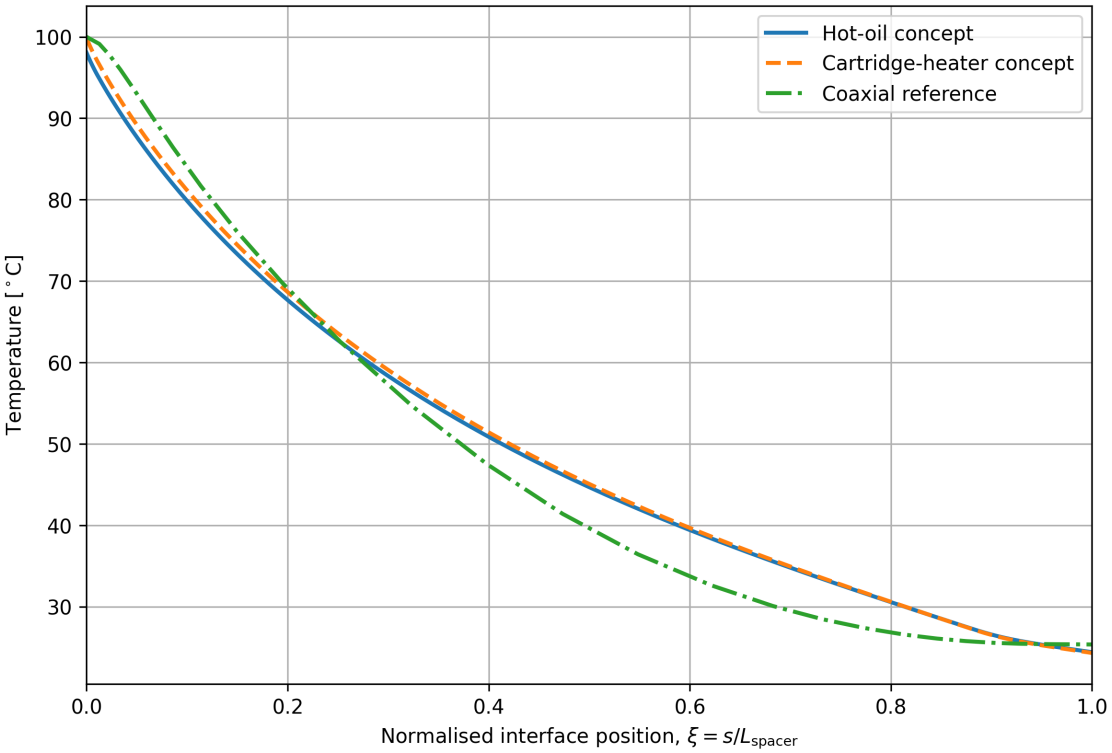


Figure 9.2: Stationary spacer-interface temperature profiles for the two heating concepts and the coaxial reference under the 100 °C upper thermal-design condition.

The overall spacer temperature difference of each heating concept is within about 1 K of the coaxial reference. The maximum local difference from the coaxial profile is about 6 K for both concepts and occurs near $\xi \approx 0.62$. The hot-oil and cartridge-heater profiles differ from each other by at most about 2 K. Both heating concepts therefore reproduce the direction and overall magnitude of the coaxial temperature difference, although the local temperature profiles are not identical.

9.1.3. Local Thermal Response

The local thermal response is evaluated at P_T, the midpoint of the spacer-gas interface. First-order fits give thermal time constants of approximately 14 min for hot-oil heating and 13 min for cartridge heating. The corresponding simulated responses and fitted curves are shown in Figure 9.3.

Four fitted time constants correspond to approximately 54 min for hot-oil heating and 50 min for cartridge heating. The calculated temperature continues to change slowly beyond these times. The fitted time constants therefore characterise the local response at P_T and are not used as a criterion for complete thermal equilibrium of the test bench.

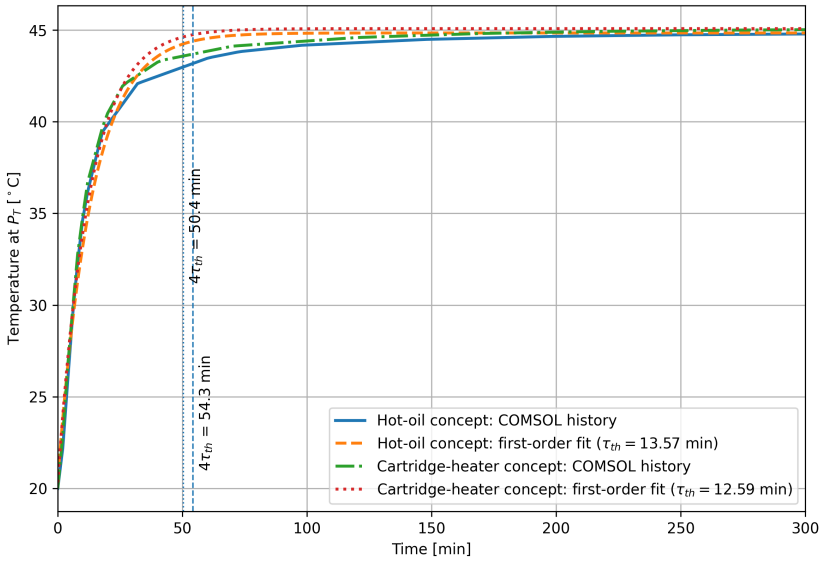


Figure 9.3: Temperature response at the midpoint P_T of the spacer-gas interface and corresponding first-order fits for the two heating concepts.

9.2. Stationary DC Field Redistribution Under Thermal Conditions

The stationary electrical analysis evaluates whether the integrated geometry concentrates the electric field at the intended spacer–gas interface and how temperature-dependent conductivity redistributes this field. All electrical results in this section are calculated for the 60 kV numerical screening case.

9.2.1. Whole-Domain electric field Distribution

For the temperature-independent conductivity reference defined in Chapter 8, the elevated electric field is concentrated around the electrode-spacer region and along the spacer-gas interface. Most of the surrounding chamber remains in a comparatively low-field region, as shown in Figure 9.4.

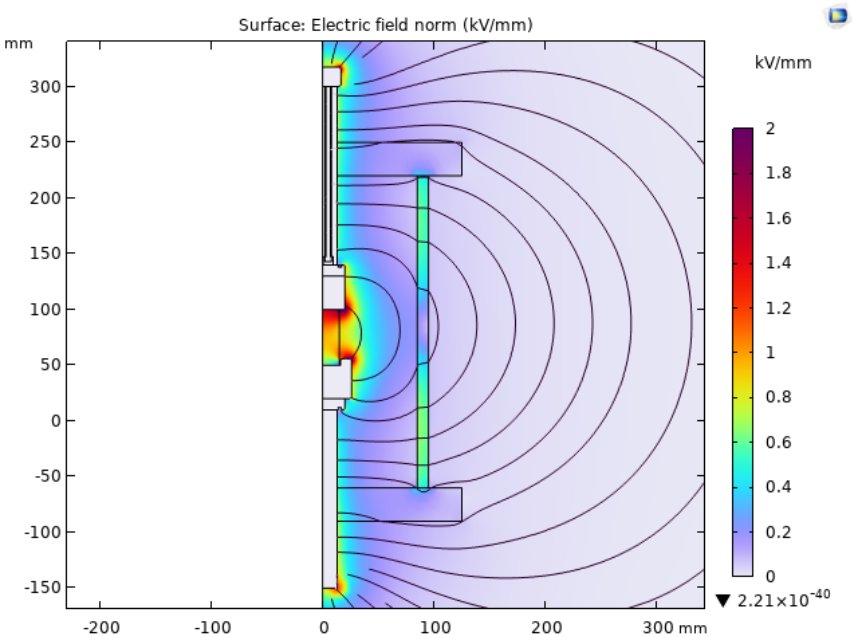


Figure 9.4: Whole-domain electric field distribution of the integrated test-bench geometry for the 60 kV numerical screening case.

The calculated distribution is consistent with the field-selectivity requirement of the test bench. The intended electrode-spacer region carries the principal electrical stress, while the chamber does not form a competing high-field region. This provides the numerical screening evidence for FR-E3. Local solver maxima at idealised geometric junctions are not used as physical field values; the quantitative comparisons are based on the finite spacer-gas interface profiles defined in Chapter 8.

9.2.2. Coaxial Reference Response

The coaxial reference spacer has two gas-facing surfaces. Figure 9.5 identifies these as the upper and lower spacer–gas interfaces used for the electric field extraction.

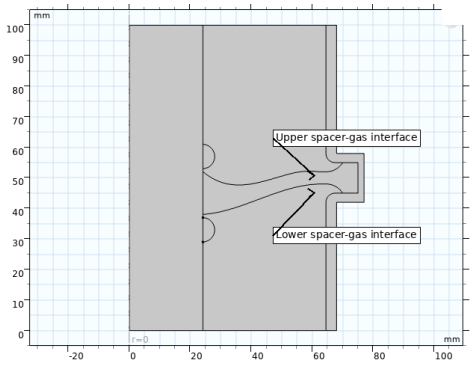


Figure 9.5: Coaxial reference geometry showing the upper and lower spacer-gas interfaces used for the electric field profiles.

Figure 9.6 compares the stationary electric field magnitude along both interfaces with and without the imposed temperature gradient. Without the temperature gradient, the two interfaces show similar field distributions. Including temperature-dependent conductivity changes the field distribution, with the strongest redistribution occurring along the lower interface.

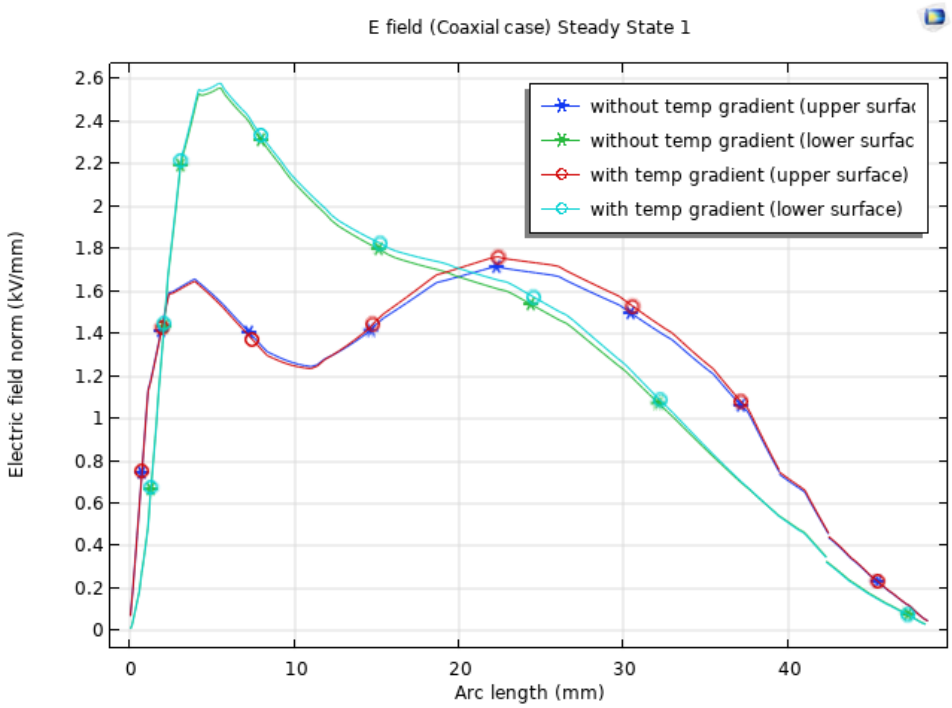


Figure 9.6: Stationary electric field magnitude along the upper and lower spacer–gas interfaces of the coaxial reference, with and without the imposed temperature gradient.

The coaxial reference shows the same qualitative conductivity-driven field redistribution as the test-bench arrangement. The comparison is used only as supporting evidence; point-by-point numerical agreement between the two geometries is not assumed.

9.2.3. Test-Bench Interface-Field Redistribution

The stationary spacer–gas interface field was calculated for a reference case with temperature-independent epoxy conductivity and for two HV-hot temperature distributions. The first thermal case gives a realised spacer temperature difference of 51.6 K, slightly above the intended experimental range of 40 K to 50 K. A second case with a realised temperature difference of 85.7 K is included as a high-gradient sensitivity calculation. Figure 9.7 compares the three stationary field profiles.

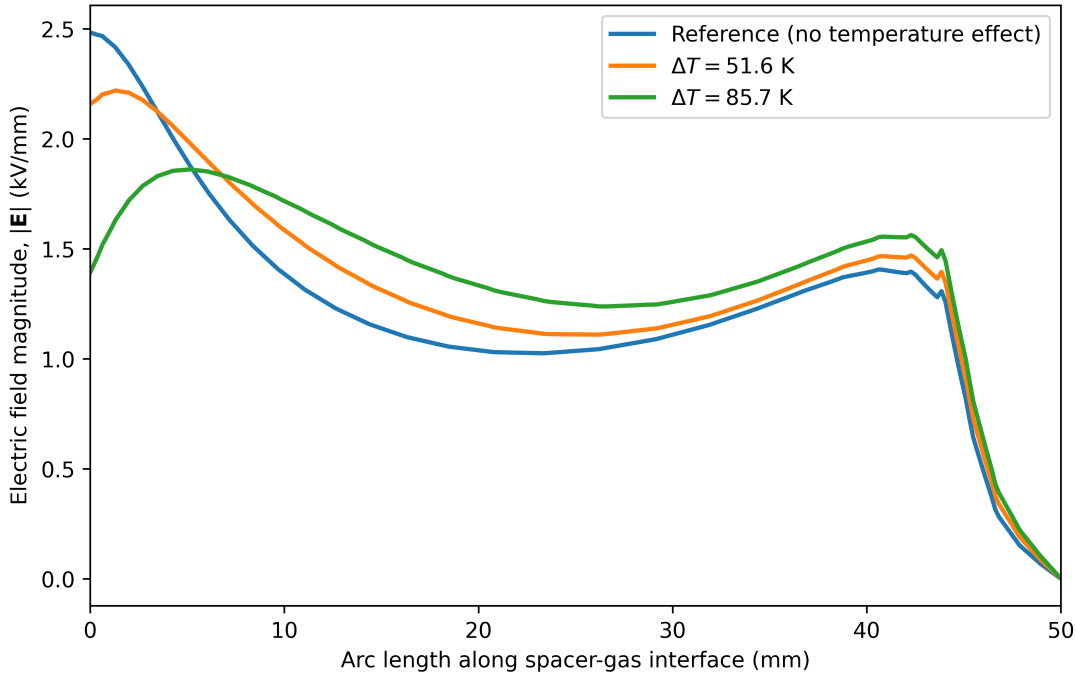


Figure 9.7: Stationary electric field magnitude along the test-bench spacer–gas interface for the temperature-independent reference and the two HV-hot thermal cases at the 60 kV numerical screening case.

For the temperature-independent reference, the HV-side regional maximum is approximately 2.48 kV mm^{-1} at the start of the interface. At ΔT = 51.6 K, this maximum decreases to approximately 2.22 kV mm^{-1} and moves about 1.3 mm into the interface. The central minimum increases from approximately 1.03 kV mm^{-1} to 1.11 kV mm^{-1}, while the grounded-side regional maximum increases from approximately 1.41 kV mm^{-1} to 1.47 kV mm^{-1}.

The redistribution becomes stronger in the 85.7 K sensitivity case. The HV-side regional maximum decreases to approximately 1.86 kV mm^{-1} and shifts to $s \approx 5.1$ mm. The central minimum increases to approximately 1.24 kV mm^{-1}, and the grounded-side regional maximum increases to approximately 1.56 kV mm^{-1}.

Relative to the reference case, the HV-side regional maximum decreases by about 11 % at 51.6 K and by about 25 % at 85.7 K. Over the same cases, the grounded-side maximum increases by about 4.5 % and 11 %, respectively. The ratio of the HV-side to grounded-side regional maxima consequently decreases from 1.77 to 1.51 and then to 1.19. The stationary field therefore becomes less concentrated at the hot HV end and more evenly distributed towards the central and grounded-side regions as the temperature-dependent conductivity distribution becomes stronger.Table 9.1 summarises these changes.

Table 9.1: Stationary spacer–gas interface field metrics for the temperature-independent reference and the two HV-hot thermal cases.

Quantity	Reference	ΔT = 51.6 K	ΔT = 85.7 K
HV-side maximum (kV mm^{-1})	2.48	2.22	1.86
HV-side maximum position (mm)	0.0	1.3	5.1
Central minimum (kV mm^{-1})	1.03	1.11	1.24
GND-side maximum (kV mm^{-1})	1.41	1.47	1.56
$E_{\mathrm{HV,max}}/E_{\mathrm{GND,max}}$	1.77	1.51	1.19

The 85.7 K case is used only as a sensitivity case. Its prescribed hot-side temperature is 393 K, compared with 353 K for the 51.6 K case. The cases therefore differ in both ΔT and absolute temperature, so the comparison does not isolate the effect of ΔT alone.

9.3. Time-Dependent DC Field Formation

The time-dependent electrical calculation evaluates how the spacer-gas interface field approaches the stationary DC distribution during DC pre-stress. The detailed transient profiles are presented for the realised temperature difference of 51.6 K. The 85.7 K sensitivity case is compared later using the whole-interface convergence metric.

9.3.1. Transient Interface-Field Development

The field distribution at $t_{\mathrm{pre}} = 0$ corresponds to the initial capacitive field distribution at the end of the voltage ramp. The field then changes while the applied DC voltage is maintained. Figure 9.8 compares the initial distribution with the calculated profiles after 1 h and 4 h of DC pre-stress and with the stationary DC distribution.

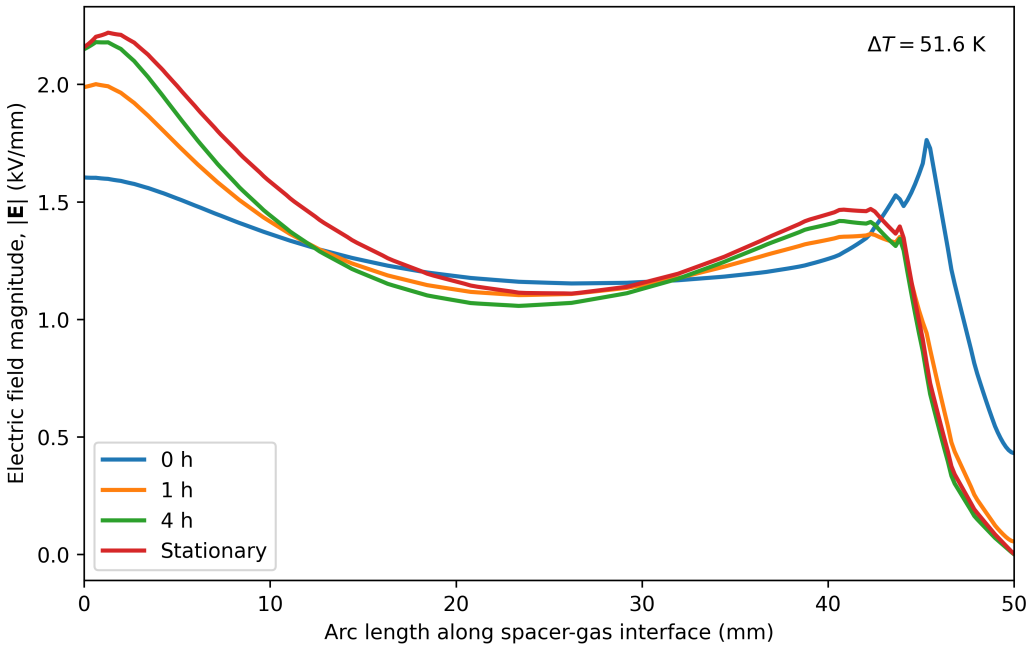


Figure 9.8: Early development of the spacer–gas interface field for ΔT = 51.6 K, compared with the stationary DC distribution.

The initial capacitive distribution differs substantially from the stationary DC distribution. The largest differences occur near both ends of the interface, including a pronounced grounded-side peak in the initial distribution. After 1 h, the HV-side field has moved towards the stationary profile, while differences remain over the central and grounded-side regions. The 4 h profile is closer to the stationary distribution over most of the interface.

The later development is shown in Figure 9.9. The 4 h, 12 h, and 24 h profiles progressively approach the stationary DC distribution.

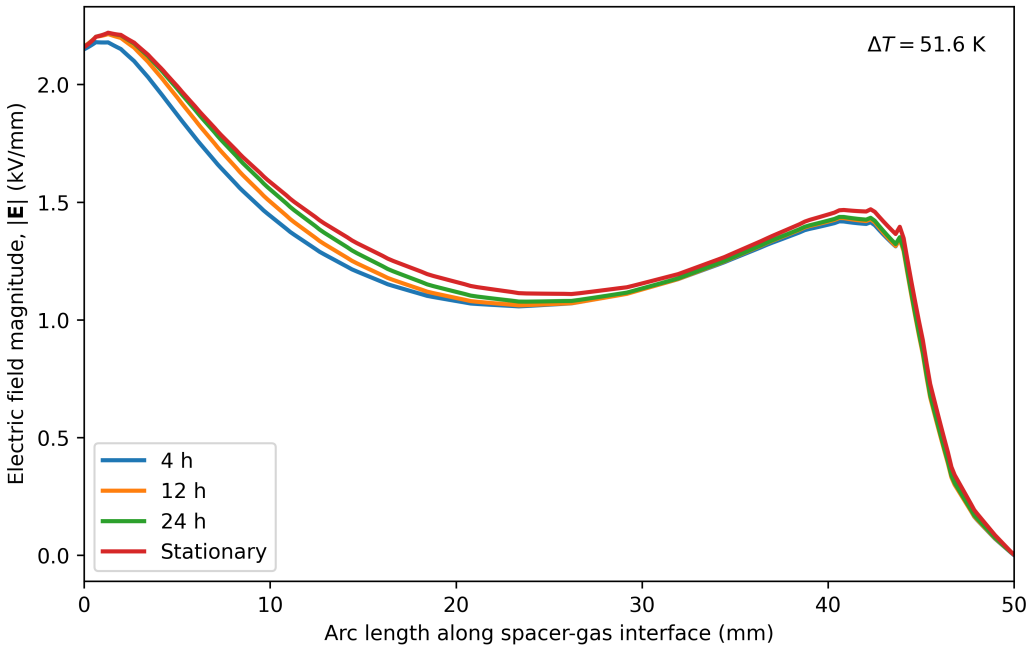


Figure 9.9: Later development of the spacer–gas interface field for $\Delta T = 51.6\,\mathrm{K}$, compared with the stationary DC distribution.

The HV-side region is already close to the stationary distribution at the later pre-stress durations. Smaller differences remain in the central and grounded-side regions after 24 h. The approach to the stationary DC field is therefore spatially non-uniform and cannot be judged from one interface location alone.

9.3.2. Whole-Interface Convergence

The whole-interface deviation D_E, defined in Chapter 8, quantifies the difference between each transient field profile and its corresponding stationary DC distribution. Figure 9.10 compares the 51.6 K case with the 85.7 K high-gradient sensitivity case.

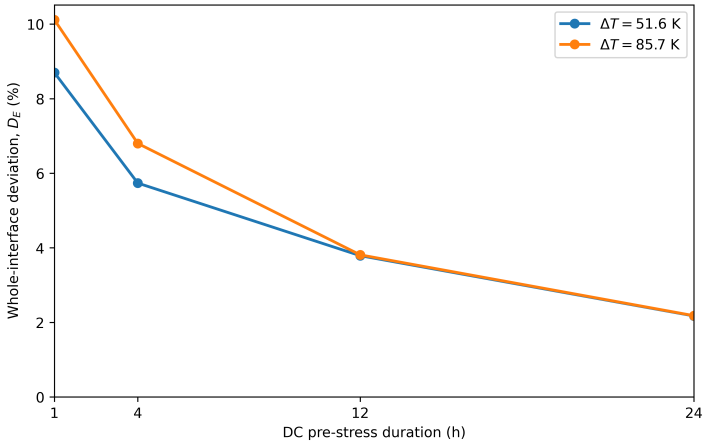


Figure 9.10: Whole-interface deviation from the stationary DC field distribution for the two HV-hot thermal cases.

For $\Delta T = 51.6\,\mathrm{K}$, D_E decreases from approximately 8.7 % after 1 h to 5.7 % after 4 h. It decreases further to approximately 3.8 % after 12 h and 2.2 % after 24 h.

The high-gradient case shows a larger deviation during the first hours. Its D_E value decreases from approximately 10.1 % after 1 h to 6.8 % after 4 h. After 12 h, however, the deviations of the two thermal cases are both approximately 3.8 %, and after 24 h both are approximately 2.2 %.

The field therefore continues to change over the complete interface for many hours after the voltage ramp. The stronger thermal condition produces a larger early deviation, but the difference between the two cases becomes small at the later pre-stress durations. A remaining D_E of about 2.2 % after 24 h also shows that exact agreement with the stationary DC distribution is not reached within the simulated duration.

9.3.3. Regional Relaxation

Table 9.2 compares the local deviation from the stationary DC field at the HV-side, central, and grounded-side reference locations defined in Chapter 8.

Table 9.2: Local deviation from the stationary DC field distribution at the three reference locations. Negative values indicate a transient field below the stationary value.

ΔT	t_{pre}	HV side (%)	Centre (%)	GND side (%)
51.6 K	1 h	-10.3	-0.1	-7.2
51.6 K	4 h	-1.8	-3.6	-3.8
51.6 K	12 h	-0.2	-3.5	-2.9
51.6 K	24 h	0.0	-2.6	-2.5
85.7 K	1 h	-10.2	-6.2	-9.7
85.7 K	4 h	-3.0	-7.6	-5.9
85.7 K	12 h	-0.1	-5.5	-4.6
85.7 K	24 h	0.0	-2.6	-3.5

Both thermal cases show a clear spatial difference in the approach to the stationary DC field. The HV-side region approaches the stationary value fastest and is essentially converged by 12 h. The central and grounded-side regions change more slowly and still differ from the stationary values after 24 h. The central response is also non-monotonic, which shows that convergence cannot be judged from one interface location alone.

Over the 1 h to 12 h interval, the apparent relaxation time at the HV side is approximately 3.0 h for the 51.6 K case. The HV-side value decreases to approximately 2.5 h for the 85.7 K case. The corresponding grounded-side values are approximately 12.1 h and 14.7 h. The lower HV-side value in the hotter case is consistent with the higher local epoxy conductivity.

The grounded-side result does not follow the same trend. Its local temperature increases from approximately 303 K to 309 K, for which the conductivity model predicts a shorter local ε/σ relaxation time. The larger τ_{app} therefore does not indicate slower local material relaxation. The grounded-side residual decreases at different rates over the sampled intervals and is affected by field redistribution over the complete spacer. The calculated τ_{app} therefore describes the selected time interval and is not a material time constant.

9.4. Chapter conclusions

- Under the 100 °C upper thermal-design condition, the maximum calculated temperatures are approximately 298 K in the PMMA chamber and 370 K in the PEEK components near the heated end. The temperature distribution is consistent with the adopted material placement.
- The hot-oil and cartridge-heater concepts produce spacer temperature differences of approximately 74 K and 76 K, compared with 75 K for the coaxial reference. Their fitted midpoint thermal time constants are approximately 14 min and 13 min, respectively.
- At the 60 kV numerical screening case, the principal electrical stress is concentrated in the electrode-spacer region and along the spacer-gas interface. The chamber remains in a comparatively low-field region.

- Temperature-dependent epoxy conductivity shifts the stationary field away from the hot HV end. The HV-side regional maximum decreases from 2.48 kV mm^{-1} in the temperature-independent reference to 2.22 kV mm^{-1} at ΔT = 51.6 K and 1.86 kV mm^{-1} at ΔT = 85.7 K.
- For ΔT = 51.6 K, the whole-interface deviation from the stationary DC distribution decreases from approximately 8.7 % after 1 h to 2.2 % after 24 h. The 85.7 K case reaches a similar deviation at the later pre-stress durations.
- The approach to the stationary DC field is spatially non-uniform. Over the 1 h to 12 h interval, the HV-side apparent relaxation times are approximately 3.0 h and 2.5 h for the 51.6 K and 85.7 K cases. The corresponding grounded-side values are approximately 12.1 h and 14.7 h.

10

Test-Bench Qualification and Experimental Method

This chapter defines the qualification checks and experimental method for the designed test bench. The method combines the design requirements with the thermal and electric field results to establish controlled conditions before each voltage application. It specifies the commissioning and acceptance checks, voltage application, measurements, event classification, reset procedure, test matrix, and data analysis required for the planned surface-flashover investigation.

10.1. Test Conditions

The planned experimental comparison varies three test variables: thermal condition, voltage polarity, and DC pre-stress duration. In this chapter, a test denotes one voltage application under a specified thermal condition, polarity, and DC pre-stress duration, ending at a disruptive discharge or the prescribed stop voltage.The thermal condition is either an unheated ambient-temperature reference, HV-side heated, or grounded-side heated. The two heated conditions require $|\Delta T|$ = 40–50 K. The allowable residual temperature difference and stability period for the unheated reference are established during commissioning and acceptance tests. Within each matched comparison, the remaining method settings are kept fixed, while quantities that cannot be fixed exactly are measured and recorded. Table 10.1 summarises the resulting test conditions and required records.

Table 10.1: Test variables, controlled conditions, required records, and model-derived quantities.

Group	Quantities
Test variables	thermal condition (unheated reference, HV-side heated, or grounded-side heated); voltage polarity; DC pre-stress duration
Controlled conditions	field-defining electrode–spacer geometry; spacer-specimen basis; electrode surface condition; assembly and chamber configuration; measurement arrangement; pre-stress voltage U_{pre}; waveform used to reach U_{pre}; voltage-rise procedure
Required test record	test and spacer-specimen identifiers; specimen, electrode, assembly, and previous electrical history; voltage polarity; commanded voltage sequence and measured voltage waveform; assigned and actual DC pre-stress duration; hold start and end times; T_{HV}; T_{GND}; realised ΔT; ambient temperature; air pressure; relative humidity; earth-return-current recording; discharge-signal recording; optical recording; event classification; exclusion or censoring reason
Model-derived quantities	spacer-temperature distribution and time-dependent interface electric field distribution during DC pre-stress, calculated from the measured electrode temperatures and voltage history

Tests are performed in atmospheric air near 1 bar. Pressure, ambient temperature, and relative humidity are measured for every test and included in the complete test record, as required by FR-V1 and FR-D1 in Table 4.1. IEC 60060-1 provides the general framework for the voltage and atmospheric

measurements [59].

Each primary test uses a fresh, previously unflashed spacer specimen from the same production batch. This prevents previous specimen exposure from becoming an additional variable in the primary comparison. The test record identifies the specimen formulation, fabrication route, batch, preparation, storage condition, assembly condition, and previous electrical exposure, as required by FR-D3 in Table 4.1. Tests using previously flashed specimens, if performed, are kept separate from the primary comparison.

10.2. Commissioning and Acceptance Tests

Before research measurements begin, the realised test bench must pass the commissioning and acceptance tests. The checks cover the mechanical and environmental condition, thermal system, electrical and measurement system, optical arrangement, safety functions, and complete test setup. Measurement uncertainty is included in the relevant acceptance decisions following JCGM 100 [76].

Thermal-model validation is performed during non-energised operation. Measured and calculated temperatures are compared at the same positions and boundary conditions using temporary calibrated sensors. The comparison includes measurement and model uncertainty following ASME V&V 20 and JCGM 100 [76], [77]. Agreement supports the thermal model at the measured positions only.

The required sensitivity of the earth-return-current channel follows from an order-of-magnitude calculation using the epoxy-conductivity model in Equation 8.4, the interface-field range of approximately 1–2.1 kV/mm obtained in Chapters 5 and 9, and the nominal spacer cross-section. The calculated bulk-conduction contribution ranges from below 1 pA to approximately 30 pA over the numerical temperature range. The total earth-return current can be higher because surface, gas, charging, and stray-current contributions are also present. The low-current channel therefore requires pA-scale sensitivity; its offset, drift, noise floor, linearity, usable range, and recovery are established during commissioning and acceptance tests.

Applied-voltage measurements follow IEC 60060-1 and IEC 60060-2 [59], [78]. A tracer-gas leak test is used only when required after the pressure-hold check [79]. Electrical safety checks follow the applicable university procedures and EN 50191 [80]. The test bench is released for experimental use only after all required checks in Figure 10.1 have passed.

The commissioning and acceptance checks for the realised test bench are summarised in Figure 10.1.

10.3. Voltage Application

Voltage is applied only after the prescribed thermal condition satisfies the acceptance criteria established during test-bench qualification. For a heated condition, the measured values of T_{HV}, T_{GND}, and ΔT must be within the accepted range and sufficiently stable. The unheated ambient-temperature reference must satisfy its separately established residual-ΔT and stability criteria. The electrodes remain grounded until these conditions are met.

The voltage application consists of a rise to the pre-stress voltage U_{pre}, a DC pre-stress period, and the voltage rise to flashover. The DC pre-stress duration, t_{pre}, starts when the measured voltage reaches U_{pre} and ends when the voltage rise to flashover begins. For a zero-duration pre-stress condition, the voltage rise to flashover begins when U_{pre} is reached.

The value of U_{pre} is fixed before the experimental comparison. Preliminary non-disruptive tests on the commissioned test setup are used to confirm a voltage that can be maintained for the longest planned DC pre-stress duration without a disruptive discharge, non-target hardware discharge, or violation of a subsystem limit. The selected value must remain below the 50 kV maximum operating voltage. A common U_{pre} and the same waveform used to reach it are retained within matched comparisons. The applied-voltage waveform is measured according to IEC 60060-1 and IEC 60060-2 [59], [78].

After the prescribed DC pre-stress duration, the voltage is increased using a fixed voltage rise rate until a disruptive discharge occurs or the prescribed stop voltage is reached. The rise rate is selected during preliminary tests and then kept unchanged within matched comparisons. Rising-voltage breakdown measurements can depend on the applied voltage–time characteristic; the selected waveform must

Area	Check / method	Acceptance basis	Retained record
Mechanical and environmental	Geometry and assembly Electrode gap, alignment, spacer seating and field-defining dimensions checked against the drawings. Pressure and gas condition Mechanical pressure hold, leak check and dry-air condition check.	Drawing tolerances satisfied; as-built geometry remains consistent with the accepted field geometry. Mechanical design pressure: 6 bar(g). No leakage, cracking, crazing, seal extrusion or permanent deformation. Experimental gas condition: atmospheric air near 1 bar(a).	Dimensions; pressure; gas temperature; RH; leakage/deformation observations; inspection result.
Thermal	Thermal conditions Establish HV-side heated, grounded-side heated and unheated reference conditions. Measure T_{HV}, T_{GND}, overshoot and settling. Model validation Compare measured and calculated temperatures at identical accessible positions using temporary calibrated sensors.	Heated conditions: $\lvert\Delta T\rvert$ = 40-50 K for both gradient directions. Unheated reference: residual ΔT and stability satisfy the limits established during qualification. Component temperature: $T_{peak} + U_T + \Delta T_{overshoot} \leq T_{rated,min}$. Model agreement is assessed at the measured positions and within measurement/model uncertainty.	T_{HV}, T_{GND}, ΔT, T_{peak}, overshoot, settling, temporary-sensor data and model-measurement differences.
Electrical and measurement	Voltage chain Check DC source, series resistor, calibrated divider, waveform, timing and both polarities. Low-current channel Determine offset, drift, noise floor, linearity, usable range and recovery. Discharge channel Apply a repeatable test signal and check amplitude response, timing and recovery.	Maximum operating voltage: U ≤ 50 kV. Commanded and measured voltage histories agree within the established measurement uncertainty; both polarities are supported. Low-current channel provides pA-scale sensitivity. Fast channel resolves the required discharge transients. No non-target discharge occurs from auxiliary hardware within the intended non-disruptive operating range.	Voltage waveform/timing; divider check; low-current offset, noise, drift, linearity and range; discharge-channel response; non-target events.
Optical	Check direct and mirror views using a reference target. Verify focus, reflections and synchronisation with the electrical acquisition. Repeat under the imposed thermal condition.	Spacer surface, both spacer-end regions and the relevant gas region remain visible. Earliest visible discharge region and initial visible propagation direction can be resolved. Microscopic inception is not required.	Reference image; optical timing; focus/exposure; field-of-view check; mirror visibility under heating.
Safety	Functional checks of access interlocks, emergency isolation, controlled discharge and grounding, heater shutdown, over-temperature protection and pressure protection.	HV cannot be applied under an unsafe enclosure condition. Shutdown returns the setup to a defined safe state. Thermal and pressure protection operate as intended. Relevant checks are repeated after affected hardware or wiring changes.	Safety-check record; trip or functional-test result; corrective action; repeat-check result.
Integrated readiness check **Complete test setup operated under the most demanding planned non-disruptive condition: full thermal gradient, longest planned DC pre-stress, maximum planned U_{pre}, both polarities and both heated-side configurations.**	**Interaction checks** **Heating does not disturb the low-current measurement; voltage application does not disturb temperature control; thermal loading does not obstruct the optical view; the air condition remains within established limits.**	**Release decision** **PASS: all required checks satisfied → release for experimental use.** **FAIL: correct fault → repeat affected check(s) → repeat integrated readiness check.**	

Figure 10.1: Commissioning and acceptance map for the test bench.

therefore be reproducible and free from unacceptable overshoot [81]. The voltage rise should also remain short relative to the multi-hour electric field redistribution identified in Chapter 9, so that it does not introduce an additional uncontrolled DC pre-stress period. Figure 10.2 shows the prescribed sequence in voltage magnitude; the sign is set by the selected polarity.

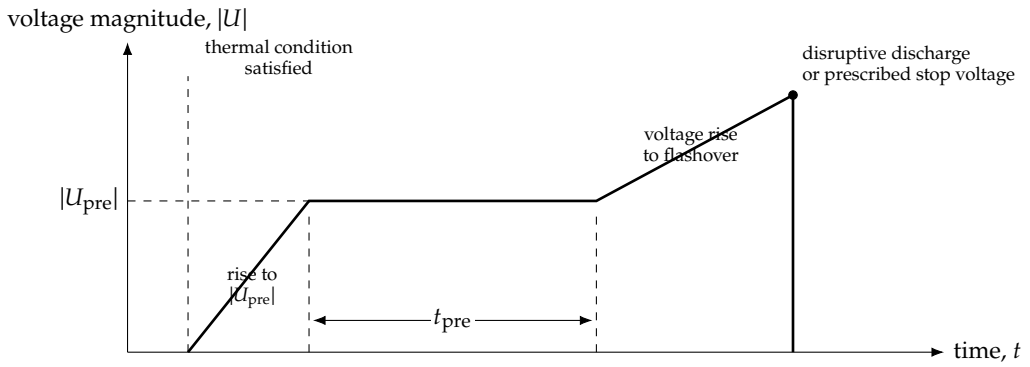


Figure 10.2: Voltage application sequence for one test; time intervals are not to scale.

10.4. Measurements

Each test combines electrical, thermal, environmental, and optical measurements. The electrical measurements comprise the applied voltage and earth-return current, while a separate fast channel records discharge transients. The electrode temperatures and atmospheric conditions are measured throughout the test, and an optical recording is used to capture any visible discharge event. The electrical signals and optical recording use a common time reference so that the applied voltage, current response, and visible discharge development can be compared. Figure 10.3 shows the measurement arrangement.

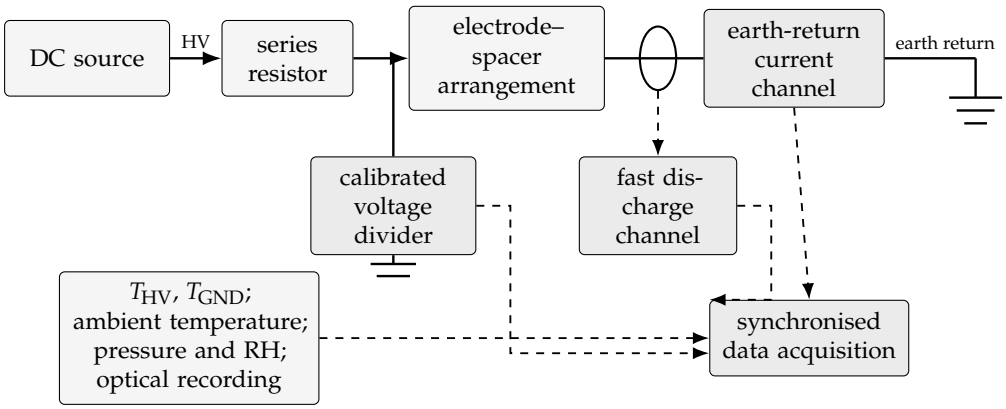


Figure 10.3: Measurement arrangement and synchronised acquisition.

The two electrode temperatures are measured throughout each test. The realised temperature difference is defined as

$$\Delta T = T_{\mathrm{HV}} - T_{\mathrm{GND}}.$$

For a heated condition, the sign of ΔT identifies the thermal-gradient direction, while its magnitude gives the temperature difference between the electrodes. These two temperatures do not define the temperature distribution inside the spacer. Instead, they are used as boundary values for the thermal calculation. The calculated spacer-temperature distribution is then transferred to the electrical model through the one-way thermal–electrical coupling described in Chapter **??**. The resulting time-dependent interface electric field distribution is therefore calculated rather than measured.

The earth-return current is a circuit-level measurement. It can contain bulk conduction through the spacer, surface conduction, gas current, charging current, and stray leakage. It therefore cannot by itself

demonstrate local electric field redistribution or surface-charge accumulation. A separate fast channel records transient discharge signals and, when a disruptive discharge occurs, its associated transient.

The optical recording is synchronised with the electrical measurements. It is used to determine the earliest visible discharge region and the initial visible propagation direction relative to the spacer surface. It does not identify the microscopic inception point. The classification assigned to the observed event is defined separately in Section 10.5.

10.5. Event Classification

Each test is first checked against the prescribed test conditions defined in Section 10.1. It is used in the primary surface-flashover analysis only when those conditions can be verified from the required test record. For a valid test, the optical recording is used to classify the visible discharge path. A *confirmed surface flashover* follows the gas–spacer interface between the main electrodes. A *gas-gap discharge* propagates through the gas away from the spacer surface. A discharge at the feedthrough, chamber wall, support, auxiliary insulation, or other non-target hardware is classified as a *non-target hardware discharge*. An event is classified as *indeterminate* when the visible path cannot be assigned unambiguously to one of these classes; this includes a mixed surface–gas path. A current transient or voltage disturbance alone is not sufficient to classify an event as a surface flashover.

The event classification determines whether the result is treated as an exact surface-flashover observation, a right-censored observation, or an excluded test. Figure 10.4 defines this decision rule.

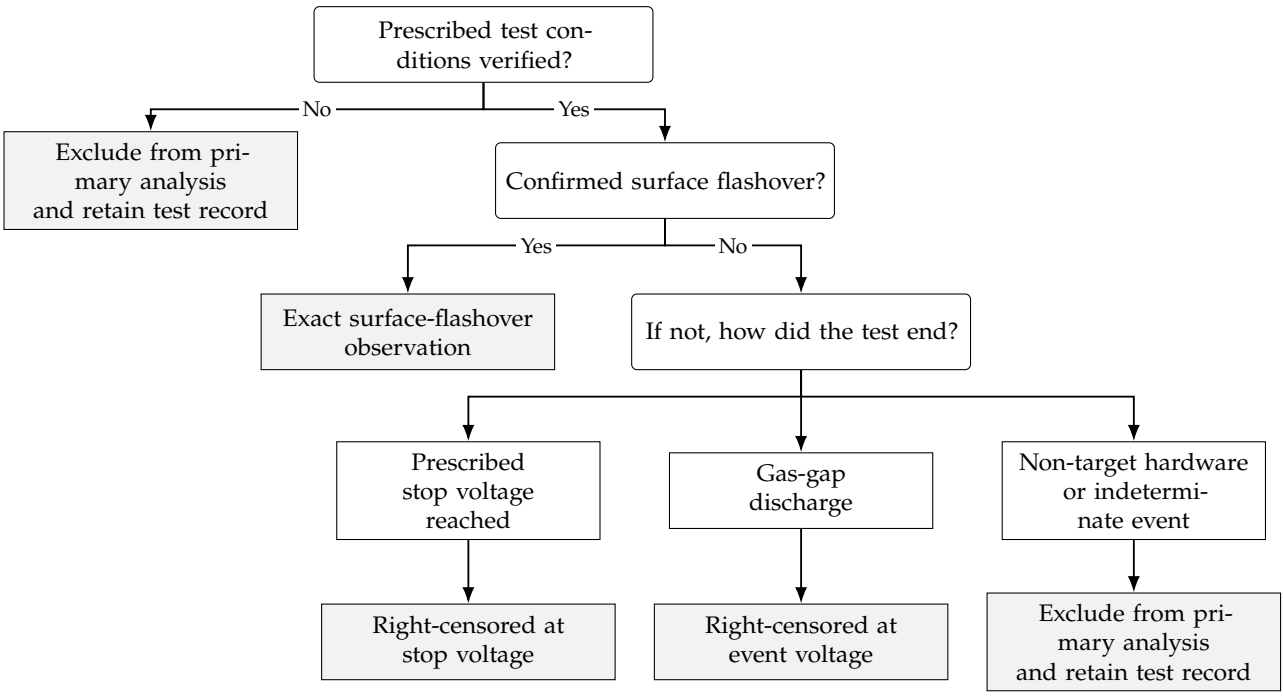


Figure 10.4: Classification and treatment of test outcomes.

Right-censored observations are retained in the statistical analysis following IEC 62539 [57]. Gas-gap discharges are also reported separately for each test condition. For a confirmed surface flashover, the surface-flashover voltage V_F is the measured applied voltage at the event time. The corresponding earliest visible discharge region and initial visible propagation direction are retained for the RQ2 comparison. Records from non-target hardware and indeterminate events remain available for diagnosing the test setup but are not included in the primary surface-flashover analysis.

10.6. Reset Between Tests

After each voltage application, the source is isolated, the high-voltage circuit is discharged through the approved discharge path, and the main electrodes are visibly grounded and shorted. The tested

specimen is removed, and the electrodes, spacer contacts, chamber wall, feedthrough, and auxiliary insulation are inspected for discharge marks, deposits, contamination, or mechanical change. The next specimen is installed according to the specimen rule in Section 10.1. Filtered dry air is then passed through the chamber near atmospheric pressure until the accepted pressure, gas temperature, and relative humidity are restored. The next test begins only after the prescribed electrode temperatures and temperature difference also satisfy their qualified stability criteria. Evacuation is not included in the baseline reset because the chamber has not been qualified for external pressure.

The reset duration is not defined by one fixed waiting time. Koch et al. showed that the outcome of a preceding voltage application can affect subsequent recovery in pressurised SF_6 [82]. Surface-charge decay also depends on the insulating material, gas, enclosure, and initial charge distribution [31]. The published SF_6 waiting times are therefore not transferred to the present atmospheric-air arrangement. The required recovery period is instead established on the realised test bench.

Successive tests are treated as independent only after the prescribed reset has been qualified against a long-reset reference. The measured thermal and environmental quantities and the grounded response of the earth-return-current channel must return to their qualified baseline ranges. This current response is used as a reset indicator, but no absolute current threshold is taken as proof that surface charge or gas-ion populations have fully recovered. Reference tests are used to check that the preceding event type and a further extension of the reset do not produce a practically relevant change in the next result. The detailed qualification, equivalence checks, and ordered-sequence checks are given in Appendix H.

10.7. Test Matrix

The experimental design combines three thermal conditions, two voltage polarities, and three DC pre-stress durations, giving $3 \times 2 \times 3 = 18$ test conditions. The pre-stress durations are 0, 12, and 24 h. The 0 h condition follows the definition in Section 10.3. The 12- and 24 h conditions represent intermediate- and late-duration cases from the time-dependent calculations in Chapter 9; the 24 h condition is not assumed to represent a stationary electric field distribution. Table 10.2 shows the complete matrix and the matched comparisons used for RQ1–RQ3.

Table 10.2: Test matrix and matched comparisons for RQ1–RQ3.

(a) Complete condition matrix

Thermal condition	Positive polarity	Negative polarity
Unheated ambient-temperature reference	0, 12, 24 h	0, 12, 24 h
HV-side heated	0, 12, 24 h	0, 12, 24 h
Grounded-side heated	0, 12, 24 h	0, 12, 24 h

(b) Matched comparisons

Effect examined	Matched comparison	Other research factors kept unchanged
RQ1: thermal condition	Unheated reference ↔ HV-side heated; unheated reference ↔ grounded-side heated	Polarity and DC pre-stress duration
RQ2: voltage polarity	Positive ↔ negative	Thermal condition and DC pre-stress duration
RQ2: thermal-gradient direction	HV-side heated ↔ grounded-side heated	Polarity, DC pre-stress duration, and target $\lvert\Delta T\rvert$
RQ3: DC pre-stress duration	0 h ↔ 12 h; 0 h ↔ 24 h	Thermal condition and polarity

The unheated condition provides the reference for RQ1. Comparison with either heated condition determines how the surface-flashover response changes when the imposed thermal condition is introduced. This comparison includes both temperature elevation and temperature non-uniformity and therefore does not isolate the effect of ∇T from the accompanying change in absolute temperature. The comparison between HV-side and grounded-side heating more directly examines the effect of reversing the thermal-gradient direction at matched target $|\Delta T|$.

A predetermined target number n of valid observations is planned for each test condition. The value of

n is fixed before the main test series. The choice uses preliminary data, the expected scatter and censoring rate, the prescribed confidence level, and the required precision of the primary comparisons [57], [81]. Confirmed surface flashovers and right-censored observations defined in Section 10.5 both remain in the planned dataset. A censored observation is not replaced because it is censored; only tests excluded under the rules of Section 10.5 may be repeated. Observations used for commissioning or preliminary method setting are kept separate from the main research dataset.

The test conditions are distributed over blocks to reduce the influence of test order. Where changing the heated side requires thermal conditions to be grouped, the order of the three thermal groups is rotated between blocks. The six combinations of polarity and DC pre-stress duration are randomised within each thermal group. Observations for each test condition are distributed across blocks rather than collected consecutively. Reset qualification and the checks for independence between successive tests follow Section 10.6 and Appendix H.

10.8. Data Analysis

The exact and right-censored voltage observations defined in Section 10.5 are analysed together. A probability distribution is not selected in advance. Weibull, Gumbel, and lognormal distributions are considered, and censoring is retained in the analysis. A distribution is retained only when the applicable adequacy checks in IEC 62539 indicate that it represents the observations sufficiently well [57]. IEC 62539 is limited in scope to AC voltage testing, but states that its statistical techniques may also be applied to DC failure tests with appropriate care.

When an adequate probability model is obtained, each test condition is described by the 50% surface-flashover voltage V_{50} and the spread of the fitted distribution. A confidence interval is also reported at the confidence level fixed before the main test series. The same confidence level is used for all matched comparisons. Each comparison in Table 10.2 reports the absolute difference in V_{50} and the relative change with respect to the first listed condition. For RQ1 and RQ3, changes in distribution spread are also examined. A fitted spread parameter is compared directly only when the same distribution family adequately represents both matched conditions. The lower-tail quantity V_{10} is reported only when the number and range of observations provide sufficient support for that percentile. If a surface flashover is confirmed but its earliest visible region cannot be resolved, its voltage remains an exact surface-flashover observation for the voltage-distribution analysis. Its RQ2 location is reported as unresolved.

For RQ2, the optical record is evaluated only for confirmed surface flashovers. The earliest visible surface-flashover region is assigned using the interface coordinate s, measured from the HV-side end of the 50 mm exposed spacer interface. Three regions are fixed before the main test series:

$$\begin{aligned} \text{HV-side region:} &\quad 0 \le s \le 10 \text{ mm}, \\ \text{central region:} &\quad 10 < s < 40 \text{ mm}, \\ \text{grounded-side region:} &\quad 40 \le s \le 50 \text{ mm}. \end{aligned}$$

The number and proportion of confirmed surface flashovers first visible in each region are reported for the matched polarity and thermal-gradient-direction comparisons. The initial visible propagation direction is classified as towards increasing s (grounded side), towards decreasing s (HV side), bidirectional, or unresolved. If none of the candidate distributions adequately represents the observations, no model-dependent V_{50} or V_{10} is reported. The exact surface-flashover voltages, censoring voltages, and event counts are reported instead. Gas-gap discharges are not included in the denominator of the surface-flashover-region proportions.

Results obtained for the thermal configuration represented in Chapter 9 may be compared qualitatively with the calculated direction and time dependence of the interface-field redistribution. The calculations use the hot-oil upper thermal-design condition and therefore do not provide a quantitative prediction for every 40–50 K experimental condition or for the surface-flashover event itself. Agreement would indicate consistency with the calculated electric field redistribution, but would not identify the underlying charge-transport mechanism.

10.9. Chapter Conclusions

The experimental method leads to the following conclusions:

1. The proposed test matrix combines thermal condition, voltage polarity, and DC pre-stress duration to address RQ1–RQ3. The unheated-to-heated comparison represents the effect of the complete imposed thermal condition rather than the temperature gradient alone.
2. A surface-flashover voltage is assigned only when the optical record confirms a discharge along the gas-spacer interface. Other test outcomes are treated as censored or excluded according to the predefined classification rules.
3. The reset time between successive tests must be established on the realized test bench. Neither literature waiting times nor an absolute earth-return-current threshold is sufficient to demonstrate independence.
4. The statistical analysis does not assume a probability distribution in advance. Experimental trends may be compared qualitatively with the calculated electric field redistribution, but this comparison cannot identify the underlying charge-transport mechanism.

11

Discussion

This chapter discusses the engineering significance of the test-bench design and the electro-thermal calculations developed in the preceding chapters. The discussion considers whether the design supports controlled comparison of thermal condition, voltage polarity, and DC pre-stress, what the numerical results establish about the intended electrical and thermal behaviour, and which conclusions still require physical qualification or flashover measurements.

11.1. Design Evidence and Experimental Boundary

The principal strength of the test-bench design is that the variables required for the planned comparisons can be changed without intentionally changing the field-defining electrode–spacer arrangement. Either electrode can be heated, voltage polarity can be reversed, and the spacer can be replaced while retaining the same local test geometry. The floating cartridge-heater architecture is the preferred candidate for physical qualification because it avoids the external fluid-circulation system. The hot-oil architecture remains the alternative if the floating-secondary insulation cannot be qualified. These conclusions concern design capability; alignment, sealing, thermal control, and integrated HV performance still require checks on the realised test bench.

Numerical checks support the intended behaviour of the design, but at different levels. The electrode–spacer geometry reproduces the principal interface-field behaviour of the coaxial reference, while the electro-thermal model predicts the temperature distribution and conductivity-driven electric-field redistribution for the represented geometry. The thermal calculation uses a reduced-order representation of heat transfer in the enclosed air. These checks support the design and the numerical calculations, but they do not establish the physical performance of the realised test bench.

The numerical model therefore provides the temperature distribution and the time-dependent electric-field distribution during DC pre-stress; it does not predict the surface-flashover event. A calculated change in interface field is evidence of changed electrical stress, not evidence of a changed surface-flashover voltage distribution or earliest visible discharge region. These experimental outcomes depend on the complete test arrangement and remain to be determined from physical tests.

11.2. DC Pre-Stress and Flashover Interpretation

IEC TS 62271-318 uses the general definition of disruptive discharge for an insulation failure that completely bridges the insulation under test [17]. In the present test method, a confirmed surface flashover is treated as one disruptive-discharge class. Its visible path follows the gas–spacer interface between the main electrodes. Gas-gap and non-target discharges are classified separately. The classification places the target surface-flashover event within the general IEC framework while retaining the distinction required by the test method.

A direct-voltage waveform does not by itself establish a stationary DC electric-field distribution. IEC TS 62271-318 defines DC steady state as the condition in which at least 90% of the resistive field

distribution has been established [17]. The calculations in Chapter 9 show that the approach to this condition is spatially non-uniform. The HV-side field is already close to its stationary value after 12 h, while the grounded-side region continues to change between 12 and 24 h. Complete stationarity over the full interface is therefore not demonstrated within the simulated duration.

The preceding voltage history also affects how a flashover result can be interpreted. Pan et al. obtained their statistical flashover data using a continuous voltage rise from zero at 1 kV/s. The near-flashover surface-charge distribution in the same study was obtained separately using an initial 20 min hold followed by 2 kV voltage steps with further holds [15]. The two procedures establish different electrical histories. The reconstructed charge distribution from the stepwise procedure therefore cannot be assumed to represent the charge condition preceding every continuous-ramp flashover result.

The 0, 12, and 24 h DC pre-stress durations defined for the present test method are comparison conditions rather than assumed stationary states. The 12 and 24 h conditions represent different stages of the calculated electric-field development. The 0 h condition contains no additional hold after the pre-stress voltage is reached. A change in the measured surface-flashover voltage distribution with pre-stress duration would show that the response depends on the preceding electrical history. Such a change would not by itself identify the charge-transport mechanism responsible for that dependence.

11.3. Interpretation of the DC Field Redistribution

The thermal gradient redistributes the calculated electric field along the spacer–gas interface rather than changing it uniformly. In the stationary hot-oil case, the field at the immediate heated HV edge decreases by about 13%. The grounded-side regional maximum increases by about 30%, and the central part of the interface is also more strongly stressed. The calculation therefore indicates redistribution towards the central and grounded-side regions rather than a general reduction of electrical stress.

The HV-edge reduction does not represent the change across the complete HV-side region. The HV-side regional maximum changes only slightly and moves approximately 2.7 mm along the interface from the HV edge. The ratio of the HV-side to grounded-side regional maxima decreases from 1.77 to 1.34. The two end regions therefore become less electrically unequal. The largest calculated regional field nevertheless remains on the HV side.

The calculated redistribution is consistent with the temperature-dependent bulk conductivity represented in the model. The hotter epoxy is more conductive and supports a smaller share of the stationary voltage drop. Electrical stress therefore shifts towards colder parts of the spacer. Liang et al. reported the same broad tendency in a basin-type spacer, where the calculated high-field region shifted towards the colder grounded shell as the conductor-side thermal gradient increased [52]. The comparison supports the direction of the calculated effect, not its magnitude, because the geometries and electrical conditions differ. The quoted changes were obtained for the 60 kV numerical screening case under the hot-oil upper thermal-design condition. The spacer temperature difference in this case is about 74 K. These magnitudes should not be extrapolated quantitatively to the intended 40–50 K experimental conditions.

The transient result shows that thermal and electrical development occur on different time scales. The local midpoint thermal response develops mainly within about one hour, although a slower thermal tail remains. The conductivity-controlled electric-field distribution develops for much longer. The grounded-side field is still about 3.9% below the stationary value after 24 h, while the sampled central response is not monotonic. Thermal stabilisation of the test bench therefore does not imply electrical stationarity of the spacer. The sampled central response also shows that one first-order relaxation description is inadequate for the complete interface.

The remaining 24 h difference may reflect continued physical redistribution, numerical residual, or both. A longer-duration calculation together with numerical-sensitivity checks would be required to separate these contributions. Chapter 9 evaluates electric-field magnitude along the spacer–gas interface rather than a separately extracted tangential component. The calculation therefore describes the broad redistribution of electrical stress. It does not provide a separate tangential-field result and cannot determine the earliest visible discharge region.

11.4. Competing Influences on the Earliest Visible Discharge Region

The conductivity-driven electric-field redistribution cannot by itself determine the earliest visible discharge region. Heating the epoxy changes its conductivity and redistributes the stationary DC electric field towards colder parts of the spacer. Gas heating can act differently because the local gas number density depends on temperature and pressure. These influences need not favour the same interface region. The optical record can therefore be compared with the calculated field redistribution, but it cannot identify microscopic discharge inception or establish one controlling mechanism.

The gas-side influence is also conditional. At fixed pressure, increasing gas temperature reduces the local number density and increases the reduced electric field for a given electric-field magnitude. The chamber pressure may also change during heating, so temperature alone does not define the gas-side electrical condition. Gas temperature, pressure, and local electric field must therefore be considered together. A gas-side contribution could modify or oppose the bulk-conductivity trend, but its magnitude remains experimentally unresolved in the present work.

Published thermal-gradient experiments likewise do not establish a universal hot-side or cold-side rule. Li et al. associated positive streamer development with the larger voltage drop towards the colder grounded region after HV-side heating [10]. Hering et al. observed root points and surface traces in the region towards which their calculated high field had moved after long DC stress [9]. These observations were obtained in different arrangements and under different electrical histories. The earliest visible discharge region should therefore be treated as an experimental result of the complete test condition rather than inferred from thermal-gradient direction alone.

Pan et al. illustrate why a physically reasonable bulk-conductivity field calculation may still be insufficient for flashover interpretation. Their smooth stationary calculation became more uniform as the thermal gradient increased, although the measured flashover strength decreased. When the reconstructed surface-charge distribution obtained close to flashover was included, the calculated local-field trend became consistent with the measured flashover trend [15]. The present electrothermal model has a related limitation: it calculates temperature-dependent bulk-conductivity redistribution but does not calculate the local surface-charge distribution associated with an actual flashover. Agreement between a future optical trend and the calculated redistribution would therefore support consistency with this mechanism, but would not prove that bulk conductivity alone caused the observed change.

Gremaud et al. provide a complementary limitation. Solid conduction alone did not reproduce all long-duration observations in their gas-insulated spacer study, while including a small gas-side current improved agreement [14]. Bulk solid conduction therefore need not describe the complete long-duration electrical behaviour. Surface-flashover voltage and optical observations can reveal systematic dependence on thermal condition, polarity, or DC pre-stress duration. These observations cannot by themselves identify whether the change arose from bulk conduction, surface charge, gas-side transport, or another discharge-related process.

The electrothermal model therefore provides one physically motivated interpretation of the electrical condition established during DC pre-stress. A future experimental trend that follows the calculated redistribution would support consistency with that interpretation, but would not establish causation. Stronger mechanism attribution would require additional evidence, such as surface-charge measurements or suitable current and discharge diagnostics.

Table 11.1 summarises what the principal future observations could support and where their interpretation must stop.

Table 11.1: Interpretation limits for the principal future flashover observations.

Observation	What it would support	What it would not establish
Change in the surface-flashover voltage distribution between matched conditions	The changed test condition affects the flashover response of the complete electrode–spacer arrangement.	Which physical mechanism caused the change.
Dependence of the surface-flashover voltage distribution on DC pre-stress duration	The flashover response depends on the preceding DC pre-stress duration.	Whether the dependence arises from bulk conduction, surface charge, gas-side transport, or another process.
Systematic change in the earliest visible discharge region with polarity or thermal-gradient direction	The changed condition affects where the discharge first becomes optically visible.	The microscopic inception point or a unique physical mechanism.
Change in distribution spread between matched conditions	The changed condition affects the statistical spread of the surface-flashover voltage.	The physical mechanism responsible for the change in spread.
Change in initial visible propagation direction	The changed condition affects the visible development of the discharge after it is first resolved.	The microscopic inception point or the mechanism controlling propagation.

11.5. Uncertainty, Transferability, and Evidence Boundaries

The quantitative interpretation of the electrothermal calculation depends strongly on the adopted epoxy conductivity. The temperature dependence of conductivity sets both the conductivity contrast across the spacer and the time scale of the calculated DC field redistribution. These properties have not been measured for the final spacer material. Specimen-specific interpretation therefore requires measurement of the bulk conductivity and characterisation of the surface conductivity. For the direct electric-field simulation route, IEC TS 62271-318 also requires experimental verification of the simulation, relevant material and gas characterisation, and demonstrated scalability [17]. These steps have not been completed for the present model. Its results therefore remain numerical design evidence rather than experimentally verified predictions of the DC transition time.

Experimental comparability introduces a separate uncertainty. A difference between matched test conditions is interpretable only when uncontrolled variation and carry-over from preceding tests are sufficiently controlled. Koch et al. showed for pressurised SF_6 that the outcome of one voltage application can change the ion density before the next and thereby affect the subsequent breakdown probability [82]. Their numerical waiting times are not applicable to the present air–epoxy arrangement. The reset criterion and test-to-test independence must therefore be established on the realised test bench rather than inferred from a fixed waiting time taken from another gas system.

Transferability must be separated into mechanism-level and quantitative claims. The general mechanism by which temperature-dependent solid conductivity redistributes the stationary DC electric field is relevant beyond the present arrangement. The proposed experiments use a reduced geometry in atmospheric air near 1 bar. They do not reproduce the gas composition, pressure, dimensions, or rated voltage of full-scale HVDC GIS. The 6 bar(g) value is a mechanical design pressure only. It is not the experimental gas condition or evidence of flashover performance at GIS pressure.

The scalability required for direct transfer of the numerical model to full-size DC GIS has not been demonstrated [17]. The present calculations should therefore not be used as a quantitatively validated full-scale field model. Within this boundary, the thesis addresses the main design question through the test-bench design, numerical assessment, and test method. These outputs define how RQ1–RQ3 can be investigated under controlled conditions, but they do not provide experimental answers to those questions. The calculated electric-field distributions provide physically motivated expectations for future measurements rather than measurements of surface-flashover behaviour.

11.6. Chapter conclusions

- The test bench preserves the field-defining electrode–spacer arrangement while polarity, heated side, and spacer specimen are changed; physical qualification is still required.
- At 60 kV, the immediate HV-edge field decreases by about 13% and the grounded-side regional maximum increases by about 30%; the HV side remains dominant.
- Electrical redistribution is slower than the local thermal response. The grounded-side field remains about 3.9% from stationary after 24 h, so complete stationarity is not demonstrated.
- The model resolves conductivity-driven DC field redistribution, not surface-flashover behaviour; flashover-voltage distributions and earliest visible discharge regions require experimental measurement.
- The numerical results are arrangement-specific and are not directly transferable to the intended 40–50 K tests or full-scale HVDC GIS. RQ1–RQ3 remain experimental.

12

Conclusion

The objective of this master thesis, to design and numerically assess a reduced-scale gas–epoxy test bench and to define its qualification requirements and test method, is met. The main thesis question was:

> *What design of a reduced-scale gas–epoxy test bench enables controlled future investigation of RQ1–RQ3 under HVDC GIS-relevant conditions?*

The main conclusions are:

- The developed test bench retains one field-defining electrode–spacer arrangement while voltage polarity, heated side, and DC pre-stress duration can be varied independently. The selected geometry preserves the principal interface-field behaviour of the coaxial reference, with the mean interface field differing by 2.2%, and has a maximum operating voltage of 50 kV DC.
- The scientific contribution is an integrated methodology that combines the common electrode–spacer geometry with controlled thermal loading, time-dependent electrothermal calculation, diagnostic access, and a defined qualification and test method. This provides a common basis for relating the imposed thermal and electrical conditions to comparable future surface-flashover measurements.
- Either electrode can be heated to impose the required 40–50 K temperature difference without changing the electrode–spacer geometry. Two heating concepts were developed: floating cartridge heating is preferred for physical qualification, while hot-oil heating remains the alternative.
- In the 60 kV hot-oil numerical screening case, with the HV electrode heated and the grounded electrode colder, the thermal gradient redistributes the DC interface field. The immediate hot-HV-edge field decreases by about 13%, while the central minimum and grounded-side regional maximum increase by about 38% and 30%, respectively. The HV-to-GND regional-maximum ratio decreases from 1.77 to 1.34, although the largest regional field remains on the HV side.
- Under the same HV-hot/GND-cold condition, field formation is strongly position dependent. Between 1 and 12 h, the interval-based apparent relaxation times are about 3.2 h on the hot HV side and 15.8 h on the colder grounded side. The HV-side field is close to stationary after 12 h, whereas the grounded-side deviation remains about 3.9% after 24 h. Together with the non-monotonic central response, this shows that one common relaxation time cannot describe field formation along the complete interface. DC pre-stress duration must therefore be controlled in future tests.
- The developed test bench and test method establish the experimental basis for RQ1–RQ3. They enable controlled comparison of thermal gradient, polarity, thermal-gradient direction, and DC pre-stress duration so that their effects on surface-flashover voltage and the earliest visible discharge region can be determined experimentally.

Manufacture and physical qualification are the next steps before these measurements are carried out.

12.1. Recommendations

The following work is recommended:

- **Construct and qualify the test bench.** Manufacture the proposed test bench and verify its electrical, thermal, mechanical, and measurement performance before flashover testing.
- **Carry out the experiments for RQ1–RQ3.** Use the defined test method to determine the effects of thermal gradient, polarity, thermal-gradient direction, and DC pre-stress duration on surface-flashover behaviour.
- **Extend the simulation model.** Include surface-charge transport, gas-ion transport, and relevant charge injection or trapping mechanisms to obtain a more complete description of DC field development along the spacer interface.

References

[1] European Network of Transmission System Operators for Electricity (ENTSO-E), "Opportunities for a more efficient european power system by 2050: Infrastructure gaps report, TYNDP 2024," European Network of Transmission System Operators for Electricity (ENTSO-E), Infrastructure Gaps Report, Apr. 9, 2025. Accessed: Jun. 25, 2026. [Online]. Available: https://eepublicdownloads.blob.core.windows.net/public-cdn-container/tyndp-documents/TYNDP2024/foropinion/Infrastructure_Gaps_Report.pdf.

[2] European Network of Transmission System Operators for Electricity (ENTSO-E), "Offshore network development plans 2024: European offshore network transmission infrastructure needs, Pan-european summary," European Network of Transmission System Operators for Electricity (ENTSO-E), TYNDP 2024 Report, Jan. 2024. Accessed: Jun. 25, 2026. [Online]. Available: https://www.entsoe.eu/publications/ondp2024/web_entso-e_ONDP_PanEU_240226.pdf.

[3] European Network of Transmission System Operators for Electricity (ENTSO-E), "Technology factsheets," European Network of Transmission System Operators for Electricity (ENTSO-E), Technical report, Mar. 2021.

[4] T. S. Sudarshan and R. A. Dougal, "Mechanisms of surface flashover along solid dielectrics in compressed gases: A review," *IEEE Transactions on Electrical Insulation*, vol. 21, no. 5, pp. 727–746, 1986. DOI: 10.1109/TEI.1986.348922.

[5] A. Winter and J. Kindersberger, "Transient field distribution in gas-solid insulation systems under DC voltages," *IEEE Transactions on Dielectrics and Electrical Insulation*, vol. 21, no. 1, pp. 116–128, Feb. 2014. DOI: 10.1109/TDEI.2013.004110. [Online]. Available: https://doi.org/10.1109/TDEI.2013.004110.

[6] A. Winter and J. Kindersberger, "Stationary resistive field distribution along epoxy resin insulators in air under DC voltage," *IEEE Transactions on Dielectrics and Electrical Insulation*, vol. 19, no. 5, pp. 1732–1739, Oct. 2012. DOI: 10.1109/TDEI.2012.6311522. [Online]. Available: https://doi.org/10.1109/TDEI.2012.6311522.

[7] M. Schueller, U. Straumann, and C. M. Franck, "Time dependence of spacer charging in SF6 under DC stress," Conference paper, Oct. 2012, ISBN: 9781467312523. DOI: 10.3929/ethz-b-000059497. [Online]. Available: https://doi.org/10.3929/ethz-b-000059497.

[8] CIGRE Working Group D1.03, "Gas insulated system for HVDC: DC stress at DC and AC systems," CIGRE, Technical Brochure 506, Aug. 2012, 79 pp. Accessed: Jul. 14, 2026. [Online]. Available: https://www.e-cigre.org/publications/detail/506-gas-insulated-system-for-hvdc-dc-stress-at-dc-and-ac-systems.html.

[9] M. Hering, R. Gremaud, J. Speck, S. Großmann, and U. Riechert, "Flashover behaviour of insulators with inhomogeneous temperature distribution in gas insulated systems under DC voltage stress," in *2014 IEEE International Conference on High Voltage Engineering and Application (ICHVE)*, (Poznań, Poland), IEEE, 2014, pp. 1–4, ISBN: 978-1-4799-6613-4. DOI: 10.1109/ICHVE.2014.7035430. [Online]. Available: https://doi.org/10.1109/ICHVE.2014.7035430.

[10] C. Li, J. Hu, C. Lin, and J. He, "The potentially neglected culprit of DC surface flashover: Electron migration under temperature gradients," *Scientific Reports*, vol. 7, no. 1, pp. 1–11, Jun. 12, 2017, Art. no. 3271, ISSN: 2045-2322. DOI: 10.1038/s41598-017-03657-1. [Online]. Available: https://doi.org/10.1038/s41598-017-03657-1.

[11] M. Schueller, U. Straumann, and C. M. Franck, "Role of ion sources for spacer charging in SF_6 gas insulated HVDC systems," *IEEE Transactions on Dielectrics and Electrical Insulation*, vol. 21, no. 1, pp. 352–359, Feb. 2014, ISSN: 1070-9878. DOI: 10.1109/TDEI.2013.004019. [Online]. Available: https://doi.org/10.1109/TDEI.2013.004019.

[12] M. Schueller, R. Gremaud, C. B. Doiron, and C. M. Franck, "Micro discharges in HVDC gas insulated systems," *IEEE Transactions on Dielectrics and Electrical Insulation*, vol. 22, no. 5, pp. 2879–2888, Oct. 2015, ISSN: 1070-9878. DOI: 10.1109/TDEI.2015.004835.

[13] Y. Gao et al., "Surface charge distribution measurement before and after DC flashover: A novel insight to the influence of surface charge on flashover voltage," in *2018 IEEE International Conference on High Voltage Engineering and Application (ICHVE)*, Athens, Greece, Sep. 2018, pp. 1–4. DOI: 10.1109/ICHVE.2018.8642199.

[14] R. Gremaud et al., "Solid-gas insulation in HVDC gas-insulated system: Measurement, modeling and experimental validation for reliable operation," in *Proceedings of the 46th CIGRE Session*, (Paris, France), CIGRE, Aug. 2016, D1-101. [Online]. Available: https://www.e-cigre.org/publications/detail/d1-101-2016-solid-gas-insulation-in-hvdc-gas-insulated-system-measurement-modeling-and-experimental-validation-for-reliable-operation.html.

[15] C. Pan et al., "Contribution of temperature gradient to insulation performance of disk-insulator at DC voltage—part II: Surface flashover properties," *IEEE Transactions on Dielectrics and Electrical Insulation*, vol. 33, no. 2, pp. 1430–1439, Apr. 2026, First published online in 2025, ISSN: 1070-9878. DOI: 10.1109/TDEI.2025.3614138. [Online]. Available: https://doi.org/10.1109/TDEI.2025.3614138.

[16] A. P. Purnomoadi, A. R. Mor, and J. J. Smit, "Spacer flashover in gas insulated switchgear (GIS) with humid SF6 under different electrical stresses," *International Journal of Electrical Power and Energy Systems*, vol. 116, p. 105 559, Mar. 2020, ISSN: 0142-0615. DOI: 10.1016/j.ijepes.2019.105559.

[17] *High-voltage switchgear and controlgear — part 318: DC gas-insulated metal-enclosed switchgear for rated voltages including and above 100 kV*, Geneva, Switzerland: International Electrotechnical Commission, Sep. 2024. Accessed: Jun. 25, 2026. [Online]. Available: https://webstore.iec.ch/en/publication/66210.

[18] A. K"uchler, *High Voltage Engineering: Fundamentals – Technology – Applications*. Berlin, Heidelberg: Springer Vieweg, 2017, ISBN: 978-3-642-11992-7. DOI: 10.1007/978-3-642-11993-4.

[19] S. Nijdam, J. Teunissen, and U. Ebert, "The physics of streamer discharge phenomena," *Plasma Sources Science and Technology*, vol. 29, no. 10, p. 103 001, 2020. DOI: 10.1088/1361-6595/abaa05.

[20] A. Iqbal et al., "Influence of discharge polarity on streamer breakdown criterion of ambient air in a non-uniform electric field," *Journal of Physics D: Applied Physics*, vol. 56, no. 3, p. 035 204, 2023. DOI: 10.1088/1361-6463/aca2b4.

[21] R. Nakane, K. Takabayashi, K. Kato, and H. Okubo, "Electric field analysis and electrical insulation performance for gas-solid composite insulation in HVDC-GIS," in *Proceedings of the 20th International Symposium on High Voltage Engineering*, Paper ISH2017-247, Buenos Aires, Argentina: ISH, Aug. 2017. Accessed: Jul. 14, 2026. [Online]. Available: https://www.e-cigre.org/publications/detail/ish2017-247-electric-field-analysis-and-electrical-insulation-performance-for-gas-solid-composite-insulation-in-hvdc-gis.html.

[22] E. Volpov, "Dielectric strength coordination and generalized spacer design rules for HVAC/DC SF6 gas insulated systems," *IEEE Transactions on Dielectrics and Electrical Insulation*, vol. 11, no. 6, pp. 949–963, Dec. 2004, ISSN: 1070-9878. DOI: 10.1109/TDEI.2004.1387818. [Online]. Available: https://ieeexplore.ieee.org/document/1387818.

[23] B. Lutz and J. Kindersberger, "Surface charge accumulation on cylindrical polymeric model insulators in air: Simulation and measurement," *IEEE Transactions on Dielectrics and Electrical Insulation*, vol. 18, no. 6, pp. 2040–2048, Dec. 2011. DOI: 10.1109/TDEI.2011.6118642. [Online]. Available: https://doi.org/10.1109/TDEI.2011.6118642.

[24] T. Yasuoka, Y. Hoshina, M. Shiiki, M. Takei, A. Kumada, and K. Hidaka, "Insulation characteristics in DC-GIS: Surface charge phenomena on epoxy spacer and metallic particle motions," in *Proceedings of the CIGRE Session 2018*, Paper D1-103, Paris, France: CIGRE, Aug. 2018. Accessed: Jul. 14, 2026. [Online]. Available: https://www.e-cigre.org/publications/detail/d1-103-2018-insulation-characteristics-in-dc-gis-surface-charge-phenomena-on-epoxy-spacers-and-metallic-particle-motions.html.

[25] M. Schueller, R. Gremaud, C. B. Doiron, and C. M. Franck, "Micro discharges in HVDC gas insulated systems," *IEEE Transactions on Dielectrics and Electrical Insulation*, vol. 22, no. 5, pp. 2879–2888, Oct. 2015. DOI: 10.1109/TDEI.2015.004835. [Online]. Available: https://doi.org/10.1109/TDEI.2015.004835.

[26] R. Suda et al., "Charge accumulation phenomena of silica-filled epoxy resin spacer under DC field," in *Proceedings of the 19th International Symposium on High Voltage Engineering*, Paper ISH2015-318, Pilsen, Czech Republic, Aug. 2015.

[27] K. Nakanishi, A. Yoshioka, Y. Arahata, and Y. Shibuya, "Surface charging on epoxy spacer at DC stress in compressed SF6 gas," *IEEE Transactions on Power Apparatus and Systems*, vol. PAS-102, no. 12, pp. 3919–3927, 1983, ISSN: 0018-9510. DOI: 10.1109/TPAS.1983.317931.

[28] K. J. Åström, *Control system design: Lecture notes for me 155a*, Department of Mechanical and Environmental Engineering, University of California, Santa Barbara, 2002.

[29] H. Fujinami, T. Takuma, M. Yashima, and T. Kawamoto, "Mechanism and effect of DC charge accumulation on SF6 gas insulated spacers," *IEEE Power Engineering Review*, vol. 9, no. 7, p. 62, 1989, ISSN: 0272-1724. DOI: 10.1109/MPER.1989.4310816. [Online]. Available: https://ieeexplore.ieee.org/document/4310816.

[30] J. Kindersberger and C. Lederle, "Surface charge decay on insulators in air and sulfurhexafluorid—part I: Simulation," *IEEE Transactions on Dielectrics and Electrical Insulation*, vol. 15, no. 4, pp. 941–948, Aug. 2008. DOI: 10.1109/TDEI.2008.4591214. [Online]. Available: https://doi.org/10.1109/TDEI.2008.4591214.

[31] J. Kindersberger and C. Lederle, "Surface charge decay on insulators in air and sulfurhexafluorid – part II: Measurements," *IEEE Transactions on Dielectrics and Electrical Insulation*, vol. 15, no. 4, pp. 949–957, Aug. 2008, ISSN: 1070-9878. DOI: 10.1109/TDEI.2008.4591215.

[32] M. Hallas, M. Kosse, K. Juhre, M. Secklehner, and V. Hinrichsen, "Determination of AC test currents for thermo-electric laboratory stresses on gas-insulated HVDC systems," in *Proceedings of the 2020 Virtual CIGRE Canada Conference and Expo*, (Toronto, Canada), CIGRE, Oct. 2020. DOI: 10.26083/tuprints-00014130. [Online]. Available: https://doi.org/10.26083/tuprints-00014130.

[33] U. Straumann, M. Schuller, and C. M. Franck, "Theoretical investigation of HVDC disc spacer charging in SF6 gas insulated systems," *IEEE Transactions on Dielectrics and Electrical Insulation*, vol. 19, no. 6, pp. 2196–2205, 2013, ISSN: 1070-9878. DOI: 10.1109/TDEI.2012.6396980.

[34] X. Li, S. Han, W. Wang, Z. Geng, and X. Lin, "Influence of volume and surface conductivity on the transient surface charge characteristics of DC-GIL insulator under thermal–electric coupled fields," *IET Science, Measurement and Technology*, vol. 16, no. 8, pp. 479–490, Oct. 2022, ISSN: 1751-8830. DOI: 10.1049/smt2.12121.

[35] Y. Luo, J. Tang, Z. Pan, and C. Pan, "How temperature and pressure affect the electric field distribution in HVDC GIS/GIL: A numerical study," *IEEE Transactions on Dielectrics and Electrical Insulation*, vol. 28, no. 4, pp. 1334–1342, Aug. 2021. DOI: 10.1109/TDEI.2021.009452. [Online]. Available: https://doi.org/10.1109/TDEI.2021.009452.

[36] C. Li, J. Hu, C. Lin, and J. He, "The potentially neglected culprit of dc surface flashover: Electron migration under temperature," *Scientific reports*, vol. 7, 1 Dec. 2017, ISSN: 2045-2322. DOI: 10.1038/S41598-017-03657-1. [Online]. Available: https://pubmed.ncbi.nlm.nih.gov/28607418/.

[37] U. Riechert, U. Straumann, R. Gremaud, and M. Callavik, "Compact gas-insulated systems for high voltage direct current transmission: Design and testing," in *IEEE/PES Transmission and Distribution Conference and Exposition*, vol. 2016-July, Institute of Electrical and Electronics Engineers Inc., Jul. 2016, ISBN: 9781509021574. DOI: 10.1109/TDC.2016.7520069.

[38] J. J. Lowke, "Theory of electrical breakdown in air—the role of metastable oxygen molecules," *Journal of Physics D: Applied Physics*, vol. 25, no. 2, pp. 202–210, 1992. DOI: 10.1088/0022-3727/25/2/012. [Online]. Available: https://doi.org/10.1088/0022-3727/25/2/012.

[39] R. Morrow and J. J. Lowke, "Electrical breakdown in air and in SF6," *Australian Journal of Physics*, vol. 48, pp. 453–460, 1995. DOI: 10.1071/PH950453. [Online]. Available: https://doi.org/10.1071/PH950453.

[40] M. Hering, J. Speck, S. Grossmann, and U. Riechert, "Influence of gas temperature on the breakdown voltage in gas-insulated systems," *IEEE Transactions on Dielectrics and Electrical Insulation*, vol. 24, no. 1, pp. 401–408, 2017, ISSN: 1070-9878. DOI: 10.1109/TDEI.2016.006099.

[41] P. Han et al., "Contribution of temperature gradient to insulation performance of disc-insulator at dc voltage-part i: Surface charge accumulation," *IEEE Transactions on Dielectrics and Electrical Insulation*, 2025, ISSN: 15584135. DOI: 10.1109/TDEI.2025.3616953. [Online]. Available: https://ieeexplore.ieee.org/document/11192564.

[42] Huntsman Corporation, *ARALDITE CY 5910 / ARADUR HY 1102 / ACCELERATOR DY 062 / ARALDITE DW 9134 / Silica Flour*, Technical product data, Breakdown strength: 26–29 kV/mm for a 3 mm specimen, tested according to IEC 60243-1. Accessed: Jul. 31, 2026. [Online]. Available: https://products.huntsman.com/products/araldite-cy-5910-silica.

[43] M. S. Chung, B.-G. Yoon, P. H. Cutler, and N. M. Miskovsky, "Theoretical analysis of the enhanced electric field at the triple junction," *Journal of Vacuum Science & Technology B*, vol. 22, no. 3, pp. 1240–1243, 2004. DOI: 10.1116/1.1689309. [Online]. Available: https://doi.org/10.1116/1.1689309.

[44] B. Qi, C. Gao, C. Li, and J. Xiong, "The influence of surface charge accumulation on flashover voltage of GIS/GIL basin insulator under various voltage stresses," *International Journal of Electrical Power & Energy Systems*, vol. 105, pp. 514–520, Feb. 2019, ISSN: 0142-0615. DOI: 10.1016/j.ijepes.2018.08.036.

[45] M. Hering, J. Speck, S. Großmann, and U. Riechert, "Field transition in gas-insulated HVDC systems," *IEEE Transactions on Dielectrics and Electrical Insulation*, vol. 24, no. 3, pp. 1608–1616, Jun. 2017, ISSN: 1070-9878. DOI: 10.1109/TDEI.2017.006534.

[46] F. Yildirim and C. Korasli, "Statistical approach for determining breakdown voltage of gas-insulated cables," Tech. Rep., 1992. [Online]. Available: https://ieeexplore-ieee-org.tudelft.idm.oclc.org/document/204870.

[47] R. Gremaud et al., "Surface charge decay on HVDC insulators: Temperature and field effects," in *2013 IEEE International Conference on Solid Dielectrics (ICSD)*, (Bologna, Italy), IEEE, 2013, pp. 1056–1059. DOI: 10.1109/ICSD.2013.6619685. [Online]. Available: https://doi.org/10.1109/ICSD.2013.6619685.

[48] T. Wendel, J. Kindersberger, and M. Hering, "Influence of field strength and temperature on the space charge distribution in epoxy under DC stress," in *2018 IEEE International Conference on High Voltage Engineering and Application (ICHVE)*, (Athens, Greece, Sep. 10–13, 2018), IEEE, 2018, pp. 1–4, ISBN: 978-1-5386-5086-8. DOI: 10.1109/ICHVE.2018.8641892. [Online]. Available: https://doi.org/10.1109/ICHVE.2018.8641892.

[49] M. Hallas, M. Kosse, K. Juhre, M. Secklehner, and V. Hinrichsen, "Determination of AC test currents for thermo-electric laboratory stresses on gas-insulated HVDC systems," in *CIGRE Canada Conference*, Oct. 2020. [Online]. Available: https://tuprints.ulb.tu-darmstadt.de/14130/1/2020.07.17%20Cigre%20Canada.pdf.

[50] G.-m. Ma et al., "Measurement and simulation of charge accumulation on a disc spacer with electro-thermal stress in SF_6 gas," *IEEE Transactions on Dielectrics and Electrical Insulation*, vol. 25, no. 4, pp. 1221–1229, Aug. 2018, ISSN: 1070-9878. DOI: 10.1109/TDEI.2018.007141. [Online]. Available: https://doi.org/10.1109/TDEI.2018.007141.

[51] P. Han et al., "Contribution of temperature gradient to insulation performance of disk-insulator at DC voltage—part I: Surface charge accumulation," *IEEE Transactions on Dielectrics and Electrical Insulation*, vol. 33, no. 2, pp. 1420–1429, Apr. 2026, First published online in 2025, ISSN: 1070-9878. DOI: 10.1109/TDEI.2025.3616953. [Online]. Available: https://doi.org/10.1109/TDEI.2025.3616953.

[52] H. Liang, W. Li, H. Yao, and B. Du, "DC/AC electric field regulation by functionally graded spacers under temperature gradients," *IET Science, Measurement & Technology*, vol. 19, no. 1, Nov. 29, 2025, Art. no. e70037, ISSN: 1751-8822. DOI: 10.1049/smt2.70037. [Online]. Available: https://doi.org/10.1049/smt2.70037.

[53] B. Zhang, Z. Qi, and G. Zhang, "Thermal gradient effects on surface charge of HVDC spacer in gas insulated system," in *2016 IEEE Conference on Electrical Insulation and Dielectric Phenomena (CEIDP)*, (Toronto, Canada), IEEE, 2016, pp. 703–706. DOI: 10.1109/CEIDP.2016.7785563. [Online]. Available: https://doi.org/10.1109/CEIDP.2016.7785563.

[54] Q. Hu, Q. Li, Z. Liu, N. Xue, J. Wang, and M. Haddad, "Surface charge accumulation characteristics on DC GIL three-post insulators considering the influence of temperature gradient," *CSEE Journal of Power and Energy Systems*, vol. 9, no. 5, pp. 1926–1934, Sep. 2023, ISSN: 2096-0042. DOI: 10.17775/CSEEJPES.2021.09240. [Online]. Available: https://doi.org/10.17775/CSEEJPES.2021.09240.

[55] H.-y. Zhou, G.-m. Ma, C.-r. Li, C. Shi, and S.-c. Qin, "Impact of temperature on surface charges accumulation on insulators in SF_6-filled DC-GIL," *IEEE Transactions on Dielectrics and Electrical Insulation*, vol. 24, no. 1, pp. 601–610, Feb. 2017, ISSN: 1070-9878. DOI: 10.1109/TDEI.2016.005838. [Online]. Available: https://doi.org/10.1109/TDEI.2016.005838.

[56] S. Zhao, J. Kindersberger, M. Hering, and K. Juhre, "Measurement of surface potential at the gas–solid interface for validating electric field simulations in gas-insulated DC systems," in *Proceedings of the 47th CIGRE Session*, (Paris, France, Aug. 26–31, 2018), CIGRE, Aug. 2018, D1-102. [Online]. Available: https://www.e-cigre.org/publications/detail/d1-102-2018-measurement-of-surface-potential-at-the-gas-solid-interface-for-validating-electric-field-simulations-in-gas-insulated-dc-systems.html.

[57] IEC, "Guide for the statistical analysis of electrical insulation breakdown data," International Electrotechnical Commission, Tech. Rep. IEC 62539:2007 (IEEE 930), 2007.

[58] International Electrotechnical Commission, *High-voltage switchgear and controlgear – part 1: Common specifications for alternating current switchgear and controlgear*, International Electrotechnical Commission, 2021.

[59] International Electrotechnical Commission, *High-voltage test techniques – part 1: General terminology and test requirements*, International Electrotechnical Commission, Apr. 2025. [Online]. Available: https://webstore.iec.ch/en/publication/65088.

[60] H. Li, "Characterisation of HVDC gas insulated systems," PhD thesis, Cardiff University, Cardiff, United Kingdom, Aug. 2023.

[61] J. L. Davidson, T. J. Williams, and A. G. Bailey, "Electrostatic discharges between charged insulators and grounded spheres," *Journal of Electrostatics*, vol. 56, no. 1, pp. 29–42, 2002. DOI: 10.1016/S0304-3886(01)00202-9.

[62] A. H. Cookson, "Recent progress in high-voltage gas breakdown," in *Proceedings of the 3rd International Conference on Properties and Applications of Dielectric Materials*, Tokyo, Japan, Jul. 1991, p. 62. DOI: 10.1109/ICPADM.1991.172075.

[63] T. Hasegawa, K. Yamaji, M. Hatano, H. Aoyagi, Y. Taniguchi, and A. Kobayashi, "DC dielectric characteristics and conception of insulation design for DC GIS," *IEEE Transactions on Power Delivery*, vol. 11, no. 4, pp. 1776–1782, 1996, ISSN: 0885-8977. DOI: 10.1109/61.544257. [Online]. Available: https://ieeexplore.ieee.org/document/544257.

[64] Z. Huang, Y. Zhang, H. Wang, and J. Li, "Improved electrical resistivity-temperature characteristics of oriented hBN composites for inhibiting temperature-dependence DC surface breakdown," *Applied Physics Letters*, vol. 123, no. 10, Sep. 2023, ISSN: 0003-6951. DOI: 10.1063/5.0166638.

[65] SMC Corporation, *High purity fluoropolymer tubing TL/TIL series: Super PFA*, Manufacturer catalogue, TL0604 specifications. Accessed: Jul. 25, 2026. [Online]. Available: https://www.smcworld.com/catalog/en/fitting_tube/TL-TIL-E/6-7-p0501-0514-tl-th-td_en/data/6-7-p0501-0514-tl-th-td_en.pdf.

[66] The Dow Chemical Company, *XIAMETER pmx-200 silicone fluid, 5–20 cst*, Technical Data Sheet, Form No. 95-515-01 B, 2017. Accessed: Jul. 25, 2026. [Online]. Available: https://www.dow.com/documents/95/95-0/95-515-xiameter-pmx-200-si-fluid1.pdf.

[67] The Dow Chemical Company, *Typical properties of dow silicone fluids*, Form No. 01-4678-01, 2019. Accessed: Jul. 25, 2026. [Online]. Available: https://www.dow.com/documents/01/01-4678-01-typical-properties-of-dow-silicone-fluids.pdf.

[68] Nexans. "HFIX stranded - 4 mm^2." Nexans reference 84009100, Accessed: Jul. 25, 2026. [Online]. Available: https://www.nexans.co.kr/en/products/Building/HFIX-450-723283/product~84009100~.html.

[69] ERIKS, *PMMA datasheet*, ERIKS. Accessed: Jun. 19, 2026. [Online]. Available: https://static.eriksgroup.com/nl-be/datasheets/transparante%20kunststoffen/eriks%20-%20pmma%20datasheet.pdf.

[70] Victrex plc, *VICTREX PEEK polymer: Material properties guide*, Technical properties guide, Victrex plc, 2020. Accessed: Jun. 19, 2026. [Online]. Available: https://www.victrex.com/-/media/downloads/materials-properties/material-properties-guide_us-4-20.pdf.

[71] Parker Hannifin Corporation, *O-Ring Handbook*, PTD 5705 EN, PDF edition 09/2025, Parker Prädifa Technology Division, Sep. 2025. Accessed: Jun. 19, 2026. [Online]. Available: https://www.parker.com/content/dam/Parker-com/Literature/Praedifa/Catalogs/Catalog_O-Ring-Handbook_PTD5705-EN.pdf.

[72] Parker Hannifin Corporation, *PTFE Seals: Design Guide*, PTD 3354 EN, PDF edition 03/2024, Parker Prädifa Technology Division, Mar. 2024. Accessed: Jun. 19, 2026. [Online]. Available: https://www.parker.com/content/dam/Parker-com/Literature/Praedifa/Catalogs/Catalog_PTFE-Seals_PTD3354-EN.pdf.

[73] S. M. ElSherbiny, G. D. Raithby, and K. G. T. Hollands, "Heat transfer by natural convection across vertical and inclined air layers," *Journal of Heat Transfer*, vol. 104, no. 1, pp. 96–102, 1982. DOI: 10.1115/1.3245075.

[74] E. Seran, M. Godefroy, E. Pili, N. Michielsen, and S. Bondiguel, "What we can learn from measurements of air electric conductivity in 222rn-rich atmosphere," *Earth and Space Science*, vol. 4, no. 2, pp. 91–106, 2017. DOI: 10.1002/2016EA000241.

[75] N. Zebouchi, H. Li, and M. A. Haddad, "Development of future compact and eco-friendly hvdc gas-insulated systems: Shape optimization of a dc spacer model and novel materials investigation," *Energies*, vol. 13, no. 12, p. 3288, 2020. DOI: 10.3390/en13123288.

[76] Joint Committee for Guides in Metrology, "Evaluation of measurement data—guide to the expression of uncertainty in measurement," Joint Committee for Guides in Metrology, Tech. Rep. JCGM 100:2008, 2008. DOI: 10.59161/JCGM100-2008E. [Online]. Available: https://www.bipm.org/en/doi/10.59161/jcgm100-2008e.

[77] American Society of Mechanical Engineers, *Standard for verification and validation in computational fluid dynamics and heat transfer*, ASME V&V 20-2009, American Society of Mechanical Engineers, 2009. [Online]. Available: https://www.asme.org/codes-standards/find-codes-standards/standard-for-verification-and-validation-in-computational-fluid-dynamics-and-heat-transfer.

[78] International Electrotechnical Commission, *High-voltage test techniques—part 2: Measuring systems*, IEC 60060-2:2025, International Electrotechnical Commission, Apr. 2025. [Online]. Available: https://webstore.iec.ch/en/publication/107039.

[79] International Organization for Standardization, *Non-destructive testing—leak testing—tracer gas method*, ISO 20485:2017, International Organization for Standardization, 2017. [Online]. Available: https://www.iso.org/standard/68190.html.

[80] European Committee for Electrotechnical Standardization, *Erection and operation of electrical test equipment*, EN 50191:2010, CENELEC, 2010.

[81] W. Hauschild and W. Mosch, *Statistical Techniques for High-Voltage Engineering* (IEE Power Series 13), trans. by P. Perkins. London, United Kingdom: Peter Peregrinus Ltd., 1992, ISBN: 978-0-86341-205-9.

[82] M. Koch, U. Straumann, and C. M. Franck, "Determination of waiting times between successive breakdown experiments," in *2012 Annual Report Conference on Electrical Insulation and Dielectric Phenomena*, IEEE, 2012, pp. 349–352. DOI: 10.1109/CEIDP.2012.6378792.

[83] A. H. Cookson, "Review of high voltage gas breakdown and flashover of insulators in compressed sulfur hexafluoride," in *Proceedings of the 3rd International Conference on Properties and Applications of Dielectric Materials*, vol. 1, IEEE, 1991, pp. 369–376, ISBN: 0-87942-569-5.

[84] X. Li, M. Wan, W. Wang, Z. Geng, and X. Lin, "Temperature and electric field distribution of tri-post insulator in DC-GIL based on numerical multiphysics modelling," *IET Generation, Transmission & Distribution*, vol. 17, no. 6, pp. 1232–1242, Mar. 2023. DOI: 10.1049/gtd2.12729.

[85] A. De Lorenzi, L. Grando, A. Pesce, P. Bettini, and R. Specogna, "Modeling of epoxy resin spacers for the 1 MV DC gas insulated line of ITER neutral beam injector system," *IEEE Transactions on Dielectrics and Electrical Insulation*, vol. 16, no. 1, pp. 77–87, Feb. 2009, ISSN: 1070-9878. DOI: 10.1109/TDEI.2009.4784554.

[86] H. Y. Zhou, G. M. Ma, C. R. Li, C. Shi, and S. C. Qin, "Impact of temperature on surface charges accumulation on insulators in SF6-filled DC-GIL," *IEEE Transactions on Dielectrics and Electrical Insulation*, vol. 24, no. 1, pp. 601–610, Feb. 2017, ISSN: 1070-9878. DOI: 10.1109/TDEI.2016.005838. [Online]. Available: https://ieeexplore.ieee.org/document/7873520.

[87] I. M. Bortnik and C. M. Cooke, "Electrical breakdown and the similarity law in SF6 at extra-high-voltages," *IEEE Transactions on Power Apparatus and Systems*, vol. PAS-91, no. 5, pp. 2196–2203, Sep. 1972. DOI: 10.1109/TPAS.1972.293203.

[88] H. Y. Zhou, G. M. Ma, C. R. Li, C. Shi, and S. C. Qin, "Impact of temperature on surface charges accumulation on insulators in SF6-filled DC-GIL," *IEEE Transactions on Dielectrics and Electrical Insulation*, vol. 24, no. 1, pp. 601–610, Feb. 2017, ISSN: 1070-9878. DOI: 10.1109/TDEI.2016.005838.

[89] T. Hasegawa, F. Endo, K. Yamaji, T. Rokunohe, M. Hatano, and T. Yamagiwa, "Development of insulation structure and enhancement of insulation reliability of 500 kv dc GIS," *IEEE Transactions on Power Delivery*, vol. 12, no. 1, pp. 194–202, 1997, ISSN: 0885-8977. DOI: 10.1109/61.568241. [Online]. Available: https://ieeexplore.ieee.org/document/568241.

[90] CIGRE JWG D1/B3.57, "Dielectric testing of gas-insulated HVDC systems," CIGRE, Technical Brochure 842, Sep. 2021. [Online]. Available: https://www.e-cigre.org/publications/detail/842-dielectric-testing-of-gasinsulated-hvdc-systems.html.

[91] International Electrotechnical Commission, *High-voltage switchgear and controlgear – part 203: Gas-insulated metal-enclosed switchgear for rated voltages above 52 kv*, International Electrotechnical Commission, 2022.

[92] D. Alperin, "The effect of heat flux on heat transfer oil," M.S. thesis, Texas Tech University, Dec. 1986.

[93] International Electrotechnical Commission, *Electric strength of insulating materials – test methods – part 1: Tests at power frequencies*, International Electrotechnical Commission, Mar. 2013. [Online]. Available: https://webstore.iec.ch/en/publication/1101.

[94] V. Rudnev, D. Loveless, and R. L. Cook, *Handbook of Induction Heating*, 2nd ed. CRC Press, 2017, ISBN: 9781466553958. DOI: 10.1201/9781315117485.

[95] H. Koch, *Gas Insulated Substations*. Wiley, 2014, p. 1108, ISBN: 9781118570722.

[96] K. Subramanya and T. R. Chelliah, "DC bias impact analysis on the capability of power transformer and failure risks," *Engineering Failure Analysis*, vol. 163, p. 108 537, Sep. 2024, ISSN: 1350-6307. DOI: 10.1016/j.engfailanal.2024.108537.

[97] S. V. Tewari, R. Chandra, S. K. Sharma, R. Sarathi, A. Sharma, and K. C. Mittal, "Surface potential decay of PMMA and POM in air," *Materials Research Express*, vol. 2, no. 4, p. 045 301, 2015. DOI: 10.1088/2053-1591/2/4/045301. [Online]. Available: https://doi.org/10.1088/2053-1591/2/4/045301.

[98] Watlow Electric Manufacturing Company, *FIREROD® cartridge heaters*, Product catalogue, Accessed 16 June 2026, Watlow Electric Manufacturing Company, 2016. [Online]. Available: https://www.watlow.com/-/media/documents/catalogs/cartridge1-31.ashx.

[99] *2012 Annual Report Conference on Electrical Insulation and Dielectric Phenomena*, 14–17 October 2012, IEEE Dielectrics and Electrical Insulation Society, Montreal, QC, Canada: IEEE, Oct. 2012, ISBN: 978-1-4673-1253-0.

[100] G. de Vahl Davis, "Natural convection of air in a square cavity: A bench mark numerical solution," *International Journal for Numerical Methods in Fluids*, vol. 3, no. 3, pp. 249–264, 1983. DOI: 10.1002/fld.1650030305.

[101] R. J. A. Janssen and R. A. W. M. Henkes, "Accuracy of finite-volume discretizations for the bifurcating natural-convection flow in a square cavity," *Numerical Heat Transfer, Part B: Fundamentals*, vol. 24, pp. 191–207, 1993. DOI: 10.1080/10407799308955889.

[102] M. Koch, "Prediction of breakdown voltages in novel gases for high voltage insulation," Doctoral thesis, ETH Zurich, Zurich, Switzerland, 2015. DOI: 10.3929/ethz-a-010411940. [Online]. Available: https://doi.org/10.3929/ethz-a-010411940.

[103] P. Simka, U. Straumann, and C. M. Franck, "SF6 high voltage circuit breaker contact systems under lightning impulse and very fast transient voltage stress," *IEEE Transactions on Dielectrics and Electrical Insulation*, vol. 19, no. 3, pp. 855–864, Jun. 2012, ISSN: 1070-9878. DOI: 10.1109/TDEI.2012.6215088.

[104] S. Okabe, J. Takami, and T. Tsuboi, "Breakdown voltage-time characteristics and insulation testing of gas insulated switchgear," *IEEE Transactions on Dielectrics and Electrical Insulation*, vol. 15, no. 3, pp. 741–748, Jun. 2008, ISSN: 1070-9878. DOI: 10.1109/TDEI.2008.4543111.

[105] S. Wellek, *Testing Statistical Hypotheses of Equivalence and Noninferiority*, 2nd ed. Boca Raton, Florida, USA: CRC Press, 2010, ISBN: 978-1-4398-0818-4.

[106] DuPont, *Teflon® PFA fluoropolymer resins*, Product handbook / technical data document, Accessed 16 June 2026, DuPont. [Online]. Available: https://www.chemours.com/en/brands-and-products/teflon-fluoropolymers.

[107] *Gb series magnetic drive gear pump: Technical data*, Manufacturer datasheet, accessed 2026-06-17, Micropump, 2026.

[108] *Gather magnetic drive gear pumps: Product catalogue*, Manufacturer/distributor catalogue, accessed 2026-06-17, GATHER Industrie, 2024.

[109] *E5cc/e5ec digital temperature controller datasheet*, Manufacturer datasheet, accessed 2026-06-17, Omron, 2026.

[110] *3200 series temperature/process controller*, Manufacturer product documentation, accessed 2026-06-17, Eurotherm, 2026.

[111] International Organization for Standardization and International Electrotechnical Commission, *General requirements for the competence of testing and calibration laboratories*, ISO/IEC 17025:2017, ISO and IEC, 2017. [Online]. Available: https://www.iso.org/standard/66912.html.

[112] International Organization for Standardization, *Geometrical product specifications (GPS)—inspection by measurement of workpieces and measuring equipment—part 1: Decision rules for verifying conformity or nonconformity with specifications*, ISO 14253-1:2017, International Organization for Standardization, 2017. [Online]. Available: https://www.iso.org/standard/70137.html.

[113] Health and Safety Executive, "Safety requirements for pressure testing," Health and Safety Executive, Guidance Note GS4, 2012, Web guidance updated 10 March 2021. [Online]. Available: https://www.hse.gov.uk/pubns/gs4.htm.

[114] Joint Committee for Guides in Metrology, "Evaluation of measurement data—the role of measurement uncertainty in conformity assessment," Joint Committee for Guides in Metrology, Tech. Rep. JCGM 106:2012, 2012. DOI: 10.59161/JCGM106-2012. [Online]. Available: https://doi.org/10.59161/JCGM106-2012.

[115] International Electrotechnical Commission, *High-voltage test techniques—charge-based measurement of partial discharges*, IEC 60270:2025, International Electrotechnical Commission, Jun. 2025. [Online]. Available: https://webstore.iec.ch/en/publication/65087.

[116] *Helisol®: Heat transfer fluids, technical product brochure*, Manufacturer technical brochure, accessed 2026-06-17, Wacker Chemie AG, 2026.

[117] *Otg-f fibre optic temperature sensor: Product documentation*, Manufacturer product documentation, accessed 2026-06-17, Opsens Solutions, 2026.

[118] *Neoptix t1 fibre optic temperature probe: Datasheet*, Manufacturer datasheet, accessed 2026-06-17, Neoptix, 2026.

[119] *Screw plug immersion heaters: Specification sheet*, Manufacturer specification sheet, accessed 2026-06-17, Watlow Electric Manufacturing Company, 2019.

[120] *Stainless steel immersion heater for light-weight oil with thermostat*, Manufacturer product documentation, accessed 2026-06-17, DwyerOmega, 2026.

[121] T. L. Bergman, A. S. Lavine, F. P. Incropera, and D. P. DeWitt, *Fundamentals of Heat and Mass Transfer*, 8th ed. Wiley, 2018, ISBN: 978-1-119-35388-1.

[122] M. Escudier, *Introduction to Engineering Fluid Mechanics*. Oxford University Press, 2017, ISBN: 978-0-19-871987-8. DOI: 10.1093/oso/9780198719878.001.0001. [Online]. Available: https://doi.org/10.1093/oso/9780198719878.001.0001.

[123] Durex Industries, *Cartridge heaters*, Manufacturer catalogue, Rev. 6-22-23, 2023. Accessed: Jul. 25, 2026. [Online]. Available: https://www.durexindustries.com/documents/products/Cartridge%20Heaters%206-22-23.pdf.

[124] Copper Development Association Inc., *The copper advantage: A guide to working with copper and copper alloys*. Accessed: Jul. 25, 2026. [Online]. Available: https://live.copper.org/publications/pub_list/pdf/a1360.pdf.

[125] COMSOL AB. "Heat conduction in a finite slab." COMSOL Multiphysics 6.4 Application Library, Heat Transfer Module, Accessed: Jul. 27, 2026. [Online]. Available: https://doc.comsol.com/6.4/doc/com.comsol.help.models.heat.heat_conduction_in_slab/heat_conduction_in_slab.html.

A

Detailed Engineering Drawings

A.1. Final Assembly and Interface Integration

The complete test cell is assembled through the interfaces defined above. The heating and sensing components are installed within the rod assemblies, after which the rods, adaptors, electrodes, spacer, PMMA tube and PEEK chamber-end parts are brought together to form the complete arrangement shown in Figure A.1. The figure is included only as a visual overview of the final integration.

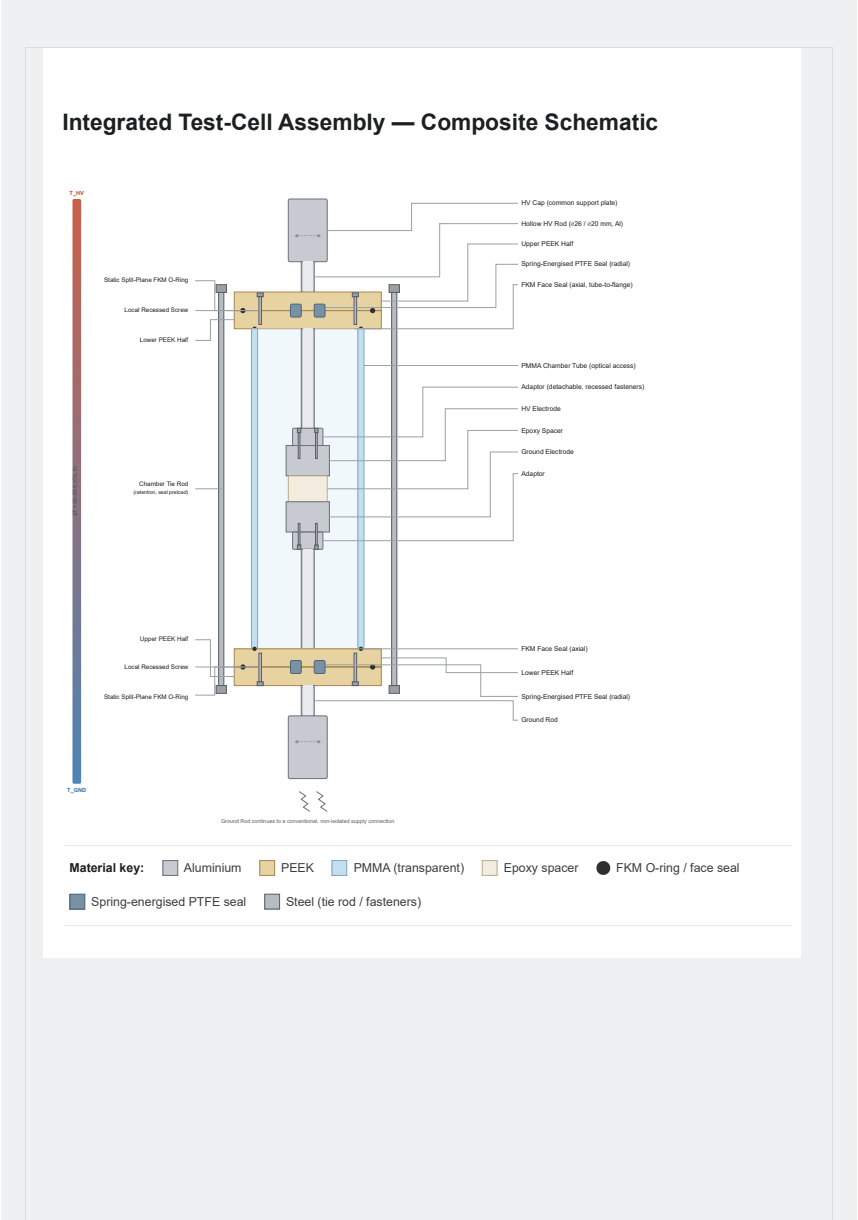
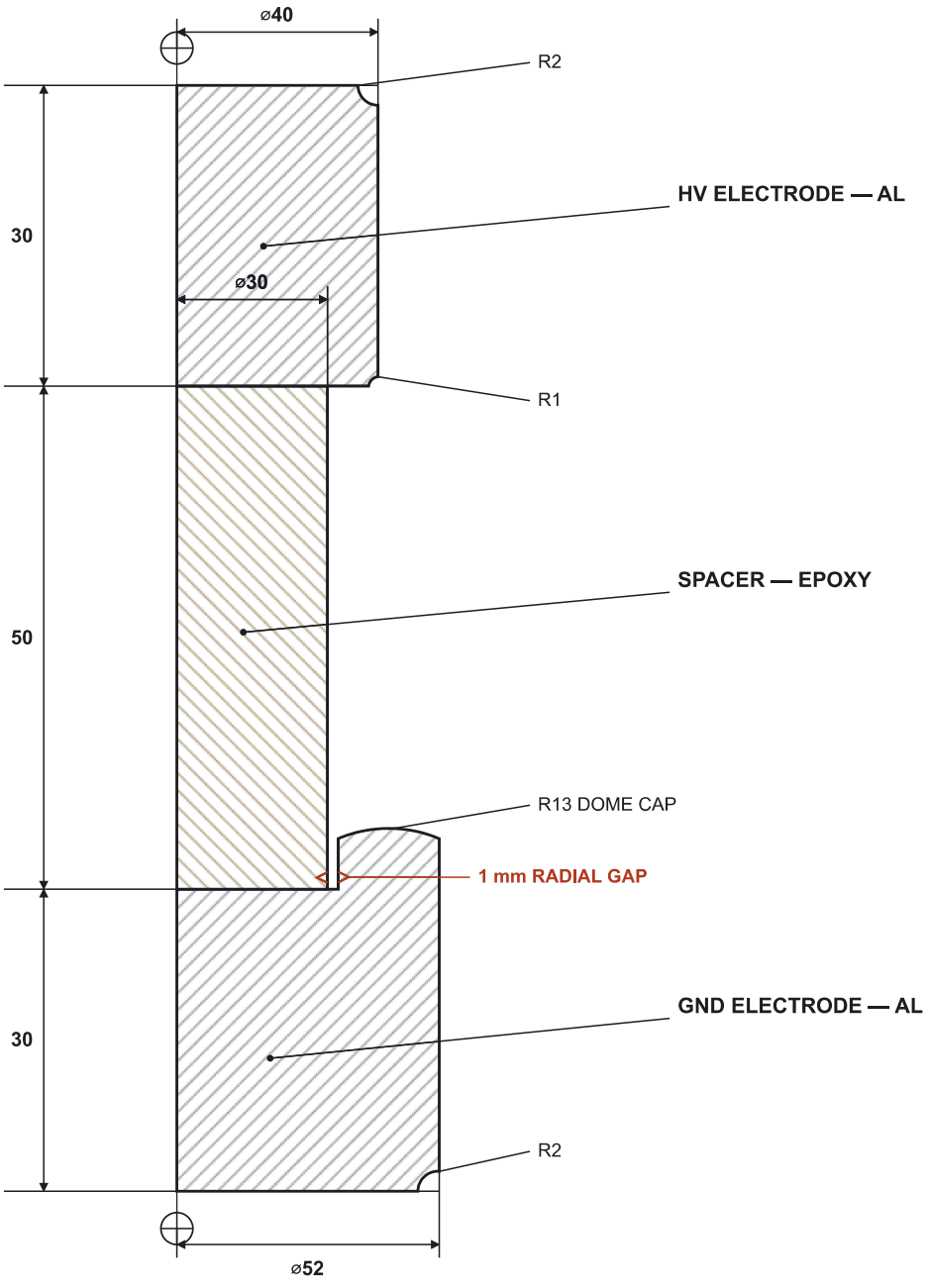


Figure A.1: Visual overview of the integrated test-cell assembly. The schematic is not to scale and is included only to illustrate the integration of the main components.

DRAWN TO SCALE 2:1 — VERIFY BY MEASUREMENT ON PLOTTED SHEET

PRINT AT 100% / ACTUAL SIZE ON A3 — DO NOT "FIT TO PAGE"



AXIS OF SYMMETRY (r = 0)

NOTES

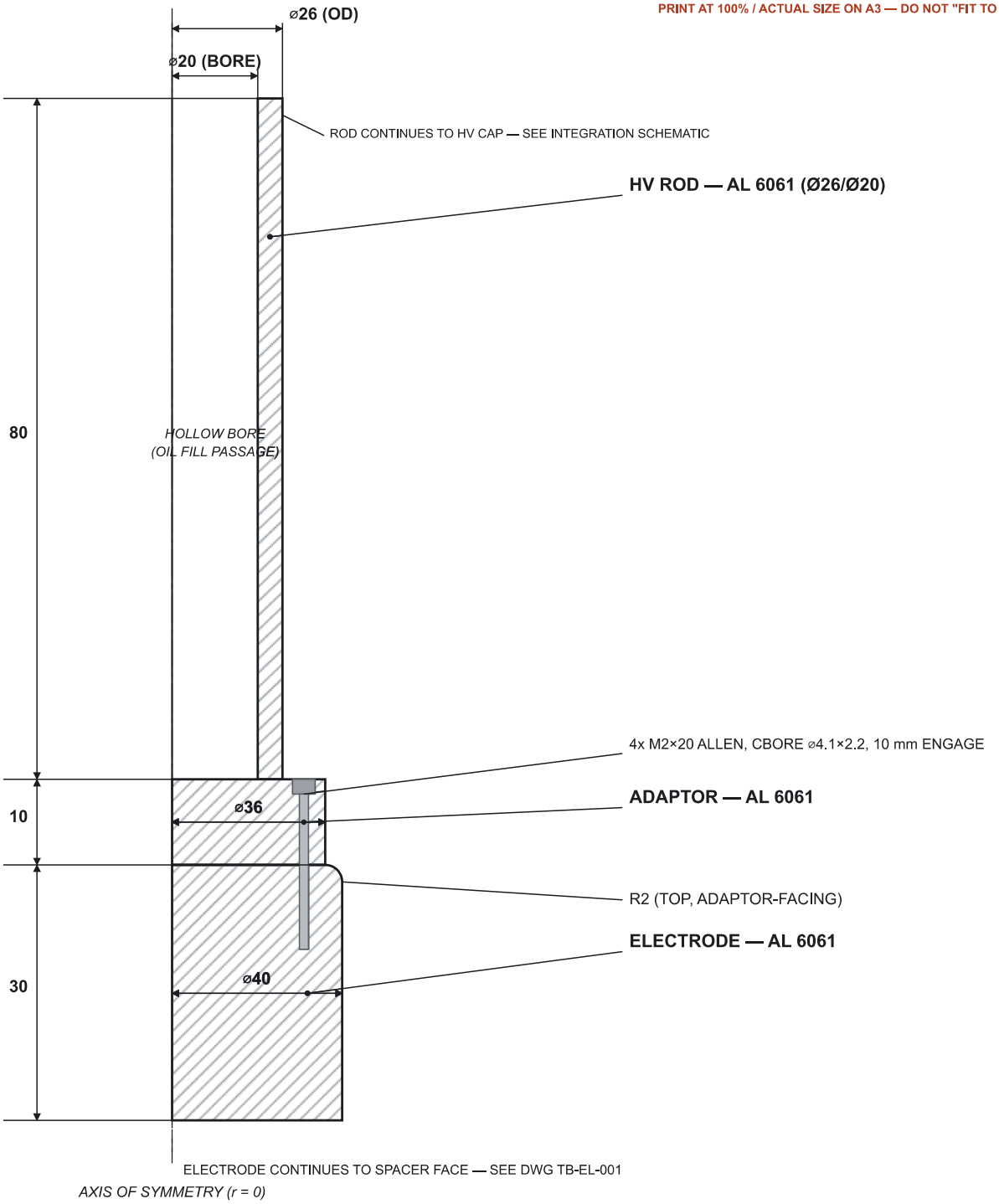
1. Half-section, axisymmetric about r = 0. Drawing plotted at true 2:1 scale.
2. Material: aluminium (electrodes), epoxy (spacer).
3. Maintain 1 mm radial clearance, spacer to GND nose.
4. Break sharp edges; unspecified fillets R1. All dimensions in mm.
5. Rod bore and tie-rod interfaces: see DWG TB-EL-002.

PROJECT **REDUCED SCALE TEST BENCH**	104	DWG NO **TB-EL-001**	REV **A**
		SCALE **2:1**	UNITS **mm**
TITLE **ELECTRODE-SPACER ASSEMBLY** MATERIAL: SEE CALLOUTS — MATCHES CH.5/CH.7 ELECTRODE–SPACER GEOMETRY		DRAWN —	DATE **2026-08-03**

DRAWN TO TRUE SCALE 2:1 — VERIFY BY MEASUREMENT ON PLOTTED A3 SHEET

SHEET 1 OF 2 — HALF SECTION

PRINT AT 100% / ACTUAL SIZE ON A3 — DO NOT "FIT TO PAGE"



NOTES

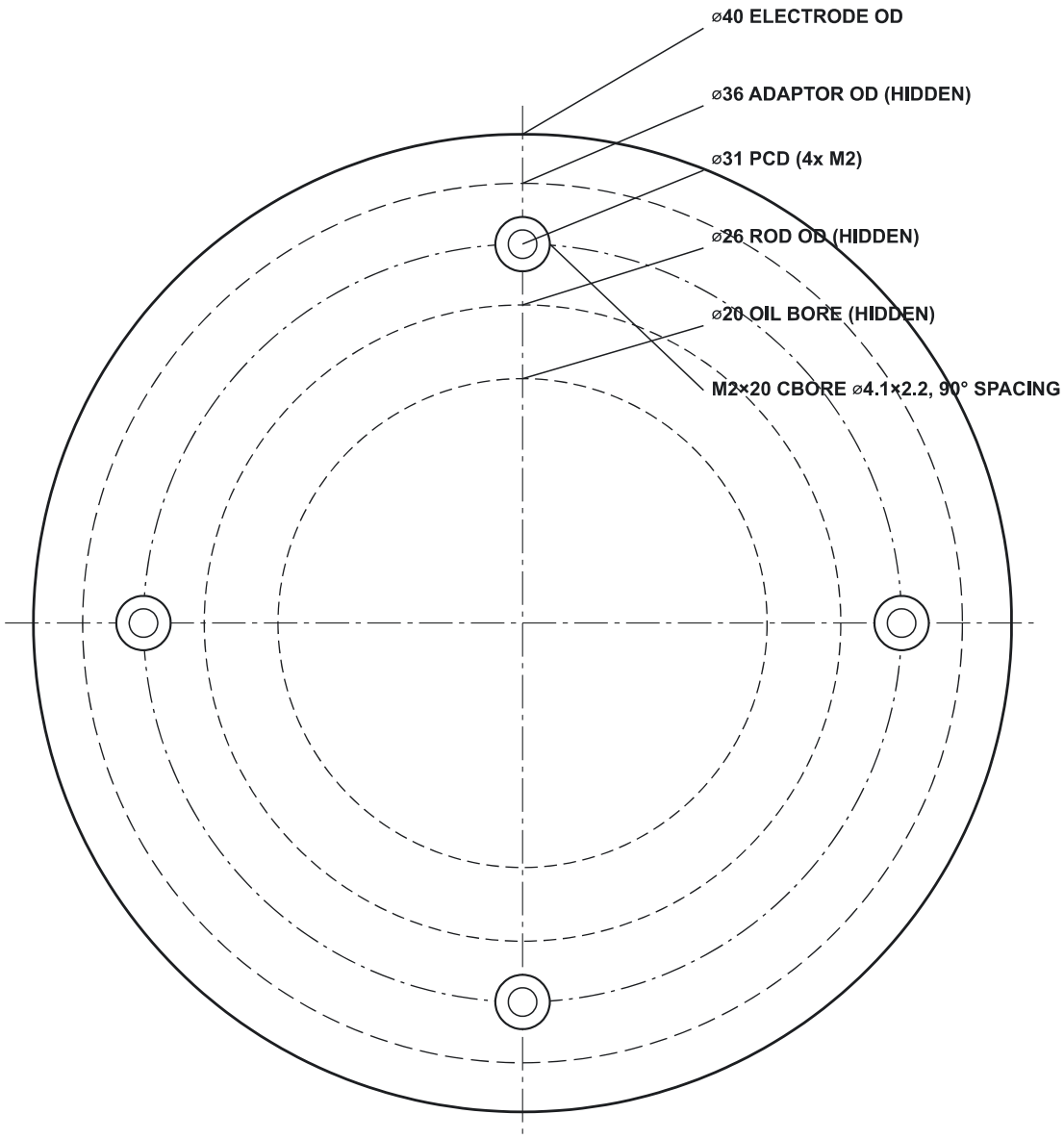
1. Half-section, drawn to true 2:1 scale on A3 (measure directly on printed sheet).
2. Rod: Al 6061, ⌀26/⌀20, wall t = 3 mm, L = 80 mm inside chamber.
3. Adaptor bore ⌀26 (h7/g6) receives rod; adaptor is NOT tapped.
4. Electrode: 4x M2×20 socket-head (Allen) cap screws, tapped blind, 10 mm engagement.
5. Ra 0.8 all mating/exposed HV faces; ISO 2768-mK; dims in mm.
6. GND rod: solid or end-capped; no oil bore required.

PROJECT **REDUCED SCALE TEST BENCH**	105	DWG NO **ROD-ASSY-001**	REV **D**
		SCALE **2:1**	UNITS **mm**
TITLE **ELECTRODE-ADAPTOR-AL ROD ASSEMBLY** MATERIAL: AL 6061 — MATES ELECTRODE Ø40×30 (DWG TB-EL-001)		DRAWN —	DATE **2026-08-03**

TOP VIEW — DRAWN TO TRUE SCALE 5:1

SHEET 2 OF 2 — TOP VIEW

PRINT AT 100% / ACTUAL SIZE ON A3 — DO NOT "FIT TO PAGE"



NOTES

1. Top view only, all dimensions in mm; hidden circles shown dashed.
2. Adaptor OD = ⌀36, seats on electrode's flat face (clear of top R2 fillet).
3. Fasteners: 4x M2×20 full-thread socket-head at 90° on ⌀31 PCD; adaptor holes are clearance + counterbore.
4. Counterbore-to-rod-OD and counterbore-to-adaptor-OD margins ≈ 0.45 mm each side — confirm before machining.
5. Deburr/polish all exposed metal edges; ISO 2768-mK general tolerance.

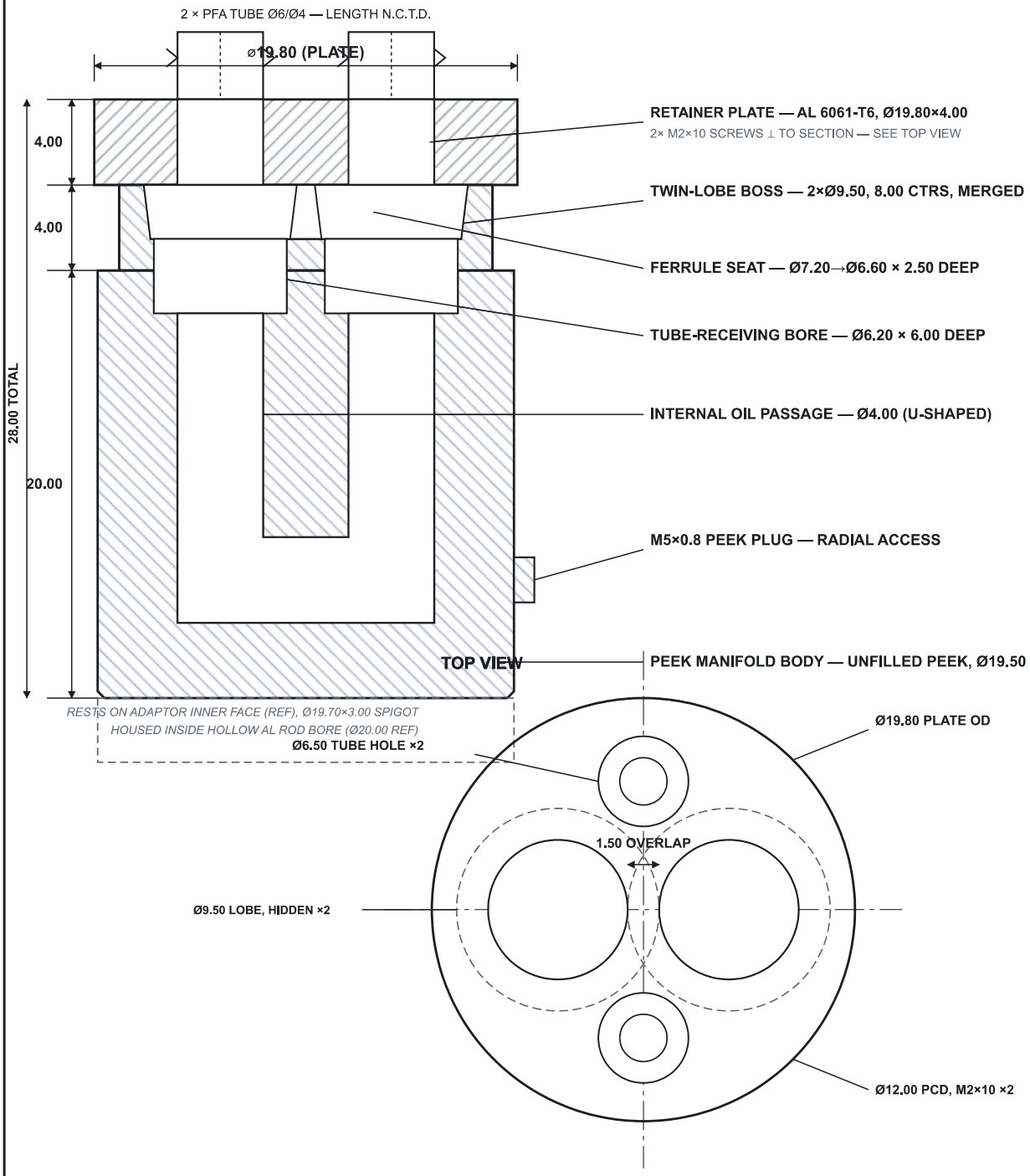
PROJECT **REDUCED SCALE TEST BENCH**	106	DWG NO **ROD-ASSY-001**	REV **D**
		SCALE **5:1**	UNITS **mm**
TITLE **ELECTRODE-ADAPTOR-AL ROD ASSEMBLY** MATERIAL: AL 6061 — MATES ELECTRODE Ø40×30 (DWG TB-EL-001)		DRAWN —	DATE **2026-08-03**

SCALE 5:1 (NOMINAL) — VERIFY BY MEASUREMENT ON PLOTTED SHEET

SHEET 1 OF 4 — ASSEMBLY SECTION + TOP VIEW

PRINT AT 100% / ACTUAL SIZE ON A3 — DO NOT "FIT TO PAGE"

FRONT SECTION — THROUGH BOTH TUBE AXES



TOP VIEW

NOTES

1. Tubes enter PEEK receiving bores directly — no separate tube-socket part.
2. Boss lobes intentionally overlap (1.50); internal ferrule seats remain separate.
3. Tighten M2 screws until plate contacts boss (hard stop) — do not rely on torque alone.
4. Leak-test full oil passage before installing in aluminium rod. Dims in mm.
5. Whole assembly sits inside the hollow Al rod; manifold rests directly on the adaptor's inner face (Ø19.70 spigot, location/support only, not the primary oil seal). Preliminary — see DWG TB-TH-002…004 for part detail.

BILL OF MATERIALS

1 · PEEK U-manifold · unfilled PEEK · 1 2 · Retainer plate · Al 6061-T6 · 1 3 · PFA tube Ø6/Ø4 · Super-PFA · 2
4 · Compression ferrule · virgin PTFE · 2 5 · M2×10 SHCS · SS A4-70 · 2 6 · Cross-bore plug · unfilled PEEK · 1
7,8 · Adaptor / insert (ref) · Al 6061-T6 · —

PROJECT REDUCED SCALE TEST BENCH	107	DWG NO TB-TH-001	REV A
		SCALE 5:1	UNITS mm
TITLE U-MANIFOLD ASSEMBLY SUPERSEDES EARLIER 5 mm PLATE / SEPARATE TUBE-SOCKET DESIGN		DRAWN —	DATE 2026-08-03

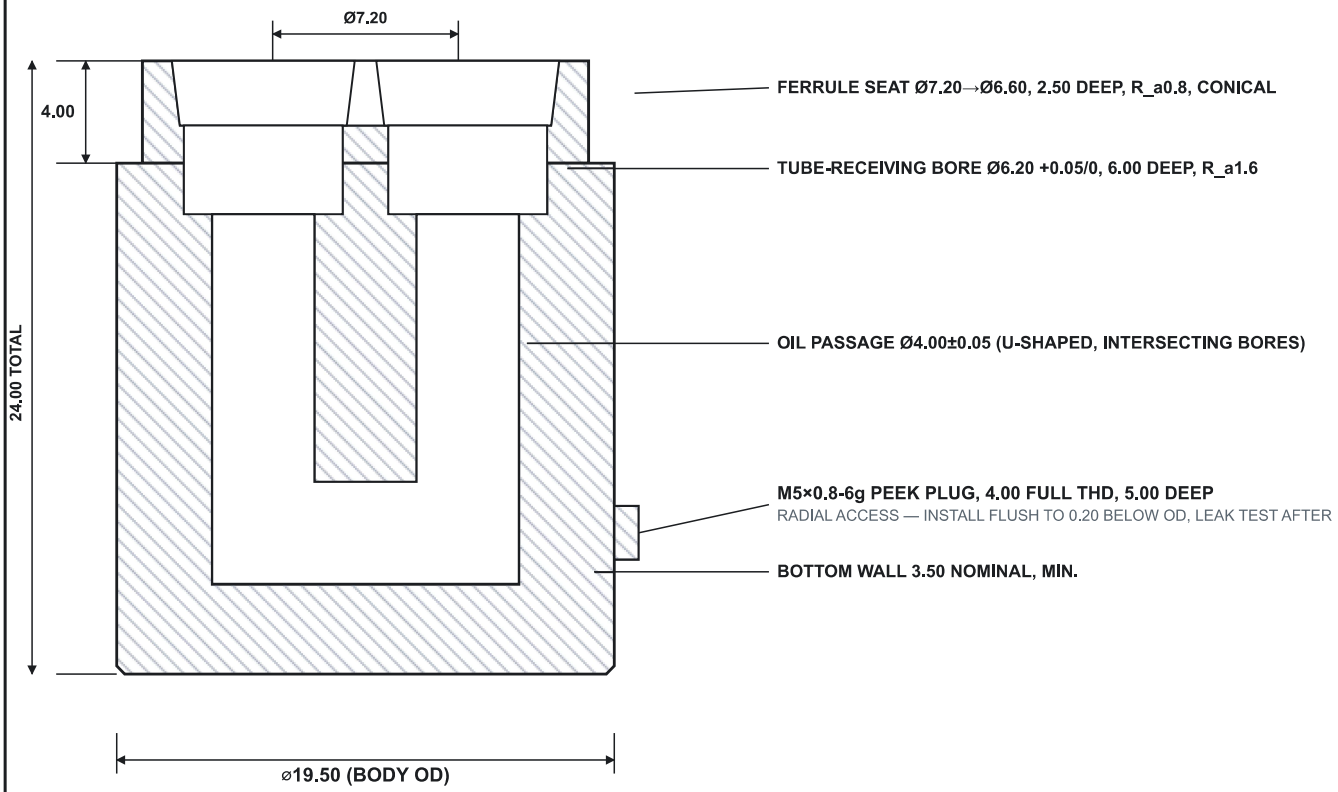
SCALE 5:1 (NOMINAL) — VERIFY BY MEASUREMENT ON PLOTTED SHEET

SHEET 2 OF 4 — DETAIL SECTION + TOP VIEW

PRINT AT 100% / ACTUAL SIZE ON A3 — DO NOT "FIT TO PAGE"

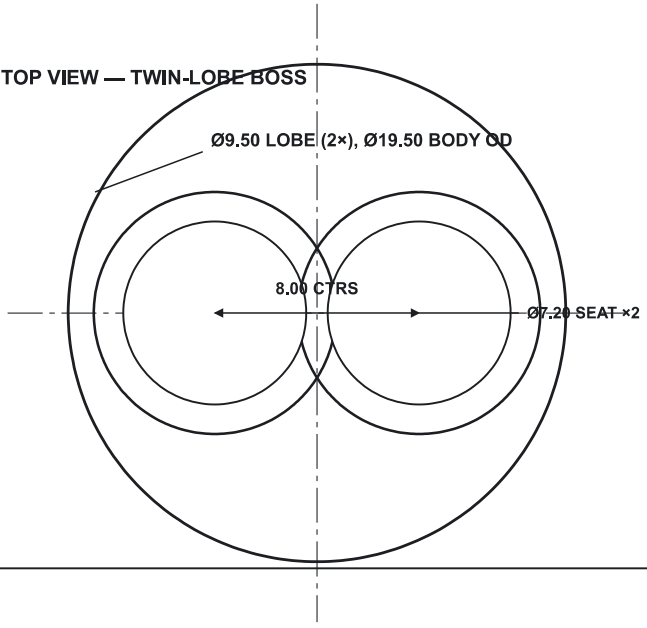
FRONT SECTION — PEEK BLOCK ONLY

MATERIAL: UNFILLED NATURAL PEEK (VICTREX 450G OR APPROVED EQUIVALENT)



BOTTOM CHAMFER 0.30×45°, GENERAL EDGE BREAK 0.20 MAX

TOP VIEW — TWIN-LOBE BOSS



NOTES

1. Boss is one continuous merged twin-lobe feature — do not label as two separate bosses.
2. Ferrule seats remain two separate features; minimum ligament between seats = 0.80.
3. Clean and inspect the complete Ø4 oil-flow passage after machining; leak-test before use.
4. Cross-bore plug thread provides mechanical retention; sealant is not the sole retaining feature.
5. General untoleranced linear dims ±0.10, angles ±0.5°, unless noted. All dims in mm.
6. Preliminary — not for manufacture.

PROJECT **REDUCED SCALE TEST BENCH**	108	DWG NO **TB-TH-002**	REV **A**
		SCALE **5:1**	UNITS **mm**
TITLE **PEEK U-MANIFOLD BLOCK** MATES RETAINER PLATE (TB-TH-003), MATES ADAPTOR POCKET Ø19.70×3.00		DRAWN —	DATE **2026-08-03**

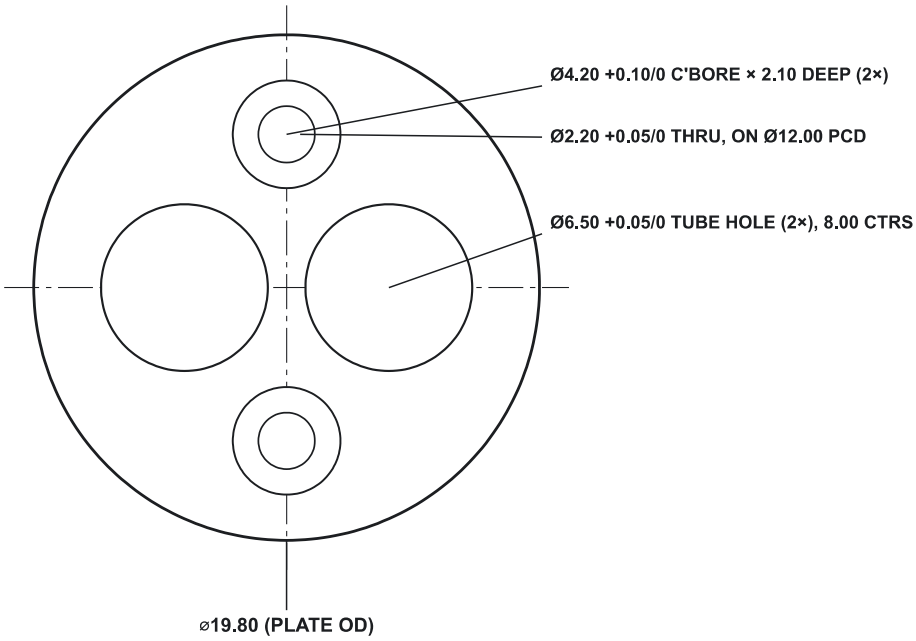
SCALE 5:1 (NOMINAL) — VERIFY BY MEASUREMENT ON PLOTTED SHEET

SHEET 3 OF 4 — TOP VIEW + SECTION

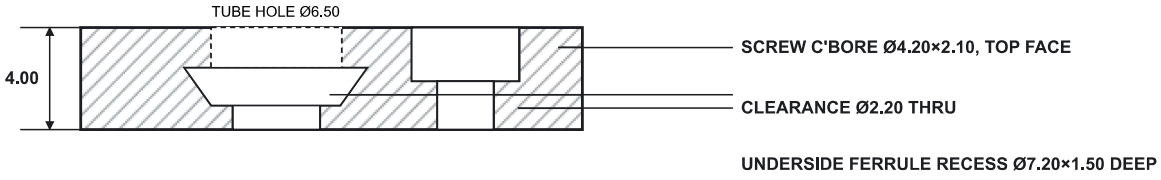
PRINT AT 100% / ACTUAL SIZE ON A3 — DO NOT "FIT TO PAGE"

MATERIAL: ALUMINIUM 6061-T6

TOP VIEW



SECTION A-A — THROUGH TUBE HOLE + SCREW C'BORE



TOP FLATNESS 0.03, BOTTOM FLATNESS 0.05
PARALLELISM 0.05, OUTER CHAMFER 0.30×45°

NOTES

1. Plate holes guide the tubes only — they are not the oil seal.
2. Screw heads shall remain below the insert-landing (top) surface.
3. Top face lands the aluminium insert; bottom face contacts the PEEK twin-lobe boss.
4. Surface finish R_a≤1.6 µm all faces. All dims in mm.
5. M2×0.4-6H mating threads are in the PEEK body (TB-TH-002), not this plate.
6. Preliminary — not for manufacture.

PROJECT **REDUCED SCALE TEST BENCH**	109	DWG NO **TB-TH-003**	REV **A**
		SCALE **5:1**	UNITS **mm**
TITLE **ALUMINIUM RETAINER PLATE** CORRECTS EARLIER 5 mm THICKNESS — NOW 4.00 mm		DRAWN —	DATE **2026-08-03**

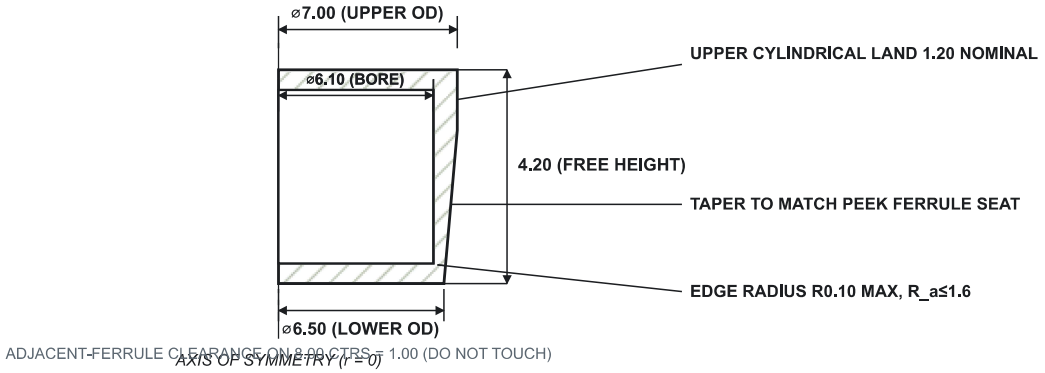
SCALE 10:1 — VERIFY BY MEASUREMENT ON PLOTTED SHEET

SHEET 4 OF 4 — TWO DETAILS, ONE SHEET

PRINT AT 100% / ACTUAL SIZE ON A3 — DO NOT "FIT TO PAGE"

A — PTFE COMPRESSION FERRULE (QTY 2, IDENTICAL) — SCALE 10:1

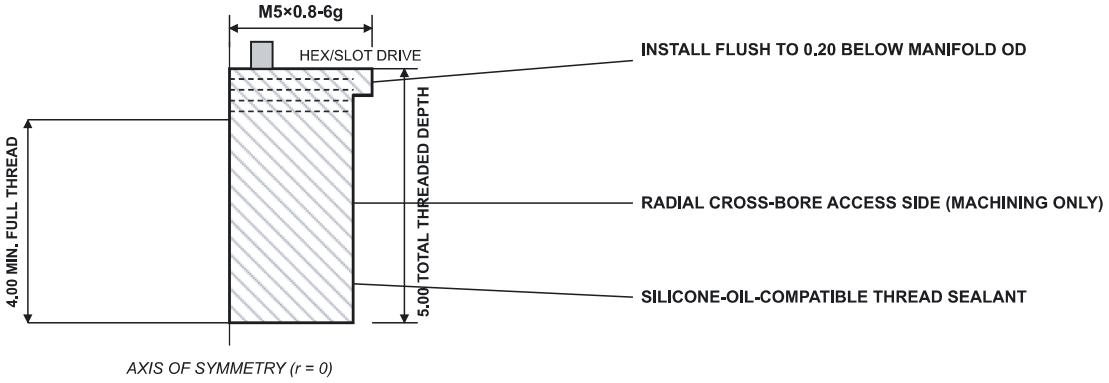
MATERIAL: VIRGIN PTFE — NO GLASS, CARBON OR METALLIC FILLER — AXISYMMETRIC HALF-SECTION, CENTRELINE LEFT



ADJACENT-FERRULE CLEARANCE ON 9.00 CTRS — 1.00 (DO NOT TOUCH)

B — CROSS-BORE CLOSURE PLUG (QTY 1) — SCALE 10:1

MATERIAL: UNFILLED PEEK — AXISYMMETRIC HALF-SECTION, CENTRELINE LEFT



NOTES

1. Ferrule: 4.20 free height into 4.00 closed cavity (2.50 PEEK seat + 1.50 plate recess) ≈ 0.20 compression.
2. Tighten retainer screws until plate contacts boss (hard stop sets compression, not torque). Ferrule qty: 2.
3. Ferrule is a custom part — confirm performance by prototype leak testing.
4. Plug seals the manifold's radial cross-bore — that bore exists purely for drilling access to the internal U-passage and must be plugged after machining. Thread gives mechanical retention; leak-test after install. Qty: 1.
5. All dims in mm, general untoleranced dims ±0.10 unless noted. Preliminary — not for manufacture.

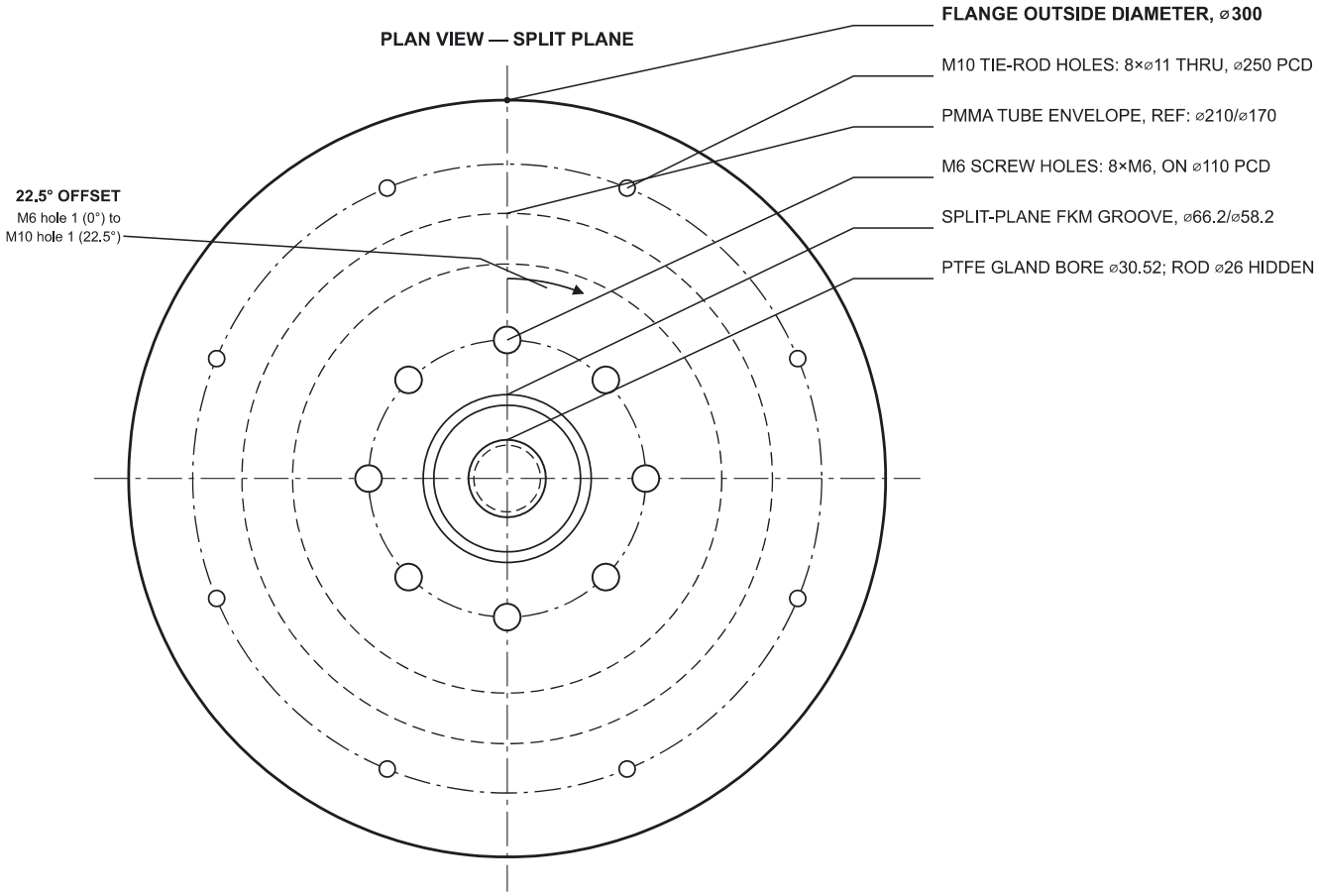
PROJECT **REDUCED SCALE TEST BENCH**	110	DWG NO **TB-TH-004**	REV **B**
		SCALE **10:1**	UNITS **mm**
TITLE **PTFE FERRULE & CROSS-BORE PLUG DETAIL** A: MATES PEEK SEAT Ø7.20→Ø6.60 — B: MATES CROSS-BORE, BOTH IN TB-TH-002		DRAWN —	DATE **2026-08-04**

PLAN 1:2 (TRUE) — SECTION 1:1 (TRUE) ON A3

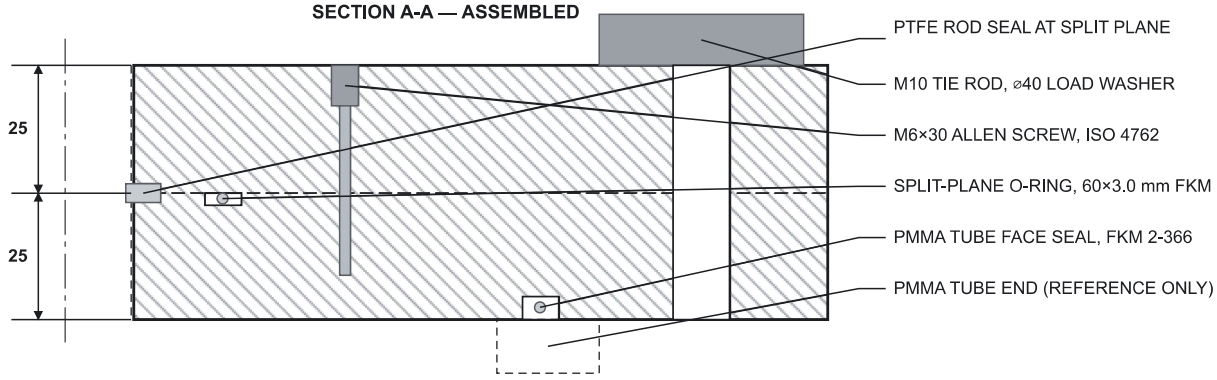
SHEET 1 OF 4 — ASSEMBLY

PRINT AT 100% / ACTUAL SIZE ON A3 — DO NOT "FIT TO PAGE"

PLAN VIEW — SPLIT PLANE



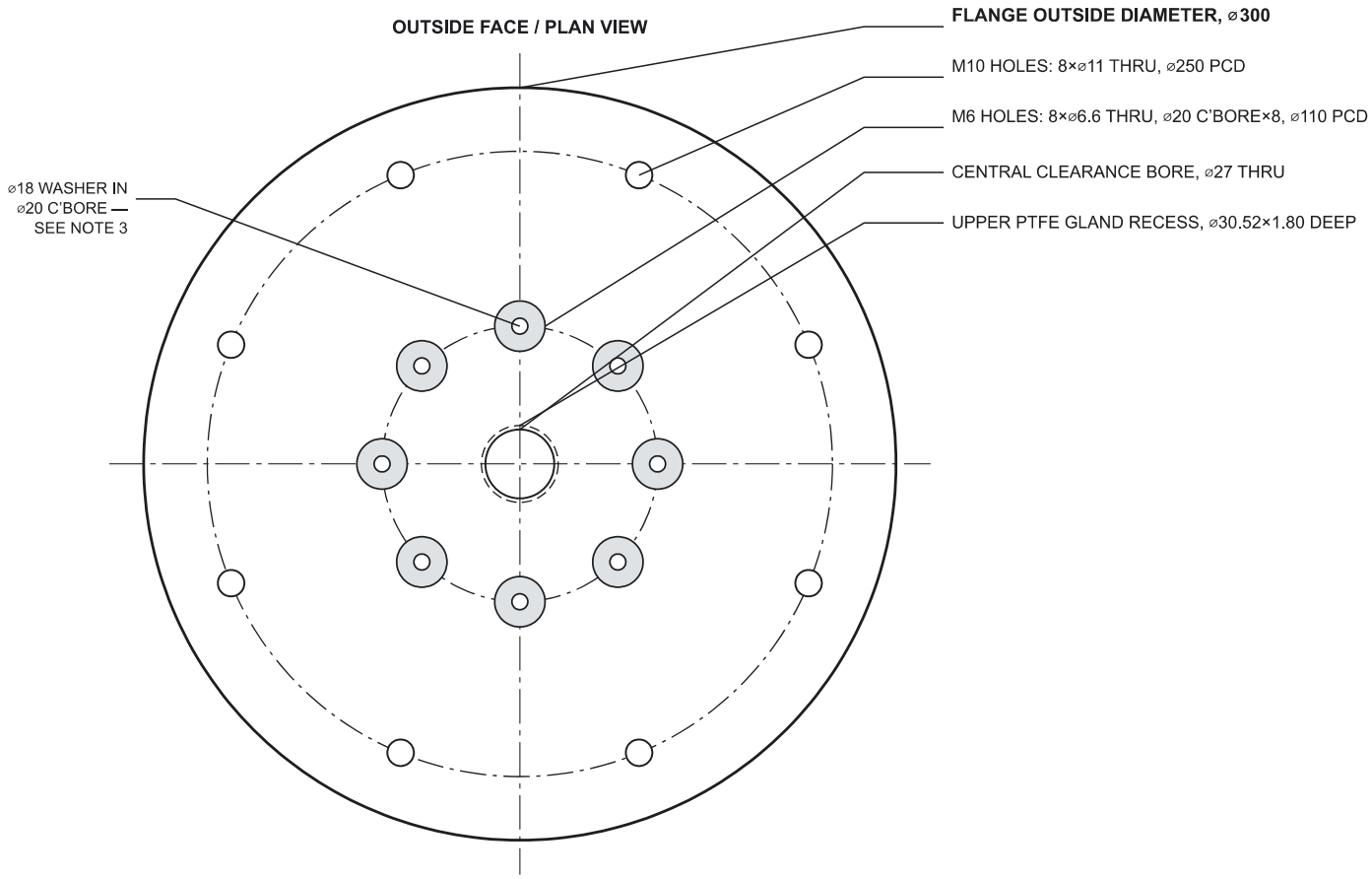
SECTION A-A — ASSEMBLED

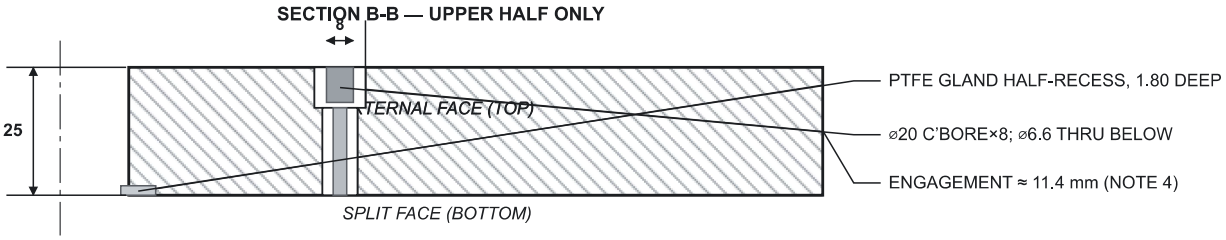


NOTES

1. Upper and lower PEEK halves are each 25 mm thick. Full split-face contact is the hard stop.
2. 8×M10 tie rods (⌀250 PCD) carry the chamber-separation load; 8×M6 Allen screws (⌀110 PCD) close the split gland and maintain local seal contact.
3. M6 pattern starts at 0°; M10 pattern offset 22.5° to avoid radial fastener alignment.
4. Design basis: 0.6 MPa differential pressure, ≈13.6 kN chamber-end load for ⌀170 ID. Seal dimensions require final supplier confirmation.
5. **PRELIMINARY — NOT FOR MANUFACTURE — FINAL SEAL-SUPPLIER CONFIRMATION REQUIRED.**

PROJECT **REDUCED SCALE TEST BENCH**	111	DWG NO **TB-EL-002**	REV **A**
		SCALE **1:2 / 1:1**	UNITS **mm**
TITLE **COMMON HV/GND PEEK END-FLANGE ASSEMBLY** MATERIAL: NATURAL UNFILLED PEEK 450G OR CERTIFIED EQUIVALENT		STATUS **PRELIM.**	DATE **2026-08-03**

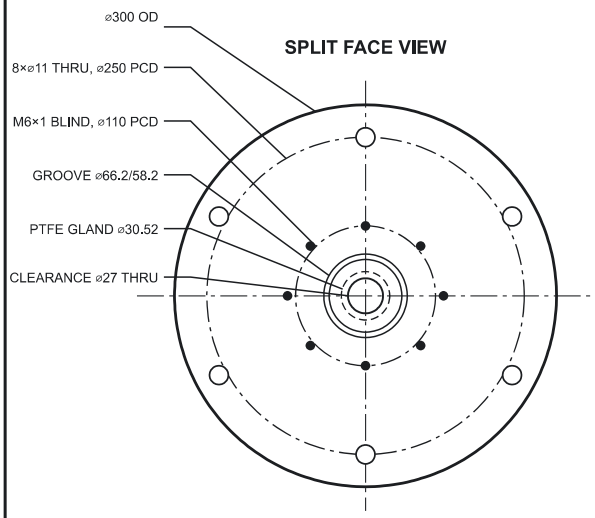


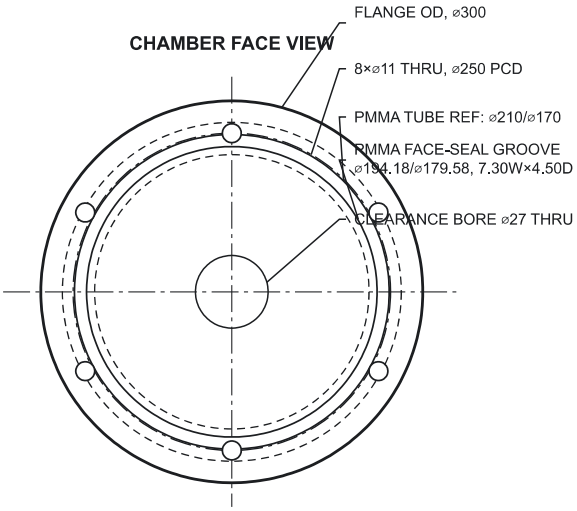


NOTES

1. Material: natural unfilled PEEK 450G or certified electrically insulating equivalent; certificate required.
2. Split face is a sealing/hard-stop surface: flatness 0.10 mm; finish Ra ≤ 0.8 µm, except PTFE gland surfaces Ra ≤ 0.4 µm.
3. 8× M6 socket-head cap screws: ISO 4762 A4-80, M6×30. Use ⌀18 mm load-spreading washer inside the ⌀20 mm counterbore (a ⌀20 washer leaves no clearance); alternative: enlarge counterbore to ⌀22 for a ⌀20 washer.
4. Engagement check: 25 half-thickness − 8 c'bore − 1.6 washer = 15.4 mm free; with M6×30 screw, effective thread engagement ≈ 30 − (17 PEEK-below-c'bore + 1.6 washer) ≈ 11.4 mm.
5. General tolerances ISO 2768-m; break sharp edges 0.2–0.4 mm; remove all burrs.
6. **PRELIMINARY — NOT FOR MANUFACTURE — FINAL SEAL-SUPPLIER CONFIRMATION REQUIRED.**

PROJECT **REDUCED SCALE TEST BENCH**	112	DWG NO **TB-EL-003**	REV **A**
		SCALE **1:2 / 1:1**	UNITS **mm**
TITLE **UPPER PEEK FLANGE HALF** MATERIAL: NATURAL UNFILLED PEEK 450G OR CERTIFIED EQUIVALENT		STATUS **PRELIM.**	DATE **2026-08-03**





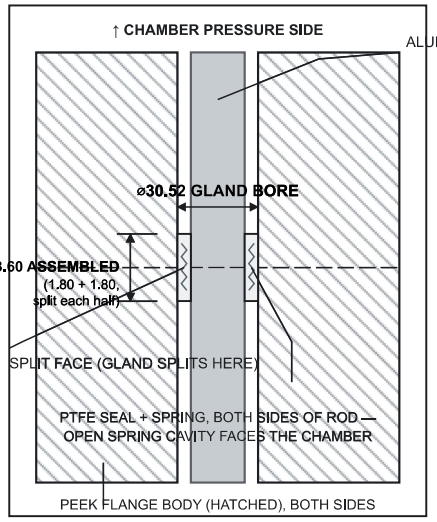
Section detail of the split O-ring groove, blind M6 thread and PMMA face-seal groove is given as SECTION A-A (assembled, DWG TB-EL-002) and DETAILS A–C (DWG TB-EL-005).

NOTES

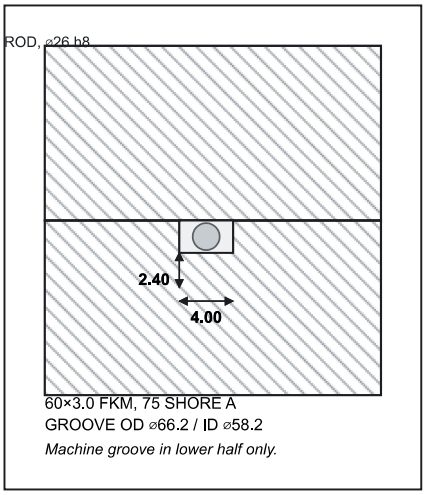
1. No radial interference-fit recess is included for the PMMA tube. Tube centring is established during assembly; the flat PMMA end bears on the PEEK sealing face.
2. Split face is the full-face hard stop. Machine the 60×3.0 mm FKM split-plane O-ring groove in this half only (Ø66.2/Ø58.2, 2.40 deep).
3. PMMA seal: Parker/AS568 2-366 FKM, 183.52×5.33 mm, 75 Shore A, or approved equivalent. Confirm final stock and supplier tolerances.
4. PMMA contact land and seal face: Ra ≤ 1.6 µm. Groove base/sides: Ra ≤ 3.2 µm. Flatness of chamber face 0.10 mm.
5. Blind M6×1 threads: minimum full thread 12 mm, total drilled depth 16 mm, drill-point allowance **included — 9 mm PEEK nominally remains beneath each blind hole. PRELIMINARY, NOT FOR MANUFACTURE.**

PROJECT **REDUCED SCALE TEST BENCH**	113	DWG NO **TB-EL-004**	REV **A**
		SCALE **1:4 VIEWS**	UNITS **mm**
TITLE **LOWER/CHAMBER-SIDE PEEK FLANGE HALF** MATERIAL: NATURAL UNFILLED PEEK 450G OR CERTIFIED EQUIVALENT		STATUS **PRELIM.**	DATE **2026-08-03**

DETAIL A
SPRING-ENERGISED PTFE ROD SEAL

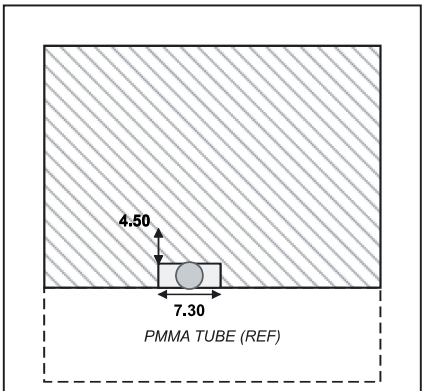


DETAIL B
SPLIT-PLANE FKM O-RING



60×3.0 FKM, 75 SHORE A
GROOVE OD ⌀66.2 / ID ⌀58.2
Machine groove in lower half only.

DETAIL C
PMMA TUBE-END STATIC FKM FACE SEAL

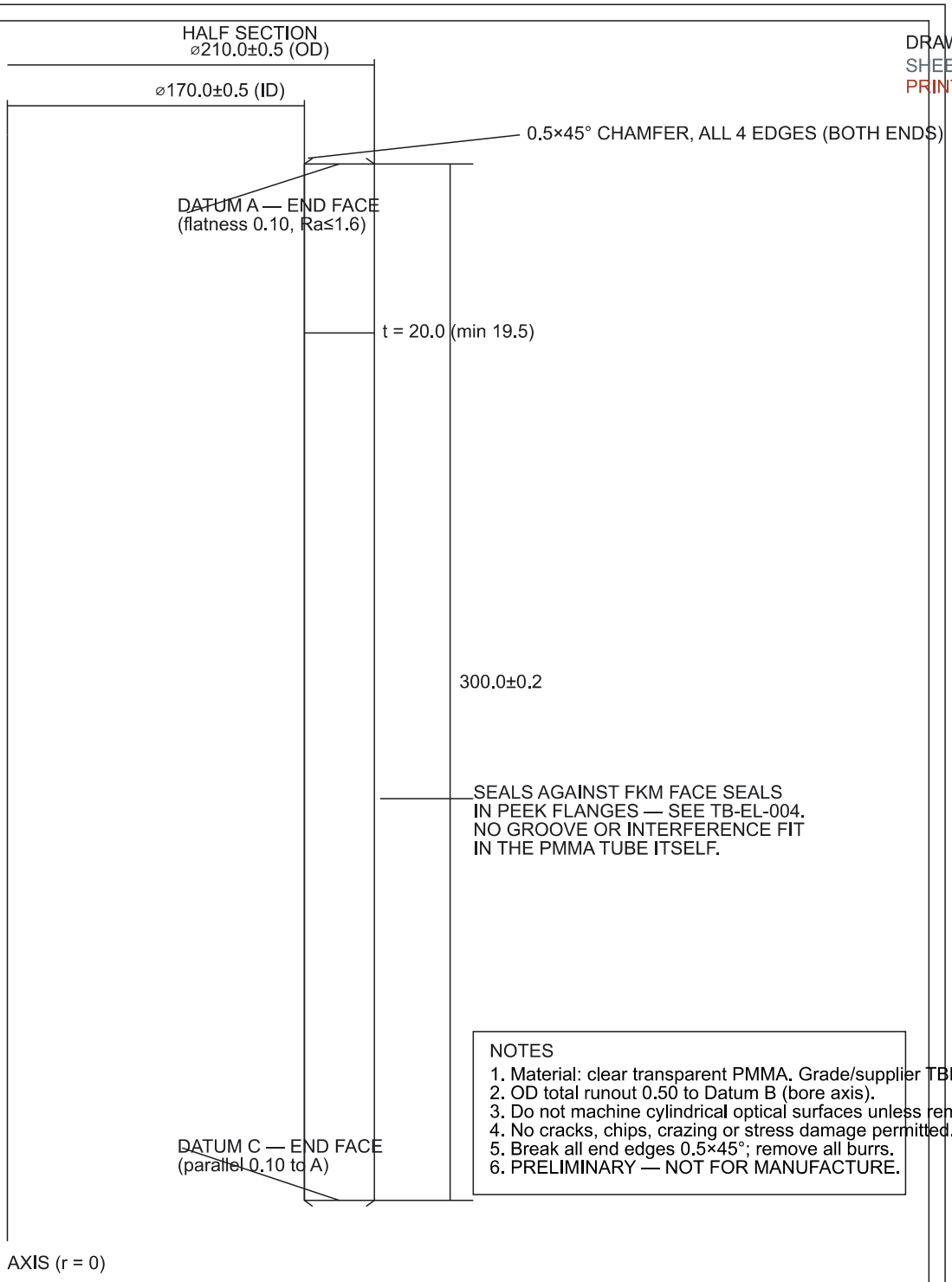


O-RING: FKM 2-366, 183.52×5.33, 75 SHORE A
GROOVE OD ⌀194.18; ID ⌀179.58 REF
PMMA tube wall ⌀210/⌀170; nominal squeeze 15.6%.

NOTES

1. PTFE rod seal basis: spring-energised symmetric seal for ⌀26 rod; gland bore ⌀30.52 H8, assembled axial width 3.60 mm (1.80 mm split into each PEEK half). Supplier part number, jacket compound and spring material remain to be confirmed.
2. Split-plane O-ring: 60×3.0 mm FKM, 75 Shore A; groove OD ⌀66.2, ID ⌀58.2, depth 2.40. Nominal squeeze 20%. Machine groove in lower half only.
3. PMMA face seal: FKM 2-366, 183.52×5.33 mm, 75 Shore A; groove OD ⌀194.18, radial width 7.30±0.10, depth 4.50. Nominal squeeze 15.6%.
4. Local fasteners: 8×M6×30 ISO 4762 A4-80 socket-head cap screws on ⌀110 PCD. Upper holes ⌀6.6 thru with ⌀20×8 counterbores (⌀18 washer); lower holes M6×1 blind, 16 deep.
5. **This drawing set defines a preliminary design for thesis documentation and detailed review. It is NOT a pressure-vessel certification or release-for-manufacture package.**

PROJECT: REDUCED SCALE TEST BENCH	114	DWG NO: TB-EL-005	REV: A
TITLE: SEAL GLAND AND FASTENER DETAILS MATERIAL: NATURAL UNFILLED PEEK 450G OR CERTIFIED EQUIVALENT		SCALE: NTS	UNITS: mm
		STATUS: PRELIM.	DATE: 2026-08-03



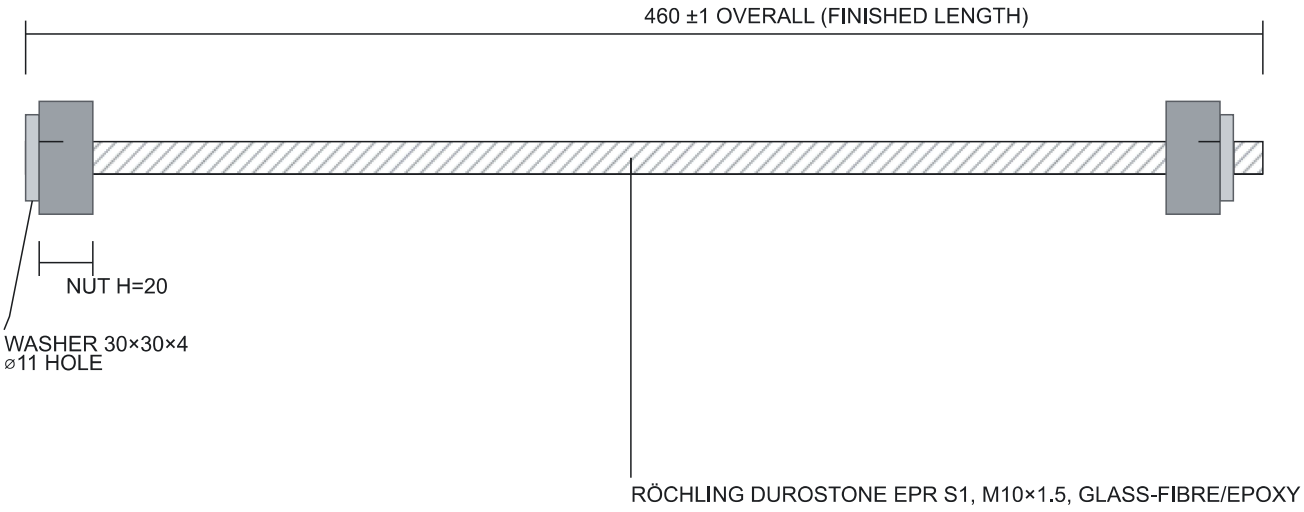
DRAWI
SHEET
PRINT

PROJECT REDUCED SCALE TEST BENCH	115	DWG NO TB-EL-006	REV A
		SCALE 3:1	UNITS mm
TITLE PMMA CHAMBER TUBE MATERIAL: CLEAR TRANSPARENT PMMA		STATUS PRELIM.	DATE 2026-08-03

SHE

LENGT
SHEET
PRINT

M10×1.5×460 GLASS-FIBRE/EPOXY TIE ROD, WITH HARDWARE AT EACH



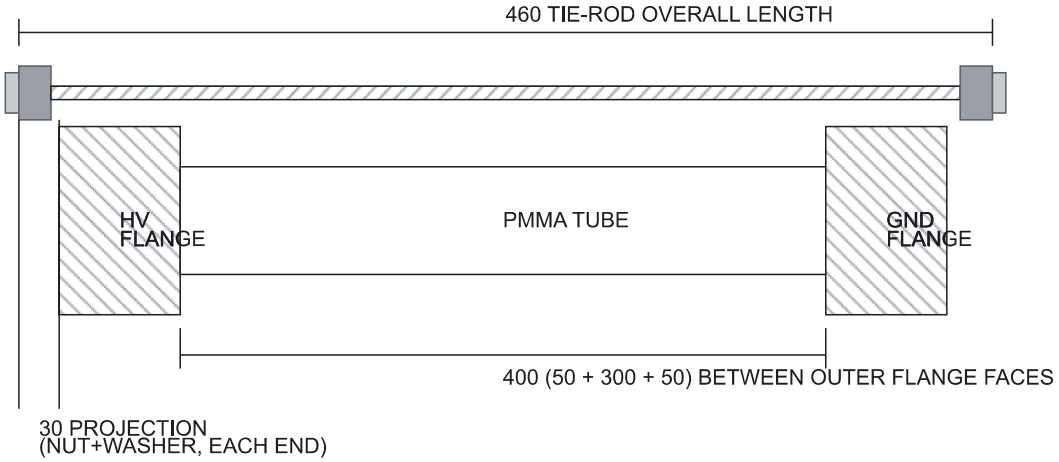
NOTES
1. Rod: 8× Röchling Durostone EPR S1, M10×1.5×460, cut from 1900 mm stock (article 100265).
2. Nuts: 16× Durostone EPM S7 hex, H=20 mm (double-height) — the H=10 nut is NOT permitted.
3. Washers: 16× Durostone EPC 308, 30×30×4, ⌀11 hole; orient sides radial/tangential.
4. Cut ends square within 0.5; break 0.5×45° max; no splintered fibres; seal cut ends with epoxy.
5. Nominal thread projection beyond each nut: 4 full pitches (min. 3).
6. Target preload: 5.00 ±0.25 kN per rod — set by calibrated load cell, not torque alone.
7. PRELIMINARY — NOT FOR MANUFACTURE.

PROJECT REDUCED SCALE TEST BENCH	116	DWG NO TB-EL-007	REV A
TITLE M10 GLASS/EPOXY TIE ROD MATERIAL: DUROSTONE EPR S1 / EPM S7 / EPC 308		SCALE 1:2 (LEN)	UNITS mm
		STATUS PRELIM.	DATE 2026-08-03

SHE

SCHEM
SHEET
PRINT

CHAMBER TUBE AND TIE-ROD ASSEMBLY — AXIAL STACK



8× tie rods on ⌀250 PCD, 45° spacing, first rod at 22.5° — see TB-EL-002 plan

BILL OF MATERIALS

ITEM	DESCRIPTION	QTY
1	PMMA tube, ⌀210/⌀170×300 (TB-EL-006)	1
2	PEEK end-flange assembly, 50 thick (TB-EL-002)	2
3	Durostone EPR S1 tie rod, M10×1.5×460 (TB-EL-007)	8
4	Durostone EPM S7 hex nut, M10, H=20	16
5	Durostone EPC 308 washer, 30×30×4, ⌀11	16
6	FKM PMMA face seal, 2-366	2

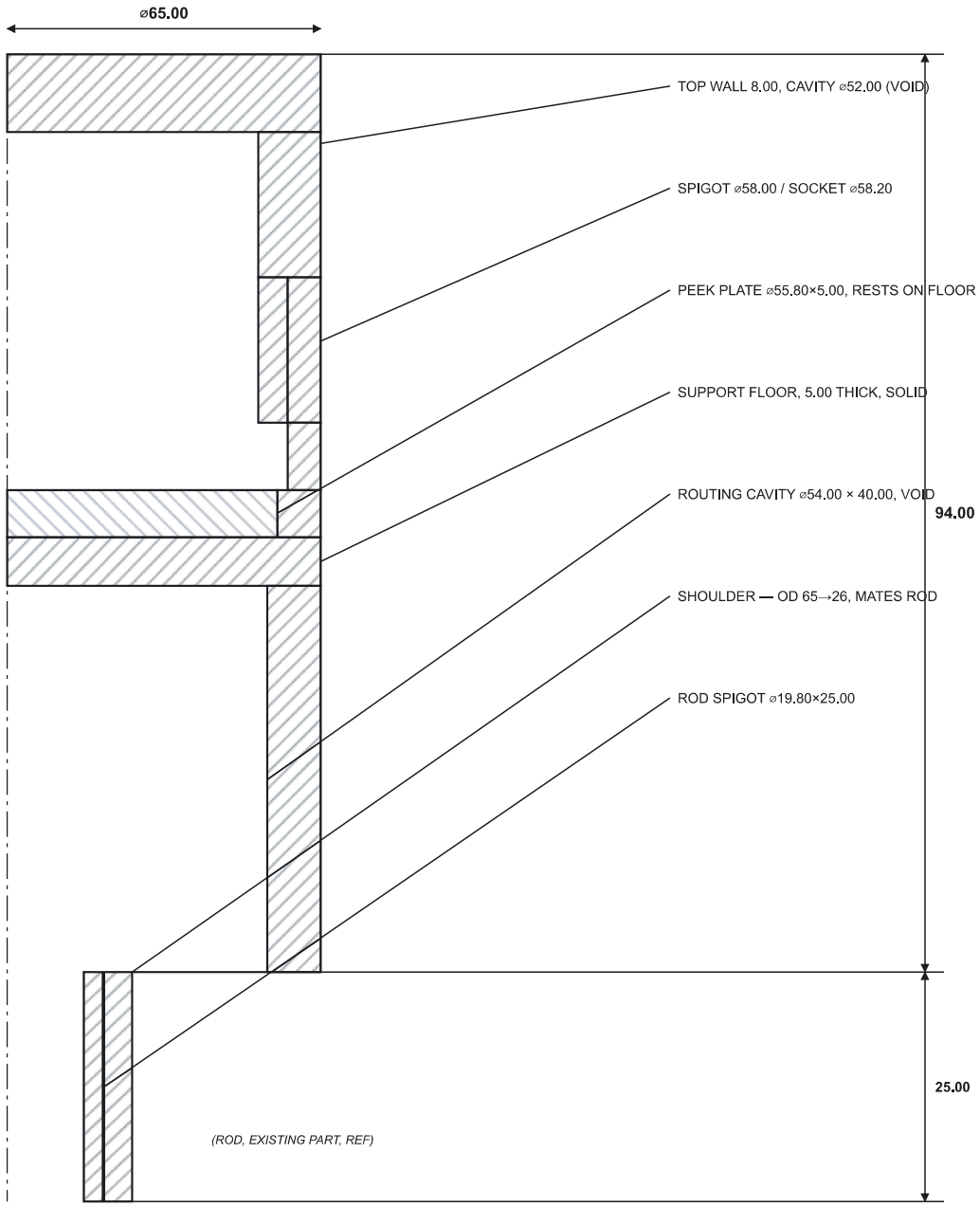
NOTES

1. Target preload 5.00 ±0.25 kN per rod; combined load per rod ≈ 9.44 kN at 0.6 MPa design basis.
2. Utilisation vs. Durostone EPM S7 (H=20) 22 kN breaking load, 50% sustained limit: ≈ 86% (max ≈ 88%).
3. H=10 mm nuts are NOT permitted — insufficient breaking load (12 kN) for this load case.
4. Tighten all 8 rods in a diametrically-opposite cross pattern, in ≥3 progressive steps.
5. Inner M6 Allen screws (TB-EL-002/003/004) are NOT part of the main chamber-retention load path.
6. Design basis: 6 bar differential pressure. This drawing is not a certified pressure-vessel rating.
7. PRELIMINARY — NOT FOR MANUFACTURE. Final acceptance requires supplier confirmation or test.
8. All dimensions in mm. Do not scale drawing.

PROJECT REDUCED SCALE TEST BENCH	117	DWG NO TB-EL-008	REV A
TITLE CHAMBER TUBE AND TIE-ROD ASSEMBLY SEE BOM ABOVE FOR MATERIALS		SCALE NTS	UNITS mm
		STATUS PRELIM.	DATE 2026-08-03

SHE

UNIVERSAL HV CAP — ASSEMBLY, HALF SECTION

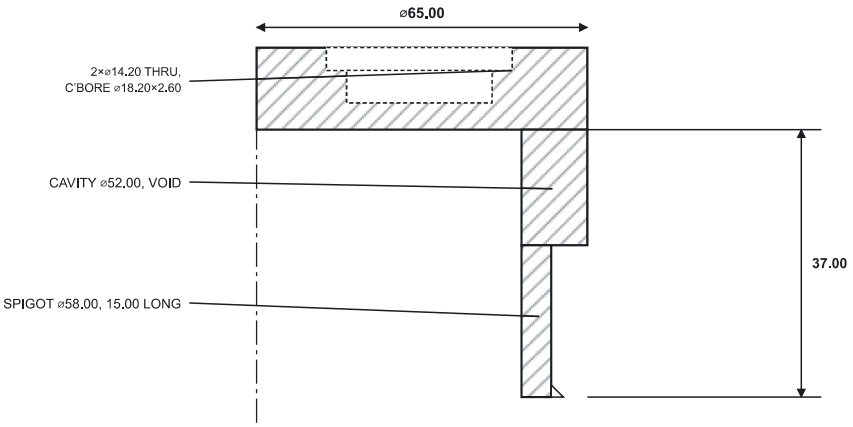


NOTES

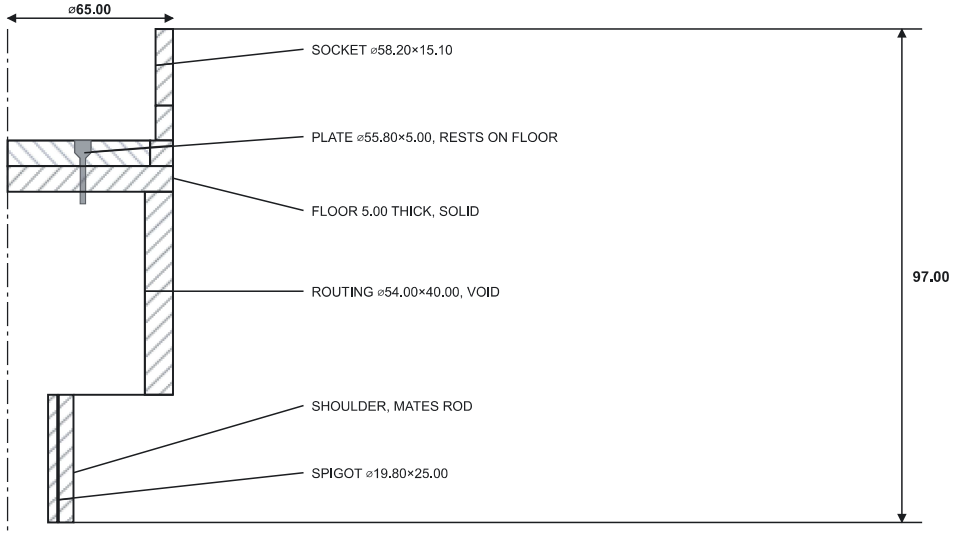
1. Both caps ⌀65.00, aluminium 6061-T6; continuous cylinder, no external step at the cap-to-cap joint.
2. Internal cavity is an open void from top wall to rod, interrupted only by the plate and the support floor.
3. No radial holes, screws or threads are made in the rod wall. See Sheet 2 for upper/lower cap detail.
4. **PRELIMINARY — NOT FOR MANUFACTURE. All dims mm.**

PROJECT **REDUCED SCALE TEST BENCH**	118	DWG NO **TB-HV-101**	REV **E**
		SCALE **1:1**	UNITS **mm**
TITLE **ASSEMBLY OVERVIEW** SIMPLIFIED 3-SHEET SET, TRUE SCALE		STATUS **PRELIM.**	DATE **2026-08-04**

A — UPPER CAP, HALF SECTION



B — LOWER CAP, HALF SECTION — PEEK PLATE SHOWN SEATED



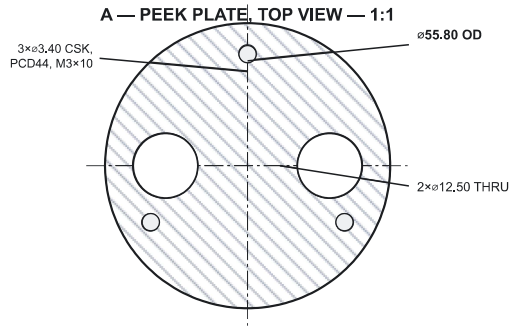
(ROD, EXISTING PART, REF)

NOTES

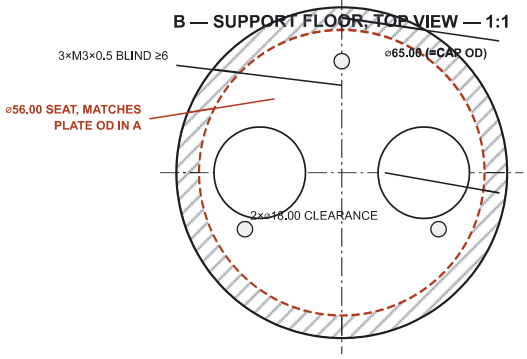
1. Axial (top to bottom): socket 15.10 · free space 6.90 · plate 5.00 · floor 5.00 · routing 40.00 · rod spigot 25.00 (total 97.00).
2. Plate rests flat on the floor's top face; the ⌀56.00 bore only guides the plate radially (0.20 clearance) — it is not a shoulder.
3. Plate fixed to floor by 3×M3×10 CSK screws, ⌀44 PCD — see Sheet 3. Cap screws 3×M3×6 bear on the upper-cap spigot only.
4. No radial holes, screws or threads in the rod wall. Material: aluminium 6061-T6 (both caps), unfilled PEEK (plate).
5. **PRELIMINARY — NOT FOR MANUFACTURE. All dims mm.**

PROJECT **REDUCED SCALE TEST BENCH**	119	DWG NO **TB-HV-102**	REV **E**
		SCALE **2:1 / 1:1**	UNITS **mm**
TITLE **UPPER CAP & LOWER CAP** A MATES B'S SOCKET — B MATES ROD ⌀26/⌀20		STATUS **PRELIM.**	DATE **2026-08-04**

A — PEEK PLATE, TOP VIEW — 1:1

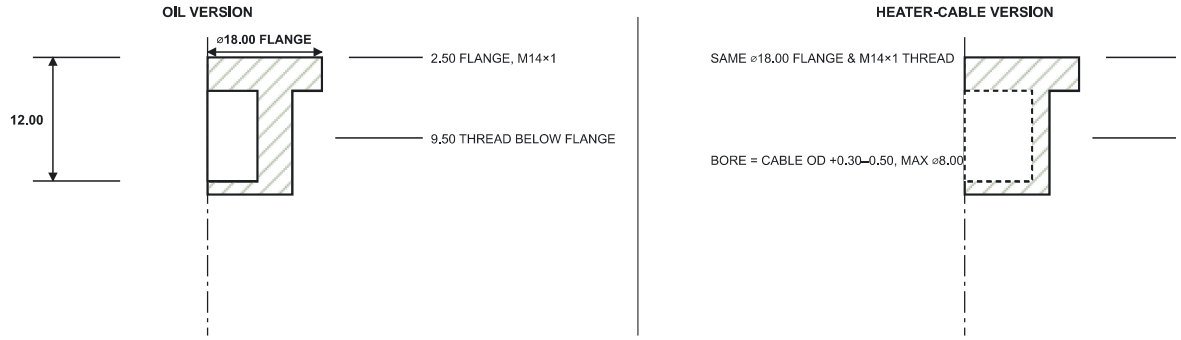


B — SUPPORT FLOOR, TOP VIEW — 1:1



C — PTFE TOP BUSHINGS, HALF SECTION — 5:1

PTFE, WITH M14×1 PEEK LOCKNUT (⌀18.00 MAX, PIN-SPANNER TYPE)



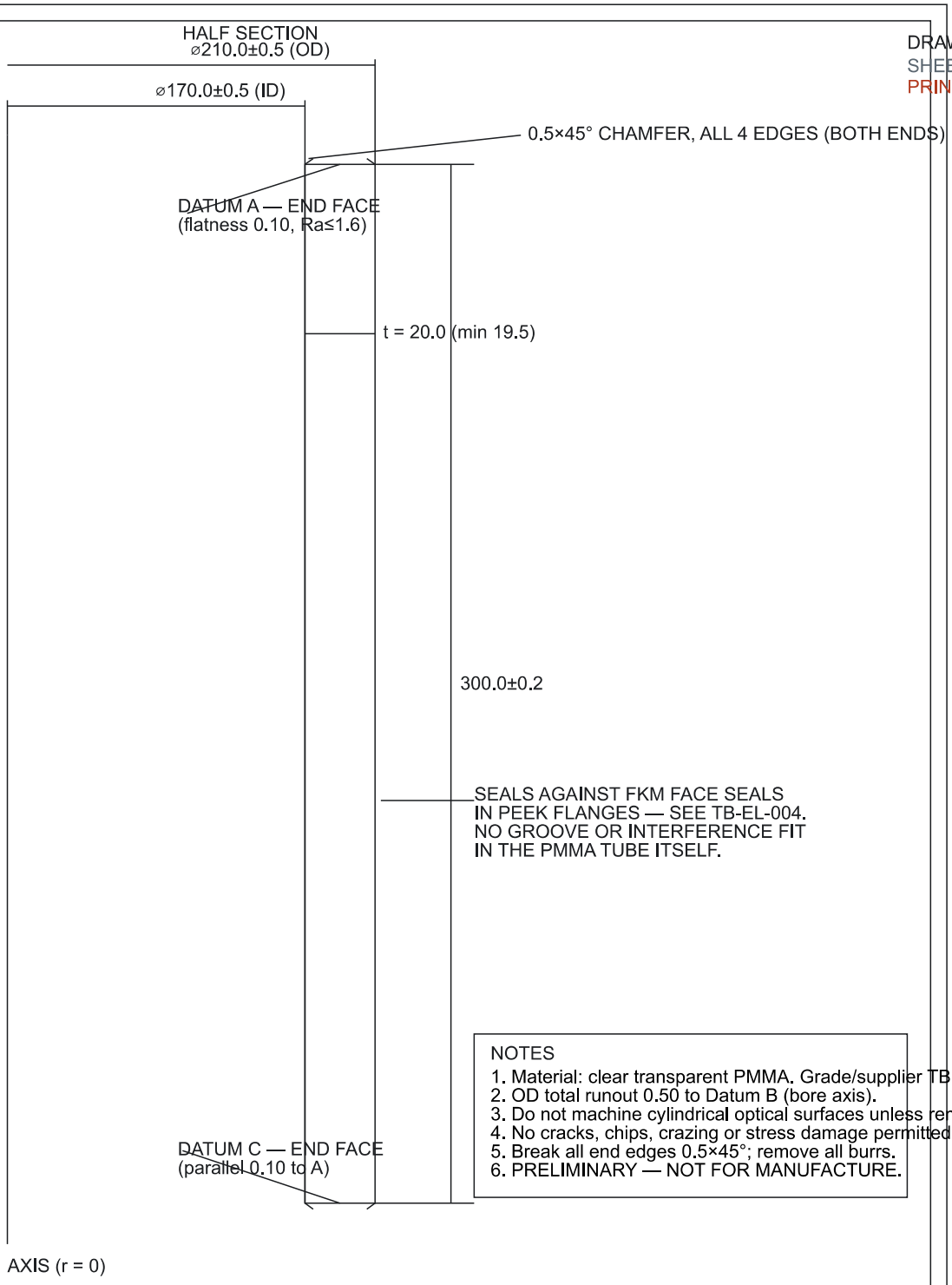
BILL OF MATERIALS

ITEM	COMPONENT	MATERIAL	QTY	ITEM	COMPONENT
1	Upper HV cap (Sheet 2A)	Al 6061-T6	1	5	Cap screw, M3×6 ISO4026
2	Lower HV cap (Sheet 2B)	Al 6061-T6	1	6	Plate screw, M3×10, CSK
3	PEEK support plate (A)	Unfilled PEEK	1	7	Oil unions / terminals (per config.)
4	PTFE top bushing + locknut (C)	PTFE / PEEK	2		

NOTES & CONFIGURATIONS

1. Two service positions, 32.00 centres (X=±16.00), serve either config: HOT-OIL — 2×⌀6/⌀4 PFA tubes, oil-return/supply unions. FLOATING-HEATER — insulated + bonded terminal, stud M6, max envelope ⌀20.00 each. Same plate/bushings serve both.
2. Only two spigot joints in the whole assembly (upper cap/lower socket; lower cap/rod bore) — no retaining ring, no radial rod holes.
3. PTFE bushings isolate tubes/cables electrically; they are NOT a pressure seal. Verify continuity between upper cap, lower cap, rod.
4. Pending hardware confirmation: union/terminal mounting dims, floor clearance vs. selected hardware, heater-cable OD.
5. **PRELIMINARY — NOT FOR MANUFACTURE. All dims mm.**

PROJECT **REDUCED SCALE TEST BENCH**	120	DWG NO **TB-HV-103**	REV **E**
		SCALE **1:1 / 5:1**	UNITS **mm**
TITLE **PLATE, FLOOR, BUSHINGS & BOM** A/B MATE LOWER CAP — C MATES UPPER CAP (SHEET 2)		STATUS **PRELIM.**	DATE **2026-08-04**



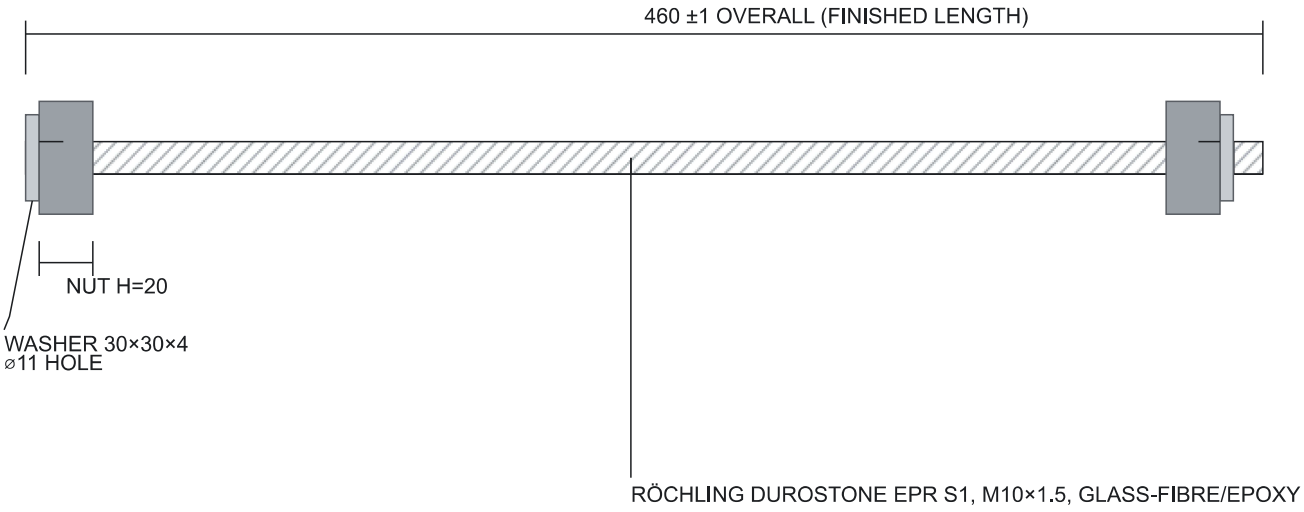
DRAWI
SHEET
PRINT

PROJECT REDUCED SCALE TEST BENCH	121	DWG NO TB-EL-006	REV A
		SCALE 3:1	UNITS mm
TITLE PMMA CHAMBER TUBE MATERIAL: CLEAR TRANSPARENT PMMA		STATUS PRELIM.	DATE 2026-08-03

SHE

LENGT
SHEET
PRINT

M10×1.5×460 GLASS-FIBRE/EPOXY TIE ROD, WITH HARDWARE AT EACH



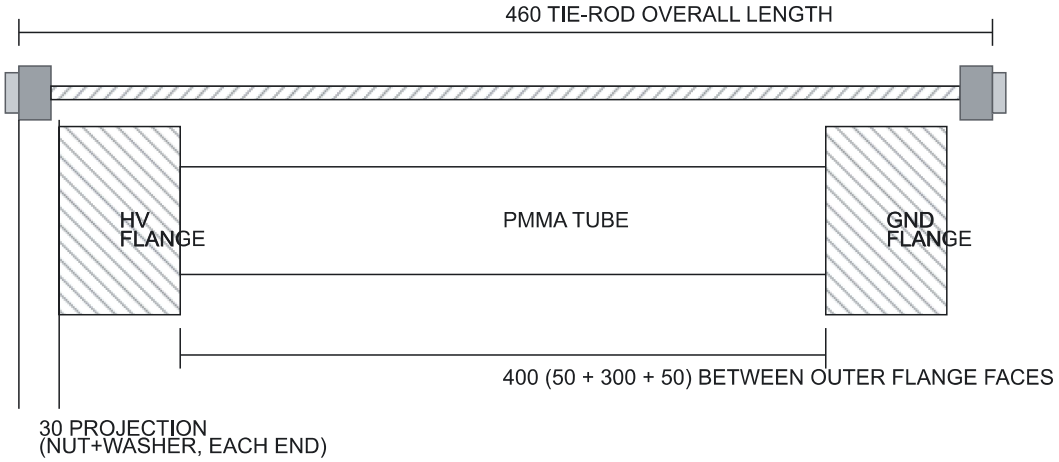
NOTES
1. Rod: 8× Röchling Durostone EPR S1, M10×1.5×460, cut from 1900 mm stock (article 100265).
2. Nuts: 16× Durostone EPM S7 hex, H=20 mm (double-height) — the H=10 nut is NOT permitted.
3. Washers: 16× Durostone EPC 308, 30×30×4, ⌀11 hole; orient sides radial/tangential.
4. Cut ends square within 0.5; break 0.5×45° max; no splintered fibres; seal cut ends with epoxy.
5. Nominal thread projection beyond each nut: 4 full pitches (min. 3).
6. Target preload: 5.00 ±0.25 kN per rod — set by calibrated load cell, not torque alone.
7. PRELIMINARY — NOT FOR MANUFACTURE.

PROJECT REDUCED SCALE TEST BENCH	122	DWG NO TB-EL-007	REV A
TITLE M10 GLASS/EPOXY TIE ROD MATERIAL: DUROSTONE EPR S1 / EPM S7 / EPC 308		SCALE 1:2 (LEN)	UNITS mm
		STATUS PRELIM.	DATE 2026-08-03

SHE

SCHEM
SHEET
PRINT

CHAMBER TUBE AND TIE-ROD ASSEMBLY — AXIAL STACK



8× tie rods on ⌀250 PCD, 45° spacing, first rod at 22.5° — see TB-EL-002 plan

BILL OF MATERIALS

ITEM	DESCRIPTION	QTY
1	PMMA tube, ⌀210/⌀170×300 (TB-EL-006)	1
2	PEEK end-flange assembly, 50 thick (TB-EL-002)	2
3	Durostone EPR S1 tie rod, M10×1.5×460 (TB-EL-007)	8
4	Durostone EPM S7 hex nut, M10, H=20	16
5	Durostone EPC 308 washer, 30×30×4, ⌀11	16
6	FKM PMMA face seal, 2-366	2

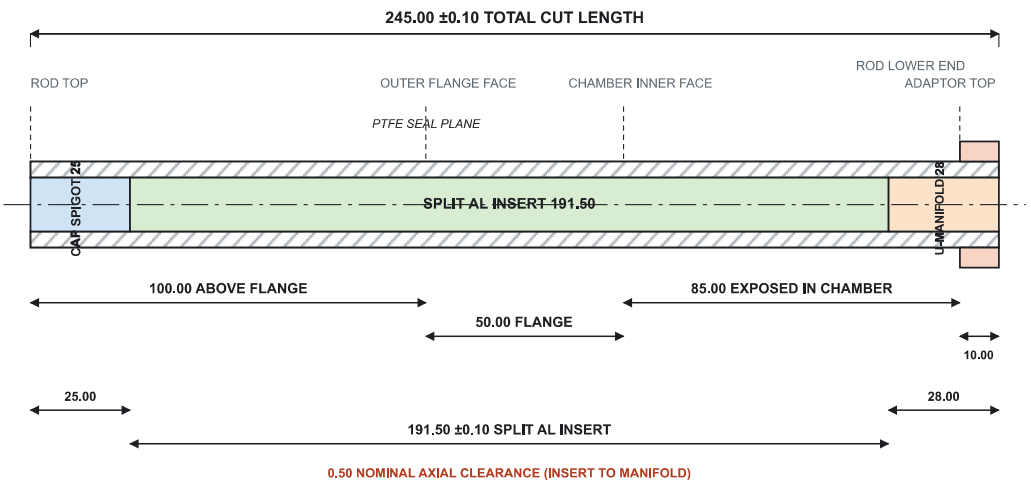
NOTES

1. Target preload 5.00 ±0.25 kN per rod; combined load per rod ≈ 9.44 kN at 0.6 MPa design basis.
2. Utilisation vs. Durostone EPM S7 (H=20) 22 kN breaking load, 50% sustained limit: ≈ 86% (max ≈ 88%).
3. H=10 mm nuts are NOT permitted — insufficient breaking load (12 kN) for this load case.
4. Tighten all 8 rods in a diametrically-opposite cross pattern, in ≥3 progressive steps.
5. Inner M6 Allen screws (TB-EL-002/003/004) are NOT part of the main chamber-retention load path.
6. Design basis: 6 bar differential pressure. This drawing is not a certified pressure-vessel rating.
7. PRELIMINARY — NOT FOR MANUFACTURE. Final acceptance requires supplier confirmation or test.
8. All dimensions in mm. Do not scale drawing.

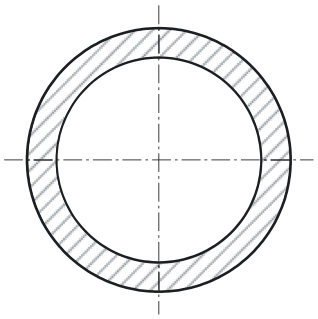
PROJECT REDUCED SCALE TEST BENCH	123	DWG NO TB-EL-008	REV A
TITLE CHAMBER TUBE AND TIE-ROD ASSEMBLY SEE BOM ABOVE FOR MATERIALS		SCALE NTS	UNITS mm
		STATUS PRELIM.	DATE 2026-08-03

SHE

HOLLOW ALUMINIUM HV ROD



END VIEW — SCALE 2:1



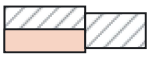
OD ⌀26 g6
BORE ⌀20.00 +0.05/0
WALL 3.00 NOM.

DETAIL A — UPPER CAP INTERFACE



⌀19.80×25.00 CAP SPIGOT
ROD END SEATS ON CAP SHOULDER

DETAIL B — ADAPTOR/ELECTRODE



10.00 ENGAGEMENT, ADAPTOR BORE ⌀26 H7
ROD LOWER FACE FLUSH
WITH ELECTRODE TOP FACE

FEATURE	VALUE
Material	Al 6061-T6
Total cut length	245.00±0.10
OD / Bore	⌀26 g6 / ⌀20+0.05
Wall thickness	3.00 nom.
Above outer flange	100.00±0.50
Flange traversed	50.00
Exposed in chamber	85.00
Adaptor engagement	10.00
Radial holes in wall	None

NOTES

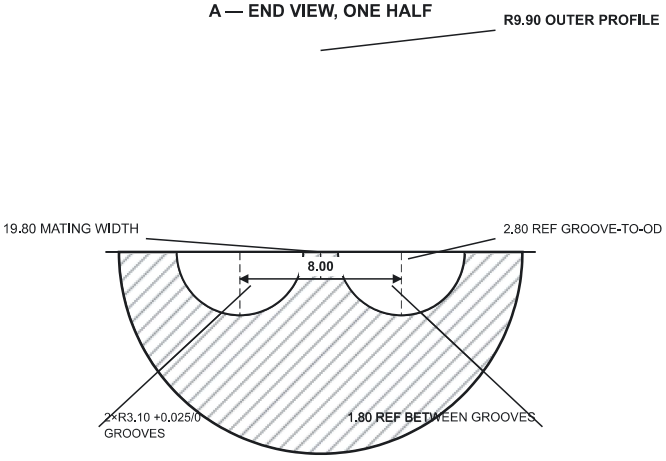
1. Rod OD continuous and smooth thru the PTFE flange-seal region; Ra≤0.8 µm over the full exposed OD, no machining steps at the seal.
2. Upper end receives the lower-HV-cap spigot ⌀19.80×25.00; 0.50×45° internal lead-in and external edge break.
3. Lower 10.00 of rod enters the adaptor ⌀26 H7 bore; rod lower face flush with adaptor lower face and electrode top face.
4. No radial screws, cross-holes or threads permitted in the 3.00 mm rod wall.
5. Bore and all end edges burr-free (protects PFA tubes and internal insert/manifold).
6. Insert length 191.50 assumes 0.50 total axial clearance to the U-manifold — see Sheet 2.
7. **PRELIMINARY — NOT FOR MANUFACTURE. All dims mm.**

PROJECT REDUCED SCALE TEST BENCH	124	DWG NO TB-HV-007	REV A
TITLE HOLLOW ALUMINIUM HV ROD SPLIT INSERT ON SHEET 2 (TB-HV-008)		SCALE SCHEM./2:1	UNITS mm
		STATUS PRELIM.	DATE 2026-08-04

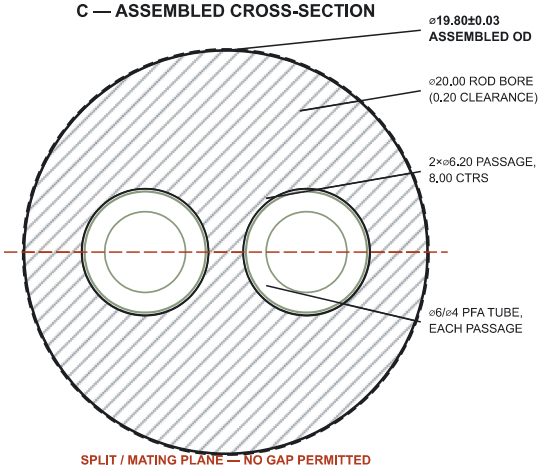
SPLIT ALUMINIUM TUBE-GUIDE INSERT

MATERIAL: ALUMINIUM 6061-T6 (OIL CONFIG.) OR PEEK (HEATER CONFIG., ELECTRICAL INSULATION) — TWO IDENTICAL HALVES PER ASSEMBLY

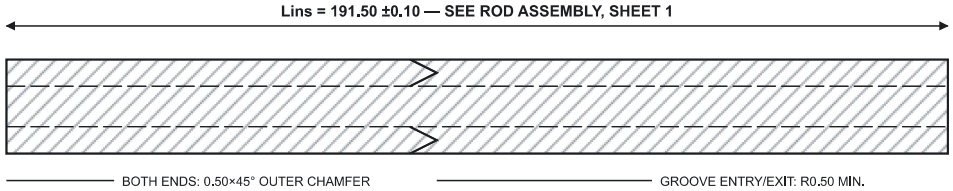
A — END VIEW, ONE HALF



C — ASSEMBLED CROSS-SECTION



B — LONGITUDINAL SIDE VIEW (SCHEMATIC)



NOTES

1. Two identical halves per assembly; one half inverted at assembly. Split plane passes through both tube centres.
2. No intentional gap permitted between the two flat mating faces. No adhesive, radial screws or rod-wall threads used for retention.
3. Insert axially captured between the lower-cap spigot (above) and the U-manifold or its retainer (below) — see Sheet 1.
4. Insert must not clamp, flatten or permanently deform the PFA tubes; it is not a pressure-containing component.
5. All PFA-contact surfaces (grooves, outer profile) Ra≤1.6 µm; remove all burrs and machining ridges.
6. Groove centres X=±4.00, Y=0 from insert centreline; grooves straight and parallel to the part axis, full length.
7. FLOATING-HEATER CONFIG.: same geometry, insert manufactured in unfilled PEEK instead of aluminium — insulates the heater cable from the surrounding aluminium rod. Dimensions and tolerances on this sheet apply to both material versions.
8. **PRELIMINARY — NOT FOR MANUFACTURE. Do not release insert length until Sheet 1 rod assembly is finalised. All dims mm.**

PROJECT **REDUCED SCALE TEST BENCH**	125	DWG NO **TB-HV-008**	REV **A**
TITLE **SPLIT ALUMINIUM TUBE-GUIDE INSERT** FITS INSIDE ROD BORE ⌀20.00 (TB-HV-007)		SCALE **4:1**	UNITS **mm**
		STATUS **PRELIM.**	DATE **2026-08-04**

B

Material Specifications for Test-Bench Construction

B.1. Purpose and Scope

This appendix defines the materials required to construct the proposed test bench. The bench was not fabricated during this thesis; the specifications therefore describe the construction basis rather than an as-built material record.

The appendix includes materials whose selection affects electrical insulation, heat transfer, sealing, mechanical stability, optical access, or experimental repeatability. Component geometry, dimensions, tolerances, surface finishes, fasteners, and assembly details are provided in Appendix A. Hydraulic and electrical sizing requirements are provided in Appendices C and D, respectively.

Commercial products are named only where their properties were used as a design or calculation reference. An equivalent product may be used when the relevant electrical, thermal, mechanical, dimensional, and chemical properties are verified before construction. Likewise, the generic material properties used in the numerical model are modelling inputs and do not automatically define the materials to be used for fabrication; see Appendix G.

B.2. Material Specifications

Table B.1 lists the material families that influence the intended operation of the test bench. The status column distinguishes fixed material choices from specifications that must be completed before construction.

Table B.1: Design-critical material specifications for the proposed test bench.

ID	Material	Main application	Required material specification	Status
M-01	Aluminium 6061	Electrodes, hollow rods, adaptors, conductive caps, and metallic supports	Aluminium 6061 is prescribed for the principal conductive and machined components. The final temper shall be recorded in the construction documentation. Geometry and fabrication requirements are defined in Appendix A.	Material fixed; temper to be finalised

Continued on the next page.

Table B.1 continued.

ID	Material	Main application	Required material specification	Status
M-02	Epoxy-resin system	Replaceable spacer specimens	The final record shall identify the resin, hardener, filler type and fraction where applicable, curing process, fabricator, and specimen batch. Relative permittivity and conductivity as a function of temperature shall be established for the material used in the experimental campaign.	Critical open specification
M-03	Clear cast PMMA	Chamber tube	Alternative Plastics clear cast acrylic tube, ∅210/∅170 mm design-reference geometry; supplier properties are given in Section B.3.3 [69].	Design-reference specification
M-04	PEEK	Chamber flanges, insulating supports, and oil-manifold parts	PEEK with suitable electrical insulation, temperature resistance, machinability, and dimensional stability. The exact grade, filler condition, and supplier data shall be documented [70].	Exact grade to be finalised
M-05	FKM elastomer	Static chamber seals	FKM compound compatible with laboratory air, the qualified temperature range, and the selected cleaning agents. Compound and hardness shall be selected together with the final seal design [71].	Compound and hardness to be finalised
M-06	Spring-energised PTFE seal system	Rod feedthroughs	The PTFE jacket compound, energiser material, temperature and chemical compatibility, and complete system identification shall be documented for the selected feedthrough seal [72].	Exact seal system to be finalised
M-07	PTFE	Oil-tube ferrules and selected insulating parts	PTFE compatible with the selected silicone fluid, the qualified operating temperature, and sustained compression. The grade used shall be recorded.	Exact grade to be finalised
M-08	Super-PFA	Hot-oil supply and return tubing	Super-PFA tubing compatible with the selected fluid and operating-temperature range. SMC TL0604 provides the reference material and product basis used in the hydraulic design; a verified equivalent may be used [65].	Reference specification
M-09	Silicone heat-transfer fluid	Hot-oil working fluid	Silicone fluid with nominal viscosity of 10 cSt at room temperature and with density, thermal expansion, and heat-capacity data consistent with the hydraulic calculation. XIAMETER PMX-200 10 cSt is the reference fluid [66], [67].	Reference specification
M-10	Copper conductors	Heater conductors, electrical connections, and floating loop	Copper conductor with the required current capacity, flexibility, and termination compatibility. Conductor cross-sections and routing requirements are defined in the relevant electrical design and sizing documentation.	Material fixed
M-11	XLPE cable insulation	Inner insulation of the external floating conductor	XLPE-insulated copper cable compatible with the composite insulation arrangement. Nexans HFIX is used as a reference specification and shall not be treated as an independently rated high-voltage cable [68].	Reference specification

Continued on the next page.

Table B.1 continued.

ID	Material	Main application	Required material specification	Status
M-12	Silicone electrical insulation	Additional common-mode insulation around the floating conductor	Electrically insulating silicone suitable for a continuous, void-controlled insulation layer. The exact grade, curing system, application method, and adhesion to adjacent materials shall be documented.	Grade and process to be finalised
M-13	PFA-insulated copper lead wire	Internal cartridge-heater connections	Copper lead wire with PFA insulation suitable for the selected heater current, local temperature, flexibility, and termination arrangement.	Exact wire specification to be finalised
M-14	PEEK or ceramic electrical insulation	Heater terminals and cable penetrations	The final material shall provide adequate dielectric behaviour, temperature resistance, dimensional stability, and mechanical strength. The selection shall be made together with the final terminal and bushing design.	Final material selection required
M-15	Laboratory air	Test-cell insulating medium	Laboratory air at approximately 1 bar absolute. Chamber pressure and temperature, together with ambient humidity, shall be recorded for each experimental run.	Fixed experimental medium

The spacer material remains the most important open specification. The generic epoxy properties and prescribed conductivity function used in the numerical model do not identify an experimentally reproducible resin system. The final experimental record must therefore link each spacer specimen to its formulation, fabrication route, batch, and electrical characterisation.

B.3. Materials of the Alternative Heating Architectures

B.3.1. Hot-Oil Architecture

The hot-oil architecture uses aluminium for conductive and heat-spreading parts, PEEK for insulating supports and the internal manifold, PTFE for compressed sealing or retention elements, Super-PFA for the contained fluid route, and silicone fluid as the heat-transfer medium. The detailed arrangement is defined in Appendix A, while the reference tubing and fluid properties used in the hydraulic calculation are documented in Appendix C.

A replacement fluid shall be accepted only after its viscosity, density, thermal expansion, and heat capacity have been checked against the hydraulic calculation. Replacement tubing shall be checked for fluid compatibility, temperature capability, and routing limitations.

B.3.2. Floating Cartridge-Heater Architecture

The floating cartridge-heater architecture uses aluminium for conductive caps and supports; PEEK, PTFE, or a qualified ceramic for terminal insulation and bushings; copper for the floating circuit; PFA for internal lead insulation; XLPE for the inner cable insulation; and silicone for the additional common-mode insulation.

The XLPE-insulated reference cable forms only one part of the complete insulation system. The cable, added silicone insulation, supports, terminations, and surrounding clearances must be qualified as an assembled system. Heater and conductor sizing is provided in Appendix D; the present material specification does not assign a high-voltage rating to the inner cable alone.

B.3.3. PMMA chamber tube

The design-reference chamber material is clear cast PMMA tube. A commercial reference is the clear cast acrylic tube supplied by Alternative Plastics, with a nominal geometry of ∅210/∅170 mm. The supplier reports a density of approximately 1.19 g/cm^3, an elastic modulus of approximately 3.2 GPa, a thermal conductivity of 0.19 W/(m K), a Vicat softening temperature of approximately 107°C and a dielectric strength of approximately 35 kV/mm [69]. These data define the preliminary material

properties used for the chamber design. The supplied tube must be checked against the required dimensions, temperature and mechanical loading before use.

B.4. Material Documentation Required Before Construction

Table B.2 defines the minimum material information that shall be retained by the future builder. The actual datasheets and certificates should form part of the construction and experimental record rather than being reproduced in full in this thesis.

Table B.2: Minimum material documentation required for construction.

Material category	Required construction record
Metallic stock	Alloy, temper, supplier, and material certificate.
Spacer material	Resin system, hardener, filler where applicable, cure cycle, fabricator, batch, and electrical characterisation.
Machined polymers	Polymer grade, filler condition, supplier, and manufacturer datasheet.
Elastomeric seals	Compound, hardness, supplier, and temperature and chemical compatibility.
Feedthrough seals	Complete seal-system identification and manufacturer design data.
Tubing and fluids	Exact product or grade, supplier, compatibility data, and the properties used in the hydraulic calculation.
Cables and electrical insulation	Conductor material, insulation material and grade, supplier data, and assembly-level qualification record where applicable.
Test medium	Chamber pressure and temperature, together with ambient humidity, for each run.

B.5. Boundary with the Engineering-Drawing Appendix

This appendix controls material families, reference specifications, and the documentation required for their use. Appendix A controls component geometry, dimensions, fits, tolerances, surface finishes, fasteners, seal-gland geometry, routing, assembly interfaces, and drawing revisions. Where a material choice changes a calculated thermal, hydraulic, or electrical property, the relevant sizing calculation shall be updated before fabrication.

The main material families are identified, but the spacer system, PMMA grade, PEEK grades, seal compounds, feedthrough seal system, silicone insulation process, and terminal-insulation material remain to be finalised before construction. Keeping these items explicit prevents the design specification from implying a level of fabrication readiness or qualification that was not reached during this thesis.

C

Thermal Sizing of the Hot-Oil Circulation Loop

C.1. Purpose and calculation method

The hot-oil loop must provide enough flow to transport the required thermal power without creating an excessive pressure drop. The sizing therefore follows four steps: determine the flow regime, calculate the tube pressure loss, estimate the thermal demand, and size the pump and reservoir. Reynolds number and Hagen–Poiseuille flow are used for the hydraulic calculation, while the transported heat is obtained from a steady-flow energy balance [121], [122]. Forced-circulation heat-transfer-oil systems use the same basic quantities: flow rate, pressure, temperature and an oil-side energy balance [92].

The calculation is a design check. It does not demonstrate the final oil-to-electrode heat transfer, which also depends on the PFA wall, solid contacts, aluminium insert, rod and electrode.

C.2. Design inputs

XIAMETER PMX-200 Silicone Fluid, 10 cSt, is used as the working-fluid basis. It was selected because its viscosity is low enough for the 4 mm tube while manufacturer data are available for the thermal and electrical properties required by the design [66]. The circulation lines use SMC TL0604 Super-PFA tubing [65].

Table C.1: Inputs used for the preliminary hydraulic sizing.

Quantity	Value	Basis
Working fluid	PMX-200, 10 cSt	Selected silicone fluid
Kinematic viscosity at 25°C, ν_{25}	10×10^{-6} m^2/s	Manufacturer property
Density at 25°C, ρ_{25}	940 kg/m^3	Manufacturer property
Volumetric expansion coefficient, β	1.08×10^{-3} K^{-1}	Manufacturer property
Specific heat at 100°C, c_p	1.76 kJ/(kg K)	Manufacturer property
Tube	SMC TL0604 Super-PFA	Selected component
Tube OD / ID	6/4 mm	Manufacturer geometry
Preliminary total tube length, L	2.0 m	Supply + return design assumption
Candidate flow range	100–300 mL/min	Preliminary design range
Nominal flow	200 mL/min	Selected operating point

The 2.0 m length is provisional. It must be replaced by the final supply-and-return length once the chamber routing is frozen.

C.3. Flow regime and pressure loss

For a tube internal diameter $D = 4$ mm, the flow area is

$$A = \frac{\pi D^2}{4} = 1.257 \times 10^{-5}\ \mathrm{m}^2. \tag{C.1}$$

The mean velocity is

$$v = \frac{\dot{V}}{A}. \tag{C.2}$$

At the nominal flow,

$$\dot{V} = 200\ \mathrm{mL/min} = 3.333 \times 10^{-6}\ \mathrm{m}^3/\mathrm{s}, \tag{C.3}$$

which gives

$$v = 0.265\ \mathrm{m/s}. \tag{C.4}$$

The Reynolds number is

$$\mathrm{Re} = \frac{vD}{\nu}. \tag{C.5}$$

At 200 mL/min,

$$\mathrm{Re} = \frac{(0.265)(0.004)}{10 \times 10^{-6}} \approx 106. \tag{C.6}$$

Table C.2: Flow velocity and Reynolds number for the candidate flow range.

Flow rate	Velocity	Reynolds number
100 mL/min	0.133 m/s	53
200 mL/min	0.265 m/s	106
300 mL/min	0.398 m/s	159

The complete operating range is therefore strongly laminar. At the nominal condition, the approximate hydrodynamic entrance length,

$$L_h \approx 0.05\,\mathrm{Re}\,D, \tag{C.7}$$

is about 21 mm, which is small compared with the provisional 2 m flow path. A fully developed laminar-flow relation is therefore adequate for the dominant straight-tube pressure loss.

At 25°C, the dynamic viscosity is

$$\mu = \rho\nu = (940)(10 \times 10^{-6}) = 9.4 \times 10^{-3}\ \mathrm{Pa\,s}. \tag{C.8}$$

For fully developed laminar flow in a circular tube, the Hagen–Poiseuille relation gives [122]

$$\Delta p_{\mathrm{tube}} = \frac{128\mu L\dot{V}}{\pi D^4}. \tag{C.9}$$

At the nominal flow,

$$\Delta p_{\mathrm{tube}} \approx 10.0\ \mathrm{kPa}. \tag{C.10}$$

A preliminary allowance of 30% is added for the U-manifold, fittings and routing that are not yet frozen:

$$\Delta p_{\text{design}} = 1.30\,\Delta p_{\text{tube}}. \tag{C.11}$$

Table C.3: Calculated tube pressure loss and preliminary design pressure loss.

Flow rate	Tube loss	With 30% allowance
100 mL/min	5.0 kPa	6.5 kPa
200 mL/min	10.0 kPa	13.0 kPa
300 mL/min	15.0 kPa	19.5 kPa

The 30% allowance is a temporary sizing assumption rather than a correlation. It should be replaced by component-specific losses after the final fittings and manifold are selected.

C.4. Heat demand and required oil temperature drop

The required oil heat transport is set by the heat lost from the heated electrode assembly. A first-order estimate is made for the conservative 100°C thermal-design condition with surroundings near 25°C, giving

$$\Delta T \approx 75\ \text{K}. \tag{C.12}$$

The aluminium rod has an outer diameter of 26 mm, an internal bore of 20 mm and a heated length of 80 mm. Its metallic cross-sectional area is

$$A_{\text{Al}} = \frac{\pi}{4}\left(D_o^2 - D_i^2\right) = 2.17 \times 10^{-4}\ \text{m}^2. \tag{C.13}$$

Using $k_{\text{Al}} = 167\ \text{W/(m K)}$ for aluminium 6061-T6, the conductive loss is bounded as

$$\dot{Q}_{\text{cond}} = k_{\text{Al}} A_{\text{Al}} \frac{\Delta T}{L} \approx 34\ \text{W}. \tag{C.14}$$

For a simple external-loss estimate, $A_s \approx 0.007\ \text{m}^2$, $h \approx 10\ \text{W/(m}^2\,\text{K)}$, and $\varepsilon \approx 0.3$ are used as conservative design assumptions. The resulting losses are

$$\dot{Q}_{\text{conv}} = h A_s \Delta T \approx 5.3\ \text{W}, \tag{C.15}$$

and

$$\dot{Q}_{\text{rad}} = \varepsilon \sigma A_s \left(T_h^4 - T_a^4\right) \approx 1.4\ \text{W}. \tag{C.16}$$

The estimated total is therefore

$$\dot{Q}_{\text{loss}} \approx 34 + 5.3 + 1.4 \approx 41\ \text{W}. \tag{C.17}$$

Because this is a simplified upper-bound calculation, the loop is sized for an order-of-magnitude thermal demand of

$$\boxed{\dot{Q}_{\text{req}} \sim 50\ \text{W}}. \tag{C.18}$$

The oil temperature drop required to transport this heat follows from the steady-flow energy balance [92], [121]

$$\dot{Q}_{\text{oil}} = \dot{m} c_p \Delta T_{\text{oil}}. \tag{C.19}$$

The oil density near 100°C is estimated from the volumetric expansion coefficient:

$$\rho_{100} \approx \frac{\rho_{25}}{1 + \beta(100 - 25)} = \frac{940}{1 + (1.08 \times 10^{-3})(75)} \approx 870 \text{ kg/m}^3. \tag{C.20}$$

At the nominal flow,

$$\dot{m} = \rho \dot{V} \approx (870)(3.333 \times 10^{-6}) = 2.90 \times 10^{-3} \text{ kg/s}. \tag{C.21}$$

With $c_p = 1.76$ kJ/(kg K) at 100°C,

$$\Delta T_{\text{oil}} = \frac{\dot{Q}_{\text{req}}}{\dot{m} c_p} \approx \frac{50}{(2.90 \times 10^{-3})(1760)} \approx 9.8 \text{ K}. \tag{C.22}$$

Hence,

$$\boxed{\Delta T_{\text{oil}} \approx 10 \text{ K}} \tag{C.23}$$

at the nominal 200 mL/min flow. The 10 K value is therefore a result of the heat-demand estimate, not an assumed input.

This calculation only establishes the sensible heat that the fluid can transport. The actual delivered heat also depends on the thermal resistance of the PFA wall, insert and contact interfaces, rod and electrode. That path must be assessed by the thermal model and by later qualification.

C.5. Pump and reservoir sizing

The nominal preliminary pressure requirement is approximately 13 kPa, while the upper design flow remains below approximately 20 kPa. The preliminary pump requirement is therefore

$$\boxed{\dot{V}_{\text{pump}} \geq 0.30 \text{ L/min} \quad \text{at} \quad \Delta p \geq 30 \text{ kPa}}. \tag{C.24}$$

The final pump must be selected from its pressure–flow curve and checked for compatibility with the selected silicone fluid and operating temperature.

The internal fluid volume of the tubing is

$$V_{\text{tube}} = \frac{\pi D^2}{4} L. \tag{C.25}$$

For $D = 4$ mm and $L = 2$ m,

$$V_{\text{tube}} \approx 25 \text{ mL}. \tag{C.26}$$

The fluid expansion from 25°C to 100°C is

$$\frac{\Delta V}{V_0} = \beta \Delta T = (1.08 \times 10^{-3})(75) \approx 0.081, \tag{C.27}$$

or approximately 8.1%. For a cold fill of 180 mL,

$$\Delta V \approx 14.6 \text{ mL}. \tag{C.28}$$

A preliminary reservoir of 250 mL with approximately 180 mL cold fill therefore leaves sufficient headspace for thermal expansion and bubble separation.

C.6. Bend-radius check

SMC specifies a recommended minimum bend radius of 35 mm for TL0604 tubing [65]. A free 180° return bend would therefore require a centreline diameter of approximately

$$2R_{\text{min}} = 70 \text{ mm}. \tag{C.29}$$

The aluminium rod provides only a 20 mm internal bore. Since

$$70 \text{ mm} > 20 \text{ mm}, \tag{C.30}$$

a free PFA return bend cannot be accommodated inside the rod. The separate lower U-manifold is therefore required to reverse the flow without forcing the selected tubing below its recommended free-bend radius.

C.7. Preliminary hydraulic specification

Table C.4: Preliminary hydraulic specification of the hot-oil loop.

Quantity	Preliminary design value
Working fluid	XIAMETER PMX-200 Silicone Fluid, 10 cSt
Tube	SMC TL0604 Super-PFA, 6/4 mm
Preliminary total tube length	2.0 m
Nominal flow	200 mL/min
Operating range	100–300 mL/min
Reynolds number at nominal flow	106
Nominal straight-tube pressure drop	10 kPa
Nominal preliminary total pressure drop	13 kPa
Pump requirement	$\geq$ 0.30 L/min at $\geq$ 30 kPa
Design heat demand	order 50 W
Required oil temperature drop at nominal flow	approximately 10 K
Preliminary reservoir	250 mL
Suggested cold fill	approximately 180 mL
Fluid expansion from 25°C to 100°C	8.1%
Flow regime	laminar
Tube recommended bend radius	35 mm

The hydraulic calculation shows that pressure loss is modest for the selected 4 mm-ID tube. At the nominal flow, the straight-tube loss is approximately 10 kPa, while the oil temperature drop required to transport the order-50 W design heat demand is approximately 10 K.

Three quantities remain provisional. The 2 m tube length must be replaced by the final routing length, the 30% local-loss allowance must be replaced by the actual fitting and manifold losses, and the order-50 W heat demand must be confirmed by the final thermal model and later bench qualification. Hydraulic capacity alone does not verify the complete oil-to-electrode heat-transfer path.

C.8. Proposed Control and Protection Logic

The hot-oil system regulates the selected hot-side electrode temperature, T_{hot}, to a prescribed setpoint $T_{\text{hot,set}}$. The circulation pump remains active throughout thermal conditioning, while the external oil

heater is the controlled actuator. The physical electrode temperatures, T_{HV} and T_{GND}, are measured independently so that the signed temperature difference

$$\Delta T = T_{HV} - T_{GND} \tag{C.31}$$

can be evaluated for either gradient direction. The oil temperature, T_{oil}, is monitored separately as a protection variable.

If $T_{oil} \geq T_{oil,max}$, the heater is disabled while circulation continues. The value $T_{oil,max}$ is the qualified protection limit of the realised loop and is governed by the lowest applicable component rating.

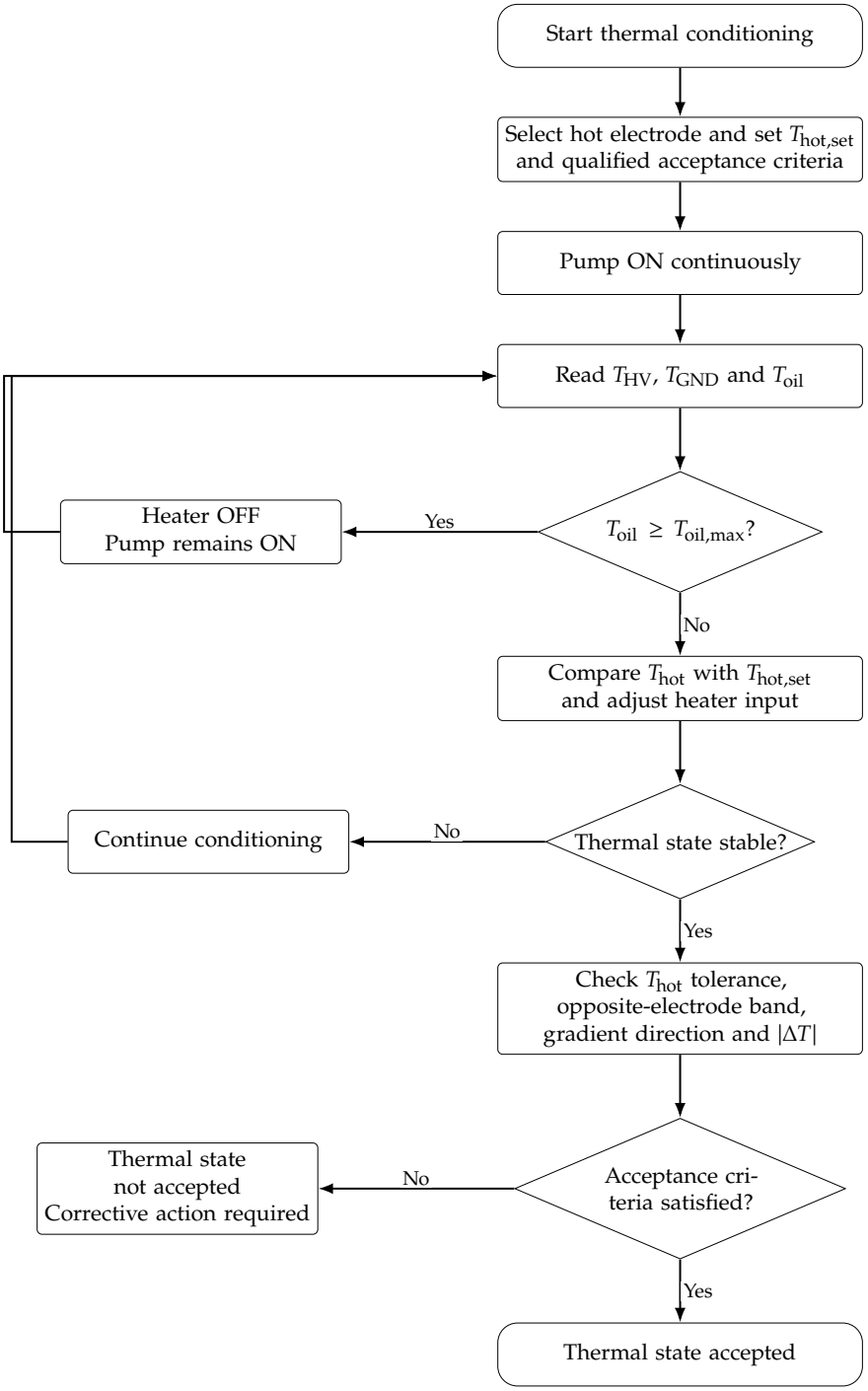


Figure C.1: Proposed control and protection logic for the hot-oil heating system. The selected hot-side electrode is temperature-controlled, while the realised gradient is checked only after the thermal state has stabilised.

The thermal state is accepted only when T_{hot} satisfies its qualified stability and setpoint criteria, the opposite-electrode temperature remains within its qualified acceptance band, the required gradient direction is established, and $|\Delta T|$ = 40–50 K. If the thermal state is stable but these acceptance criteria are not met, the condition is rejected rather than allowing the controller to continue indefinitely. The setpoint, tolerances, stability duration and protection limits are established during method qualification.

Table C.5: Functional control requirements of the hot-oil system.

Element	**Function**	**Requirement**
Circulation pump	Maintains oil circulation	$\geq$ 0.30 L/min at $\geq$ 30 kPa on the preliminary routing basis.
Oil heater	Provides controlled thermal input	Externally located; final power rating confirmed from the realised thermal response.
Temperature controller	Regulates T_{hot}	PID or equivalent feedback control.
Electrode sensors	Measure T_{HV} and T_{GND}	Independent measurements suitable for the respective electrode potentials.
Oil-temperature sensor	Provides protection input	Independent T_{oil} monitoring with heater-inhibit function.
Logger / DAQ	Records thermal history	Records T_{HV}, T_{GND} and T_{oil}.

The logic represents the baseline one-active-side operating mode. If qualification shows that the opposite electrode cannot remain within its acceptance band passively, its heating provision may be used as an additional control input.

D

Preliminary Electrical Sizing of the Floating Cartridge-Heater Circuit

D.1. Purpose and Design Basis

The floating cartridge-heater concept generates heat directly inside the selected electrode. The cartridge heater is designed to provide the dominant electrical resistance in the floating secondary circuit, while the connecting conductors have a much lower resistance. The induced electrical power is therefore dissipated mainly in the heater rather than along the floating loop.

The transformer is an existing laboratory component and is treated as fixed hardware. Its magnetic design is outside the scope of this appendix. The calculations below provide a preliminary sizing basis for the cartridge heater and floating conductor, define the electrical load that the existing transformer must supply, and screen the common-mode insulation geometry. The principal remaining feasibility check is whether the available transformer can deliver the required secondary voltage and current continuously under representative load.

An order-50 W thermal demand is used as the preliminary sizing basis because both heating concepts are intended to establish the same electrode and spacer thermal condition. The cartridge heater generates this heat directly inside the electrode and therefore avoids the intermediate fluid heat-transfer path of the hot-oil concept. The actual steady electrical input required by the realised assembly must still be established during qualification.

A 75 W cartridge is adopted to provide control margin above the preliminary thermal demand:

$$P_{\mathrm{th}} \approx 50\ \mathrm{W}, \qquad P_{h,\mathrm{rated}} = 75\ \mathrm{W}. \tag{D.1}$$

The nominal power margin is therefore

$$\frac{P_{h,\mathrm{rated}}}{P_{\mathrm{th}}} = \frac{75}{50} = 1.5. \tag{D.2}$$

The heater therefore provides approximately 50% nominal power margin. It is not intended to operate continuously at full rated power.

D.2. Preliminary Heater Rating

A low-voltage heater rating of

$$V_{h,\mathrm{rated}} = 24\ \mathrm{V} \tag{D.3}$$

is adopted as the preliminary design point. From

$$P_h = V_h I_h, \tag{D.4}$$

the rated heater current is

$$I_h = \frac{75}{24} \approx 3.13 \text{ A}. \tag{D.5}$$

The corresponding heater resistance is

$$R_h = \frac{V_h^2}{P_h} = \frac{24^2}{75} = 7.68\ \Omega. \tag{D.6}$$

The preliminary heater specification is therefore

$$\boxed{V_h = 24 \text{ V}, \quad P_h = 75 \text{ W}, \quad I_h \approx 3.13 \text{ A}, \quad R_h \approx 7.7\ \Omega}. \tag{D.7}$$

At an order-50 W operating requirement, the same resistance would require

$$V_h = \sqrt{P_h R_h} = \sqrt{50 \times 7.68} \approx 19.6 \text{ V}, \tag{D.8}$$

with

$$I_h = \frac{19.6}{7.68} \approx 2.55 \text{ A}. \tag{D.9}$$

A useful preliminary heater-side operating range is therefore

$$\boxed{V_s \approx 20\text{–}24 \text{ V}, \qquad I_s \approx 2.6\text{–}3.1 \text{ A}} \tag{D.10}$$

for approximately 50–75 W of heater power. These values define the desired operating range of the floating load; they are not measured characteristics of the existing transformer.

D.3. Floating-Loop Conductor and Resistive Losses

The heater and connecting conductors form a series circuit. Their relative heat generation is therefore set directly by their resistance ratio:

$$\frac{P_{\text{loop}}}{P_h} = \frac{R_{\text{loop}}}{R_h}. \tag{D.11}$$

A 4 mm^2 copper conductor is selected for the floating loop. A total loop length of 2 m is used as a preliminary routing assumption. Using a conservative hot-state copper resistivity of approximately

$$\rho_{\text{Cu,100}} \approx 2.3 \times 10^{-8}\ \Omega\,\text{m}, \tag{D.12}$$

based on standard copper-property data [124], the loop resistance is

$$R_{\text{loop}} = \rho \frac{L}{A} \approx 2.3 \times 10^{-8} \frac{2}{4 \times 10^{-6}} \approx 0.0115\ \Omega. \tag{D.13}$$

At the rated heater current,

$$P_{\text{loop}} = I_h^2 R_{\text{loop}} \approx (3.13)^2(0.0115) \approx 0.11 \text{ W}. \tag{D.14}$$

Compared with the 75 W cartridge,

$$\frac{P_{\text{loop}}}{P_h} \approx 0.15\%. \tag{D.15}$$

Thus,

$$\boxed{R_{\text{loop}} \ll R_h} \tag{D.16}$$

and the calculated resistive dissipation is concentrated almost entirely in the cartridge heater. The conductor current density is

$$J = \frac{3.13}{4} \approx 0.78 \text{ A/mm}^2. \tag{D.17}$$

The conductor is therefore electrically conservative. Its final construction is governed more strongly by mechanical routing and common-mode HV insulation than by copper loss.

D.4. Heater-Power Control and Thermal-Control Logic

The floating heater is controlled entirely from the grounded primary side. For the HV-hot configuration considered in this appendix, the HV-electrode temperature, T_{HV}, is the controlled thermal variable. The grounded-electrode temperature, T_{GND}, is measured independently and is used only to evaluate the realised gradient and the opposite-electrode acceptance condition. The controller therefore does not regulate ΔT directly.

For a fixed transformer configuration and operating frequency, the secondary voltage can be represented in first order by

$$V_s \approx kV_p, \tag{D.18}$$

where k is the effective transfer ratio. The value of k is presently unknown because the available transformer has not yet been characterised under the selected load. Since $R_{\text{loop}} \ll R_h$,

$$I_s \approx \frac{V_s}{R_h}, \tag{D.19}$$

and the cartridge power is approximately

$$P_h \approx \frac{V_s^2}{R_h} \approx \frac{k^2 V_p^2}{R_h}. \tag{D.20}$$

Equation D.20 describes only the control principle. The actual relation between primary excitation and heater power must be measured during loaded transformer characterisation. The same characterisation must establish the allowable primary voltage, current and thermal operating limits before controller tuning.

The proposed baseline control logic is shown in Figure D.1. The control sequence starts by defining the HV-electrode setpoint, its allowable tolerance and stability duration, the acceptable grounded-electrode temperature band, the required gradient direction, the acceptance range $|\Delta T|$ = 40–50 K, and the primary-side protection limits. During conditioning, T_{HV} is measured by the electrically isolated fibre-optic sensor, while T_{GND}, primary current and, if implemented, magnetic-core temperature are monitored independently.

If a protection limit is exceeded or a required sensor signal is lost, the primary excitation is removed and the system enters a fault/cooldown state. Under normal conditions, a PID or equivalent controller acts only on the error between $T_{\mathrm{HV,set}}$ and T_{HV}. Its demand is applied by a grounded primary-side power stage subject to the limits established during transformer characterisation. The final modulation method is not fixed at this stage. Continuous-amplitude control or whole-cycle time-proportioning may be used, provided the selected method remains within the characterised transformer operating envelope.

The thermal state is not accepted merely because T_{HV} reaches its setpoint. Once T_{HV} is stable within its qualified tolerance, the measured T_{GND} is checked against its qualified acceptance band, the required gradient direction is confirmed, and the realised $|\Delta T|$ is checked against the 40–50 K experimental range. If these criteria are not satisfied, the condition is rejected or the operating point is revised during method qualification rather than allowing the controller to drive ΔT independently.

Table D.1 summarises the functional control and measurement requirements. Exact controller settings, primary-side limits and modulation parameters remain qualification outputs because they depend on the measured response of the existing transformer and the realised thermal assembly.

Table D.1: Functional control and measurement requirements for the floating cartridge-heater circuit.

Element	Function	Requirement
HV-electrode temperature sensor	Primary thermal feedback	Fibre-optic or equivalent electrically isolated measurement of T_{HV}.
Grounded-electrode temperature sensor	Opposite-side thermal measurement	Independent T_{GND} measurement for the acceptance band, gradient direction and $\lvert\Delta T\rvert$ check.
Temperature controller	Regulates the selected hot-side electrode	PID or equivalent feedback control using $T_{\mathrm{HV,set}} - T_{\mathrm{HV}}$.
Primary-side power stage	Applies the controller demand to the transformer primary	Ground-referenced actuation; final modulation method and excitation limits fixed after loaded transformer characterisation.
Primary-current monitoring	Electrical protection of the grounded excitation circuit	I_{primary} monitored against the characterised operating limit.
Core-temperature monitoring	Thermal protection of the magnetic coupler	Recommended protection input if required by loaded transformer characterisation.
Transformer and floating loop	Transfers power across the HV boundary	Must demonstrate approximately 20–24 V at 2.6–3.1 A at the floating load under representative operating conditions.
Data acquisition / logging	Records thermal history and protection state	Records T_{HV}, T_{GND}, realised ΔT, controller demand, primary current and fault/protection state.

The logic above applies directly to the HV-hot configuration, for which the floating inductive supply is required. When the gradient is reversed and the grounded electrode is the selected hot side, the same thermal acceptance logic is retained with T_{GND} as T_{hot} and T_{HV} as T_{opposite}, but the grounded cartridge can be supplied conventionally. In both directions, the setpoint, tolerance, stability duration, opposite-electrode acceptance band and protection limits are fixed during method qualification.

D.5. Preliminary Cartridge-Heater Selection

The electrode provides sufficient internal volume for a compact industrial cartridge heater while retaining its external field-defining profile. A heater diameter near 6–6.5 mm and a sheath length of approximately 25 mm provide a suitable preliminary geometry.

For a 6.5 mm diameter and 25 mm heated length, the approximate cylindrical sheath area is

$$A_h = \pi d_h L_h \approx 5.1\ \mathrm{cm}^2. \tag{D.21}$$

The nominal surface loading is therefore

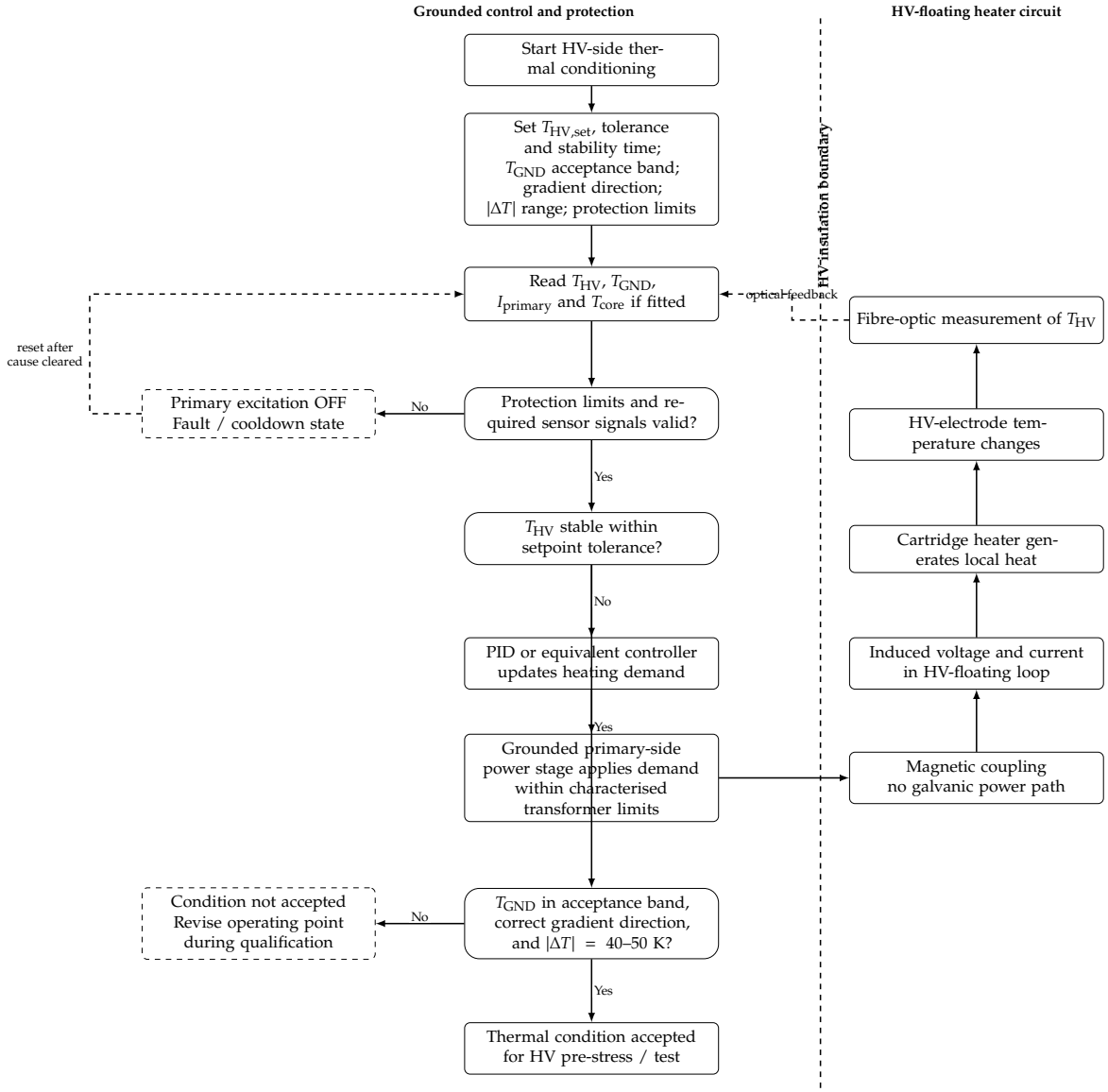


Figure D.1: Proposed control and protection logic for the floating cartridge-heater circuit in the HV-hot configuration. The HV-electrode temperature is the controlled variable. The grounded-electrode temperature and the realised $|\Delta T|$ are acceptance checks after thermal stabilisation, not independent controller targets. Electrical power crosses the HV boundary only by magnetic coupling, while the temperature feedback crosses it through the fibre-optic measurement.

$$q'' = \frac{75}{5.1} \approx 14.7\ \mathrm{W/cm^2}. \tag{D.22}$$

The Durex Industries cartridge-heater family provides a suitable commercial design basis. Durex offers cartridge heaters in this diameter range, allows voltage, wattage, length and termination to be specified, and lists a maximum current of 4 A for the 6.5 mm family and 4.2 A for the nominal 1/4-inch family [123]. The calculated current of 3.13 A remains below either limit.

The preliminary procurement specification is therefore

$$\boxed{\begin{array}{l}\text{industrial cartridge-heater family,}\\ d_h \approx 6.5\ \mathrm{mm},\\ L_h \approx 25\ \mathrm{mm},\\ V_h = 24\ \mathrm{V},\\ P_h = 75\ \mathrm{W}.\end{array}} \tag{D.23}$$

The exact ordering code, lead arrangement and machined-hole tolerance remain to be fixed with the final heater selection. The heater manufacturer's installation guidance should be used when fixing the final hole tolerance and permissible watt density in aluminium [123].

D.6. Common-Mode Insulation of the Floating Secondary

The magnetic coupling removes the galvanic connection between the grounded power supply and the HV-side heater, but it does not remove the HV-to-ground insulation requirement. The floating secondary remains near the electrode potential while the transformer core is grounded. The cable-to-core arrangement must therefore withstand the full common-mode design voltage,

$$V_{\mathrm{CM}} = 60\ \mathrm{kV}. \tag{D.24}$$

D.6.1. Model Geometry

The common-mode insulation condition was assessed using a two-dimensional electrostatic COMSOL model of the floating cable centred within the grounded transformer core. The transformer window is approximately 330×360 mm and the insulated cable has an outside diameter of approximately 28 mm. This gives minimum cable-to-core clearances of approximately 151 mm horizontally and 166 mm vertically.

As a first bulk-clearance check,

$$E_{\mathrm{bulk}} = \frac{60\ \mathrm{kV}}{151\ \mathrm{mm}} \approx 0.40\ \mathrm{kV/mm}. \tag{D.25}$$

This is a clearance-averaged field scale rather than the local electric field, because the geometry is non-uniform and part of the voltage is supported by the solid cable insulation. It nevertheless shows that the transformer window provides substantial bulk clearance. The relevant screening question is therefore the local field concentration around the insulated floating conductor.

The electrostatic model uses the following insulation stack:

$$\mathrm{Cu} \rightarrow \text{primary cable insulation} \rightarrow 12\ \mathrm{mm\ silicone} \rightarrow \mathrm{air} \rightarrow \text{grounded core}. \tag{D.26}$$

The primary cable insulation in the model is approximately 1 mm thick. The final design-reference conductor is a Nexans HFIX stranded $1 \times 4\ \mathrm{mm^2}$ XLPE-insulated cable, for which the manufacturer specifies an average insulation thickness of approximately 0.8 mm and an insulated-core diameter of 3.8–4.7 mm [68]. The HFIX conductor is used only as the inner insulated conductor and is not itself treated as a 60 kV-rated cable. With the additional 12 mm radial silicone layer, the resulting outside

diameter is approximately 27.8–28.7 mm, closely matching the approximately 28 mm geometry used in the model. The small difference between the modelled and selected primary-insulation thickness is retained as a final-verification item rather than being treated as a conservative equivalence.

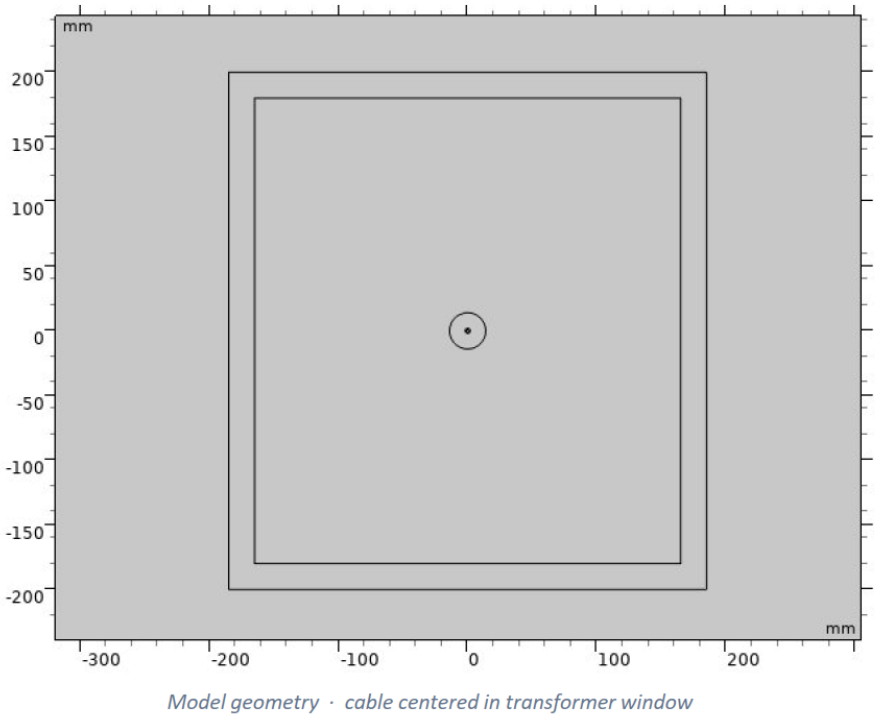


Figure D.2: Geometry used for the 60 kV common-mode insulation screening of the floating secondary.

D.6.2. Electric-Field Screening

The COMSOL model applies the 60 kV common-mode voltage to the floating conductor while the transformer core is grounded. The resulting field is concentrated close to the insulated conductor and decreases through the composite insulation and surrounding air toward the grounded core.

The unrestricted global maximum of the finite-element solution is not used as the insulation criterion because idealised edges and material junctions can produce mesh-sensitive singular values. Representative local fields are instead read away from these singular points at physically meaningful locations in the insulation stack.

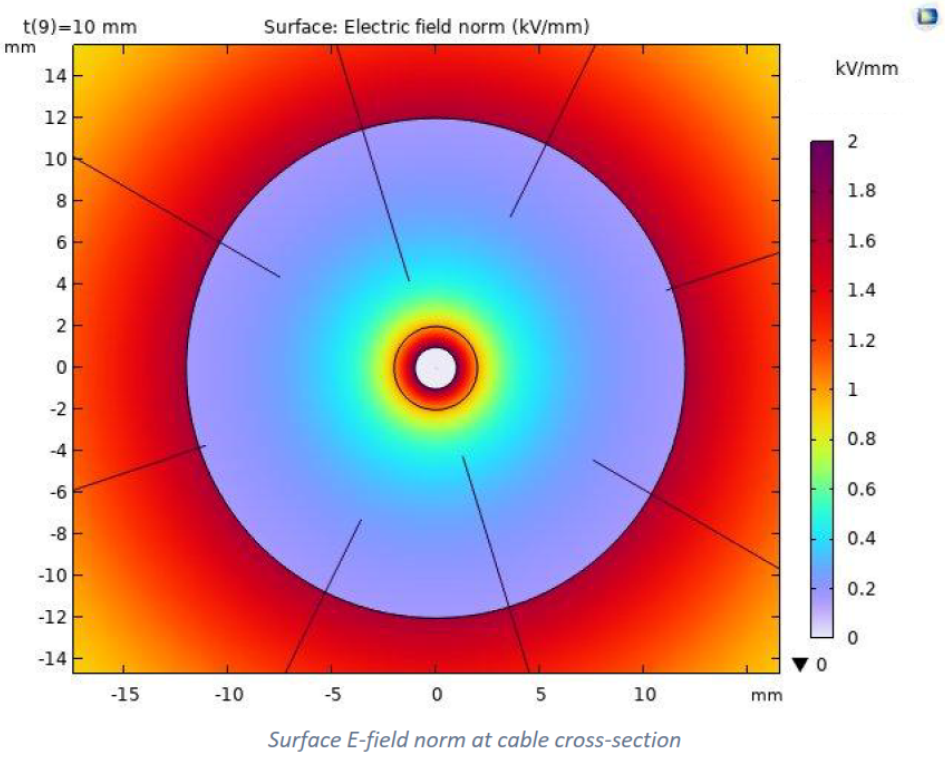


Figure D.3: Electric-field magnitude around the floating cable for the 60 kV common-mode design case. Representative local field values are taken away from mesh-sensitive singular points.

Table D.2: Representative local electric-field levels from the 60 kV transformer-window screening model.

Location / region	Representative field	Interpretation
Conductor–primary-insulation interface	~ 2.0 kV/mm	Local inner-interface field; singular corner values excluded.
Primary cable insulation, away from inner interface	~ 1.0 kV/mm	Representative field through the main cable-insulation region.
Additional silicone insulation	~ 1.2 kV/mm	Representative field within the added common-mode insulation.
Outer silicone–air surface	~ 1.2 kV/mm	Below the adopted 1.5 kV/mm air-side screening criterion.

The air-side value is the most relevant external-insulation screening result. The representative field at the outer silicone–air surface is approximately 1.2 kV/mm, below the adopted 1.5 kV/mm criterion. The 1.5 kV/mm value is a thesis design-screening criterion rather than a universal air-breakdown limit. Together with the minimum modelled 151 mm cable-to-core clearance, the electrostatic result supports the feasibility of the proposed common-mode insulation geometry at the 60 kV design-verification level.

This remains a numerical screening result rather than a physical withstand demonstration. Cable terminations, support geometry, manufacturing tolerances, contamination and nearby grounded hardware can introduce local field enhancement that is not represented by the simplified model. The completed floating-secondary-to-ground arrangement must therefore still be electrically qualified before HV operation.

D.7. Preliminary Specification and Remaining Checks

Table D.3 summarises the preliminary electrical and control design basis.

Table D.3: Preliminary design basis for the floating cartridge-heater circuit.

Quantity	Preliminary value
Thermal design demand	~ 50 W
Cartridge rated power	75 W
Cartridge voltage	24 V
Cartridge current	3.13 A
Cartridge resistance	7.68 Ω
Useful heater-power range	~ 50–75 W
Required secondary voltage	~ 20–24 V
Required secondary current	~ 2.6–3.1 A
Heater diameter	~ 6.5 mm
Heater length	~ 25 mm
Candidate heater family	Durex custom cartridge-heater family
Floating conductor	4 mm^2 Cu
Design-reference external cable	Nexans HFIX stranded 1×4 mm^2
Preliminary loop length	2 m
Loop resistance near 100°C	~ 0.0115 Ω
Loop loss at rated current	~ 0.11 W
Loop/heater loss ratio	~ 0.15%
Transformer transfer ratio k	To be measured under load
Controlled variable, HV-hot case	T_{HV}
Opposite-side acceptance variables	T_{GND}, gradient direction and realised $\lvert\Delta T\rvert$
Common-mode design voltage	60 kV
Transformer window	330×360 mm
Minimum modelled cable-to-core clearance	~ 151 mm
Representative outer silicone–air field	~ 1.2 kV/mm
Adopted air-side screening criterion	1.5 kV/mm
Final common-mode verification	Assembled electrical qualification

The preliminary calculation establishes three main points. First, a compact 24 V, 75 W cartridge heater provides nominal control margin above the order-50 W thermal design demand. Second, the 4 mm^2 floating conductor has a resistance several hundred times smaller than the heater resistance, so calculated conductor heating is negligible and the resistive dissipation is concentrated in the cartridge. Third, the concept-defining 60 kV common-mode insulation geometry passes the adopted numerical air-side screening criterion, with a representative outer silicone–air field of approximately 1.2 kV/mm compared with the 1.5 kV/mm screening value.

The principal unresolved feasibility question is the existing transformer's loaded capability. It must be shown to supply approximately 20–24 V at 2.6–3.1 A to the floating load while remaining within acceptable magnetic and thermal operating limits. The final heater termination and fit, primary-side excitation limits, controller tuning, opposite-electrode acceptance band, and completed composite-insulation arrangement also remain to be fixed or qualified on the realised system. The control logic defined in Figure D.1 therefore provides the intended functional sequence, while its numerical setpoints and protection limits remain method-qualification outputs.

E

Pressure Force and Tie-Rod Capacity Check

E.1. Purpose and design pressure

This appendix checks whether the eight M10 tie rods can carry the force produced by the chamber mechanical design pressure. The inner M6 Allen screws are not included because they close the split rod-seal gland; they are not the main chamber-retention fasteners.

The calculation starts from the specified pressure difference:

$$p_b = 6\ \text{bar} = 0.60\ \text{MPa} = 0.60\ \text{N mm}^{-2}. \tag{E.1}$$

The value is treated as an internal-to-external differential pressure. The normal experiments use air near atmospheric pressure; the 6 bar case is only the mechanical design case.

E.2. Force acting on one end flange

Pressure produces an axial force according to

$$F = pA. \tag{E.2}$$

The PMMA chamber bore has a diameter of 170 mm. However, the pressure does not necessarily stop at the bore edge. It can also enter the small contact interface between the PMMA tube end and the PEEK flange. It is stopped by the FKM face seal.

There is only one pressure: 6 bar. The larger diameter is used only to define a conservative pressure-loaded area. The outside diameter of the face-seal groove, 194.18 mm, is used as the pressure boundary. This slightly overestimates the loaded area and is therefore conservative.

The conservative projected area is

$$A_p = \frac{\pi D_p^2}{4} = \frac{\pi(194.18)^2}{4} = 29\,614\ \text{mm}^2. \tag{E.3}$$

The resulting force on one end flange is

$$F_p = p_b A_p = (0.60)(29614) = 17.77\ \text{kN}. \tag{E.4}$$

For comparison, using only the 170 mm chamber bore would give 13.62 kN. The conservative seal-boundary calculation adds 4.15 kN. This is not a second pressure load; it is the same pressure acting over the additional annular interface area.

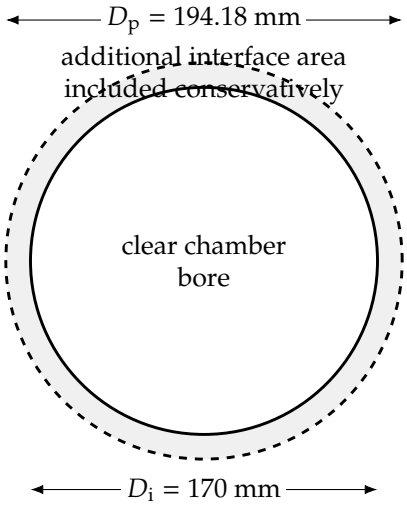


Figure E.1: Projected pressure area used in the tie-rod check. The same internal pressure acts over both regions.

E.3. Design load shared by the tie rods

A screening factor of $\gamma_F = 2.0$ is applied:

$$F_{p,d} = \gamma_F F_p = 2.0(17.77) = 35.54\,\text{kN}. \tag{E.5}$$

The chamber uses eight equally spaced tie rods. With equal load sharing, the design pressure load per tie rod is

$$F_{tr,d} = \frac{F_{p,d}}{8} = \frac{35.54}{8} = 4.44\,\text{kN}. \tag{E.6}$$

The selected value $\gamma_F = 2.0$ is a thesis-specific conservative screening factor used to test the preliminary tie-rod sizing against the simplifying assumptions of the load calculation. These include idealised load sharing between the tie rods and omission of the detailed joint-stiffness, preload and time-dependent deformation behaviour of the assembled flange system. The factor is not a pressure-vessel-code partial factor.

E.4. Capacity of one M10 tie rod

The selected fasteners are M10×1.5 A4-80 stainless-steel tie rods. The tensile stress area of one M10×1.5 thread is

$$A_s = \frac{\pi}{4}\,(d - 0.9382P)^2 = \frac{\pi}{4}\,(10 - 0.9382(1.5))^2 = 57.99\,\text{mm}^2. \tag{E.7}$$

Using the adopted minimum 0.2% proof strength of 600 MPa, the proof-load capacity of one tie rod is

$$F_{0.2} = A_s R_{p0.2,\min} = (57.99)(600) = 34.79\,\text{kN}. \tag{E.8}$$

The design pressure load uses

$$\eta_{0.2} = \frac{F_{tr,d}}{F_{0.2}} = \frac{4.44}{34.79} = 12.8\% \tag{E.9}$$

of the proof-load capacity of one tie rod.

E.5. Conservative check including preload

The preliminary preload is 5.0 kN per tie rod. In a real preloaded joint, only part of the external force normally becomes additional tie-rod load. For a simple conservative check, the complete design pressure load is added directly to the preload:

$$F_{tr,comb} = 5.0 + 4.44 = 9.44\,\text{kN}. \tag{E.10}$$

The corresponding utilisation is

$$\eta_{0.2,\mathrm{comb}} = \frac{9.44}{34.79} = 27.1\%. \tag{E.11}$$

The corresponding proof-load margin is

$$\mathrm{SF}_{0.2,\mathrm{comb}} = \frac{34.79}{9.44} = 3.68. \tag{E.12}$$

The total preliminary preload is 8(5.0) = 40.0 kN, which is slightly greater than the factored separating force of 35.54 kN. This comparison is only a preliminary closure check because PEEK creep, thermal expansion and preload scatter can reduce the available clamping force.

E.6. Result and limitations

Table E.1: Summary of the tie-rod design check.

Quantity	Result
Mechanical design pressure	6 bar
Conservative pressure-load diameter	194.18 mm
Pressure force on one end flange	17.77 kN
Factored end force, $\gamma_F = 2.0$	35.54 kN
Factored pressure load per tie rod	4.44 kN
Proof-load capacity per tie rod	34.79 kN
Pressure-only utilisation	12.8%
Conservative load including preload	9.44 kN
Utilisation including preload	27.1%
Proof-load margin including preload	3.68

On this static screening basis, the eight M10×1.5 A4-80 tie rods have sufficient direct tensile capacity for the force produced by the 6 bar mechanical design pressure. The conservative preload-inclusive load uses approximately 27% of the adopted proof-load capacity of each tie rod.

This result checks only the direct tensile capacity of the tie rods. It does not certify the complete chamber for 6 bar. Separate verification is required for flange bending and creep, washer bearing, PMMA stress, seal retention, joint opening, thermal expansion, preload loss and pressure cycling. The assembled chamber must also pass dimensional inspection, leak testing and pressure-retention testing before HV operation.

F

Derivation and Assessment of the Effective Air-Cavity Conductivity

F.1. Modelling choice and scope

The test-bench model contains an enclosed air domain surrounding the electrode–spacer assembly. Temperature differences in this region can produce buoyancy-driven natural convection in addition to molecular conduction. A resolved gas-flow model was investigated, but the tested formulations did not provide a sufficiently robust solution for the complete stepped chamber. The final thermal model therefore represents convection-enhanced heat transfer through

$$k_{\mathrm{air,eff}}(T) = 4.5\, k_{\mathrm{air}}(T). \tag{F.1}$$

The factor 4.5 is not an intrinsic material property of air. It is derived from a simplified electrode–spacer air-layer representation and then applied uniformly to the complete enclosed-air domain. This transfer is a reduced-order modelling assumption because the actual local gap width and temperature difference vary throughout the chamber.

Radiative heat transfer is solved separately. Equation (F.1) therefore represents only the reduced convection-enhanced contribution within the air domain and does not include surface-to-surface or surface-to-ambient radiation. The purpose of the approximation is to provide a stable spacer and solid temperature field for the subsequent electrical analysis. It is not intended to predict gas velocity, circulation cells, thermal boundary layers, or local convective heat-transfer coefficients.

F.2. Representative geometry and calculation inputs

The complete chamber is annular and stepped, so a single exact air-gap width cannot describe the complete domain. The primary screening calculation therefore uses the simplified electrode–spacer air region employed for the resolved-convection consistency study. Its representative air-layer width is

$$b_{\mathrm{ref}} = 45\ \mathrm{mm} = 0.045\ \mathrm{m}. \tag{F.2}$$

The dimension is measured normal to the opposing surfaces of the simplified air layer. It is not the full radial clearance of the complete test-bench chamber.

The representative high-temperature screening condition is

$$\Delta T_{\mathrm{ref}} = 74.6\ \mathrm{K}, \qquad T_f = 335.8\ \mathrm{K}. \tag{F.3}$$

The temperature difference is a simulation-based screening value and not an experimental measurement. The film temperature is used only for the transparent appendix calculation; the final COMSOL model retains temperature-dependent material functions.

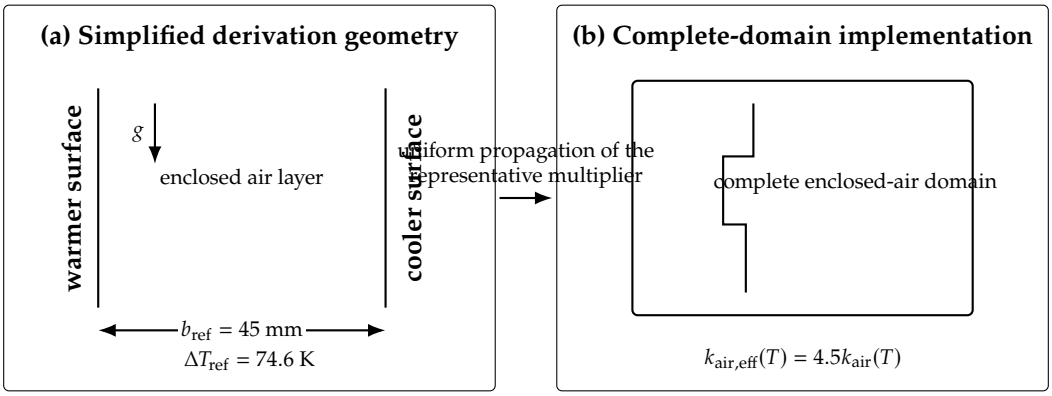


Figure F.1: Relationship between the simplified derivation geometry and the complete implementation domain. The Rayleigh–Nusselt screening calculation uses a representative 45 mm electrode–spacer air layer. The resulting multiplier is subsequently applied uniformly to the complete enclosed-air domain as a reduced-order approximation.

Table F.1: Inputs used to reproduce the Rayleigh–Nusselt screening calculation.

Quantity	Symbol	Value	Unit
Representative air-layer width	b_{ref}	0.045	m
Temperature difference	ΔT_{ref}	74.6	K
Film temperature	T_f	335.8	K
Density	ρ	1.051	$kg\,m^{-3}$
Dynamic viscosity	μ	2.01×10^{-5}	Pa s
Thermal conductivity	k_{air}	0.0288	$W\,m^{-1}K^{-1}$
Specific heat capacity	c_p	1007	$J\,kg^{-1}K^{-1}$
Thermal-expansion coefficient	$\beta = 1/T_f$	2.978×10^{-3}	K^{-1}
Gravitational acceleration	g	9.81	$m\,s^{-2}$

The derived properties are

$$\nu = \frac{\mu}{\rho} = 1.912 \times 10^{-5}\ \mathrm{m^2\,s^{-1}}, \tag{F.4}$$

$$\alpha = \frac{k_{\mathrm{air}}}{\rho c_p} = 2.721 \times 10^{-5}\ \mathrm{m^2\,s^{-1}}, \tag{F.5}$$

$$Pr = \frac{\nu}{\alpha} = 0.703. \tag{F.6}$$

F.3. Rayleigh–Nusselt derivation

F.3.1. Rayleigh number

For the representative layer,

$$Ra_b = \frac{g\beta\Delta T_{\mathrm{ref}} b_{\mathrm{ref}}^3}{\nu\alpha}. \tag{F.7}$$

Substitution gives

$$Ra_b = \frac{(9.81)(2.978 \times 10^{-3})(74.6)(0.045)^3}{(1.912 \times 10^{-5})(2.721 \times 10^{-5})} = 3.82 \times 10^5. \tag{F.8}$$

Thus,

$$\boxed{Ra_b \approx 3.8 \times 10^5.} \tag{F.9}$$

The result indicates that convection-enhanced heat transfer should not be omitted from the representative air-layer treatment. It does not determine the detailed flow pattern in the complete chamber. The result is also strongly geometry dependent because $Ra_b \propto b^3$.

F.3.2. Nusselt correlation and selected multiplier

The enclosed-air-layer correlation of ElSherbiny, Raithby, and Hollands is used as the engineering basis [73]. The three candidate branches used in the thesis are

$$Nu_1 = 0.0605 Ra_b^{1/3}, \tag{F.10}$$

$$Nu_2 = \left[1 + \left(\frac{0.104 Ra_b^{0.293}}{1 + (6310/Ra_b)^{1.36}}\right)^3\right]^{1/3}, \tag{F.11}$$

$$Nu_3 = 0.242 \left(\frac{Ra_b}{A}\right)^{0.272}, \qquad A = \frac{H}{b}. \tag{F.12}$$

Using $Ra_b = 3.82 \times 10^5$ gives

$$Nu_1 = 4.39, \qquad Nu_2 = 4.49. \tag{F.13}$$

The simplified region does not form one uniformly heated rectangular layer over a uniquely defined full height. To show the sensitivity of the aspect-ratio term, the internal chamber height $H = 0.280$ m is used as an upper axial-length estimate. This gives

$$A_{\mathrm{sens}} = \frac{0.280}{0.045} = 6.22, \tag{F.14}$$

and

$$Nu_3 = 0.242 \left(\frac{3.82 \times 10^5}{6.22}\right)^{0.272} = 4.85. \tag{F.15}$$

The formal maximum of the three evaluated branches is 4.85. The model therefore does not claim that the complete correlation returns exactly 4.5. Instead,

$$\boxed{Nu_{\mathrm{eff}} = 4.5} \tag{F.16}$$

Table F.2: Calculated Nusselt-number branches and the selected reduced-order value.

Branch	Value	Interpretation
Nu_1	4.39	Rayleigh-number scaling branch
Nu_2	4.49	Primary numerical basis for the final multiplier
Nu_3	4.85	Aspect-ratio sensitivity using $A_{\text{sens}} = 6.22$
Nu_{eff}	**4.5**	Selected reduced-order modelling value

is selected from the $Nu_2 = 4.49$ branch as a representative enhancement factor. The Nu_3 result is retained as an explicit indication of uncertainty associated with assigning a full height to the simplified local layer.

As an independent scale comparison, de Vahl Davis reported average Nusselt numbers of 1.118, 2.243, 4.519, and 8.800 at Rayleigh numbers 10^3, 10^4, 10^5, and 10^6, respectively [100]. The benchmark supports the physical plausibility of a cavity-average multiplier of order 4.5, but it does not validate the test-bench model because its square geometry and boundary conditions differ from the present arrangement.

F.4. Full-domain implementation and numerical assessment

F.4.1. COMSOL implementation

The selected multiplier is applied uniformly to the complete enclosed-air domain through

$$k_{\text{iso}} = 4.5\, k_{\text{air}}(T). \tag{F.17}$$

The base air conductivity remains temperature dependent. At the representative film temperature,

$$4.5(0.0288) = 0.1296\ \text{W m}^{-1}\text{K}^{-1}, \tag{F.18}$$

but this constant value is illustrative only and is not entered directly in the final material definition.

The final air-domain material treatment is

$$\rho = \rho_{\text{air}}(T), \qquad c_p = c_{p,\text{air}}(T), \qquad k = 4.5 k_{\text{air}}(T). \tag{F.19}$$

No gas velocity or pressure field is solved in the final model. Radiation remains separate and is implemented through the radiation physics described in Appendix G; the 4.5 multiplier is not applied to any radiative term.

The transfer assumption can be summarised as

$$\underbrace{Nu_{\text{eff}} = 4.5}_{\text{simplified-layer derivation}} \longrightarrow \underbrace{k_{\text{air,eff}}(T) = 4.5 k_{\text{air}}(T)}_{\text{complete-domain implementation}} . \tag{F.20}$$

The value 4.5 is therefore not interpreted as the exact local Nusselt number at every position in the chamber.

F.4.2. Resolved-convection assessment

A coupled flow and heat-transfer model was examined before the reduced treatment was adopted. The simplified electrode–spacer air region converged and provided a temperature-profile consistency case. The investigated complete-cavity formulations did not provide a sufficiently robust solution for the repeated electrothermal studies.

These outcomes show that the tested complete-cavity formulations were not sufficiently robust; they do not identify one unique physical cause. Janssen and Henkes demonstrate the mesh and discretisation sensitivity of enclosed natural-convection calculations, especially at high Rayleigh numbers [101]. Their bifurcation regime occurs at Rayleigh numbers of order 10^8 and therefore does not establish physical bifurcation as the cause of the present numerical behaviour.

Table F.3: Summary of the resolved-convection model assessment.

Model or solver treatment	Observed result
Simplified electrode–spacer air region	Converged and provided a usable comparison profile
Complete stationary segregated model	Residual growth or stalling
Time-dependent initialisation	Failure near initialisation
Fully coupled Boussinesq variations	Oscillation or residual stalling
Alternative density formulations	No sufficiently robust usable solution

F.4.3. Temperature-profile consistency check

The spacer-temperature profile was compared for three thermal representations:

1. conduction and radiation only;
2. resolved natural convection in the simplified electrode–spacer geometry;
3. radiation and the final effective conductivity from Equation (F.1).

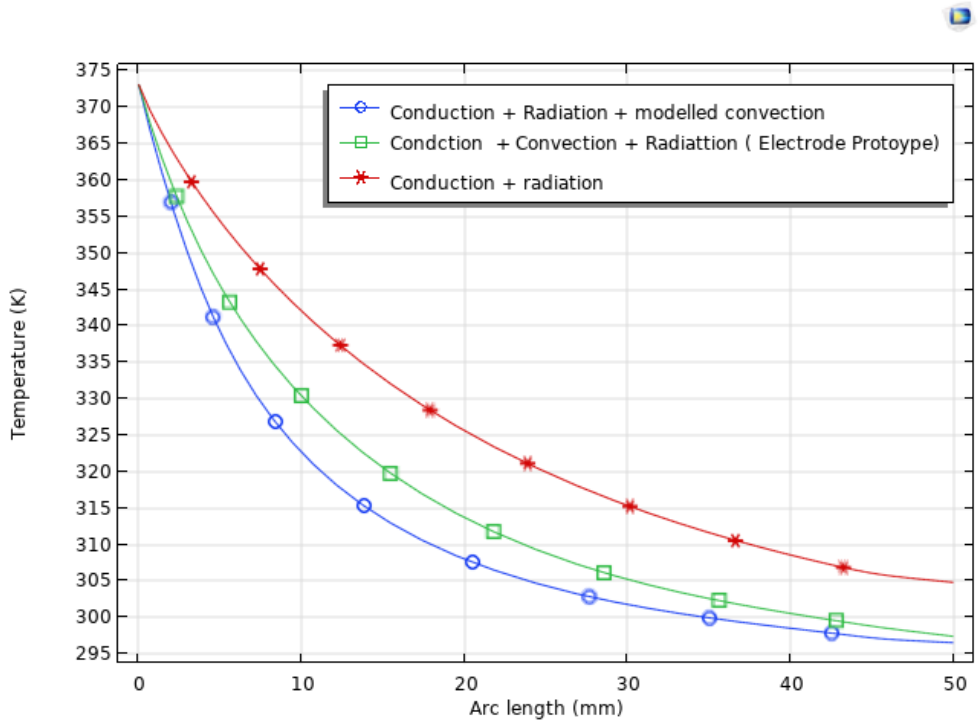


Figure F.2: Spacer-temperature profiles obtained using conduction and radiation only, resolved natural convection in the simplified electrode–spacer geometry, and the final effective-conductivity model $k_{\mathrm{air,eff}}(T) = 4.5k_{\mathrm{air}}(T)$. The resolved-flow profile is used as a qualitative consistency check and not as validation of the complete chamber.

The effective-conductivity treatment shifts the calculated spacer-temperature profile toward the simplified resolved-convection result compared with conduction and radiation alone. Exact agreement is not expected because one model resolves directional flow in a reduced geometry, whereas the other applies an isotropic conductivity enhancement throughout the complete air domain.

F.5. Limitations and future refinement

The final treatment does not resolve gas velocity, pressure, circulation cells, plume formation, boundary-layer thickness, local convection coefficients, spatial variation of the local Nusselt number, or circumferential asymmetry. The value 4.5 must therefore be interpreted as a representative global multiplier

rather than the exact local Nusselt number throughout the chamber.

After thermal commissioning, the approximation can be generalised as

$$k_{\mathrm{air,eff}}(T) = C_k k_{\mathrm{air}}(T), \tag{F.21}$$

where C_k is calibrated against measured electrode, spacer, and chamber-wall temperatures. The calibrated value should then be assessed using an independent thermal condition, such as another oil temperature or warm-up cycle. The same dataset should not be used both to calibrate the multiplier and to claim validation.

If one global multiplier cannot reproduce the measured temperature field over several conditions, separate regional multipliers may be considered. Such an extension should only be introduced when sufficient measurements are available to identify the additional parameters without overfitting. No experimental calibration or validation was performed in this thesis.

F.6. Reproducibility summary

Table F.4: Reproducibility summary for the effective air-cavity conductivity treatment.

Item	Final treatment
Gas medium	Air at approximately 1 bar
Derivation geometry	Simplified electrode–spacer air layer
Characteristic width	$b_{\mathrm{ref}} = 45$ mm
Temperature difference	$\Delta T_{\mathrm{ref}} = 74.6$ K
Film temperature	$T_f = 335.8$ K
Rayleigh number	$Ra_b = 3.82 \times 10^5$
Correlation source	ElSherbiny, Raithby, and Hollands
Calculated branches	$Nu_1 = 4.39$, $Nu_2 = 4.49$, $Nu_3 = 4.85$
Selected multiplier	$Nu_{\mathrm{eff}} = 4.5$
COMSOL air conductivity	$k = 4.5 k_{\mathrm{air}}(T)$
Implementation domain	Complete enclosed-air domain
Radiation	Solved separately
Resolved gas flow in final model	Not solved
Simplified resolved-flow model	Qualitative consistency check
Experimental calibration or validation	Not performed

To reproduce the calculation and implementation:

1. use the simplified 45 mm air-layer definition shown in Figure F.1;
2. evaluate the properties in Table F.1 at $T_f = 335.8$ K and approximately 1 bar;
3. calculate ν, α, and Ra_b using Equations (F.4)–(F.8);
4. evaluate Equations (F.10)–(F.12);
5. select $Nu_{\mathrm{eff}} = 4.5$ as defined in Equation (F.16);
6. in the complete air domain, set $k = 4.5 k_{\mathrm{air}}(T)$; retain the original temperature-dependent density and heat capacity, and solve radiation separately.

The resulting model reproduces the thermal approximation used for the final electrothermal studies. It does not reproduce a resolved gas-flow field and should not be interpreted as an experimentally validated full-cavity convection model.

G

COMSOL Model Definition and Reproducibility

This appendix records the final COMSOL implementation used for the thermal and electrical simulations reported in Chapter 9. It complements the modelling method in Chapter 8 by listing the model inputs, study sequence, solution transfer, mesh definition and post-processing quantities needed to reconstruct the calculations. The derivation of the enclosed-air heat-transfer approximation is given separately in the corresponding appendix; only its final implementation is stated here.

G.1. Model architecture and studies

The model was developed in COMSOL Multiphysics 6.2.0.415 as a two-dimensional axisymmetric representation of the test bench. Heat transfer and radiation were solved first, after which the resulting stationary temperature field was transferred to the Electric Currents interface. The electrical studies therefore used one-way sequential coupling: temperature affected the conductivity distribution, while electrical losses did not feed back into the thermal solution.

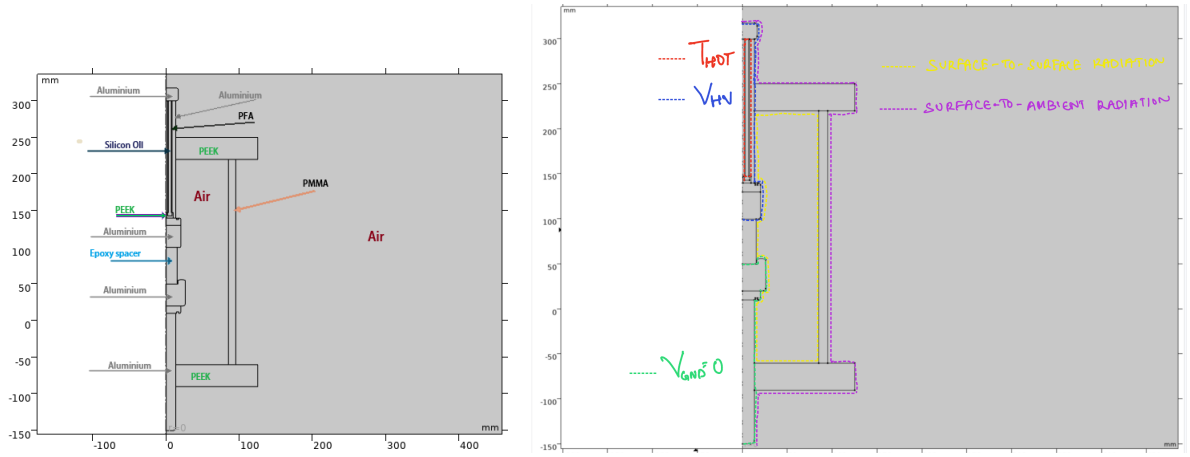
A time-dependent thermal study calculated the heating process from the initial condition, while a stationary thermal study provided the settled field

$$T_{\mathrm{ss}}(\mathbf{x}) \tag{G.1}$$

used by the electrical studies. The electrical model represents the transition from the initially permittivity-controlled field toward the conductivity-controlled DC field. It does not resolve gas ionisation, gas-ion transport, independent surface-charge transport, discharge inception or flashover propagation.

Table G.1: Final COMSOL model and study configuration.

Item	Final implementation
Spatial representation	Two-dimensional axisymmetric
Thermal physics	Heat Transfer in Solids and Surface-to-Surface Radiation
Electrical physics	Electric Currents
Coupling	Stationary thermal solution transferred to the electrical studies
Initial and ambient temperature	293 K
Oil-region temperature	100 °C
Applied electrical stress	60 kV
Voltage ramp	200 s, followed by a constant-voltage hold
Electrical output states	End of ramp (0 h), 1 h, 12 h and 24 h
DC reference	Separate stationary Electric Currents solution
Mesh	Physics controlled, *Extremely fine*
Solver configuration	COMSOL defaults; no manual tolerance or time-step changes



(a) Material-domain assignments.

(b) Principal thermal and electrical boundary groups.

Figure G.1: Final numerical representation of the test bench. The spacer–air interface used for electric-field extraction is the exposed epoxy boundary between the two electrode regions in panel (a).

Table G.2: Thermal and electrical properties used in the final model.

Material	k [W m^{-1} K^{-1}]	ρ [kg m^{-3}]	c_p [J kg^{-1} K^{-1}]	ε_r	σ [S m^{-1}]
Aluminium	237	2700	900	–	3.77×10^{7}
Epoxy	0.40	1200	1000	4.4	$\sigma_{\mathrm{ep}}(T)$
PEEK	0.25	1300	2160	3.2	2×10^{-15}
PMMA	0.31	1410	1460	3.7	1×10^{-15}
PFA	0.19	2150	1050	2.1	1×10^{-16}
Silicone oil	0.15	960	1500	2.7	1×10^{-12}
Air	$4.5k_{\mathrm{air}}(T)$	$\rho_{\mathrm{air}}(T)$	$c_{p,\mathrm{air}}(T)$	1.0	1×10^{-14}

G.2. Domains, material properties and boundary conditions

Figure G.1 identifies the material domains and the principal thermal and electrical boundary groups. The detailed dimensions are defined in the design chapters and are not repeated here.

The material properties entered in the final model are listed in Table G.2. Temperature-dependent air properties were taken from the COMSOL material definition. Natural-convection heat transfer in the enclosed air was represented by

$$k_{\mathrm{air,eff}}(T) = 4.5\, k_{\mathrm{air}}(T), \tag{G.2}$$

with radiation treated separately. The factor 4.5 is an engineering approximation rather than an intrinsic property of air.

The temperature-dependent epoxy conductivity was implemented as

$$\sigma_{\mathrm{ep}}(T) = \sigma_{\mathrm{ref}} \exp\left[\frac{E_a}{k_B}\left(\frac{1}{T_{\mathrm{ref}}} - \frac{1}{T}\right)\right], \tag{G.3}$$

where

$$\sigma_{\mathrm{ref}} = 1.0 \times 10^{-16}\ \mathrm{S\,m^{-1}}, \quad T_{\mathrm{ref}} = 293\ \mathrm{K}, \quad E_a = 0.5\ \mathrm{eV}, \quad k_B = 8.617 \times 10^{-5}\ \mathrm{eV\,K^{-1}}. \tag{G.4}$$

These values were prescribed model inputs and were not obtained from measurements on the intended specimen.

The silicone-oil region was maintained at 100 °C, while the remaining domains were initially set to 293 K. Surface-to-surface radiation was applied between the selected internal surfaces, and surface-to-ambient radiation used an ambient temperature of 293 K. The applied-potential and grounded boundaries are shown in Figure G.1b. The surface emissivities were 0.07 for aluminium, 0.85 for epoxy, 0.85 for PMMA and 0.90 for PEEK.

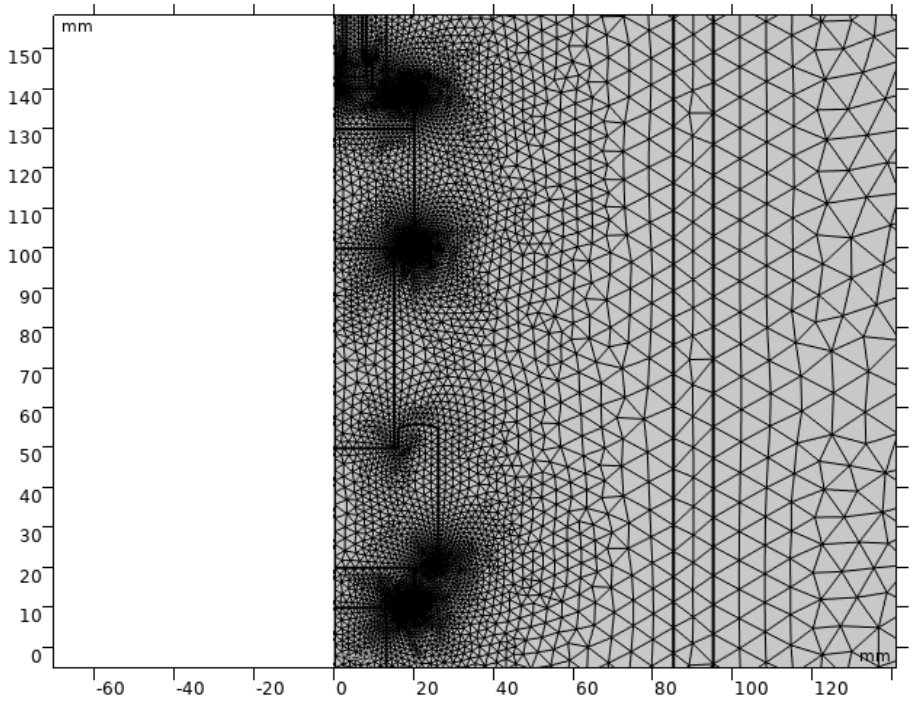


Figure G.2: Local view of the final physics-controlled mesh. The *Extremely fine* setting produces dense refinement around the spacer and electrode regions and progressively larger elements toward the outer chamber.

The applied voltage was defined by the analytic function `Vramp`,

$$V_{\mathrm{app}}(t) = V_0 \min\left(\frac{t}{T_r}, 1\right), \qquad V_0 = 60\,\mathrm{kV}, \quad T_r = 200\,\mathrm{s}. \tag{G.5}$$

The opposite electrode was assigned $V = 0$.

G.3. Mesh, study sequence and solution transfer

The final geometry was discretised using COMSOL's physics-controlled triangular mesh with the size level set to *Extremely fine*. Automatic refinement was concentrated around the spacer–electrode interfaces and other small features, while larger elements were used toward the outer chamber, as shown in Figure G.2. No separate user-defined local mesh-size feature was introduced.

No formal multi-mesh convergence sweep was performed; the mesh setting is therefore reported as a discretisation choice rather than as a demonstrated mesh-independence result. The same final mesh was used consistently for the reported thermal and electrical calculations.

In the stationary temperature-dependent electrical study, only the Electric Currents interface was solved. Variables not solved for were imported using

```
User controlled > Method:  Solution >Study:  Heat Transfer, Stationary >Current
solution (sol1).
```

Heat Transfer in Solids and Surface-to-Surface Radiation were not re-solved in this electrical step. The same one-way transfer principle was used for the time-dependent electrical study, so the stationary temperature distribution remained fixed while the electric field evolved.

The voltage was ramped from 0 to 60 kV over 200 s and then held constant. Completion of the ramp defined the pre-stress origin,

$$t_{\mathrm{pre}} = 0. \tag{G.6}$$

The end-of-ramp solution was retained as the 0 h capacitive reference, and the 1 h, 12 h and 24 h solutions represented post-ramp DC pre-stress durations. A separate stationary Electric Currents study

at the same temperature distribution and applied voltage provided the conductivity-controlled DC reference. All studies retained the default COMSOL solver configuration; no solver tolerances, nonlinear controls or time-stepping settings were manually modified.

G.4. Post-processing definitions and model boundary

The thermal quantities extracted from the model were the temperatures associated with the HV- and grounded-side electrode regions,

$$T_{\mathrm{HV}}, \qquad T_{\mathrm{GND}}, \qquad \Delta T = T_{\mathrm{HV}} - T_{\mathrm{GND}}. \tag{G.7}$$

The electric-field magnitude was evaluated along the spacer–air interface Γ visible in Figure G.1a:

$$E_{\mathrm{norm}}(s,t) = \|\mathbf{E}(s,t)\|, \tag{G.8}$$

where s denotes position along the interface between its HV-side and grounded-side ends. The whole-profile difference from the stationary reference was quantified by

$$D_E(t) = \frac{\left[\displaystyle\int_\Gamma \left(E_{\mathrm{norm}}(s,t) - E_{\mathrm{norm,ss}}(s)\right)^2 \,\mathrm{d}s\right]^{1/2}}{\left[\displaystyle\int_\Gamma E_{\mathrm{norm,ss}}^2(s)\,\mathrm{d}s\right]^{1/2}}. \tag{G.9}$$

Local deviations at the two interface ends were calculated as

$$\delta_j(t) = \frac{E_{\mathrm{norm}}(s_j,t) - E_{\mathrm{norm,ss}}(s_j)}{E_{\mathrm{norm,ss}}(s_j)} \times 100\%, \qquad j \in \{\mathrm{HV}, \mathrm{GND}\}. \tag{G.10}$$

The 1 h, 12 h and 24 h profiles were compared independently with the stationary electrical solution. The 0 h field was used only as the end-of-ramp capacitive reference.

The model provides the pre-breakdown temperature distribution and conductivity-driven electric-field evolution within the defined axisymmetric arrangement. It does not calculate circumferential asymmetry, resolved airflow, independent surface-charge transport, gas ionisation, discharge propagation or the flashover event itself.

H

Qualification of the Reset Procedure and Run-to-Run Independence

H.1. Purpose and Operational Definition

This appendix defines how the reset procedure is qualified before the research campaign and how possible dependence between successive test runs is checked. The procedure supports the test method introduced in Chapter 10. It is separate from the research matrix: the reset and its acceptance rules are fixed method conditions, whereas temperature-gradient condition, polarity, and pre-stress duration are research factors.

A breakdown sequence is useful for statistical analysis only when the preceding run does not materially change the distribution of the next result. In the present bench, memory can remain in the gas, on insulating surfaces, on the common electrodes, or in the measurement system. A fresh specimen and a fixed waiting time therefore do not, by themselves, establish independence.

The following operational definition is used:

> Successive runs are treated as independent when, after the prescribed reset, the preceding test outcome has no detectable and practically relevant effect on either the measured initial state or the result of the next reference test.

This definition does not claim that the microscopic gas-ion and surface-charge distributions are identical before every run. Those states cannot be measured completely in the proposed apparatus. Instead, the qualification combines three forms of evidence:

1. the measured electrical, thermal, and environmental state returns to its qualified reference range;
2. a preceding disruptive event and a preceding non-disruptive hold give equivalent next-test results after reset; and
3. the ordered reference sequence shows no systematic trend, clustering, or other serial dependence.

No physical reset or independence qualification was performed in this thesis. The reset duration, current limits, averaging windows, and practical-equivalence limits remain outputs of future commissioning.

H.2. Sources of Carry-Over

Table H.1 summarises the main mechanisms through which one run may affect the next.

Koch et al. showed that a preceding breakdown and a preceding withstand can leave different ion densities in an electronegative gas. At short recovery times, the calculated breakdown probability depended on the outcome of the previous test [82]. Their numerical waiting time applies to pressurised SF_6 and is not transferred to the present air–epoxy arrangement.

Table H.1: Possible sources of carry-over between successive runs.

Source	Possible effect on the next run	Available indication
Gas ions after a disruptive event	Changed start-electron availability and statistical time lag	Previous-outcome comparison; purge and recovery study
Ion depletion after a withstand	Different gas state from that following a breakdown	Previous-outcome comparison
Discharge products	Changed gas condition or increased pulse activity	Dry-air purge; fast-current record
Residual surface charge	Changed field along the gas–solid interface	Current transient; selected surface-potential measurement
Electrode erosion or conditioning	Drift in event voltage, scatter, or discharge location	Inspection; run-order analysis
Deposits or contamination	New local stress or leakage path	Inspection; slow-current signature
Specimen history	Changed surface-flashover behaviour	Fresh specimen; specimen traceability
Thermal or environmental drift	Changed gas strength and surface conduction	Pressure, temperature, and relative-humidity records
Measurement drift	Apparent change in voltage or current response	Zero checks and repeated reference measurements

Surface charge introduces a separate memory mechanism. Kindersberger and Lederle separated bulk conduction, surface conduction, and neutralisation by gas ions in their model and measurements [30], [31]. The measured decay depended on the material, gas, enclosure, and available gas volume. A single universal surface-charge recovery time is therefore not available.

The common electrodes may also change during repeated tests. Hauschild and Mosch describe conditioning, residual space charge, particle modification, and breakdown energy as possible causes of dependence in high-voltage experiments [81]. Simka et al. reduced the energy delivered to a breakdown and actively restored the gas-ion state before each impulse test [103]. Their AC ion-sweeping step is not adopted here because it would add an additional electrical history to the epoxy spacer. The general principle retained is that the gas state and electrode condition must both be controlled.

H.3. Reset Procedure and Long-Reset Reference

H.3.1. Check for Initial Apparatus Conditioning

Before the reset is qualified, a short preliminary sequence is used to check whether the new or recently serviced arrangement is still conditioning. Sacrificial specimens are used, and these observations are excluded from the independence study and the research campaign.

For each preliminary event, the event voltage, event class, visible event region, slow-current response, transient charge, and fast-pulse activity are plotted against test number. Initial observations are excluded until no continuing directional change is visible and no new electrode damage or discharge deposit is developing. Koch used the same principle by excluding preliminary AC events that showed conditioning before evaluating the retained breakdown sequence [102].

The protection resistor and source-isolation system must limit the energy delivered to a disruptive event. A hardware change, electrode cleaning, electrode replacement, visible erosion, or a non-target discharge requires the conditioning check to be repeated.

H.3.2. Physical Reset

The physical reset begins when the voltage source has been isolated. The following sequence is applied after each completed voltage application:

1. de-energise the source;
2. discharge the high-voltage circuit through the approved discharge path;
3. visibly ground and short the main electrodes;

4. remove the tested specimen;
5. inspect the electrodes, spacer contacts, chamber wall, feedthrough, and auxiliary insulation;
6. record any arc mark, deposit, contamination, or mechanical change;
7. install a fresh, previously unflashed specimen from the qualified production batch;
8. pass filtered dry air through the chamber;
9. restore the accepted pressure, gas temperature, and relative humidity;
10. restore the required electrode temperatures and temperature difference; and
11. perform the electrical and measurement checks in Section H.4.

Okabe et al. restored a GIS test arrangement after breakdown by overhauling the equipment, purging the gas, and returning it to the designated condition before testing continued [104]. This supports resetting the complete apparatus rather than relying on waiting time alone.

Evacuation is not included in the baseline procedure because the chamber has not been qualified for external pressure. The dry-air purge is performed near atmospheric pressure. The purge is recorded as a nominal number of chamber-volume exchanges,

$$N_{\mathrm{ex}} = \frac{\dot{V}_{\mathrm{air}}\, t_{\mathrm{purge}}}{V_{\mathrm{ch}}}, \tag{H.1}$$

where $\dot{V}_{\mathrm{air}}$ is the qualified volumetric flow, t_{purge} is the purge time, and V_{ch} is the chamber volume. This quantity provides a reproducible purge measure; it does not prove complete gas replacement.

H.3.3. Long-Reset Reference

A deliberately conservative reset is first used to establish the reference state. It includes the complete physical reset, a purge and grounded recovery longer than the initial routine proposal, full restoration of the thermal and environmental state, and an additional observation period during which all reset indicators remain stable.

The long reset is extended once more during commissioning. It is accepted as the reference only when the further extension produces no practically relevant change in the measured reset indicators or in the next reference result. The published SF_6 waiting times are not used as acceptance values because they do not represent the gas, pressure, solid surface, voltage history, or thermal condition of the present bench [82].

A practical starting target is ten valid long-reset reference cycles. This is not an independence requirement specified by IEC 62539. It is chosen to estimate the baseline centre and scatter with more than a minimal sample; IEC 62539 warns that serious errors may result from very small breakdown datasets and recommends at least ten specimens where possible [57]. The baseline is re-established after a change in specimen batch, electrode system, chamber configuration, or measurement chain.

H.4. Measured Reset Indicators

H.4.1. Thermal and Environmental State

The next run may begin only after the following quantities return to their qualified ranges:

$$p, \quad T_{\mathrm{gas}}, \quad RH, \quad T_{\mathrm{HV}}, \quad T_{\mathrm{GND}}, \quad \Delta T. \tag{H.2}$$

Their drift must also satisfy the limits established during bench qualification. A quantity that enters its accepted range only briefly while continuing to drift does not pass the reset gate.

H.4.2. Grounded-System Current

After grounding, the slow-current channel is recorded as $I_{\mathrm{g}}(t)$. This check confirms that the discharge circuit and electrometer have returned to their normal grounded response and that no abnormal continuing leakage or pulsed activity remains. It does not show that all surface charge has disappeared.

The accepted grounded-current range is obtained from the long-reset cycles. A routine reset passes when, for a predefined number of consecutive averaging windows,

$$I_{\mathrm{g}} \in \left[I_{\mathrm{g,L}}, I_{\mathrm{g,U}} \right], \tag{H.3}$$

and

$$\left| \frac{\mathrm{d}I_{\mathrm{g}}}{\mathrm{d}t} \right| \leq S_{\mathrm{g,max}}. \tag{H.4}$$

The averaging interval and the required number of consecutive windows are selected from the electrometer response and measured noise. No universal threshold such as $I_{\mathrm{g}} < 1$ pA is imposed. The relevant condition is return to the grounded baseline of this apparatus.

H.4.3. Current During the Prescribed Voltage Waveform

A second current check is made during a fixed part of the normal voltage-application sequence. A separate diagnostic voltage is avoided because it would introduce an additional electrical history.

The mean current over the reference interval is

$$I_{\mathrm{ref}} = \frac{1}{t_2 - t_1} \int_{t_1}^{t_2} I(t)\, \mathrm{d}t. \tag{H.5}$$

The remaining drift is represented by the fitted slope S_I over the same interval. The transient transferred charge is approximated by

$$Q_{\mathrm{tr}} = \int_{t_0}^{t_2} \left[I(t) - I_{\mathrm{ref}} \right] \mathrm{d}t. \tag{H.6}$$

These quantities describe the response of the complete circuit. They can reveal a change in bulk conduction, surface conduction, gas current, stray leakage, contact condition, or moisture, but they do not identify the individual contribution. A current signature passes only when I_{ref}, S_I, Q_{tr}, current noise, and fast-pulse activity lie within the condition-specific ranges obtained from the long-reset reference. Separate ranges are required where polarity or temperature produces a materially different current response.

An unresolved current anomaly stops the run before the final voltage rise. The bench is reset and inspected. A test completed with an unresolved anomaly is excluded from the primary dataset.

H.4.4. Selected Surface-Potential Measurements

During method qualification, selected specimens should be checked with a non-contact surface-potential instrument where this is technically practicable. Kindersberger and Lederle verified a charge-free initial state by measurement and showed that the spatial potential distribution can change shape during decay [31]. This measurement is more direct than total circuit current for detecting residual surface charge.

Measurements should compare a fresh specimen, a specimen after a representative non-disruptive DC hold, and a specimen removed after a disruptive event. Fixed measurement positions and fixed times after voltage removal are required. Routine scans are not needed before every campaign run once the fresh-specimen preparation and reset procedure have been qualified.

H.5. Carry-Over Qualification Experiment

H.5.1. Reference Condition and Test Matrix

One fixed reference condition is used throughout the qualification. It uses one polarity, one thermal condition, one pre-stress voltage and hold procedure, one final voltage-rise rate, fresh specimens from

the same production batch, and the same measurement arrangement. The chosen condition should be reproducible and sensitive to a change in the bench state.

The basic carry-over matrix is given in Table H.2. It tests the two histories identified by Koch et al.: a preceding disruptive event and a preceding withstand [82].

Table H.2: Basic carry-over qualification matrix.

Preceding outcome	Reset before next test	Next test
Confirmed surface flashover	Normal reset	Fixed reference test
Confirmed surface flashover	Extended reset	Fixed reference test
Non-disruptive withstand	Normal reset	Fixed reference test
Non-disruptive withstand	Extended reset	Fixed reference test

A clear gas-gap discharge is added as a third preceding-outcome class when enough such events are available. A hardware discharge is not treated as a factor level. It triggers inspection, correction, and renewed qualification.

The extended reset is defined before the study. It is longer than the normal reset and includes an additional period during which all measured reset indicators remain stable. It is not assumed to be a perfectly charge-free state; it provides a conservative comparison with the routine procedure.

H.5.2. Execution and Recorded Responses

Each carry-over cycle consists of the following steps:

1. perform the prescribed preceding voltage treatment on a sacrificial specimen;
2. classify the outcome;
3. apply the assigned normal or extended reset;
4. install a fresh specimen;
5. restore the fixed reference condition;
6. verify the reset indicators;
7. perform the reference voltage-rise test; and
8. record the complete electrical, optical, thermal, and environmental response.

The four combinations are randomized within practical blocks. Each block should contain all four combinations where scheduling permits. This prevents gradual apparatus drift from being confused with preceding-outcome or reset-duration effects.

A target of ten valid next-reference observations per combination is proposed, giving approximately 40 observations for the basic matrix. This is an experimental planning target rather than a standard requirement. It must be reconsidered after the baseline scatter, censoring frequency, and practical-equivalence limits are known.

The recorded response includes:

- exact confirmed surface-flashover voltage;
- censoring voltage after a gas-gap event or after reaching the stop voltage;
- event class and earliest optically resolved event region;
- I_{ref}, S_I, and Q_{tr};
- current noise and fast-pulse activity; and
- all controlled thermal and environmental quantities.

IEC 62539 distinguishes complete and censored breakdown datasets [57]. A clear gas-gap event or a run stopped without surface flashover is therefore retained as a right-censored surface-flashover

observation. A hardware event, invalid controlled state, or missing critical record is excluded and investigated.

H.6. Statistical Assessment and Acceptance

H.6.1. Practical Equivalence

Failure to find a statistically significant difference is not sufficient evidence that the carry-over effect is negligible. The largest acceptable effects are therefore defined before the qualification data are analysed. They are denoted by

$$\delta_U, \qquad \delta_I, \qquad \delta_Q, \qquad \delta_p, \tag{H.7}$$

for event voltage, reference current, transient charge, and event-class probability, respectively. The limits are based on measurement uncertainty, baseline repeatability, voltage-ramp resolution, and the smallest difference that the research campaign is intended to interpret.

Let $\Delta_{\mathrm{prev},Y}$ be the estimated effect of the preceding outcome on response Y, and let $\Delta_{\mathrm{reset},Y}$ be the effect of normal versus extended reset. Operational equivalence is accepted only when

$$CI\big(\Delta_{\mathrm{prev},Y}\big) \subset [-\delta_Y, \delta_Y] \tag{H.8}$$

and

$$CI(\Delta_{\mathrm{reset},Y}) \subset [-\delta_Y, \delta_Y]. \tag{H.9}$$

The interaction between preceding outcome and reset type is also checked because a reset may be sufficient after a withstand but not after a disruptive event. This equivalence-based interpretation follows the distinction between absence of evidence and evidence of a sufficiently small effect [105].

The voltage analysis must retain right-censored observations and should include preceding outcome, reset type, their interaction, run order, and test block. The distribution is selected after the data have been examined; this appendix does not impose a Weibull model.

H.6.2. Ordered-Sequence Checks

The carry-over comparison is the primary assessment. It is supplemented by the high-voltage sequence checks described by Hauschild and Mosch and applied by Koch [81], [102].

Run-order plot. The reference response is plotted against test number while the measurements are being performed. Separate plots are prepared for the voltage residual, I_{ref}, Q_{tr}, event class, and visible event region. A persistent rise, fall, change in scatter, cyclic pattern, or change after maintenance is investigated before testing continues.

Early-versus-late comparison. For a sufficiently long sequence of complete surface-flashover voltages, an early and a late subgroup are compared. Following the cited high-voltage precedent, the first ten and last ten valid exact observations may be used. For approximately normal, uncensored data, the variance ratio is

$$F = \frac{s_1^2}{s_2^2}, \qquad s_1^2 \geq s_2^2, \tag{H.10}$$

and, where the equal-variance assumption is acceptable, the mean comparison uses

$$t = \frac{\overline{U}_1 - \overline{U}_2}{s_p \sqrt{\frac{1}{n_1} + \frac{1}{n_2}}}, \tag{H.11}$$

with

$$s_p^2 = \frac{(n_1 - 1)s_1^2 + (n_2 - 1)s_2^2}{n_1 + n_2 - 2}. \tag{H.12}$$

A robust or censoring-aware comparison replaces these classical tests when their assumptions are not reasonable. Censored observations are not converted into exact voltages merely to enable the comparison.

Runs test. The iteration test used in the cited high-voltage literature is a runs test. It is applied to the ordered residuals after fixed block and test-condition effects have been removed. Each residual is assigned a positive or negative sign. A residual equal to zero is omitted. A run is an uninterrupted group of identical signs.

With n_+ positive residuals, n_- negative residuals, $n = n_+ + n_-$, and R observed runs, the expected number and variance are

$$\mu_R = 1 + \frac{2n_+n_-}{n}, \tag{H.13}$$

$$\sigma_R^2 = \frac{2n_+n_-\,(2n_+n_- - n)}{n^2(n-1)}. \tag{H.14}$$

For a sufficiently large sample, the standardized statistic is

$$z_R = \frac{R - \mu_R}{\sigma_R}. \tag{H.15}$$

An exact runs-test probability is preferred for a small sample. Too few runs indicate clustering of high and low results; too many indicate systematic alternation. Passing the test does not, by itself, establish independence.

Lag-one check. A lag plot and the supplementary correlation

$$r_1 = \operatorname{corr}(e_i, e_{i-1}) \tag{H.16}$$

are used to identify dependence between neighbouring residuals. The estimate is interpreted with caution for a short sequence and is not used as the sole pass–fail criterion.

H.6.3. Decision Rule

The routine reset is qualified only when all conditions in Table H.3 are met.

Failure of one criterion means that independence has not been qualified. Possible corrective actions include extending the purge or grounded recovery, improving environmental control, revising specimen handling, cleaning or replacing electrodes, reducing event energy, or correcting leakage and measurement problems. The revised reset is then qualified again.

A successful qualification is reported as follows:

> The prescribed reset restored the measured initial state, and neither the preceding outcome nor an extended reset produced a practically relevant change in the next reference result. The ordered reference sequence showed no systematic drift or non-random dependence. Successive runs are therefore treated as operationally independent within the conditions and resolution of the qualification.

Table H.3: Acceptance criteria for the reset and independence qualification.

Check	Acceptance condition
Physical reset	Grounding, inspection, specimen replacement, and dry-air purge completed
Thermal and environmental state	Values and drifts inside qualified ranges
Grounded-current response	Current level and slope inside long-reset baseline ranges
Reference-current response	I_{ref}, S_I, Q_{tr}, noise, and pulse activity inside condition-specific ranges
Normal versus extended reset	Confidence interval for each relevant effect inside its equivalence limits
Previous flashover versus withstand	Confidence interval for each relevant effect inside its equivalence limits
Outcome–reset interaction	No practically relevant interaction remains
Ordered sequence	No unexplained trend, scatter change, clustering, or alternation
Event classes	No practically relevant dependence on previous event or run order
Hardware condition	No unresolved damage, contamination, or non-target discharge path

H.7. Campaign Monitoring and Required Records

The qualification applies only to the apparatus configuration, specimen batch, operating envelope, and measurement arrangement used during the study. Reference-condition runs are therefore inserted:

- at the start and end of each experimental block;
- after electrode cleaning, adjustment, or replacement;
- after a hardware discharge or unusually energetic event;
- after a failed current or environmental reset check;
- after a long interruption in testing; and
- at fixed intervals during an extended campaign.

The main research conditions are randomized within practical blocks. Complete randomization may be impractical for long pre-stress holds, but the sequence must not place all observations from one research condition before all observations from another. Test date, block, specimen batch, operator, and electrode condition are recorded.

When a reference run fails, testing is paused and the bench is inspected and reset. Results collected since the last accepted reference run are held for review. The affected tests are repeated when the controlled initial state cannot be demonstrated.

Table H.4: Minimum record for reset and carry-over qualification.

Group	Field	Examples	Use
Reset	Time and purge	Grounding time; purge time; N_{ex}	Procedure traceability
Environment	Initial state	p, T_{gas}, RH, T_{HV}, T_{GND}, ΔT	Reset gate
Electrical	Current signature	I_{g}, current slope, I_{ref}, S_I, Q_{tr}, pulse activity	Initial-state comparison
Previous run	History	Event class; voltage history; reset type	Carry-over analysis
Next reference run	Response	Exact or censored voltage; event class; visible region	Independence assessment
Hardware	Condition	Electrode, contact, chamber, and specimen observations	Fault and conditioning check
Analysis	Sequence checks	Equivalence, early–late comparison, runs test, lag-one check	Acceptance decision

H.8. Summary

Run-to-run independence is qualified from the complete experimental sequence. Current measurements are useful reset indicators, but no absolute current threshold can establish independence. The current must return to the condition-specific baseline obtained after the conservative long reset.

The final decision combines the physical reset, reproduction of the measured initial state, direct comparison of normal and extended resets after different preceding outcomes, and checks on the ordered reference sequence. This follows established high-voltage practice for testing independence

before evaluating a breakdown distribution [81], [102], retains censored data according to IEC 62539 [57], and uses equivalence limits to distinguish an acceptably small effect from a merely non-significant result [105].